RR Lyrae stars as tracers of substructure and Galactic archaeology

Zdeněk Prudil

Dissertation
submitted to the
Combined Faculties of the Natural Sciences and Mathematics
of the Ruperto-Carola-University of Heidelberg. Germany
for the degree of
Doctor of Natural Sciences

Put forward by
Zdeněk Prudil
born in Boskovice, Czech Republic
Oral examination: 27 April 2020

RR Lyrae stars as tracers of substructure and Galactic archaeology

Referees: Prof. Dr. Eva K. Grebel

Prof. Dr. Joachim Wambsganss

Abstract

The submitted thesis encompasses several topics linked to the usage of RR Lyrae stars in various astrophysical applications related mainly to Galactic archaeology. In addition, projects related to pulsation and physical properties of RR Lyrae variables are also discussed, e.g., uncertainty in the mass of RR Lyrae stars and distortion of photometric light curves due to the shocks.

In our first study, we employed several classes of variable stars (including RR Lyrae variables) to examined a small overdensity found north from the Small Magellanic Cloud – SMCNOD. Using variable stars spatially associated with the SMCNOD we linked this overdensity with the Small Magellanic Cloud. We also speculated about its origin from the Small Magellanic Cloud, due to one of the interactions with the Large Magellanic Cloud.

Two subsequent projects focused on the spatial and kinematical study of the Galactic bulge using the RR Lyrae stars. In the central region of the Milky Way, we found two distinct groups of RR Lyrae stars that differ in their pulsation properties. We associated them with the Oosterhoff groups previously found in the Milky Way's globular clusters. Both populations are evenly distributed in the Galactic bulge and neither of them can be spatialy and kinematically associated with the Galactic bar.

The RR Lyrae stars in the solar neighbourhood and their association with the Galactic disc is discussed in the following project. We found a small population of the local RR Lyrae stars (up to ≈3 kpc distance from the Sun) that kinematically and chemically resembles the thin disc population of stars. Our finding challenges our understanding of the Galactic disc formation, which if these RR Lyrae stars are truly members of the Galactic thin disc, happened more than 10 Gyr ago.

The last two studies focus on the properties of RR Lyrae stars as variable objects and expand our current knowledge about their pulsation and physical properties. First, we expanded the current number of candidates for binary systems among RR Lyrae stars. We analyzed the variation in their ephemerides and estimated the physical parameters of a possible binary companion. Second, for the first time, we provided an extensive photometric study of the atmospheric shocks among RR Lyrae stars. We link the prominence of shocks in RR Lyrae phased light curves with their pulsation properties and discuss their selective behavior inside the Instability strip.

Zusammenfassung

Die eingereichte Arbeit umfasst mehrere Themen, die sich mit der Nutzung von RR-Lyrae-Sternen in verschiedenen astrophysikalischen Anwendungen in Verbindung mit Galaktischer Archäologie befassen. Zudem werden Projekte diskutiert, die mit der Pulsation und den physikalischen Eigenschaften von RR-Lyrae-Veränderlichen in Verbindung stehen. Als Beispiele sind die Unsicherheit der Masse von RR-Lyrae-Sternen und die Verzerrung von photometrischen Lichtkurven aufgrund von Schocks zu nennen.

In unserer ersten Studie nutzten wir mehrere Kategorien von veränderlichen Sternen (darunter RR-Lyrae-Veränderliche), um eine kleine Überdichte – genannt SMCNOD – nördlich der Kleinen Magellanschen Wolke zu untersuchen. Mittels veränderlicher Sterne, die räumlich mit SMCNOD assoziiert sind, konnten wir diese Überdichte mit der Kleinen Magellanschen Wolke in Verbindung bringen.

Zwei nachfolgende Projekte legten einen Fokus auf die räumliche und kinematische Untersuchung des Galaktischen Bulges mittels RR-Lyrae-Sternen. In der Zentralregion der Milchstraße fanden wir

zwei verschiedene Gruppen von RR-Lyrae-Sternen, die sich in ihren Pulsationseigenschaften unterscheiden. Wir assoziierten diese mit den Oosterhoff Gruppen, welche bereits zuvor in der Milchstraße zugehörigen Kugelsternhaufen gefunden wurden. Beide Populationen sind gleichmäßig im Galaktischen Bulge verteilt und keine der beiden kann aus räumlicher und kinematischer Sicht mit dem Galaktischen Balken in Verbindung gebracht werden.

Die RR-Lyrae-Sterne in der solaren Umgebung und deren Assoziierung mit der Galaktischen Scheibe wird im folgenden Projekt diskutiert. Wir fanden eine kleine Population von lokalen RR-Lyrae-Sternen (bis zu einer Entfernung von ≈3 kpc von der Sonne aus gesehen), die kinematisch und chemisch der Population von Sternen der dünnen Scheibe ähneln. Unsere Entdeckung fordert unser Verständnis der Entstehung der Galaktischen Scheibe heraus, da diese unter der Annahme, dass die RR-Lyrae-Sterne tatsächlich Mitglider der dünnen Galaktischen Scheibe sind, vor mehr als 10 Gyr stattfand.

Die letzten beiden Studien befassen sich mit den Eigenschaften von RR-Lyrae-Sternen als veränderliche Objekte und erweitern unseren derzeitigen Erkenntnisstand bezüglich deren Pulsation und physikalischen Eigenschaften. Als erstes erweiterten wir die derzeitige Anzahl von Kandidaten für Doppelsternsysteme unter den RR-Lyrae-Sternen. Wir analysierten die Variation ihrer Ephimeriden und shätzten die physikalischen Eigenschaften des möglichen Begleiters ab. Des weiteren stellten wir zum ersten Mal eine umfangreiche photometrische Studie der atmosphärischen Schocks in RR-Lyrae-Sternen zur Verfügung. Wir verknüpfen die Ausprägung von Schocks in synchronisierten RR-Lyrae-Lichtkurven mit ihren Pulsationseigenschaften und diskutieren ihr trennscharfes Verhalten im Instabilitätsstreifen.

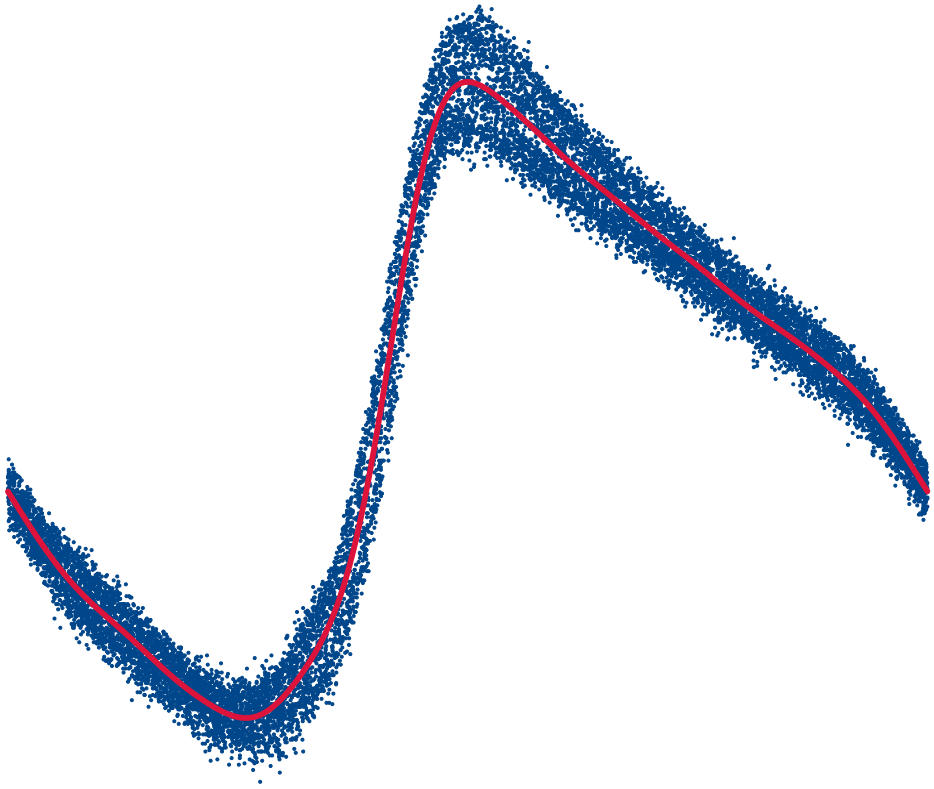

Mým rodičům, celé mé rodině

و تقدیم به فایضه چشم قهوه ای من

CONTENTS

LIST OF FIGURES

LIST OF TABLES

CHAPTER 1

INTRODUCTION

"So it begins..."

— Theoden, son of Thengel, Helm's Deep

The submitted thesis is a compilation of various projects not always directly connected to the Galactic archaeology, but more to the class of variables RR Lyrae stars as such. The initial two chapters of this thesis briefly describe the major points that are further developed in the subsequent chapters. The ensuing chapters contain *context* sections that should ease the process of understanding the studied problem. Following sections of this chapter are distilled from books Sparke & Gallagher (2007); Carroll & Ostlie (2007), and review papers Bland-Hawthorn & Gerhard (2016); D'Onghia & Fox (2016); Barbuy et al. (2018).

The Milky Way

The Milky Way (MW), the second-largest member of the Local Group of galaxies dominated by the galaxy in the constellation Andromeda (M31, in *Catalogue des Nébuleuses et des Amas d'Étoiles,* Messier 1781). It is a multi-arm barred massive spiral galaxy ($\approx 10^{12}\,M_\odot$, McMillan 2011) and it is enclosed in a cold dark matter halo, surrounded by the satellite dwarf galaxies, and their striped remnants (e.g., the Sagittarius dwarf galaxy and Sagittarius stream). Our Galaxy is a prime subject of studies focused on the Galactic archaeology, branch of astrophysics trying to disentangle the formation history of the MW. The MW can be dissected into three main components bulge, disc, and halo. The individual MW substructures will be discussed below, together with the two largest orbiting satellites, the Large and Small Magellanic Clouds (LMC and SMC). Our current view on the MW structure is predetermined by Sun's position inside the Galactic disc (see Fig. 1.1.1), from where we can see all of the MW substructures discussed below.

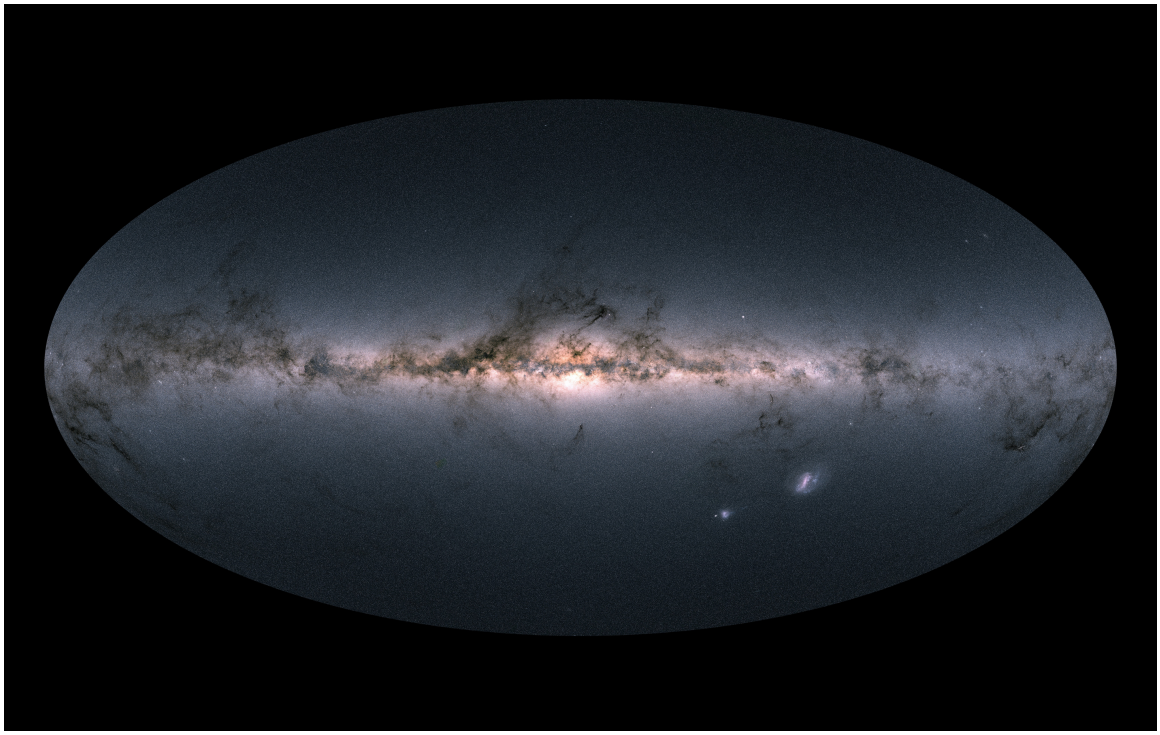

Figure 1.1.1: The map of MW as seen by the *Gaia* space telescope, the color information comes from the *Gaia* passbands; G_{BP}, G, and G_{RP} bands that represent blue, green, and red colors, respectively. *Image credit:* ESA/Gaia/DPAC, CC BY-SA 3.0 IGO

Galactic bulge

The name, Galactic bulge, refers to a central region of the MW, and its characterized by its boxy/peanut shape (discovered in the data from COBE space satellite, Weiland et al. 1994) and a supermassive black hole at its center (Sagittarius A*, Balick & Brown 1974) enclosed in a nuclear star cluster (Becklin & Neugebauer 1968). The first observation and identification of the Galactic bulge as the Galaxy component dates back to Baade (1946), who observed stars in one of the extinction-free windows. The presence of dust in the Galactic plane and its property to absorb light (extinction A_λ is wavelength-dependent $A_\lambda \propto \lambda^{-1}$) and high stellar density (problems with crowding) hampered the initial efforts to study the Galactic bulge.

Early studies considered the Galactic bulge to be formed through mergers during the formation of the MW, nowadays we recognize such formed bulges as the *classical bulges*. Later on, thanks to the near-infrared satellite COBE (Weiland et al. 1994) the boxy/peanut shape of the MW bulge has been discovered and later-on confirmed through spatial distribution studies of stars associated with the Galactic bulge (McWilliam & Zoccali 2010; Nataf et al. 2010). The boxy/peanut shape is characteristic for *pseudo bulges* which are quite common among all spiral galaxies (Barbuy et al. 2018), and originate from the buckling instabilities in the disc (Debattista et al. 2006; Martinez-Valpuesta et al. 2006). Both, the classical and

pseudo components can co-exist as it is seen in the spiral and lenticulars galaxies (Erwin et al. 2015). In general, the classical bulges share common properties with the elliptical galaxies, like pressure supported kinematics (random motion) with spheroidal rotation, high Sersic index ($n > 2$, Sérsic 1963), and are typical for early-type spiral galaxies. On the other hand, pseudo bulges are characterized by the cylindrical rotation, and low Sersic index $n > 2$ (Barbuy et al. 2018).

The MW pseudo bulge consists of the Galactic bar (Shen et al. 2010) which is supported by the intermediate-age population and can be traced, e.g., red clump stars (Wegg & Gerhard 2013). Although, whether the Galactic bulge consists of a young stellar population (< 2 Gyr) is a still matter of debate (see e.g., Bensby et al. 2017). The kinematics of the bulge stars and how they follow the Galactic bar has been studied through several spectroscopic surveys, e.g., BRAVA (Kunder et al. 2012) and ARGOS (Freeman et al. 2013; Ness et al. 2013b). Through the aforementioned spectroscopic surveys we know that the Galactic bulge has a complex metallicity distribution function, composed of 5 populations with different metallicities, varying for different Galactic coordinates, with two most pronounce populations peaking in metallicity distribution at supersolar ([Fe/H]≈ 0.1 dex) and subsolar ([Fe/H]≈ -0.25 dex) metallicities.

Galactic disc

The Galactic disc represents a major baryonic matter (stars and gas) contributor to the total baryonic mass of the MW. It is characterized as a flatten rotating structure composed of two main components *t*hin and *t*hick disc (Gilmore & Reid 1983). The MW disc has a flat rotation curve (see Fig. 1.1.2) with a circular velocity at the solar radius equal to approximately 235 km s^{-1}[1]. The disc has an assumed circular shape with a radius of roughly 15 kpc, and its width vary around 1.5 kpc (Jurić et al. 2008).

The bimodality of the Galactic disc was found by Gilmore & Reid (1983), who recognized that the stellar number density distribution with increasing distance from the Galactic plane can not be described with a single density profile. Nowadays, we believe that disc structures identified as the thin and thick disc had a different formation history that can be recovered from the kinematics and chemistry of the present-day disc stars. Based on the observational evidence we assume that the thick disc developed earlier ≈ 10 to 13 Gyr throughout few Gyr (see e.g., Haywood et al. 2013), and contain stars rich on α-elements (e.g., Mg and Ca) with lower metallicities in comparison with thin disc stars (Hayden et al. 2015; Bland-Hawthorn & Gerhard 2016; Bland-Hawthorn et al. 2019). The thick disc stars are on average kinematically hotter when compared to thin disc stars, they have higher velocity dispersion and higher values of the asymmetric drift[2] (see tab. 2.1 in Sparke & Gallagher 2007). The thin disc is, on the other hand, dynamically cold, characterized by the ordered rotation, with a very small velocity dispersion. Stars associated with thin disc have a solar-like metallicity and are depleted in α-elements (see e.g., Hayden et al. 2015; Bland-Hawthorn & Gerhard

[1] This value is based on the proper motion, and distance to the Sagittarius A* (Reid & Brunthaler 2004; Gravity Collaboration et al. 2019).

[2] The asymmetric drift describes up to what extent stars of a given population lag behind the rotational velocity.

2016; Bland-Hawthorn et al. 2019).

The Sun is located approximately at 8.178 kpc from the Galactic center (Gravity Collaboration et al. 2019), and slightly above the Galactic plane $z_\odot = 25$ pc (Jurić et al. 2008), thus inside the Galactic thin disc (based on Galactic thin disc vertical scale length $z = 300 \pm 50$ pc, Bland-Hawthorn & Gerhard 2016). From the kinematical point of view, Sun slightly deviates from the local standard of rest defined by the rotation velocity. The deviation is characterized by velocity components $(U_\odot, V_\odot, W_\odot) = (-11.1, 12.24, 7.25)\,\mathrm{km\,s^{-1}}$ (Schönrich et al. 2010; Schönrich 2012) where $U_\odot$ represent velocity toward toward the Galactic anticenter, $V_\odot$ is possitive in direction of the Galactic rotation, and $W_\odot$ velocity points toward the Galactic north pole.

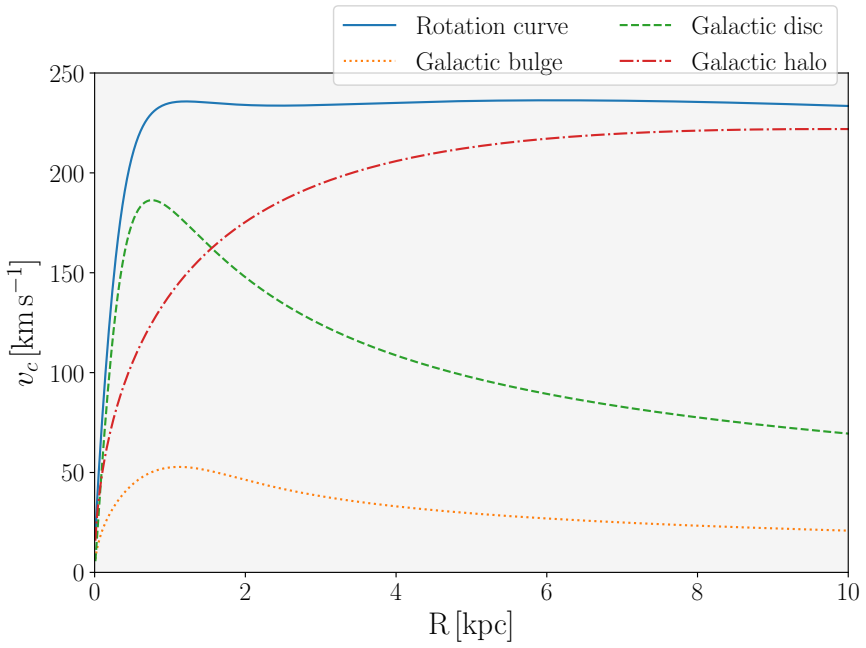

Figure 1.1.2: Example of a calculated rotation curve (solid blue line) for the MW using the `galpy` (Bovy 2015). The non-solid lines represent an individual potential contribution to the MW rotation curve; the green dashed line represents the Miyamoto-Nagai potential for the Galactic disc (Miyamoto & Nagai 1975), orange dotted line stand for the power-law density profile for the spherical bulge potential with an exponential cut-off, and the Galactic halo is represented by the Navarro-Frenk-White halo potential (Navarro et al. 1997).

Galactic halo

The MW disc and bulge are enclosed inside a nearly spherical halo (see e.g., Ibata et al. 2001; Koposov et al. 2010). The Galactic halo is a two-component system (baryonic and dark matter halo) constantly growing through accretion events. The MW halo plays an essential role in studies focused on the MW formation history and the mass estimates of the

MW. The *inner* halo (up to 20 kpc) is mainly comprised of in-situ formed stars while the *outer* halo (beyond 20 kpc) contains the fragments of the accreted galaxies and their stars (Carollo et al. 2007, 2010). Both halo components differ in chemistry, with the inner halo being more metal-rich (on average [Fe/H] = −1.6 dex, Carollo et al. 2010; Beers et al. 2012) than the outer halo (on average [Fe/H] = −2.2 dex, Carollo et al. 2010; Beers et al. 2012). The inner halo seems to be more flatten, with flattening parameter $q = 0.65$ than the outer halo $q = 0.80$ (Bland-Hawthorn & Gerhard 2016), based on the spherical density models assuming double power-law (see e.g., Sesar et al. 2011; Medina et al. 2018) with a break radius around 20 kpc. The kinematics of the halo stars are dominated by high-eccentric orbits with decreasing rotation as a function of the distance from the Galactic plane (Chiba & Beers 2000). The individual velocity components show spherical velocity ellipsoids with kinematically hot velocity dispersions (Bond et al. 2010). The total mass of the Galactic halo can be determined through kinematics of the halo stars and its substructures (e.g., streams, Gibbons et al. 2014). It is a function of the radius in which it is encompassed, and for the total mass of the MW at the virial radius we assume $M_{\rm vir} = (1.3 \pm 0.3) \times 10^{12}\,{\rm M}_\odot$.

Magellanic Clouds

The Magellanic system is composed of two dwarf irregular galaxies orbiting around the MW, the Large and Small Magellanic Clouds (LMC and SMC). Both satellites are visible from the southern hemisphere and named after the Portuguese explorer Fernão de Magalhães. They are the fourth and fifth most luminous objects in the Local Group (see tab. 1 in Sparke & Gallagher 2007) located at the distance 49.59 kpc, and 62.10 kpc for the Large and Small Magellanic Cloud, respectively (Pietrzyński et al. 2013, 2019; Graczyk et al. 2014). Both Clouds exhibit peculiar substructures most likely invoked by their gravitational interaction, e.g., bar and spiral arm in the LMC or wing in the SMC (Cioni et al. 2000). LMC and SMC are connected through the Magellanic Bridge which can be traced using neutral hydrogen H I, young and intermediate-age population (Hindman et al. 1963; Indu & Subramaniam 2015; Skowron et al. 2014). The question, whether both Clouds are connected also in the old population is a still matter of debate (see e.g., Belokurov et al. 2017; Jacyszyn-Dobrzeniecka et al. 2020).

RR Lyrae variables

The RR Lyrae stars are mostly radially pulsating giants located on the horizontal giant branch inside the instability strip. They belong to the old stellar population with ages above 10 Gyr (based on their presence in globular clusters, Catelan 2009; VandenBerg et al. 2013). They are used in a multitude of astrophysical applications, e.g., as stellar laboratories for pulsation and stellar evolution theory, as standard candles within the Local Group (pulsation periods are connected to their luminosity through the period-metallicity-luminosity relations, Catelan et al. 2004; Muraveva et al. 2015, 2018), and as tracers of the chemical composition since the shape of their light curves correspond to their metallicity. These traits make them invaluable in studies on the formation history of the MW.

RR Lyrae stars periodically (on a scale from 0.2 – to 1.0 day, Smith 1995; Catelan & Smith 2015) change their brightness with amplitudes (in the V-passband) ranging between about 0.3 mag to 1.6 mag (Dorfi & Feuchtinger 1999). They cover a broad range of effective temperatures (about 1300 K) set by the instability strip which starts approximately at 6000 K and goes up to the 7250 K on the horizontal branch (Catelan 2004). The masses of RR Lyrae stars are constrained through the stellar evolutionary models which yield masses between about $0.6\,M_\odot$ and $0.8\,M_\odot$. The metallicity distribution of RR Lyrae variables spans from 0.0 dex up to −3.0 dex (Layden 1994). The most metal-poor RR Lyrae variables found so far being CS 30317-056 and CS 22881-039 found by Hansen et al. (2011), with the iron abundances [Fe/H] equal to −2.85 dex and −2.75 dex, respectively.

The discovery of the prototype of RR Lyrae class, the RR Lyrae itself, dates back to the beginning of the 20th century to Williamina Fleming and Edward C. Pickering (Pickering 1901). Although the RR Lyrae variables have been known already prior to this discovery as so-called *cluster variables*, since they were found numerously in the globular clusters, e.g., M3, M5 and ω Cen, by Solon I. Bailey (Bailey 1902; Bailey & Pickering 1913). Bailey (1902) in his pioneering work divided the found cluster variables in the ω Cen into three subcategories; *a*, *b*, and *c* based on the shape of their light curve, where *c*-type RR Lyrae stars have short pulsation periods and low amplitudes with more symmetric light curves. The other two Bailey types *a* and *b* are characterised by asymmetric light curves with large amplitudes and long pulsation periods.

Later on, Schwarzschild (1940) proposed that RR Lyrae types *a* and *b* pulsate in the fundamental radial mode, while type *c* pulsate in the first-overtone radial mode. The subclasses *a* and *b* lie in the same region of the period-amplitude diagram (sometimes called *Bailey* diagram, see Fig. 1.2.2) and are commonly merged into one class – RRab[3]. On the other hand, *c*-type stars are located in a different region of the period-amplitude diagram and are nowadays referred to as the RRc type RR Lyrae stars. The discovery of the double-mode RR Lyrae variables came decades after the discovery of the first RR Lyrae star (Nemec 1985). The double-mode RR Lyrae stars, or RRd as they are called, pulsate in the fundamental and first-overtone mode simultaneously which makes their phased light curves appear blurry. In the Fig. 1.2.1 we depicted three examples for three subclasses of RR Lyrae stars. From this figure we see that variables of an RRab subtype have asymmetric light curves with large amplitudes, they are also more numerous than the other RR Lyrae subtypes (around ∼ 70 percent of RR Lyrae stars belong to the RRab class). The phased light curve of an RRc type star is very symmetric with low amplitude in comparison with the RRab type. The RRd type RR Lyrae stars are the least numerous out of the three RR Lyrae subclasses (roughly ∼ 5 percent), and their phased light curves have a fuzzy appearance. In practice, for the vast majority of studies we use the variables of the RRab subclass, due to their distinct pulsation properties (e.g., amplitudes and pulsation periods) that separates them from the majority of variable stars[4].

The pulsation of RR Lyrae stars is governed by the interplay between temperature and

[3] Since RR Lyrae variables of this category pulsate in the radial fundamental-mode.

[4] Even with a few dozens of epochs we can classify them into the RRab category and determine the pulsation period.

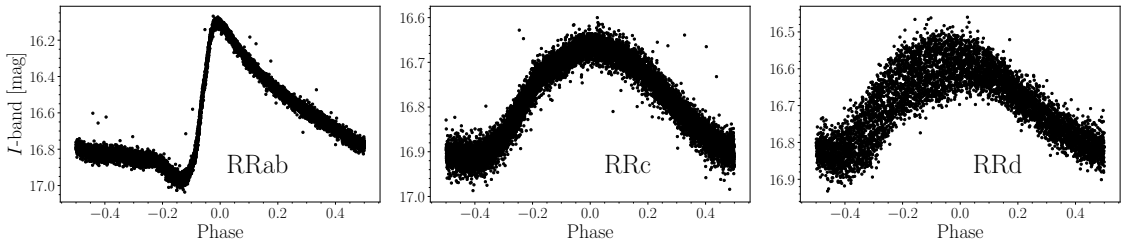

Figure 1.2.1: Example of light curves for three RR Lyrae subclasses, from the left RRab, RRc, and RRd type variable. The data were obtained from the fourth phase of the Optical Gravitational Lensing Experiment survey of the Galactic bulge (Soszyński et al. 2014).

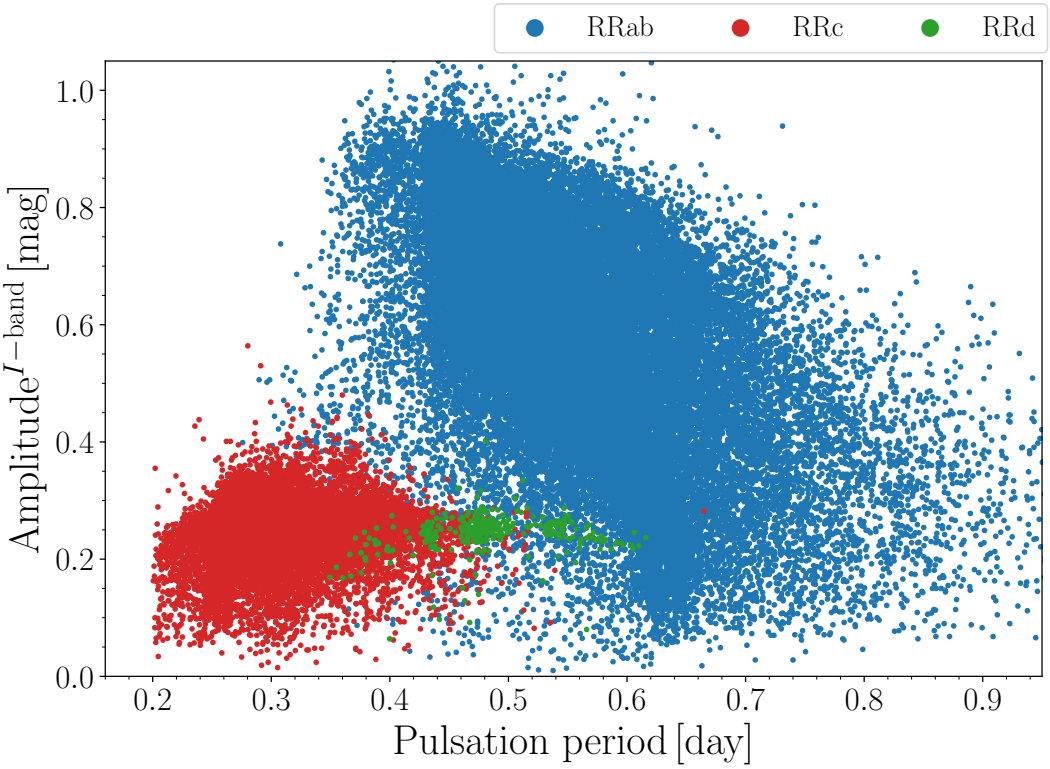

Figure 1.2.2: Period-amplitude diagram for RR Lyrae stars in the Galactic bulge. Three RR Lyrae subtypes are represented using three different colours RRab – blue, RRc – red, and RRd – green. The date used in this figure were obtained from the Optical Gravitational Lensing Experiment surve of the Galactic bulge (Soszyński et al. 2014).

pressure. The first outline of this mechanism dates back to Eddington (1926) and his proposed *Eddington's valve*. The proposed mechanism is assumed to be adiabatic since the valve

controls the heat flow without leakage. This mechanism suggests that during the compression the opacity increases, as the stellar atmosphere becomes more opaque and damps the radiation energy. Such conditions were first identified in the partially ionized layers in stellar atmospheres by Cox (1958); Cox & Whitney (1958); Zhevakin (1959). In a regular compressed stellar atmosphere, the density and temperature increase with the decreasing opacity[5] while in partially ionized zones the compression leads to further ionisation (instead of raising the temperature). Increasing opacity traps the radiation flow that raises the radiation pressure which eventually starts lifting the layer upward. As the zone starts to elevate and expand it leads to a decrease in opacity and subsequent recombination releases the damped radiation. Gravity then pulls the zone inward in a free fall and the cycle starts over. This repeating process became known as the κ mechanism that is the main driving force in the pulsation of RR Lyrae stars.

The partially ionized zones identified in RR Lyrae stars are hydrogen and helium (deeper one), their location in the stellar interior pre-set the stars' pulsation properties. If the aforementioned layers are located deeper in the star (in case of RR Lyrae stars around 5700 K) than the pulsation is damped due to the convection energy transport. If the layers lie close to the surface of the star (around 7500 K in RR Lyrae stars) the low mass and density are insufficient in effectively driving the pulsation. Therefore, the aforementioned temperature constraints define the region that we know as the instability strip.

One can look at the oscillations of pulsating variables as on the sound waves propagating through the stellar interior. Under this assumption, the time that is necessary for a sound wave to propagate across the diameter of a star (pulsation period, P) depends on the density of a star and its radius. Through the relations for adiabatic sound speed v_s:

$$v_s = \sqrt{\frac{\gamma p}{\rho}}, \tag{1.1}$$

where p represents the pressure, γ is the Poisson constant, ρ is density and from the pressure-density relation for hydrostatic equilibrium:

$$\frac{dp}{dr} = -\frac{GM\rho}{r^2}, \tag{1.2}$$

we can obtain the period-density relation, sometimes known as the *Ritter* relation (Ritter 1879):

$$P = \frac{Q}{\sqrt{\rho}} \tag{1.3}$$

where Q is a so-called pulsation constant, e.g., for an RRab subtype we assume $Q \approx 0.04$ (Smith 1995). This relation provides an explanation of why as we move from dwarfs to giants the pulsation period increases. In addition, in the Hertzsprung-Russell diagram the instability strip is almost parallel to the luminosity, thus we have the period-luminosity relations for classical pulsators like Cepheids and RR Lyrae stars.

Despite the large progress in the past two decades, there are still several open issues

[5] Follwing the Kramers' opacity law; $\kappa \approx \rho / T^{3.5}$.

connected to the RR Lyrae stars that hamper their use as standard candles and as tracers of chemical composition within the Local Group. Here we mention only those that are related to some of the projects outlined in this thesis.

The Blazhko effect

The quasi-periodic modulation of the light curve known as the Blazhko effect (Blažko 1907) affects all RR Lyrae subtypes (see e.g., Smolec et al. 2015b; Prudil & Skarka 2017; Netzel et al. 2018). The occurrence rate of the Blazhko effect among the fundamental-mode RR Lyrae stars vary from system to system, e.g., for the Galactic field and Galactic bulge approximately 40-50 per cent of the fundamental-mode RR Lyrae variables are affected (see Kovacs 2016; Prudil & Skarka 2017; Benkő et al. 2019). The Blazhko effect causes amplitude and/or phase modulation of the light curves where the amplitude changes range from mmag regime up to 1 mag during one modulation cycle (Benkő et al. 2014), an example of an RR Lyrae star affected by the Blazhko effect is in the top left-hand panel of Fig. 1.2.3. The periods of the Blazhko modulation range from several days up to a few decades (Netzel et al. 2018; Prudil & Skarka 2017; Jurcsik & Smitola 2016). The physical origin of the Blazhko effect is so far unknown, the most promising explanation of the effect lies in the 9:2 resonance between the fundamental and the 9-th overtone mode (Kolláth et al. 2011). In general, the Blazhko effect hampers the use of RR Lyrae stars as standard candles and as tracers of the metallicity, since it changes the shape of the light curves and even the mean magnitudes can be modulated (see e.g., Benkő et al. 2014; Skarka et al. 2020), therefore it introduces additional uncertainties in comparison with the non-modulated RR Lyrae variables.

The Oosterhoff dichotomy

The MW globular clusters which contain a sufficient number of RR Lyrae variables can be divided into two (three) groups based on their physical properties like; pulsation period, metallicity, and the ratio between the fundamental and first overtone pulsators (see Oosterhoff 1939; Smith 1995). Generally, the MW globular clusters that belong to the Oosterhoff group I contain RR Lyrae stars that have shorter pulsation periods (on average around 0.55 day), and higher metallicities ([Fe/H] ~ -1.3 dex) than their Oosterhoff type II counterparts (0.65 day, and -2.0 dex). Moreover, globular cluster associated with the Oosterhoff group II have a higher ratio of fundamental to first overtone pulsators (approximately 44 per cent, Smith 1995) while Oosterhoff group I clusters contain much less first-overtone pulsators (approximately 17 per cent, Smith 1995). Two globular clusters located in the Galactic bulge NGC 6441 and NGC 6338 do not fit in the Oosterhoff paradigm (Pritzl et al. 2000). Two aforementioned globular clusters contain RR Lyrae stars with long pulsation periods (above 0.65 day) while being at the same time metal-rich ([Fe/H] ~ -0.5 dex). In addition, globular clusters in the dwarf spheroidal satellite galaxies do not fit in either of Oosterhoff groups, but rather create a transition between both Oosterhoff types, and fill the Oosterhoff gap (see the bottom left-hand panel of Fig. 1.2.3). The cause for the Oosterhoff dichotomy can be several, e.g., age (van Albada & Baker 1973), metal and helium abundance (Sandage et al. 1981; Sandage 1981) of the clusters (for references see, Catelan 2009). Recently it has

been shown that the Galactic halo RR Lyrae stars exhibit smooth transition both in period and metallicity (Fabrizio et al. 2019) suggesting that the Oosterhoff dichotomy in the MW is caused by the lack of the metal-intermediate globular clusters.

Uncertainty in the mass of RR Lyrae stars

The mass estimates for RR Lyrae stars come from the stellar evolutionary models and the models of stellar pulsation (see e.g., Bono et al. 1996), which provide mass estimates in a range $0.6-0.8\,M_{\odot}$. The conventional way of acquiring precise masses through binary companions is hampered by the lack of such systems among RR Lyrae stars. To this day only one RR Lyrae variable is spectroscopically and photometrically confirmed to reside in a binary system, TU UMa (Szeidl et al. 1986; Wade et al. 1999; Liška et al. 2016). Approximately one hundred RR Lyrae stars are suspected to have a companion (see database[6], Liska & Skarka 2016). These candidates were discovered through various techniques; peculiar abundance patterns (Kennedy et al. 2014), astrometric anomalies (Kervella et al. 2019a,b), and most commonly used through the $O-C$ timings ($O-$ observed, $C-$ calculated time Hajdu et al. 2015; Liška et al. 2016; Liška et al. 2016; Prudil et al. 2019b) of brightness maxima using stars' ephemerids. Using the $O-C$ method we measure how the time of brightness maximum changes due to the possible orbital motion of a binary system with an RR Lyrae component. The middle right-hand panel of Fig. 1.2.3 shows an $O-C$ diagram for one of the promising candidates from Hajdu et al. (2015). Unfortunately, many of the candidates presumably have long orbital periods (from a few years up to several decades) which makes their confirmation as binary systems troublesome. In addition, possible detection of an eclipse during the pulsation phase can be also problematic, due to the age of the RR Lyrae stars. Their companion is likely a white dwarf or a main-sequence star, and thus contributes only marginally to the total light of the system.

Shocks in RR Lyrae stars

The movement and collisions of the stellar atmosphere during the pulsation cycle leads to distortion of the spectra and photometry of RR Lyrae variables. These effects had been first noticed by (Struve & Blaauw 1948) who reported line emissions and doubling of the Balmer lines in the spectrum of the RR Lyr (the prototype of the RR Lyrae class). These effects have been later followed-up by, e.g., Preston & Paczynski (1964) and Preston et al. (1965) who confirmed findings by Struve & Blaauw (1948). In nowadays we associate a number of effects connected to the shocks in RR Lyrae stars, beside the aforementioned line doubling and emission in the Balmer lines (see inset in the bottom right-hand panel of Fig. 1.2.3), also the distortion of the metallic lines have been reported (Chadid & Gillet 1996a,b), and helium emission and absorption lines have been observed (Preston 2009). In general, we recognize two shock features *main* and *early* shock, although other shocks have been reported to occur during the pulsation phase of an RR Lyrae star (see Chadid et al. 2014) but their origin and presence remain a matter of debate. The photometry of RR Lyrae stars is also affected by

[6] https://rrlyrbincan.physics.muni.cz/

the shocks, we recognize two main shock features in the light curve of RR Lyrae variable, the *hump* (associated with the main shock) and *bump* (associated with the early shock). The hump is located close to the brightness maximum while bump occurs right before the brightness minimum (see the bottom right-hand panel of Fig. 1.2.3). In general, the shocks hinder the interpretation of the light and radial velocity curves of RR Lyrae stars, in addition, due to the line distortions the abundance determination is impeded by the shocks.

Multi-mode RR Lyrae stars

The double-mode behaviour of some RR Lyrae variables is known since the discovery of RRd class (Nemec 1985). These stars pulsate in the fundamental and first-overtone mode with period ratios between 0.73 up to 0.75. Their position in the *Petersen* diagram (Petersen 1973) is connected to their mass, luminosity, metallicity, and effective temperature (see fig. 2 in Popielski et al. 2000). Although, in the past two decades, additional modes among all RR Lyrae subtypes have been reported, starting with a discovery of the additional mode in AQ Leo (Gruberbauer et al. 2007). In general, the most common additional modes have various period ratios, e.g, $0.61-0.63$ for group with found by Netzel et al. (2015a,c), or 0.68 for another group found in the Galactic bulge (Netzel et al. 2015b) and with different dominant mode (the first-overtone or fundamental). The stars identified as RRab variables also exhibit additional modes, although less numerously. Their period ratios vary around $0.7-0.73$, and for many members of these groups, the additional periodicity cannot be explained by the current stellar pulsation models (Smolec et al. 2016; Prudil et al. 2017). Moreover, some of the RRd stars also exhibit peculiar double-mode behaviour that does not fit in the general trend of the classical double-mode RR Lyrae variables. These stars are then referred to as the anomalous RRd variables (Soszyński et al. 2016b). In order to separate between different types of double mode pulsating variables, one can use the Petersen diagram (Petersen 1973). For an example of the Petersen diagram see the top right-hand panel of Fig. 1.2.3.

Despite the aforementioned issues, RR Lyrae stars are invaluable in many astrophysical applications as we will show in the subsequent chapters. In addition, we will address some of the listed issues and provide new a insight.

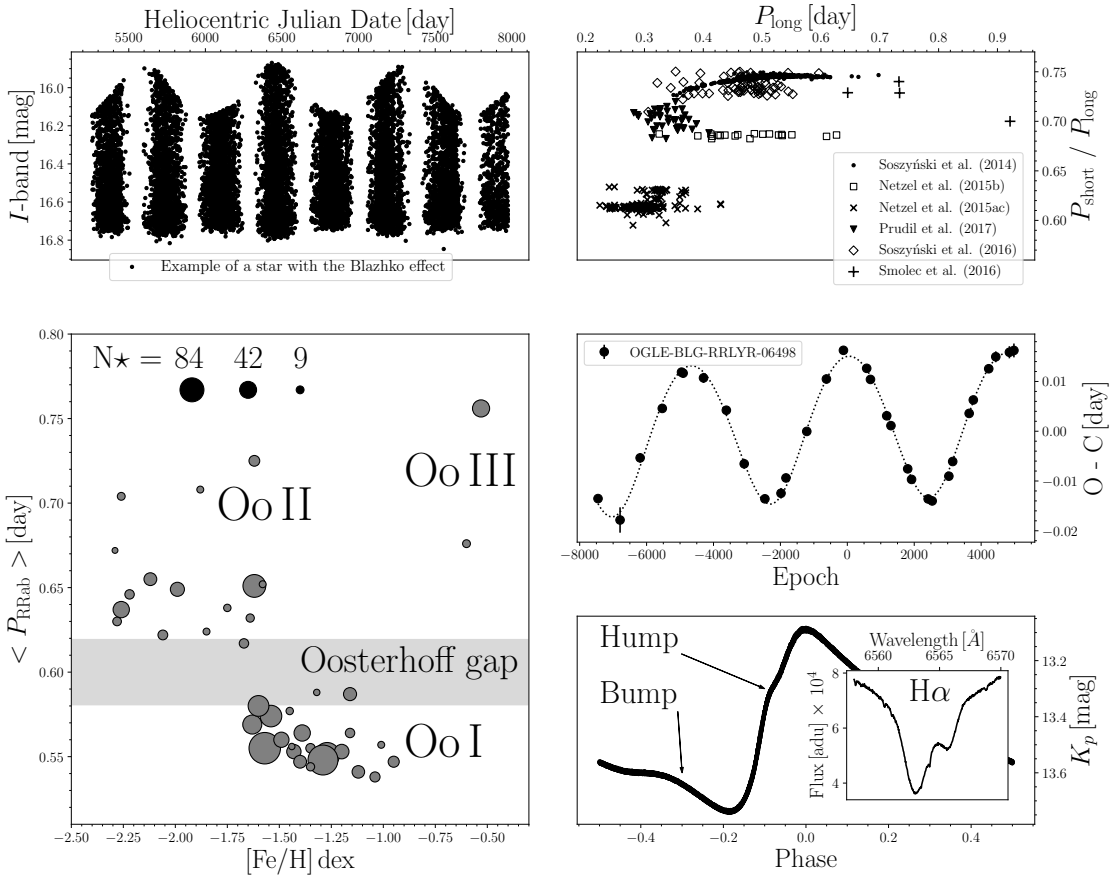

Figure 1.2.3: The mosaic of several open issues associated with the RR Lyrae stars. The top left-hand panel shows a light curve of an RR Lyrae star with the Blazhko effect, data comes from the Optical Gravitational Lensing Experiment for the Galactic bulge (Soszyński et al. 2014). The top right-hand panel shows the Petersen diagram (Petersen 1973) for multi-mode RR Lyrae stars. The black dots represent RRd stars found in the Galactic bulge, and the Magellanic system (Soszyński et al. 2014, 2016a), and the black diamonds denote the anomalous RRd variables found by (Soszyński et al. 2016b). The black triangles stand for the double-mode RR Lyrae stars found by Prudil et al. (2017). The open squares and black crosses represent multi-mode variables found by Netzel et al. (2015a,b,c). Lastly, the black pluses stand for fundamental-mode RR Lyrae stars exhibiting an additional mode found by Smolec et al. (2016). The bottom left-hand figure shows the average pulsation periods of RRab variables vs. metallicity for the MW globular clusters containing at least 5 RR Lyrae stars, data were acquired from the Catelan (2009), and references therein. The size of individual points corresponds to the number of the fundamental-mode RR Lyrae stars in a given globular cluster. The middle right-hand panel shows $O-C$ diagram for a binary candidate found by Hajdu et al. (2015) among fundamental-mode RR Lyrae stars in the Galactic bulge. The bottom left-hand panel depicts an example of a phased light curve of a fundamental-mode RR Lyrae star with highlighted regions of shocks, in addition, the inset figure shows the effect of shocks on the Hα line in the spectra of an RR Lyrae star. The data for the light curve was collected by the *Kepler* space telescope and processed by the SPEC group at Konkoly observatory (Nemec et al. 2011; Benkő 2018; Benkő et al. 2019). The spectra were obtained from the ESO archive for SV Hya (Prog. ID: 076.B-0055, obtained with the UVES echelle spectrograph).

CHAPTER 2

DATA

"Go ahead, make my day."
— Harry Callahan, Santa Cruz, California

In the following chapter, we will describe the general properties of the surveys and products used in this thesis. The subsequent chapters contain some information about the utilized data, based on the aim of the respective particular project. In the vast majority of projects, we used data from the multi-epoch photometric surveys of the MW, for studies focused on the kinematical properties we took advantage of the publicly available systemic velocities of studied stars, and astrometric products of the *Gaia* space mission.

The Optical Gravitational Lensing Experiment (OGLE)

The OGLE is a continuous (over 25 years) multi-epoch ground-based photometric survey of the densest stellar regions in the MW (Galactic disc and bulge), and its close neighbourhood (the Large and Small Magellanic Clouds). The primary goal of the OGLE survey is based on the idea of the search for dark matter through microlensing events as outlined by Paczynski (1991). During the four phases of the OGLE survey, the techniques and instruments evolved into the currently used camera with 32 CCD chips attached to the 1.3 m Warsaw Telescope at Las Campanas Observatory, in Chile. Each CCD chip provides a resolution of 2048 × 4102 pixels, and the final mosaic covers a field of view up to 1.5 degrees. In order to have information about the colour, observations are performed in two passbands V and I, where the latter observations are more numerous (Udalski et al. 1992, 2015). The continuous observations of the densest stellar regions in the MW are yielding (apart from thousands of microlensing events) also an enormous collection of hundreds of thousands of variable stars of various types (Soszyński 2018). The found variables can serve as probes of the structure of the MW and the near-by Magellanic system, as tracers of extinction, and calibrators of the

cosmological distance scales.

OGLE-IV

In the latest (fourth) phase of the OGLE project, the Galactic bulge, disc, and the Magellanic Clouds were observed together with their outskirts. The cadence of the observations of the aforementioned regions varied between 19 minutes up to three days based on the occurrence rate of the lensing events. The depth of the I-band photometry spans from 12 to 21 mag for the Galactic bulge and 13 to 21.7 mag for the Magellanic system. The estimated completeness for the densest regions in the Galactic bulge varies around 18.5 mag (Udalski et al. 2015). The number of collected epochs differs for individual variable stars, e.g., in case of RR Lyrae stars in the Galactic bulge, the number of epochs ranges from a few dozens up to ten thousand. Such a high number of epochs, and continuous observations over two decades allow a precise assessment of the variability type and permit long-term studies of the stellar variability. The fourth phase of the OGLE started in 2010 and continues to these days, the processed photometric data for individual variable stars are regularly published at the FTP site of the OGLE project[1]. The field of view of the fourth phase of the OGLE project is depicted in Fig. 2.1.1.

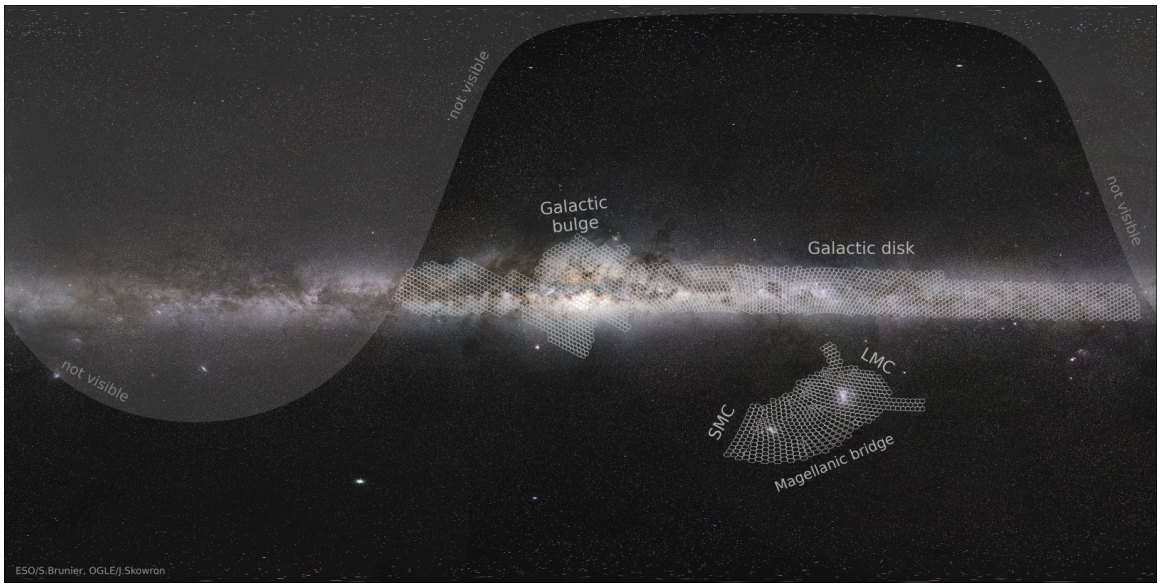

Figure 2.1.1: The map of OGLE fields observed in the fourth phase of the project marked with white dodecahedrons. *Image credit:* ESO/S. Bruiner, OGLE/J.Skowron, taken from http://www.astrouw.edu.pl/~jskowron/ogle4-sky/

[1]The data are publicly available via the OGLE collection of variable stars (OCVS) at http://www.astrouw.edu.pl/ogle/

All-Sky Automated Survey for Supernovae (ASAS-SN)

The ASAS-SN (Shappee et al. 2014; Kochanek et al. 2017) is a successor of the All-Sky Automated Survey (ASAS, Pojmanski 1997) and has been operational since 2017. It is a ground-based survey, currently consisting of six observing locations in four countries (USA, Chile, China, South Africa). Each observatory is equipped with four robotic telescopes with 14 cm diameter Nikon telephoto lenses that automatically survey the entire sky every night. Each telephoto lens is equipped with a ProLine CCD camera and covers a field of view of roughly 4.5 deg. The survey uses two passbands, the V and g (since September 2018), where each camera carries the labels from `ba` to `bh` for the V-band, and `bi` to `bt` for the g-band. The photometric depth of the survey goes down to 18 mag, and saturates roughly at 10 mag for both aforementioned passbands (Kochanek et al. 2017). To overcome the saturation limit, the ASAS-SN implemented the *saturation correction* from its predecessor ASAS (Pojmanski 2002). The primary goal of ASAS-SN is a search for bright transients, particularly nearby supernovae. Due to its whole sky coverage, the ASAS-SN survey imposes a negligible observational bias toward a particular galaxy type for the occurrence of various transients. The current field of view with a colour-coding based on a number of collected epochs is depicted in Fig. 2.2.1.

Besides transients, ASAS-SN collects data on cataclysmic variables[2] and variable stars. The light curves of individual objects are computed on the fly using aperture photometry with 2 pixel radius (1 pixel $\approx 8''$), and are available at the ASAS-SN website[3]. The ASAS-SN contains also pre-computed light curves for over 600 thousands variable stars, of which over forty-four thousand are RR Lyrae stars (Shappee et al. 2014; Jayasinghe et al. 2018, 2019).

Gaia

Gaia is a space satellite developed and operated by the European Space Agency (ESA). Its primary mission is to map the positions and movements of more than 1 billion stars. The satellite was launched in December 2013 and started collecting data in February 2014. *Gaia* is located at the L2[4] point, therefore on the night-side of the Earth, away from the Sun. L2 is especially advantageous since the emanating light from the Earth will not interfere with the observation, and we have full access to the celestial plane during a whole year (Gaia Collaboration et al. 2016a).

The setup on the *Gaia* space satellite consists of three instruments: astrometric instrument, photometric instrument, and grism (grating plate and four prisms) spectrometer (Gaia Collaboration et al. 2016a). The astrometric instrument collects data in the broad G-passband (covering wavelengths between 3300 Å to 10500 Å) on 62 CCDs. The practically unfiltered

[2] Cataclysmic variables, sometimes called *novae*, are binary stars composed of a beneficiary (white dwarf) and donor (a star that filled its Roche lobe). Due to the mass transfer, material rich on hydrogen builds up on the white dwarf, and at certain points is ignited (fused to helium).

[3] `https://asas-sn.osu.edu/`

[4] The Lagrange points (L1, L2 ... L5) are locations in space where the combination of the gravitational potential of two massive bodies (e.g., Sun and Earth) is equal to the orbital motion of a smaller object (e.g., a space telescope).

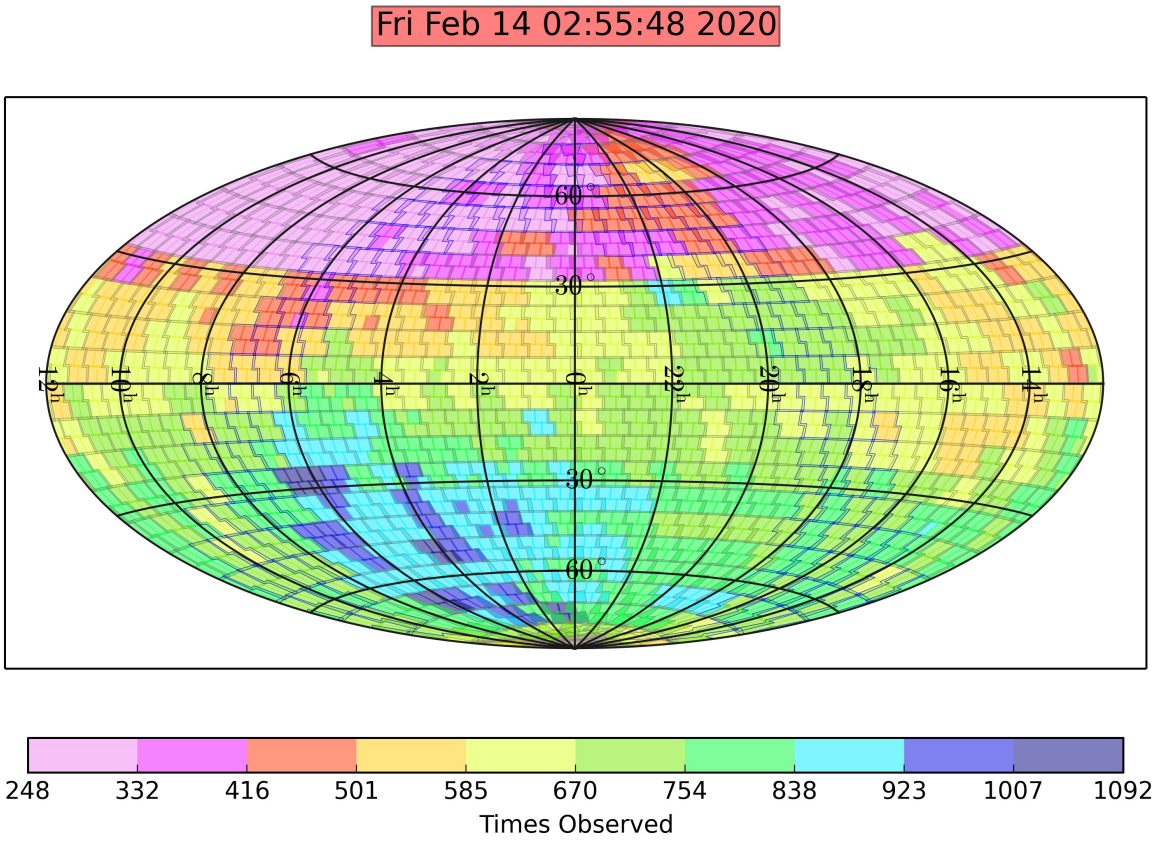

Figure 2.2.1: The map of ASAS-SN fields observed since its comission in 2017, with a colour-coding reprensenting the number of epochs colected until the date in the title. *Image credit:* ASAS-SN website, http://www.astronomy.ohio-state.edu/asassn/index.shtml

light then allows reaching a high signal-to-noise ratio, which is particularly important for the astrometric and variability survey. The photometric instruments consist of the prism photometers covering the blue (G_{BP} – from 3300 Å to 6800 Å), and red (G_{RP} – from 6300 Å to 10500 Å) part of the visible spectrum. It measures the spectral energy distribution (SED) of the observables, and provides their classification (star, galaxy, etc.), and physical parameters (e.g., metallicity, effective temperature, surface gravity). The spectrometer collects spectra of medium resolution ($R \sim 11000$) covering the region around the Calcium triplet (from 8450 Å to 8720 Å). Its purpose is to provide the sixth dimension to the astrometric solution, through the radial velocity measurements of the Doppler-shifted Calcium lines, down to the 17th magnitude. It also provides abundances of several elements (e.g., Fe, Mg, Ca), and atmospheric parameters for stars brighter than 12 mag (Gaia Collaboration et al. 2016a; Recio-Blanco et al. 2016).

The processing of the raw data and publishing *Gaia* catalogues is done by the *Gaia* Data Processing and Analysis Consortium (DPAC). Since *Gaia* is commissioning, two data re-

leases (DR) were published so far (Gaia Collaboration et al. 2016b, 2018a). In the latest *Gaia* DR2 positions and apparent magnitudes (in the *G*-band photometry) of approximately 1.7 billion sources were published (Gaia Collaboration et al. 2018a). Over 7 million median radial velocities of stars brighter than 12 mag have been published from the measurements of the onboard spectrograph. The variable star catalogue of the new data release consists of 0.5 million variable stars (Roelens et al. 2018; Mowlavi et al. 2018; Clementini et al. 2019a; Rimoldini et al. 2019). In addition, parallaxes and proper motions of 1.3 billion objects became available as well. Figure 2.3.1 depicts the mean magnitude distribution of the sources detected in *Gaia* DR2.

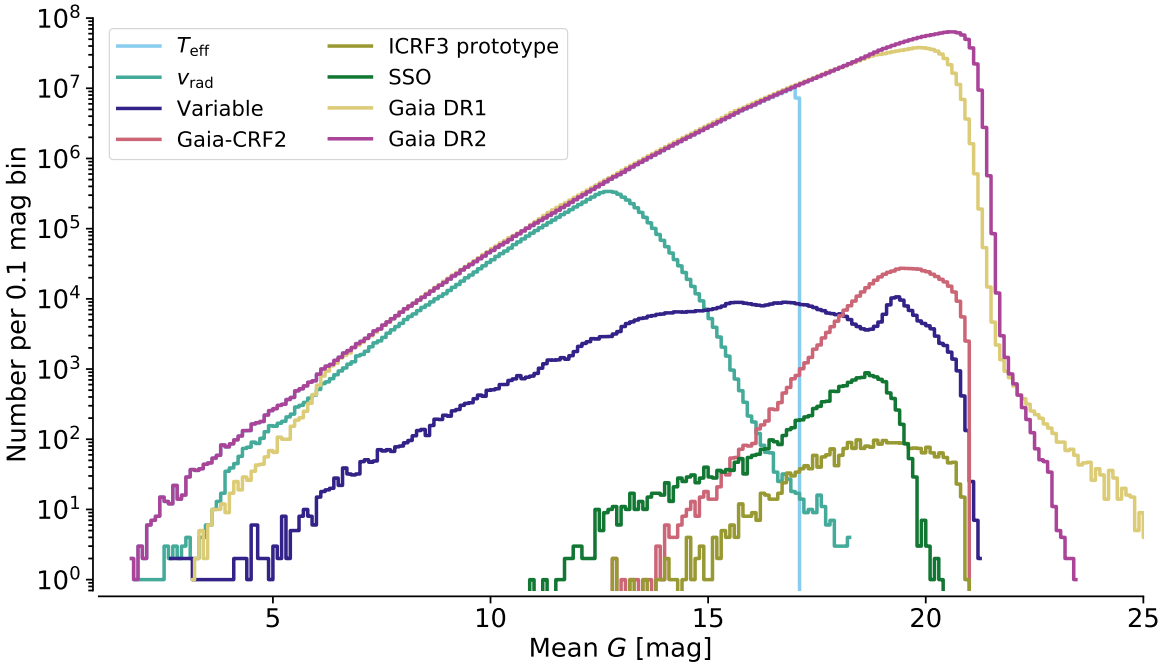

Figure 2.3.1: The mean magnitude distribution of all *Gaia* DR2 sources (light violet line) with determined effective temperatures (cyan line) and with measured radial velocities (light green line). The magnitude distribution of variable sources is depicted using a dark violet line. For comparison, the magnitude of the *Gaia* DR1 sources is included using a yellow line. The dark green line represents Solar system objects (SSO). The dark yellow line represents the International Celestial Reference Frame (ICRF2 prototype) catalogue of quasars, while the pink line stands for the celestial reference frame (CRF2) containing extragalactic sources such as quasars (Gaia Collaboration et al. 2018b). *Image credit:* Fig. 1 in Gaia Collaboration et al. (2018a).

CHAPTER 3

PHOTOMETRIC STUDY OF THE SMCNOD USING VARIABLE STARS FROM THE OGLE-IV SURVEY

> "People keep asking if I'm back and I haven't really had an answer, but yeah, I'm thinking I'm back."
>
> — John Wick

Abstract: We present a study of a recently discovered stellar overdensity near the northern edge of the Small Magellanic Cloud (SMCNOD). We exploited variable stars from the fourth release of the Optical Gravitational Lensing Experiment (OGLE). We used mainly pulsating variable stars and investigated their potential association with the SMCNOD using their spatial distribution and distances. We found four rather spatially concentrated anomalous Cepheids and eight evenly dispersed RR Lyrae stars to be most likely members of this overdensity. The anomalous Cepheids inside the SMCNOD trace possible intermediate-age population with ages ranging between $2-4.5$ Gyr. The age distribution of anomalous Cepheids seems to be in good agreement with the age distribution of anomalous Cepheids in the SMC. Using empirical relations for RR Lyrae stars we determined the median metallicity for the possible old population in the SMCNOD to be $[\mathrm{Fe/H}]_{\mathrm{SMCNOD}} = -1.71 \pm 0.21$ dex, which is in agreement with the median metallicity of the old SMC population. The density profile for anomalous Cepheids shows a small anomaly at the position of the SMCNOD, on the other hand, the RR Lyrae variables show no such deviation. The probability of finding the observed number of variable stars at the location of the SMCNOD by chance is very low for anomalous Cepheids (0.7 %) but high for RR Lyrae stars (13.0 %). Based on its variable stars content, we thus confirm the presence of a modest overdensity in intermediate-age stars in the SMCNOD and conclude that it probably has its origin in the SMC rather than to be the remnant

of an accreted dwarf galaxy.

This chapter is based on our published paper : **Prudil, Z.**, Grebel, E. K., Dékány, I., Smolec, R.,: Photometric study of the SMCNOD using variable stars from the OGLE-IV survey, 2018, MNRAS, 480, 669

Context

The Magellanic System is an important nearby cosmological laboratory. It consists of the Large and the Small Magellanic Cloud (LMC and SMC), and the Magellanic Bridge and Stream that were most likely formed through the interaction between both Clouds and possibly the Milky Way (Gardiner et al. 1994; Gardiner & Noguchi 1996; Connors et al. 2006; Diaz & Bekki 2011, 2012; D'Onghia & Fox 2016). In addition, the Magellanic system may include a number of ultra-faint dwarf spheroidal galaxies (e.g., Bechtol et al. 2015; Drlica-Wagner et al. 2015, 2016). The SMC is a smaller counterpart of the LMC with an estimated mass between $1-5\times10^9\,M_\odot$ (Kallivayalil et al. 2006). The SMC is an irregular, star-forming, low-metallicity, gas-rich dwarf galaxy. It has an elongated shape. Its northern part is younger and closer to us, while the south-western part is older and more distant (Haschke et al. 2012b; Jacyszyn-Dobrzeniecka et al. 2016). The SMC consists of several substructures, e.g., the Wing (Cioni et al. 2000) which together with the central region shows the most active star-formation in the SMC.

Recently, a small stellar overdensity, 8° north of the center of the SMC, was found by Pieres et al. (2017). They used data from the Dark Energy Survey (DES, The Dark Energy Survey Collaboration 2005) and the MAGellanic SatelLITEs Survey (MagLiteS, Drlica-Wagner et al. 2016) to trace and study this overdensity. Pieres et al. (2017) called this feature the Small Magellanic Cloud Northern Over-Density (SMCNOD). According to Pieres et al. (2017) it contains mainly intermediate-age stars (~ 6 Gyr with a metallicity of Z = 0.001) with a small fraction of young stars (~ 1 Gyr, Z = 0.01). The center of the SMCNOD is estimated to be located at $\mathrm{R.A._{J2000}} = 12.00$ deg and $\mathrm{Dec_{J2000}} = -64.80$ deg, and the structure has an ellipticity of $\epsilon = 0.6$ with a position angle of 350.9°. Based on its colour-magnitude diagram (CMD), Pieres et al. (2017) estimate the distance to the SMCNOD to be the same as the distance to the SMC (i.e., a distance modulus of $(m-M)_0^{\mathrm{SMC}} = 18.96 \pm 0.02$, de Grijs & Bono 2015).

Pieres et al. (2017) also discuss several possible origins of the SMCNOD. One involves a past LMC - SMC encounter, which would result in an enhanced star formation activity in both objects (SMC and LMC) and imply that the SMCNOD consists of material that was tidally stripped from the SMC. The second possibility involves resonant stripping in dwarf-dwarf encounters (D'Onghia et al. 2009) which might lead to the formation of shells comparable with the SMCNOD. The third hypothesis suggests that the SMCNOD is a small dwarf galaxy currently orbiting around and/or being tidally disrupted by the SMC. This would imply a fairly low metallicity and a narrower age distribution for the SMCNOD in comparison with the SMC.

In this paper, we explore the nature of the SMCNOD using variable stars. We present an analysis of photometric data of variable stars from the Optical Gravitational Lensing Experiment IV (OGLE-IV, Udalski et al. 2015). In Sect. 3.2 we study the SMCNOD using variable stars of various types located in the range of the coordinates of this apparent feature. Wherever possible we determine stellar distances, masses, ages, and metallicities. We discuss the spatial distribution of the variable stars and their metallicities in comparison with the main body of the SMC. Section 3.3 contains a field star analysis where we divided the northern outskirts of the SMC into small ellipses with the same proportions as the SMCNOD. Furthermore, we discuss differences between the variable stars in these selected comparison fields and the variable stars inside the SMCNOD. Whether the variable stars at the location of the SMCNOD represent a significant overdensity is explored in Sect. 3.4. In Section 3.5 we summarise our findings.

Data analysis

For the purpose of this study, we have explored the latest release of OGLE-IV data of the Magellanic Clouds (Soszyński et al. 2017a). We used publicly available data for variable stars in OGLE-IV for the SMC to study the recently discovered SMCNOD (Pieres et al. 2017). In the following subsections, we briefly discuss the different types of variable stars used in our study.

Eclipsing binaries

Eclipsing binaries (EBs) can be invaluable tools. They can serve as laboratories for testing stellar evolution theory and for constraining the rate of mass transfer and mass loss. Binary systems offer a possibility to measure directly stellar properties like mass, temperature, radius, surface gravity, and absolute magnitude. Perhaps most importantly, in the context of stellar population studies, they can serve as distance indicators in the Milky Way and nearby stellar systems (Pietrzyński et al. 2013; Graczyk et al. 2014).

The OGLE-IV data release for EBs contains over 48 000 objects in the Magellanic system (Pawlak et al. 2016), of which 8 401 belong to the SMC. The top panel of Fig. 3.2.1 shows their distribution in equatorial coordinates, highlighting those 6 EBs whose positions overlap with the SMCNOD.

In the bottom panel of Fig. 3.2.1 we plotted the CMD of the EBs found in the SMC. The six binaries that overlap with the SMCNOD do not have any V-band OGLE-IV photometry. Therefore, we used G-band magnitudes from Gaia DR–2 (Evans et al. 2018), for the aforementioned EBs. Using the coefficients from table 3 in Jordi et al. (2010), we transformed these G-magnitudes into the V-band and used those in the CMD in Fig. 3.2.1.

The basic properties of these six binaries can be found in Table 3.2.1. We note that they all belong to the eclipsing detached/semi-detached subtype. The binaries found at the position of the SMCNOD fall on the brighter end of the I-band magnitude distribution. The shape of their light curves suggests that they may belong to the group of β Persei, late-type eclipsing systems. From these six binary systems, four seem to have similar I-band magnitudes,

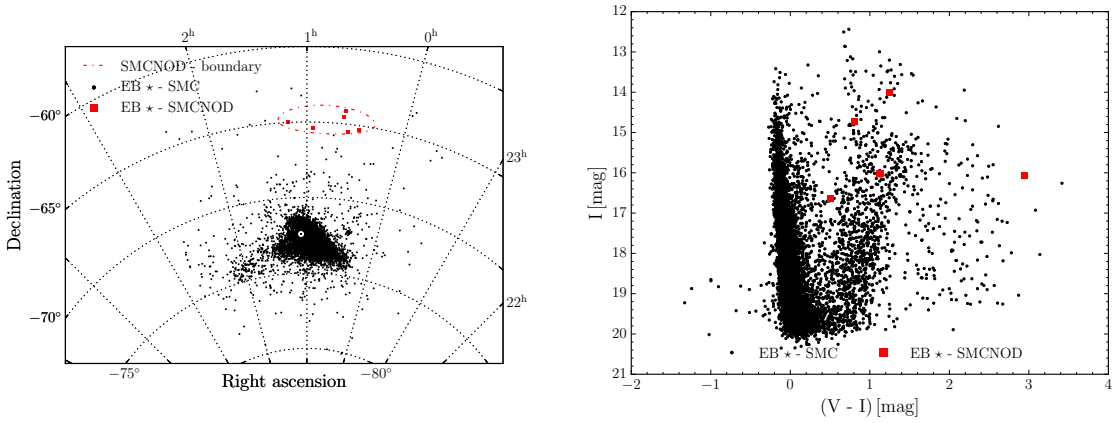

Figure 3.2.1: Spatial distribution and CMD for eclipsing binaries (EBs) in the SMC. The left-hand panel shows the distribution of EBs in equatorial coordinates for the SMC (black dots). Red squares represent EBs that lie at similar coordinates as the SMCNOD. The red dash-dotted ellipse indicates the approximate position of the SMCNOD. The white circle denotes the apparent kinematic center of the SMC (Stanimirović et al. 2004). The right-hand panel displays a CMD of the EBs seen towards the SMC with the same colour coding as in the upper panel.

in addition, two of them share almost the same location in the CMD (OGLE-SMC-ECL-6334 and OGLE-SMC-ECL-6349, see lower panel of Fig. 3.2.1). Under the assumption that they lie inside the SMCNOD their approximate mean absolute magnitude would be $\simeq -3$ mag (assuming that the SMCNOD and the SMC lie at the same distance, Pieres et al. 2017). This would be in agreement with their evolved state inferred from their CMD locus (post-main-sequence). Detached evolved systems with longer orbital periods have been found and used to study the structure of the Milky Way and to determine the distance to the SMC (see, Helminiak et al. 2013; Graczyk et al. 2014). To determine individual distances we would need additional information about the studied systems, e.g. near-infrared photometry, radial velocity curves, or light curve modeling. Unfortunately, neither of these is currently available. Thus, the association of the four aforementioned binaries with the SMCNOD remains tentative.

Classical Cepheids

Classical Cepheids (hereafter referred to as CCs) are radially pulsating Population I variables with periods ranging from a few hours up to several weeks. They are well-established distance indicators in the Milky Way and in extragalactic systems.

Thanks to their continuing star formation activity the SMC and LMC contain a large number of CCs (e.g., Haschke et al. 2012a,b). In the OGLE-IV photometry, we can find 9 649 CCs, of which almost 5 000 belong to the SMC (Soszyński et al. 2015b). Fig. 3.2.2 shows the celestial distribution of CCs in the SMC. None of the CCs overlap with the SMCNOD. Most of them are concentrated in the central regions with very few located in the outskirts of the

Table 3.2.1: Basic properties of the six eclipsing binaries that lie at the same coordinates as the SMCNOD. Column 1 contains the name of the star in the form OGLE-SMC-ECL-ID, but only the ID number itself is listed here for brevity. Columns 2 and 3 contain equatorial coordinates (J2000). Mean I-band and V-band magnitudes can be found in columns 4 and 5, respectively. Column 6 contains orbital periods.

ID	R.A. [deg]	Dec [deg]	I [mag]	V [mag]	P [day]
6268	6.93404	-65.31314	16.627	17.133	1.3383077
6319	8.65396	-65.49322	14.731	15.543	3.6228675
6334	9.18079	-64.10989	16.028	17.152	1.5717865
6349	9.44271	-64.54739	16.021	17.157	4.0081439
7162	14.01704	-65.36956	13.998	15.247	0.8175277
7856	17.87579	-64.95067	16.061	19.000	1.9892185

SMC (see, e.g., Haschke et al. 2012b). The lack of CCs in the SMCNOD suggests a lack of stars younger than a few hundred million years.

Anomalous Cepheids

Anomalous Cepheids (hereafter ACs) are radial pulsators with rather short pulsation periods (ranging from a few hours up to two days). The ACs are believed to be relatively massive (up to 2 $M_\odot$, Marconi et al. 2004), metal-deficient helium-burning stars. They are often found in nearby dwarf galaxies (see Kinemuchi et al. 2008; Bernard et al. 2009), but their occurrence in globular clusters is very rare with one confirmed case (Zinn & Dahn 1976). The origin of ACs is still unclear; there are two main hypotheses to explain them. They may either be metal-poor intermediate-age (1 – 6 Gyr) stars or merged binary stars older than 10 Gyr. Importantly, they follow a P-L relation and can be used as standard candles (Soszyński et al. 2015a).

The OGLE-IV photometry for the SMC contains 119 ACs (Soszyński et al. 2015a), of which approximately two-thirds pulsate in the fundamental mode while the rest are first-overtone pulsators. Fig. 3.2.3 shows their spatial distribution. As noted by Soszyński et al. (2015a), the radial distribution of ACs in the SMC is similar to that of its RR Lyrae stars, but in the outskirts, there is an excess of ACs compared to RR Lyrae stars (see fig. 7 in Soszyński et al. 2015a). Four ACs are located at the same range of coordinates as the SMCNOD. If they do lie in the outskirts of the SMC, these four ACs would be somewhat unusual considering the paucity of ACs in other border regions of the SMC. In addition, their spatial concentration resembles the densest regions of the SMC. To explore a possible membership of these four ACs in the SMCNOD we calculated their distances using the procedure from Jacyszyn-Dobrzeniecka et al. (2016) and the coefficients for ACs from Soszyński et al. (2015a).

First, we calculated the reddening-insensitive Wesenheit magnitude ($W_{I,V-I}$, Madore 1976) for each star that later served for estimating distance:

$$W_{I,V-I} = I - 1.55 \cdot (V - I). \tag{3.1}$$

I and V represent mean magnitudes in those passbands. For calculating errors we adopted

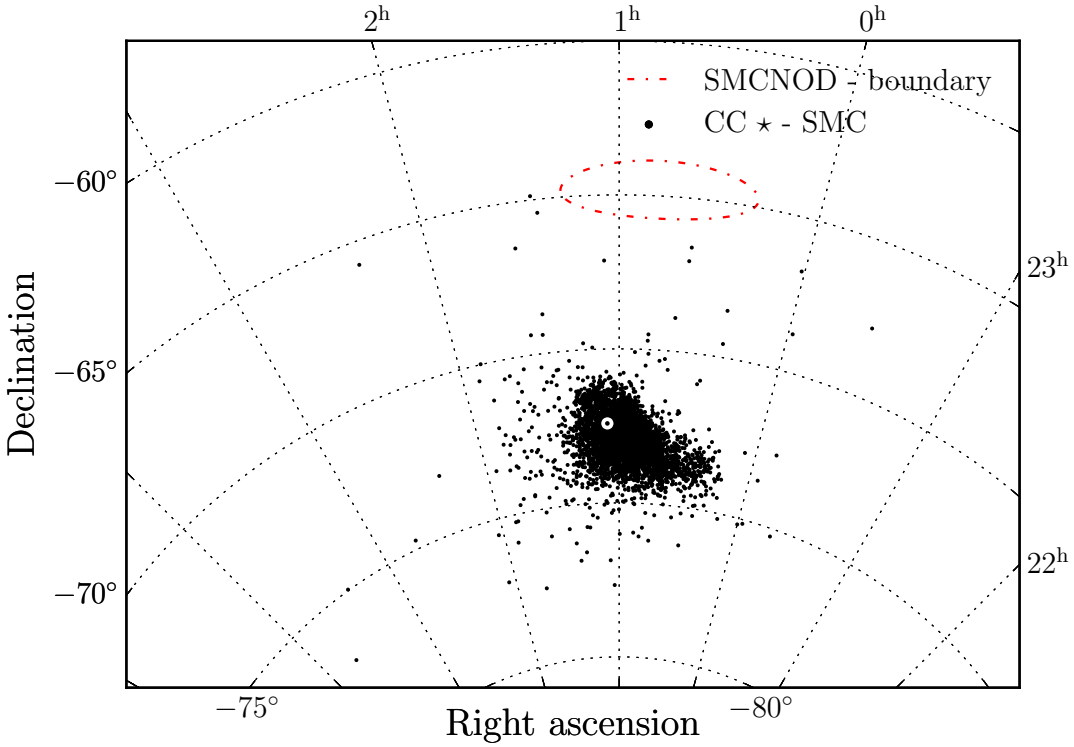

Figure 3.2.2: Similar as Fig. 3.2.1 but for classical Cepheids in the SMC.

the error of the zero point in the OGLE-IV photometry for the SMC as $\sigma_{V,I} = 0.02$ mag (Jacyszyn-Dobrzeniecka et al. 2016). Subsequenty, we calculated the reference Wesenheit magnitude using the P-L relations from Soszyński et al. (2015a) for the dominant pulsation mode:

$$W_{\rm ref} = a_{\rm SMC} \cdot \log P + b_{\rm SMC}, \tag{3.2}$$

where $a_{\rm SMC} = -2.85 \pm 0.15$ and $b_{\rm SMC} = 17.01 \pm 0.03$ for the fundamental mode and $a_{\rm SMC} = -3.69 \pm 0.15$ and $b_{\rm SMC} = 16.64 \pm 0.05$ for the first overtone. The distances relative to the mean distance of the SMC were computed by

$$d = d_{\rm SMC} \cdot 10^{0.2 \cdot (W_{I,V-I} - W_{\rm ref-F/1O})}, \tag{3.3}$$

where for the distance to the SMC, we adopted the value from de Grijs & Bono (2015) of $d_{\rm SMC} = 61.94 \pm 3.38$ kpc. The individual errors in the distances were calculated using error

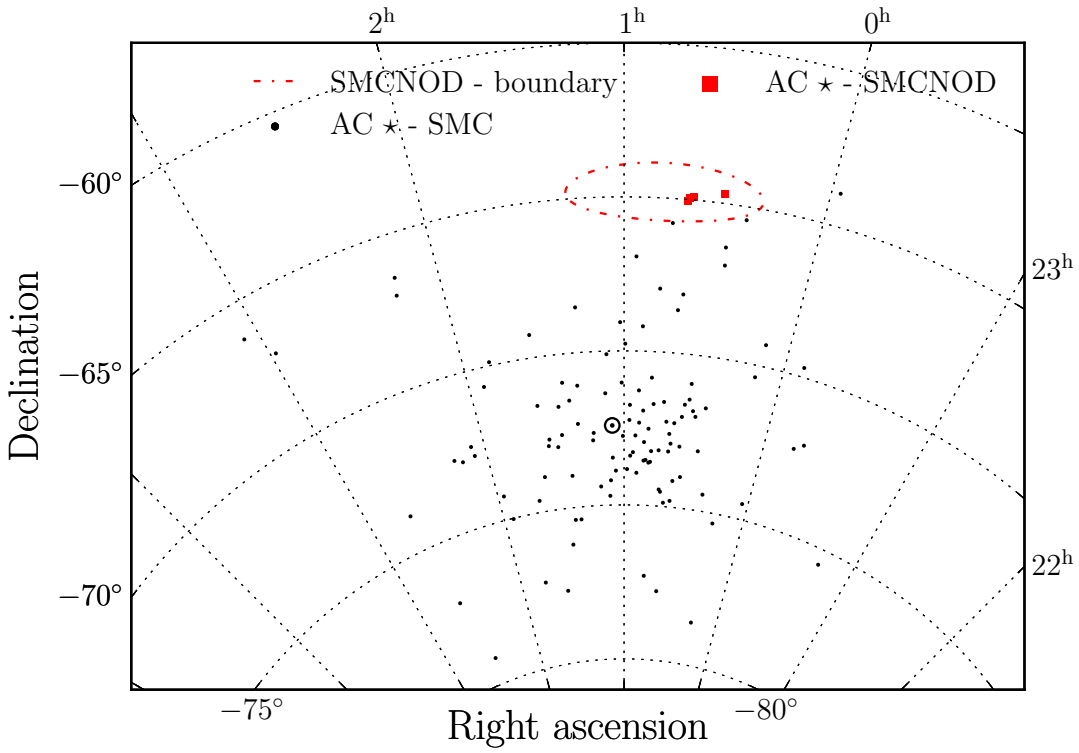

Figure 3.2.3: Spatial distribution of ACs in the SMC. The red squares indicate ACs seen in projection against the SMCNOD location.

propagation. The basic properties of the four ACs that lie at the same coordinates as the SMCNOD are listed in Table 3.2.2. The distances for the remaining ACs can be found in the supplementary material online.

Fig. 3.2.4 shows a declination vs. distance plot of the ACs. The SMCNOD presumably lies at the same distance as the SMC (Pieres et al. 2017). The SMC has a significant depth in intermediate-age stars along the line of sight (SMC disc 4.23 ± 1.48 kpc, Subramanian & Subramaniam 2009, using red clump stars). Using the aforementioned depth, the scale height h_z of the SMC is 1.97 ± 0.69 kpc (using eq. 7 in Haschke et al. 2012b). We did not derive the depth extent of the SMC using the ACs due to their low numbers in the SMC. Based on the analysis done by Pieres et al. (2017) (half-light radius equal to $r_h = 2.1$ kpc), we assume that the SMCNOD has the same scale height as the SMC. By comparing the calculated distances and the SMCNOD scale height, four ACs, within the errors, are consistent with a position inside the SMCNOD.

Table 3.2.2: Basic properties of ACs in the coordinate and distance range of the SMCNOD. Column 1 provides the star ID in the form OGLE-SMC-ACEP-ID, column 2 contains the pulsation mode, column 3 and 4 provide equatorial coordinates (J2000), and the last two columns contain distances with errors. The full table for all analysed ACs in the SMC is available as supplementary material for followig paper Prudil et al. (2018b).

ID	mode	R.A. [deg]	Dec [deg]	d [kpc]	σ_d [kpc]
016	F	7.55325	-64.69511	59.48	3.89
027	1O	9.83200	-64.90775	66.58	4.50
031	F	10.12183	-64.93772	68.46	4.49
034	F	10.24825	-65.06083	62.97	3.97

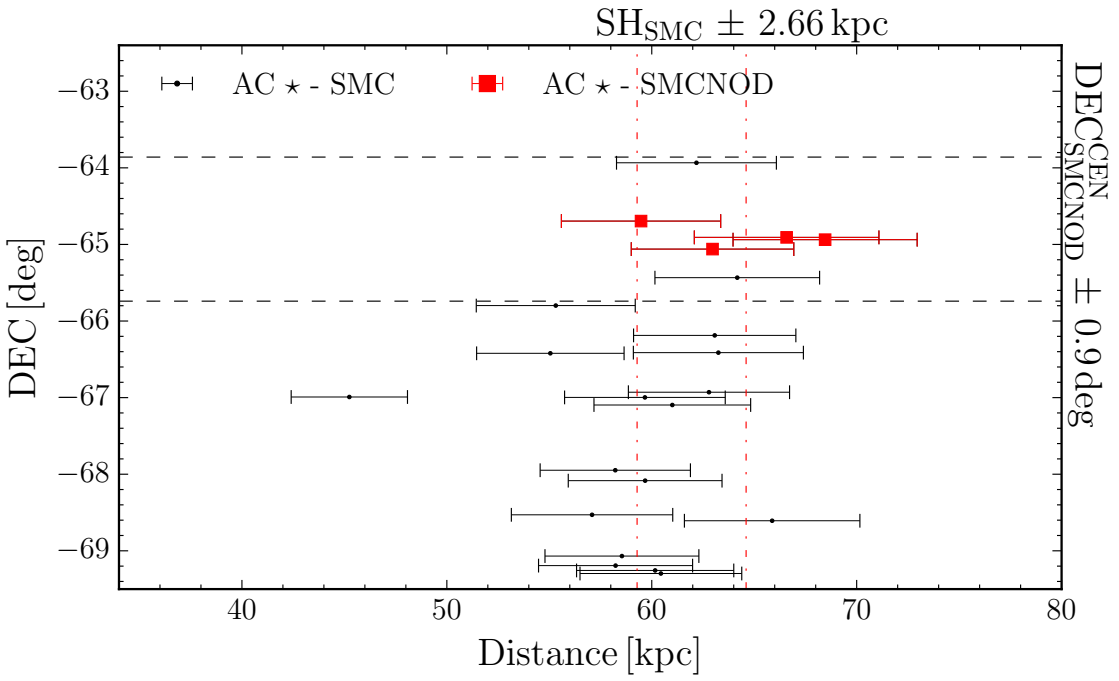

Figure 3.2.4: Declination (J2000) vs. distance for the ACs. The black dots represent ACs from the OGLE-IV photometry for the SMC and the red squares stand for ACs that presumably lie in the SMCNOD. The horizontal black dashed lines indicate lower and upper borders in declination for the SMCNOD. The red dash-dotted lines represent the assumed distance boundaries of the SMCNOD, based on the maximum scale height.

Apart from the distance estimation, ACs can constrain the ages of stellar populations in a given system. The assessment of the age of a given AC is done through its mass and absolute magnitude in the V and I-band. To determine the M_V and M_I we used the extinction maps from Schlafly & Finkbeiner (2011) (for the reddening $E(B-V)$ and extinction A_V) and equation 7 from Hamanowicz et al. (2016) to calculate the extinction in the I-band, A_I:

$$A_I = 1.969 \cdot E(B-V). \tag{3.4}$$

Table 3.2.3: Table for calculated masses of the ACs that lie inside the SMCNOD. Column 1 lists star IDs in the same format as in Table 3.2.2, column 2 contains masses in solar units, and the subsequent columns 3 - 6 provide ages in Gyr for a given metallicity Z. We used evolutionary tracks with overshooting (non-canonical models, Pietrinferni et al. 2004) and we assumed a mass loss with a free parameter η equal to 0.4 (Reimers 1975; Girardi et al. 2000).

		Z=0.0003	Z=0.0006	Z=0.001	Z=0.002
ID	M [$M_\odot$]	Age [Gyr]	Age [Gyr]	Age [Gyr]	Age [Gyr]
016	1.261	2.31	2.36	2.44	2.63
027	1.081	4.06	4.16	4.31	4.65
031	1.261	2.31	2.36	2.44	2.63
034	1.292	2.28	2.33	2.41	2.59

With the previously acquired distances we obtained estimates for the absolute magnitudes in both passbands. Following the procedure from Fiorentino & Monelli (2012) we determined masses of the ACs within the SMCNOD with the equations from Marconi et al. (2004):

$$\log M_{\mathrm{F}} = -0.97 - 0.53 M_I - 1.55 \log P + 1.44\,(M_V - M_I) \tag{3.5}$$

$$\log M_{1\mathrm{O}} = -1.29 - 0.58 M_I - 1.79 \log P + 1.54\,(M_V - M_I)\,, \tag{3.6}$$

where F and 1O represent the first overtone and fundamental mode, respectively. The resulting masses are in solar units. For the age estimate we used stellar evolutionary models from the BaSTI database[1] (Pietrinferni et al. 2004). The results can be found in Table 3.2.3. We assumed non-canonical models with the commonly assumed mass loss parameter $\eta = 0.4$ (Girardi et al. 2000) and four different possible metallicities $Z = (0.0003, 0.0006, 0.001, 0.002)$. The broad metallicity range was selected based on the metallicity–age distribution (see fig. 14 in Cignoni et al. 2013) of the SMC. From this table (Tab. 3.2.3), we see that the ACs inside the SMCNOD are most likely members of an intermediate-age population, which is in good agreement with the conclusions of Pieres et al. (2017). We acknowledge that non-canonical models (with overshooting in the stellar interior) are more suitable for ages below 4 Gyr during the hydrogen-burning phase. Thus we decided to recalculate ages also for canonical models (without overshooting) and compare them with ages calculated using non-canonical models. The difference between the two groups varies around 0.02 Gyr and is therefore negligible at these ages.

RR Lyrae stars

RR Lyrae stars are Population II stars, mostly radially pulsating variables, located on the horizontal branch of the Hertzsprung-Russell diagram. They can be used to study stellar pulsations and evolution and are unambiguous indicators of populations older than 10 Gyr.

OGLE-IV contains over 45 000 RR Lyrae stars in the Magellanic system, of which 6 572

[1] http://albione.oa-teramo.inaf.it/

lie in the SMC. Of the whole sample of RR Lyraes in the SMC more than 5 000 belong to the RRab type, over 800 are first overtone pulsators, and more than 600 are RRd-type variables. We decided to use only the fundamental-mode RR Lyraes. Their spatial distribution is plotted in Fig. 3.2.5. This figure demonstrates that RR Lyrae stars show a roughly spheroidal distribution with a pronounced concentration towards the central regions of the SMC (see also Haschke et al. 2012b; Jacyszyn-Dobrzeniecka et al. 2017). Thirteen RR Lyrae stars have celestial positions overlapping with the SMCNOD.

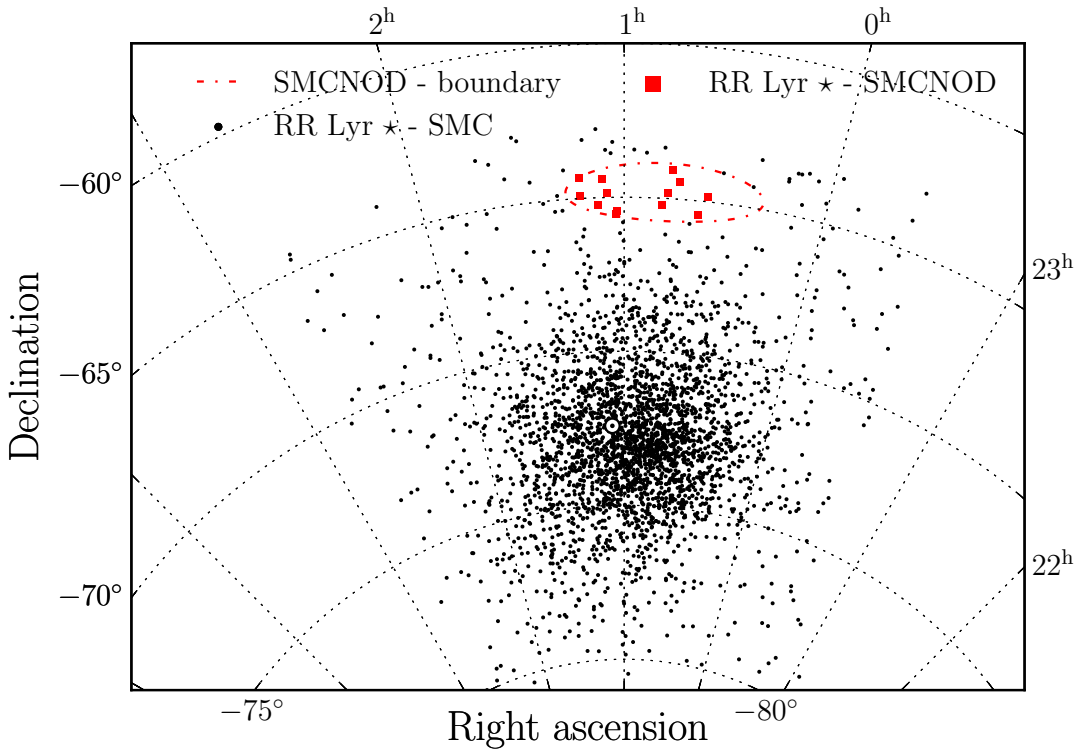

Figure 3.2.5: Similar figure as the Fig. 3.2.1 but for RR Lyrae stars in the SMC.

In order to test whether these thirteen RR Lyraes could plausibly be a part of the SMCNOD, we calculated distances of individual RR Lyrae stars in the SMC. For the distance estimation, we used similar procedures as described in Skowron et al. (2016) and Jacyszyn-Dobrzeniecka et al. (2017). First, we removed stars that had no mean magnitude in the V-band and no value for the Fourier parameter φ_{31}^{I}. Second, we omitted stars with amplitudes of $A_I < -5 \cdot \log P - 1$ in order to remove possible blends. This cut removed 76 stars from the short-period end of the period-amplitude diagram. In addition, many RR Lyrae stars

exhibit a quasi-periodic modulation of the light curve known as the Blazhko effect (for a review, see Szabó 2014). It is assumed that almost 50 % of the fundamental-mode RR Lyraes display this effect (see Prudil & Skarka 2017; Benkő et al. 2010). It is generally presumed that stars exhibiting the Blazhko effect are not suitable for determining their metallicities via a Fourier analysis of their light curves and thus subsequent distances. To remove stars that show this effect we used equation 2 from Prudil & Skarka (2017) and omitted RR Lyraes that lie more than 4σ below this fit. In the end, we were left with 2 991 RRab-type pulsators. Subsequently, we fitted truncated Fourier-series to the I-band light-curves of the remaining stars, of the form

$$m(t) = A_0^I + \sum_{k=1}^{n=6} A_k^I \cdot \cos\left(2\pi k \frac{HJD - M_0}{P} + \varphi_k^I\right). \tag{3.7}$$

In this equation the A_k^I represent amplitudes, the heliocentric Julian date, HJD, is the time of the observation, M_0 is the time of brightness maximum, P represents the pulsation period, and the φ_k^I are the phases. The next step was to calculate the metallicity $[\mathrm{Fe/H}]_{\mathrm{S05}}$ using the relation from Smolec (2005):

$$[\mathrm{Fe/H}]_{\mathrm{S05}} = b_1 + b_2 \cdot P + b_3 \cdot \varphi_{31} + b_4 \cdot A_2^I, \tag{3.8}$$

where the coefficients b are $b_1 = -6.125 \pm 0.832$, $b_2 = -4.795 \pm 0.285$, $b_3 = 1.181 \pm 0.113$, and $b_4 = 7.876 \pm 1.776$. The errors in the metallicity derived from Eq. 3.8 were estimated using a Monte Carlo error simulation. Using Equation 3.8 we obtained metallicities on the Jurcsik (1995) scale. To calculate distances, we first transformed this metallicity to the Carretta et al. (2009) scale through the equation 3 from Kapakos et al. (2011):

$$[\mathrm{Fe/H}]_{\mathrm{C09}} = 1.001 \cdot [\mathrm{Fe/H}]_{\mathrm{J95}} - 0.112. \tag{3.9}$$

With the resulting metallicities, we could then proceed with the distance estimation in the following manner. First, we calculated the Wesenheit magnitude for an individual RR Lyrae star using Equation 3.1. Afterwards, we used an equation from Braga et al. (2015) to calculate the absolute Wesenheit magnitude:

$$W_{I,V-I}^{abs} = a_1 + a_2 \cdot \log P + a_3 \cdot ([\mathrm{Fe/H}]_{\mathrm{C09}} + 0.04), \tag{3.10}$$

where the parameters a are $a_1 = -1.039 \pm 0.007$, $a_2 = -2.524 \pm 0.021$ and $a_3 = 0.147 \pm 0.04$. Subsequently, using the distance modulus we got the distance in kpc:

$$d = 10^{\left(W_{I,V-I} - W_{I,V-I}^{abs} + 5\right) \cdot 0.2}. \tag{3.11}$$

The errors for individual distances were calculated using error propagation, where we assumed $\sigma_{V,I} = 0.02$ mag (Jacyszyn-Dobrzeniecka et al. 2017) for the uncertainties in the OGLE-IV passbands V and I. The basic properties of the RR Lyrae stars that coincide in projection with the SMCNOD can be found in Table 3.2.4.

Fig. 3.2.6 shows the declination vs. distance for individual stars. To constrain the RR Lyraes based on their possible association with the SMCNOD we assumed the scale height

Table 3.2.4: Properties of RR Lyrae stars that lie at the same coordinates as the SMCNOD. Column 1 contains the ID of a star in the form OGLE-SMC-RRLYR-ID, columns 2 and 3 provide right ascension and declination (J2000), columns 4 and 5 contain distances with errors, similar to columns 6 and 7 that contain metallicities and their errors. The full table for all analysed RR Lyrae stars in the SMC is available as supplementary material in Prudil et al. (2018b).

ID	R.A. [deg]	Dec [deg]	d [kpc]	σ_d [kpc]	[Fe/H]	$\sigma_{\mathrm{[Fe/H]}}$
3542	8.78842	-64.83892	66.73	2.82	-1.98	0.45
3633	9.43142	-65.45781	60.39	2.16	-1.72	0.31
3851	10.96179	-64.44103	59.76	1.82	-1.70	0.14
3941	11.47646	-64.06644	5.85	0.17	-1.29	0.04
3973	11.73700	-64.80486	56.10	2.45	-1.27	0.49
4054	12.19496	-65.20972	59.31	2.04	-0.78	0.29
4566	15.55129	-65.45931	64.63	2.20	-2.18	0.25
4581	15.63971	-65.54542	57.70	1.87	-1.59	0.22
4685	16.24354	-64.84886	17.29	0.51	-1.72	0.07
4738	16.63004	-64.40250	76.23	3.03	-2.50	0.39
4777	16.94008	-65.23344	61.27	2.16	-2.05	0.29
4960	18.25642	-64.33211	71.51	2.39	-2.27	0.23
4965	18.30121	-64.92725	60.01	1.82	-1.56	0.14

of the old population of the SMC to be 2.0 ± 0.4 kpc (Haschke et al. 2012b), thus within a possible range up to 2.4 kpc. Overall, out of 13 RR Lyrae stars that share the coordinates with the projected location of the SMCNOD, 8 are consistent with the assumed scale height for the SMCNOD within the errors. This result is based on the assumption that SMCNOD shares the same scale height as the SMC (based on the half-light radius equal to $r_{\mathrm{h}} = 2.1$ kpc, Pieres et al. 2017).

Analysis of the spatial distribution

In this section, we explore whether the four ACs and eight RR Lyrae stars whose positions and distances coincide with the SMCNOD stand out in comparison with the overall stellar densities in the SMC outskirts. We created a set of 14 contiguous ellipses in equatorial coordinate space with the same size as the SMCNOD in the previous plots (see Figs. 3.2.1, 3.2.3, 3.2.5 for reference). These ellipses were distributed around the SMCNOD in the outskirts of the OGLE-IV photometry and include the northern boundaries of the SMC. Their minor and major axes, at the distance of the SMC, are 1.02 and 7.98 kpc, respectively.

Anomalous Cepheids

First, we looked at the ACs and their distribution in the constructed ellipses (see the Fig. 3.3.1). The red dash-dotted ellipse represents the SMCNOD and the blue ellipses represent the area considered in addition. The meaning of the points is the same as in Fig. 3.2.3. From this

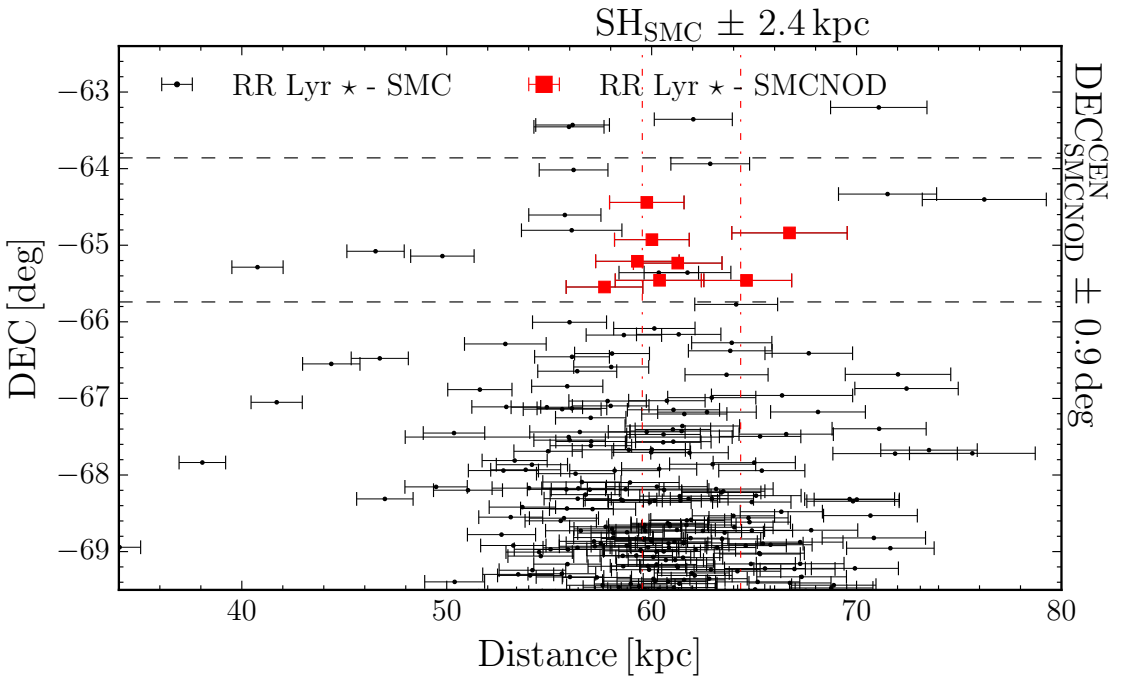

Figure 3.2.6: Same as Fig. 3.2.4, but for RR Lyrae stars. The red squares stand for RR Lyraes that probably belong the SMCNOD. The black dots represent the remaining RR Lyraes in the SMC. The red dash-dotted lines represent assumed distance boundaries for the SMCNOD, based on the maximum scale height. In addition, the dashed horizontal lines represent the adopted boundary in declination for the SMCNOD.

plot, we clearly see that only some of the surrounding ellipses contain AC stars (ellipses 6, 7, 9, 12 and 13). In addition, the ellipses 9 and 13 contain the majority of the ACs that fell into the outlined boundaries (nine out of thirteen).

Therefore, the ACs found at the coordinates of the SMCNOD together with ellipses 9 and 13 appear to constitute an extension of the distribution of the ACs from the SMC. In addition, four ACs from the SMCNOD seem to form a tight group in coordinate space. Such an overdensity of ACs in equatorial coordinates in the SMC outskirts stands out as compared with other regions of the SMC outskirts. Furthermore, applying the procedure from Section 3.2.3 we estimated ages and masses for the ACs within the ellipses 9 and 13 and compared them with the values for the SMCNOD. We found that the ages for the ACs in these ellipses are approximately in the same range as for the SMCNOD ACs (around 2.8 Gyr for Z=0.001). Therefore, the ACs in ellipses 9 and 13 most likely also belong to the intermediate-age population (see Fig. 3.3.2).

RR Lyrae stars

In Fig. 3.3.3 we analysed the projected spatial distribution of the RR Lyrae stars by subdividing the northern outer regions of the SMC into elliptical fields of the approximate size of the

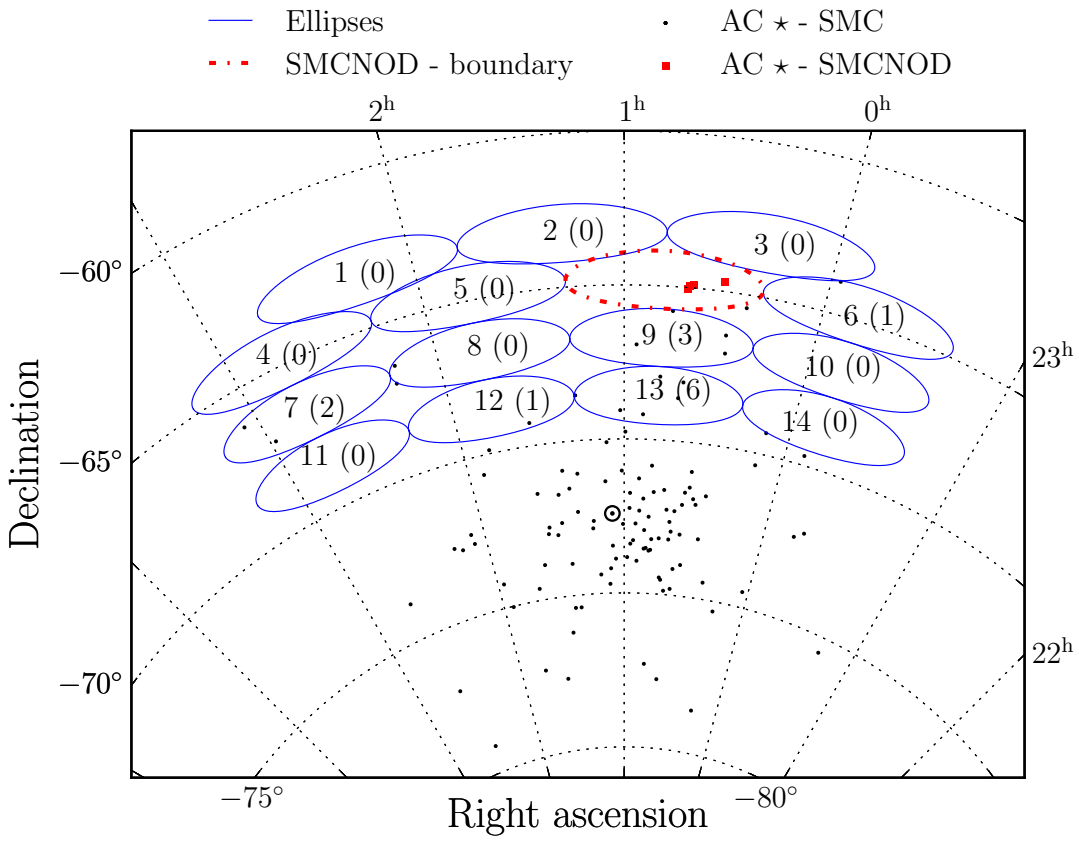

Figure 3.3.1: Field star analysis for the ACs in the SMC. The panel shows the spatial distribution of ACs in the SMC with the red dash-dotted ellipse marking the position of the SMCNOD and blue ellipses representing the test fields. The numbers inside the ellipses stand for the designation of the given ellipse with the number of ACs within the scale height (number in brackets). The ACs that lie inside the SMCNOD are represented by red squares. Black dots stand for ACs in the SMC. The Sun symbol denotes the apparent kinematic center of the SMC (Stanimirović et al. 2004).

SMCNOD. The same symbols as in Fig. 3.3.1 are used. We see an excess of RR Lyraes in the ellipses 9 and 13 that are located between the central region of the SMC and the SMCNOD. The SMCNOD looks almost like an extension of this higher-density region. In the ellipses 9 and 13, we also see a large number of RR Lyraes that share the same scale height as the main body of the SMC. Of the total number of 31 RR Lyrae stars in ellipse 9, 16 stars lie within one scale height of the SMC. For ellipse 13, 72 out of total number 123 RR Lyraes share the distance range of one SMC scale height, which is something we would expect based on the density profile for RR Lyrae stars in the SMC (see § 3.4.1).

The metallicity distribution (on the Jurcsik (1995) scale) is shown in Fig. 3.3.4 for ellipses close to the SMCNOD and with a large number of RR Lyrae stars. Only stars that

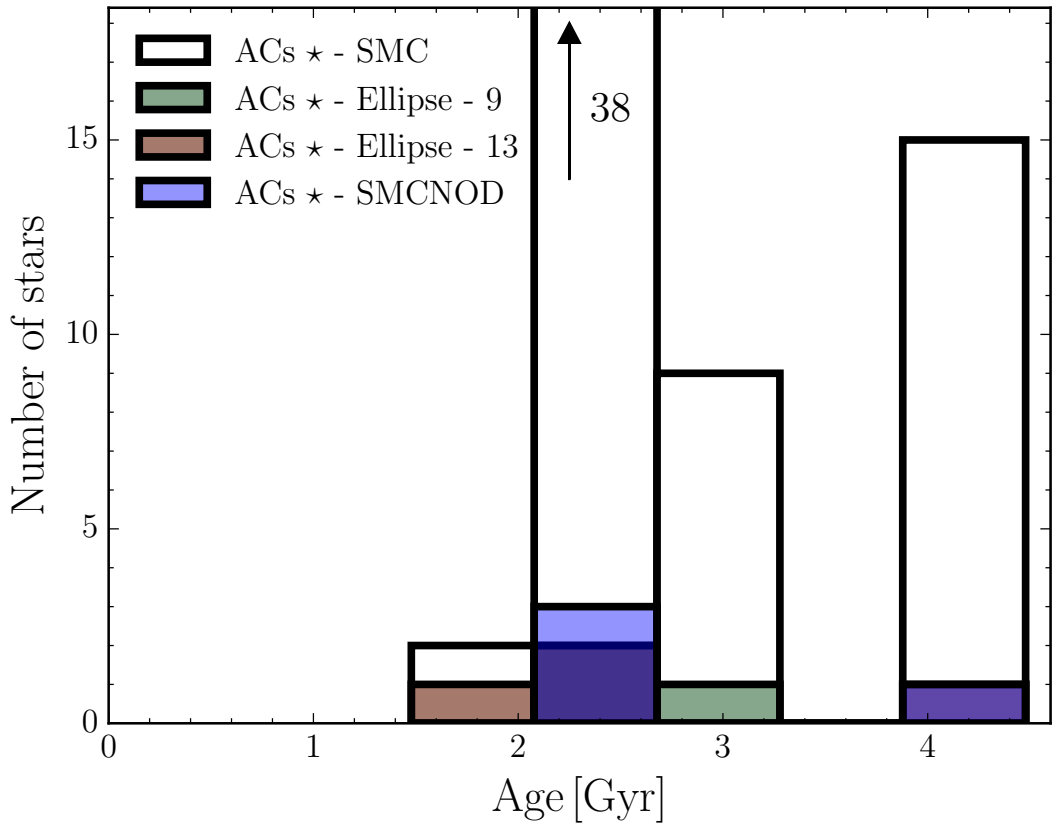

Figure 3.3.2: Distribution of ages for ACs in the SMC (transparent), Ellipse 9 (green columns), 13 (red columns) and SMCNOD (blue columns). To increase clarity, we decreased the vertical axis range and marked the best populated bin range with an arrow and the number of the stars included.

fell into a distance range of one scale height of the SMC (and SMCNOD, respectively) were included in this plot. Other ellipses were too distant in equatorial coordinates (ellipse 12 - containing five RR Lyraes) or contain only a few RR Lyrae at a set scale height range (ellipse 8 - containing two RR Lyraes) for the SMC. The median values of the metallicities are $[\mathrm{Fe/H}]_{\mathrm{SMCNOD}} = -1.71 \pm 0.21$ dex, $[\mathrm{Fe/H}]_{\mathrm{Ellipse-9}} = -1.79 \pm 0.28$ dex and $[\mathrm{Fe/H}]_{\mathrm{Ellipse-13}} = -1.75 \pm 0.20$ dex. The number of RR Lyrae stars in each case were 8, 16, and 72, respectively. The median metallicity calculated for RR Lyraes in the SMC in our study is -1.69 ± 0.21 dex. For comparison, Skowron et al. (2016) found the metallicity of the RR Lyrae population of the SMC to be -1.77 ± 0.48 dex (on the Jurcsik (1995) scale, using 3 560 fundamental mode RR Lyraes) or -1.70 dex with an intrinsic spread of the metallicity distribution function of 0.27 dex on the Zinn & West (1984) scale (Haschke et al. 2012b). It is clearly seen from the metallicities that the ellipses 9 and 13 within the same R.A. range share similar metallicities

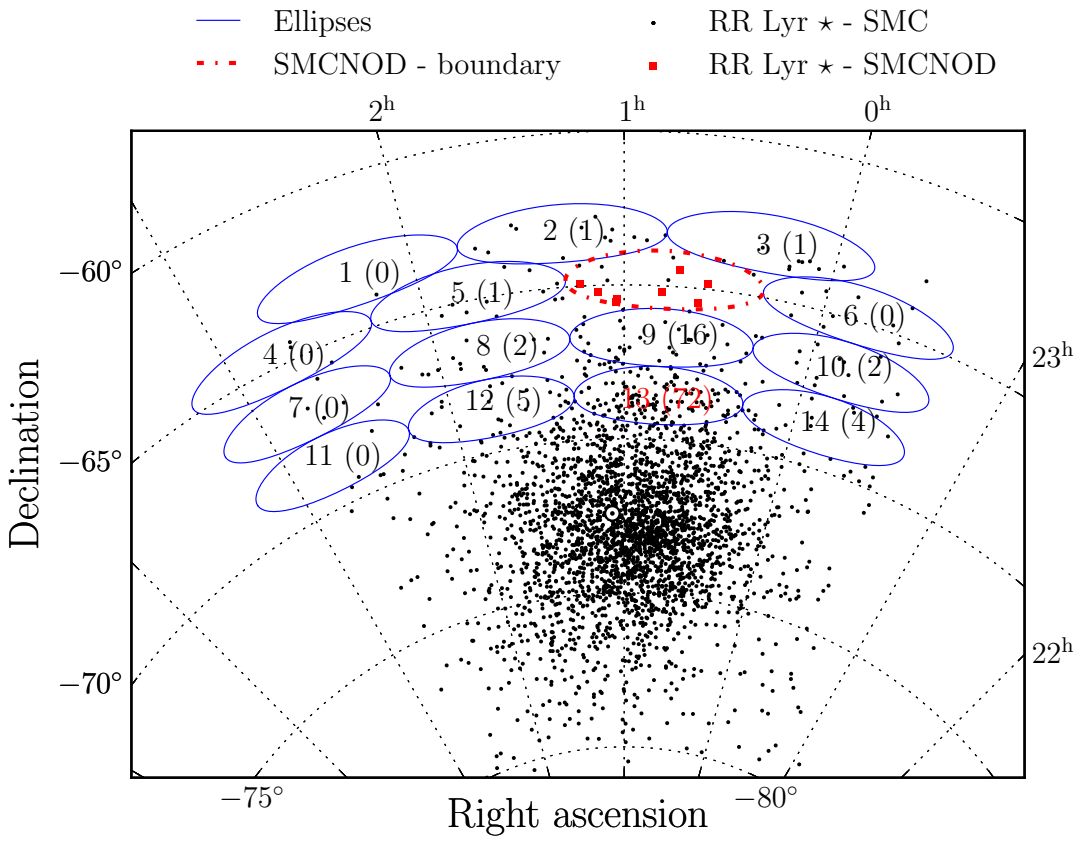

Figure 3.3.3: Same as in Fig. 3.3.1 but for RR Lyrae stars of type ab.

with the SMCNOD and the SMC as a whole. Only ellipse 8, with different R.A. ranges, has a different median metallicity ($[Fe/H]_{Ellipse-8} = -2.79 \pm 0.53$ dex) than the other plotted ellipses. We acknowledge that within the errors, the metallicities are similar. In addition, we note that low number statistics might have affected our results for ellipse 8, since it contains only 2 RR Lyraes. Furthermore, the very low metallicity for ellipse 8 should be taken with a grain of salt, since the empirical relation for the metallicity of RR Lyraes has been calibrated only up to -2.1 dex.

RR Lyrae subtypes

Up to this point, we only considered RR Lyraes that pulsate in the fundamental mode. However, the first-overtone and double-mode pulsators also occupy the northern outskirts of the SMC. Distance estimation for RRc/RRd type stars can be onerous, therefore we decided to base our reasoning strictly on their position in the CMD (see Fig. 3.3.5) for a given ellipse.

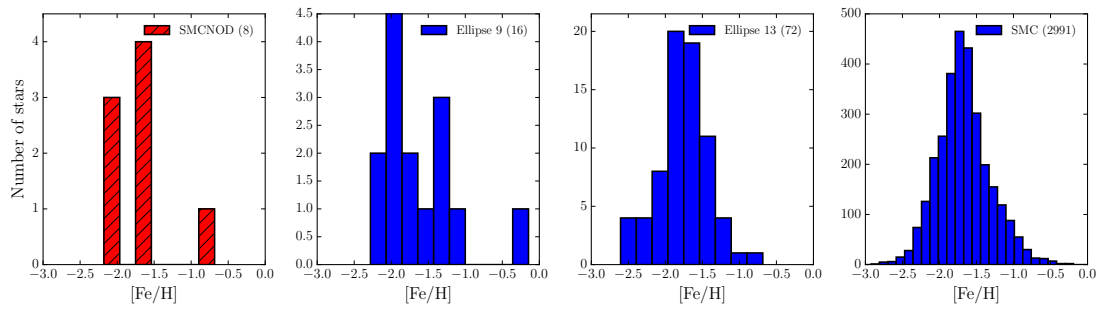

Figure 3.3.4: Metallicity distribution for the SMCNOD, selected ellipses, and the SMC overall. The vertical axis depicts the number of stars and the horizontal axis represents metallicity (on the Jurcsik 1995, scale) with the same range for all distributions. The numbers in brackets represent the total number of RR Lyraes shown.

The blue points represent fundamental mode pulsators, red points stand for the first-overtone variables, and green triangles correspond to RRd type stars.

Based on equatorial coordinates and location in the CMD, the SMCNOD contains probably two first-overtone RR Lyrae out of four potential candidates. On the other hand, in the ellipses below the SMCNOD (9 and 13 thus closer to the SMC main body) the situation is somewhat different. The aforementioned ellipses contain in total 17 and 26 RRc type stars, respectively.

Out of these, approximately eleven first-overtone pulsators in ellipse 9 and 25 in ellipse 13 lie in a similar magnitude region in the CMD as the fundamental mode pulsators found at the distance range of the SMC. Therefore, the most populated ellipses with the RRab pulsators in the SMC outskirts contain a quite significant number of RRc-type stars. In general in the SMC for each RRc-type star, we can find more than 6 fundamental-mode pulsators (5 105 RRab-type stars and 801 RRc-type stars). Therefore the number of first-overtone pulsators in the SMCNOD and in ellipse 13 roughly corresponds to the expected ratio of RRc-type stars. On the other hand, the nearby ellipse 9 contains a higher number of first-overtone variables.

Double-mode pulsators can also be found in the coordinate range of the SMCNOD and in ellipses 9 and 13. Based on its position in the CMD, the SMCNOD presumably contains only one RRd-type star. The aforementioned ellipses contain a higher number of double-mode pulsators. Ellipse 9 contains 8 RRd-type stars. Based on the CMD all lie within the scale height of the SMC. For ellipse 13 we found 28 RRd type variables to share the position in the coordinate space and all of them seem to lie within the scale height of the SMC. Similar to the first-overtone pulsators, double-mode variables are also abundant in ellipse 9. Ellipse 13 and the SMCNOD, on the other hand, contain on average the expected ratio of double-mode pulsators in comparison with the overall ratio for the SMC.

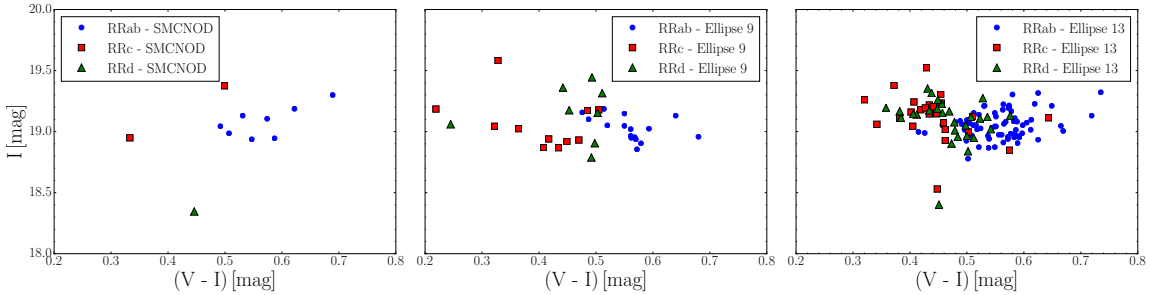

Figure 3.3.5: From left to right: Colour-magnitude diagrams for SMCNOD, ellipse 9, and 13, respectively. The blue points represent the fundamental mode pulsators, red squares stand for the first-overtone variables and green triangles represent RRd type stars.

Detection limitations of the SMCNOD

In this section, we explore the possibility whether variable stars that were found inside the SMCNOD truly create an overdensity or are just a part of the expected density profile of the SMC outskirts.

Cartesian coordinate system and density profile

In order to test whether the SMCNOD can be detected using variable stars, we transformed equatorial coordinates and distances for ACs and RR Lyrae stars into a three-dimensional Cartesian coordinate system. We used the equations 12, 13, and 14 from Jacyszyn-Dobrzeniecka et al. (2016) in the following form:

$$x = -d \cdot \cos(\mathrm{Dec}) \sin(\mathrm{R.A.} - \mathrm{R.A._{cen}}) \tag{3.12}$$

$$y = d \cdot (\sin(\mathrm{Dec}) \cos(\mathrm{Dec_{cen}})) - \mathrm{d} \cdot \cos(\mathrm{Dec}) \sin(\mathrm{Dec_{cen}}) \cos(\mathrm{R.A.} - \mathrm{R.A._{cen}}) \tag{3.13}$$

$$z = (d - d_{\mathrm{SMC}}) \cdot (\cos(\mathrm{Dec}) \cos(\mathrm{Dec_{cen}}) \cos(\mathrm{R.A.} - \mathrm{R.A._{cen}})) + (\mathrm{d} - \mathrm{d_{SMC}}) \cdot \sin(\mathrm{Dec}) \sin(\mathrm{Dec_{cen}}), \tag{3.14}$$

where $\mathrm{R.A._{cen}}$ and $\mathrm{Dec_{cen}}$ denote the coordinates of the apparent kinematic center of the SMC (Stanimirović et al. 2004). The results of this transformation for ACs are depicted in Fig. 3.4.1. The top left and the two bottom panels of Fig. 3.4.1 show ACs in the SMC in a 3D Cartesian coordinate system overplotted with the kernel density estimate. In the x vs. y plane, ACs found in the SMCNOD cluster in a similar fashion as in Fig. 3.2.3, while in x vs. z and y vs. z they follow a narrow sequence. In addition, this tail sequence seems to be elongated towards the larger distances. This effect is also observed in RR Lyrae stars (see Fig. 3.4.2). This effect can be related to the interaction between the Magellanic clouds since we a see similarly elongated distribution of the CCs in the SMC. We note that accounting for errors this trend could disappear. The panel on the top right displays the density profile of

the ACs in the SMC, which was constructed in the following way:

First, we utilized Cartesian coordinates and calculated an elliptical radius for the elongated shape of the SMC using the median axis ratio 1 : 1.10 : 2.13 from Jacyszyn-Dobrzeniecka et al. (2017) and the following equation:

$$r = \sqrt{x^2 + y^2 \mathrm{p}^{-2} + z^2 \mathrm{q}^{-2}}, \tag{3.15}$$

where p and q represent the ratios between y-x (1.10/1.0) and z-x (2.13/1.0), respectively (Jacyszyn-Dobrzeniecka et al. 2017). The radius r then served as a scale for the density profile, where we counted the number of stars from the center of the SMC towards the outskirts in 3D shell-like bins. The bin size of the individual ranges in the density profile was 2.5 kpc in order to encompass all four ACs found in the SMCNOD. From this plot, we see that the density of ACs at the galactocentric distance of the SMCNOD does slightly deviate from the power-law (blue line) fitted to the density profile of the ACs. This anomaly lies more than one σ above the density profile. We note that the lower number of ACs in the northern outskirts of the SMC may have affected our results.

In Fig. 3.4.2 the distribution of the SMC RR Lyrae stars is plotted in the Cartesian coordinate system (top left and bottom panels). The top right panel shows the density profile of their distribution. From the Cartesian distribution, we see that RR Lyrae stars are numerous in the outskirts of the SMC. They do not seem to form any noticeable overdensity at the position of the SMCNOD (see contours for kernel density estimation). A similar situation can be seen also for the density profile of RR Lyrae stars. At the position of the SMCNOD, we do not observe any anomaly that would stand out. It is important to note that the bin sizes for ACs and RR Lyrae stars were selected to comprise as many stars associated with the SMCNOD as possible. Therefore, our density profiles are slightly contaminated with stars occupying the same bin range (2.5 kpc and 3 kpc for ACs and RR Lyraes, respectively). Thus, despite this contamination in the density profile for old population RR Lyrae stars, we do not observe a statistically significant deviation that would stand out in the outskirts of the SMC.

Probability of finding stars in the SMCNOD

For this analysis, we assumed that the distribution in the Cartesian coordinate system (x, y, and z) of ACs and RR Lyraes in the SMC is Gaussian. Then, we simply integrated Gaussian functions for the Cartesian coordinates with respect to the boundaries set by variables inside the SMCNOD.

First, we analysed ACs, using the positions of the ACs in the SMCNOD as boundary conditions for the integration of the three distributions. In the top panel of Fig. 3.4.3 we see the distributions for x, y, and z coordinates overplotted with the Gaussian distribution (blue dashed lines). The red vertical lines denote the average values of ACs found in the SMCNOD for a given dimension. The probabilities calculated for each coordinate were multiplied with the number of ACs in the SMC and divided by the number of ACs in the SMCNOD. The resultant probability of finding four ACs at the position of the SMCNOD is less than 1.0 %.

To estimate the probability of finding eight RR Lyrae stars at the position of the SMCNOD we proceeded in the same way as in the case of the ACs. We calculated probabilities for each

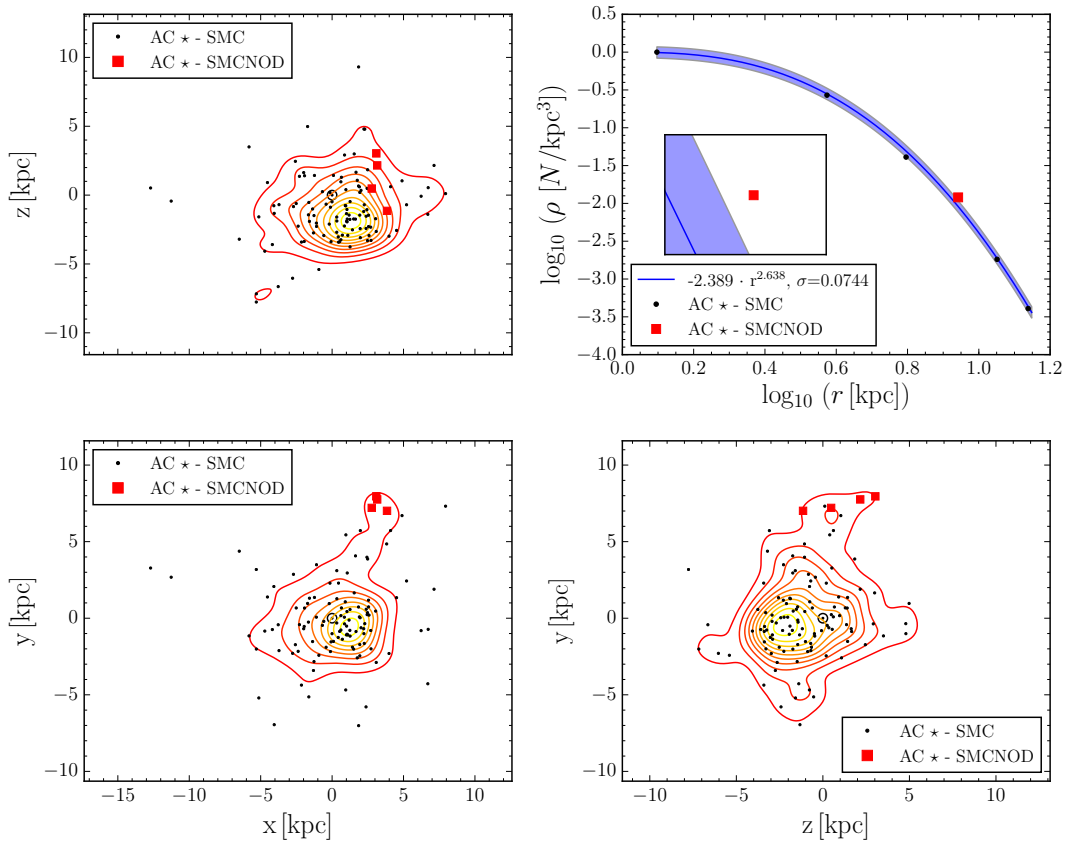

Figure 3.4.1: The top left and the two bottom panels display ACs (black dots) in the Cartesian coordinate system centered on the SMC's dynamical center. The red squares represent ACs found at the equatorial coordinates of the SMCNOD. The Sun symbol denotes the apparent kinematic center of the SMCNOD. In addition, we overplotted the spatial distribution of ACs using kernel density estimation with ten contour levels. The top right panel displays the density profile for ACs calculated based on their apparent kinematic center and stretching towards the outskirts of the SMC (with bin size 2.5 kpc). The black points represent bins for ACs and the red square (at $\log_{10} r = 0.942$ kpc) stands for four ACs found in the SMCNOD.

coordinate using boundary conditions set by the eight RR Lyrae stars located inside the SMCNOD. The bottom panel of Fig. 3.4.3 depicts the distributions for x, y, and z Cartesian coordinates with dashed lines representing a Gaussian distribution. The integration ranges (of RR Lyrae stars in the SMCNOD) for each coordinate are denoted by red vertical lines. The resulting probability was then multiplied by the number of studied RR Lyrae stars and divided by the number of assumed RR Lyraes within the SMCNOD. Thus the probability of finding eight RR Lyrae stars at the position of the SMCNOD is equal to 13.0 %. Therefore the probability is almost 20 times higher than the probability for finding four ACs.

This finding seems to be consistent with the density profiles of the SMC (Fig. 3.4.1 and

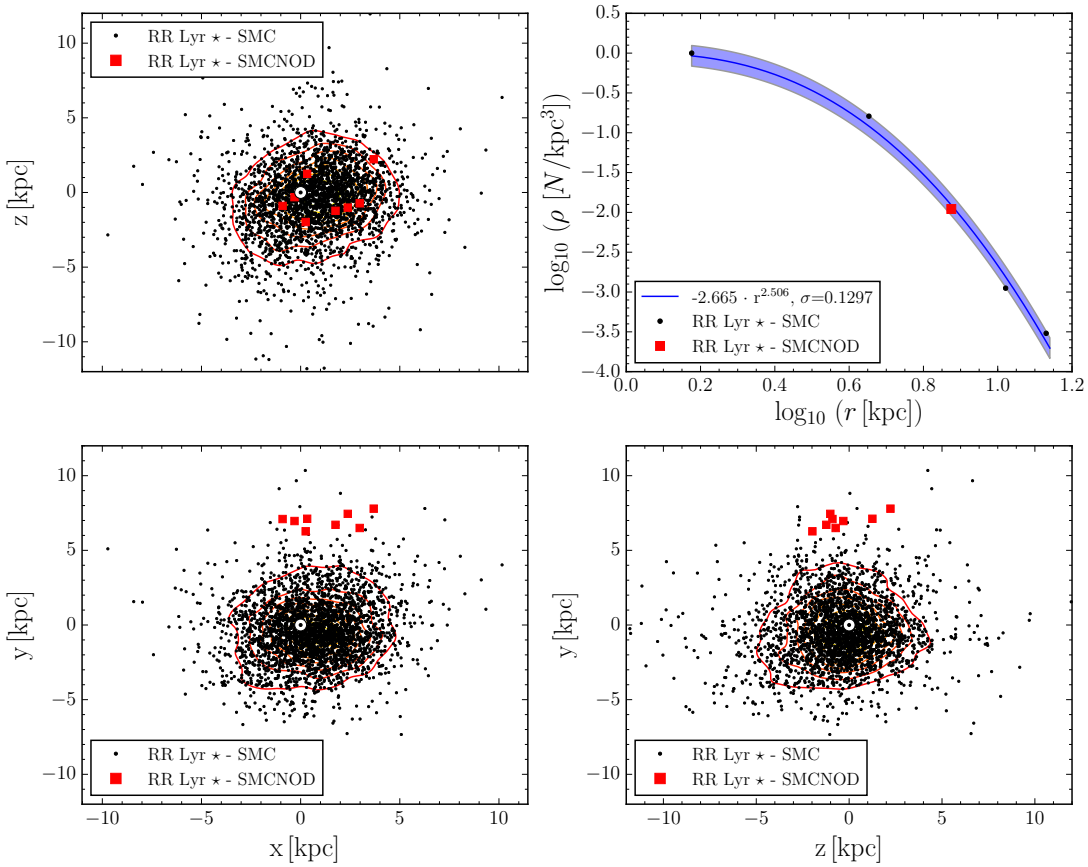

Figure 3.4.2: Similar to Fig. 3.4.1, but for RR Lyrae stars. The density profile in the top right corner was constructed by using annuli with a width of 3 kpc. In addition, the red square in the upper right panel (at $\log_{10} r = 0.875$ kpc) represents RR Lyrae stars in the SMCNOD based on their radius r with respect to the kinematic center of the SMC.

3.4.2). ACs at the possition of the SMCNOD slightly stand out and the probability of finding them at that position is very small, while RR Lyrae stars smoothly follow the power-law for the SMC and we do not observe any deviation, which is in an agreement with the calculated probability, which is rather high for this region of the SMC. Therefore, RR Lyraes seem to be evenly distributed across the SMC outskirts without forming any overdensity similar to the SMCNOD. Integration ranges and further details can be found in Table 3.4.1. We note that the calculated probabilities comprise only stars that belong to the SMCNOD while the density profiles also contain stars that occupy the same bin range as the variables found in the SMCNOD.

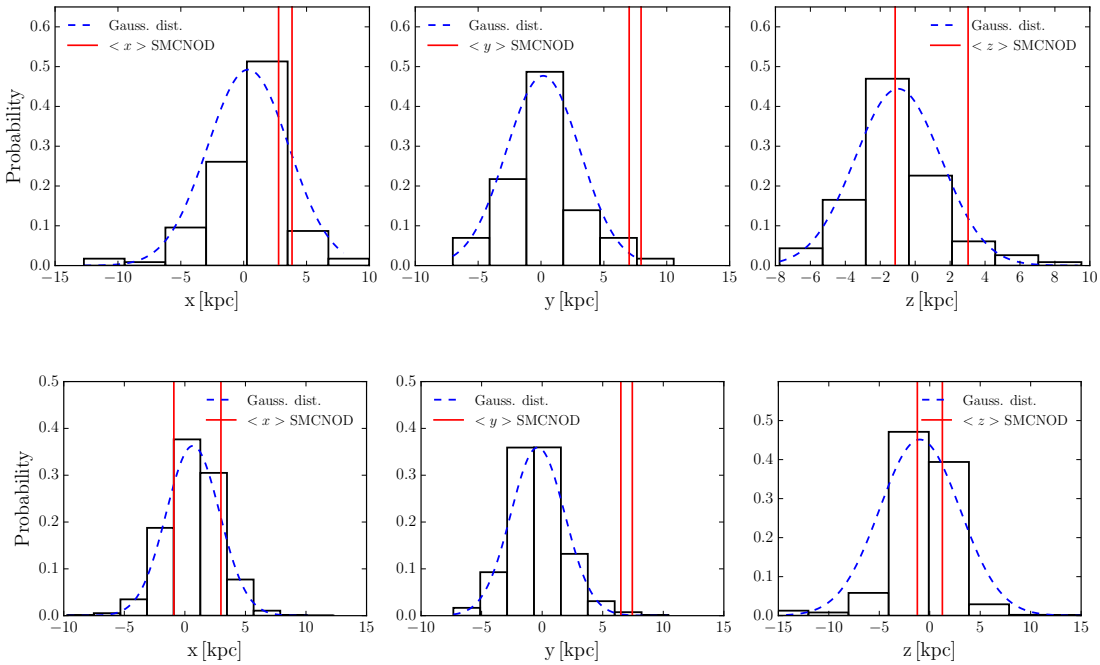

Figure 3.4.3: The distribution of Cartesian coordinates for ACs (top three panels) and RR Lyraes (bottom three panels). The dashed blue lines represent a Gaussian distribution and the red vertical lines mark the integration ranges of a given coordinate for variables found in the SMCNOD.

Summary and conclusions

In this chapter, we used variable stars from the OGLE-IV survey to trace and study the recently discovered stellar overdensity, SMCNOD, in the northern outskirts of the SMC. Using photometric data for the variables located at and near the SMC we studied their spatial, metallicity, and age distribution. We found that none of the CCs lie at the coordinates of the SMCNOD but prefer the more central star-forming regions of the SMC (see also Haschke et al. 2012b). The lack of young pulsators in the SMCNOD suggests that this overdensity does not contain stars younger than a few hundred million years consistent with the findings of Pieres et al. (2017) from a deep CMD of this region. In the R.A. vs. Dec plane, we found six EBs at the same coordinates as the SMCNOD. To verify their association with the SMCNOD, a thorough analysis of their infrared photometry and radial velocity curves or light curve modeling would be required.

We found four ACs coinciding with the coordinate and distance range of the SMCNOD. We calculated their ages, which range from 2 to 4.5 Gyr. This agrees very well with the intermediate-age population scenario suggested by Pieres et al. (2017) for the SMCNOD. In addition, a similar age distribution is also seen in the SMC in general. Based on our performed tests, ACs occur rarely in the SMC outskirts and their high presence (σ excess

Table 3.4.1: Table for properties used to calculate the probability of detecting variable stars at the position of the SMCNOD. Column 1 denotes the Cartesian components, columns 2 and 3 contain probability and boundary conditions for the given components based on the properties of the ACs in the SMCNOD. Columns 4 and 5 contain the same information as columns 2 and 3 but with respect to RR Lyraes found in the SMCNOD. The last row represents the calculated probability for finding the same number of variables at the location and distance of the SMCNOD (4 ACs and 9 RR Lyraes).

	ACs		RR Lyraes	
	Prob. %	Boundary [kpc]	Prob. %	Boundary [kpc]
x	8.68	(2.78; 3.84)	67.80	(-0.91; 3.68)
y	0.58	(7.01; 7.95)	0.13	(6.27; 7.79)
z	47.48	(-1.15; 3.03)	38.89	(-1.98; 2.22)
Total	0.69 %		13.0 %	

in density profile, see 3.4.1) at the location of the SMCNOD just by a chance is unlikely (less than 1.0 % probability, see 3.4.2). Therefore, we suggest that the ACs are indeed likely members of the SMCNOD overdensity.

We also found thirteen fundamental-mode RR Lyrae stars at the coordinates of the SMCNOD. Using their period-metallicity-luminosity relation we were able to estimate their distances and separate those that lie in the foreground/background from those that most likely lie within the SMCNOD. From thirteen RRab-type stars sharing the same coordinates as the SMCNOD, eight lie at the same distance range as the SMC (within the errors), and thus probably lie inside the SMCNOD (based on distance estimated by Pieres et al. 2017). The median metallicity of these pulsators is found to be around $[\mathrm{Fe/H}]_{\mathrm{SMCNOD}} = -1.71 \pm 0.21$ dex as derived from the Fourier analysis of their light curves, which agrees well with the metallicity of the RRab variable population of the SMC $[\mathrm{Fe/H}]_{\mathrm{SMC}} = -1.77 \pm 0.48$ dex (Skowron et al. 2016). The RR Lyrae stars seem to be evenly distributed across the outskirts of the SMC and we do not see any excess in the density profile. In addition, the probability of finding eight of them at the location of the SMCNOD is higher than in the case of ACs (13.0 %, see Sec. 3.4.2). We therefore conclude that these RR Lyrae stars may, but need not be a part of the SMCNOD overdensity. They are consistent with being part of the extended old population of the SMC as such. That supports the CMD-based finding of Pieres et al. (2017) that an old population, if present in the SMCNOD, is small.

Overall, we showed that the SMCNOD can be traced with the AC stars that probably belong to an intermediate-age population and possibly also with old RR Lyrae stars. The RR Lyrae stars that may be members of the SMCNOD have a similar median metallicity as the SMC. Moreover, the similarity in the properties of the pulsating variables in the SMCNOD, SMC outskirts and in the SMC's main body suggests that the SMCNOD is not a remnant of a smaller, accreted satellite, given its inferred metallicity, which would be inconsistent with, for instance, the metallicity-luminosity relation for dwarf galaxies (see, e.g., Grebel et al. 2003). Furthermore, our calculated ages and metallicities rule out the potential merger of a primordial galaxy mentioned in Pieres et al. (2017). The stellar population properties of the SMCNOD as indicated by its putative pulsating variable star members are consistent with

those of the bulk SMC population. Hence the origin of the SMCNOD lies more likely in the SMC itself and may be possibly a somewhat older and less prominent counterpart of the luminous loop features in the outskirts of the SMC found and discussed by de Vaucouleurs & Freeman (1972), Bruck (1980), and Gardiner & Hatzidimitriou (1992), among others.

CHAPTER 4

ON THE OOSTERHOFF DICHOTOMY IN THE GALACTIC BULGE: I. SPATIAL DISTRIBUTION

> "Though a candle burns in my house, there is nobody home."
>
> — J. O'Neill, Abyss

Abstract: We present a study of the Oosterhoff (Oo) dichotomy in the Galactic bulge using 8 141 fundamental mode RR Lyrae stars. We used public photometric data from the Optical Gravitational Lensing Experiment (OGLE) and the Vista Variables in the Vía Láctea survey (VVV). We carefully selected fundamental mode stars without modulation and without association with any globular cluster located toward the Galactic bulge. Subsequently, we identified and separated the Oosterhoff groups I and II on the basis of their period-amplitude distribution and using a relation fitted to the Oosterhoff I locus. Both Oosterhoff groups were then compared to observations of two bulge globular clusters and with models of stellar pulsation and evolution. We found that some of the variables classified as Oo II belong to a third Oo group. The Oosterhoff II variables are more metal-poor on average, more massive, and cooler than their Oosterhoff I counterparts. The analysis of their spatial distribution shows a systematic difference between *foreground*, central and *background* regions in the occurrence of the Oosterhoff II group. The difference between the Oo I and II groups is also seen in their distance distributions with respect to the Galactic bar, but neither group is associated with the bar.

This chapter is based on our published paper : **Prudil, Z.**, Dékány, I., Catelan, M., Smolec, R., Grebel, E. K., Skarka, M.: On the Oosterhoff dichotomy in the Galactic bulge: I. Spatial distribution, 2019, MNRAS, 484, 4833

Context

The RR Lyrae stars are helium-core burning, radially pulsating variables, found in old stellar systems. Thanks to their visual and infrared period-metallicity-luminosity relations, they are highly useful distance indicators within the Local Group of galaxies (Alcock et al. 1997; Clementini et al. 2003; Monelli et al. 2017). Their contribution has been recognized in studies involving the Milky Way and its components like the Galactic bulge (Dékány et al. 2013; Pietrukowicz et al. 2015), Galactic halo (Sesar et al. 2013), and Galactic disc (Dékány et al. 2018), and also the Large and Small Magellanic Clouds (Haschke et al. 2012a,b; Jacyszyn-Dobrzeniecka et al. 2017). Moreover, they have been proven to be useful in estimating the metallicity distribution function of a given system. Using their pulsation periods and light curve parameters we can estimate their individual metallicities (Jurcsik & Kovacs 1996; Smolec 2005; Hajdu et al. 2018). The RR Lyrae stars are divided into three sub-classes based on their mode of pulsation: The most common fundamental-mode (RRab) variables, the first-overtone (RRc) variables, and the double-mode (RRd) pulsators, which pulsate simultaneously in the fundamental mode and the first overtone.

Although RR Lyrae stars have been extensively studied in the past decades, there are still several open questions regarding their physical nature. For example, the uncertainty in their mass (due to the lack of a dynamical mass determination in binary systems, see Hajdu et al. 2015; Liška et al. 2016), the modulation of their light curves known as the Blazhko effect (see Szabó 2014; Smolec 2016, for extensive reviews), and the Oosterhoff dichotomy (Oosterhoff 1939).

Oosterhoff (1939) noticed that five Milky Way globular clusters (from hereon referred as GCs) can be divided into two classes based on the mean of the pulsation periods of RR Lyrae stars within them. Later on, Oosterhoff extended his analysis using additional globular clusters with RR Lyrae stars (Oosterhoff 1944). Nowadays, many of the Milky Way globular clusters can be separated into objects containing either RR Lyrae stars belonging to the Oosterhoff type I (Oo I) or Oosterhoff type II (Oo II) group. The Oo I clusters are more metal-rich ([Fe/H] $\geqslant -1.7$ dex), contain RR Lyraes that have short pulsation periods (around 0.55 days for RRab stars), and seem to be deficient in first-overtone pulsators (which provide less than 20 % of the RR Lyrae population). On the contrary, the Oo II clusters are mostly metal-poor ([Fe/H] $\leqslant -1.7$ dex), they have RR Lyraes with longer pulsation periods on average (0.65 days for RRab stars) and a rather high fraction of RRc stars (around 40 %).

Over the past decades several explanations of the Oosterhoff dichotomy have been proposed, for example, the existence of a hysteresis zone (van Albada & Baker 1973) implying two crossings of RR Lyraes through the instability strip (IS). van Albada & Baker suggest that Oo II RR Lyraes evolve from the blue to the red edge of the IS, while Oo I RR Lyraes evolve in the opposite direction, from the red to the blue edge of the IS. In other studies, Sandage et al. (1981) and Sandage (1981) examined zero-age-horizontal branch models and suggested a

higher helium abundance in Oo II clusters in order to explain the difference. Overall, a general consensus has not yet been reached (Catelan 2009).

The aforementioned solutions are in tension with the observed properties of RR Lyraes in the two GCs NGC 6441 and NGC 6388. These two GCs stand out from the classical Oosterhoff scheme since they contain RR Lyrae stars with long pulsation periods and high metallicities, [Fe/H] = -0.53 ± 0.11 dex and [Fe/H] = -0.60 ± 0.15 dex for NGC 6441 and NGC 6388 (Armandroff & Zinn 1988), respectively. They create their own Oo III group (Pritzl et al. 2000). Interestingly, when we compare the population of RR Lyraes in low-mass galaxies outside the Milky Way in the Local Group, we find that these objects do not fall into either Oosterhoff group. The Magellanic Clouds, other dwarf galaxies and their GCs fall between the classical Oosterhoff groups and create a so-called Oosterhoff-intermediate population (Catelan 2009). Therefore, we no longer see a bimodality but rather an Oosterhoff continuum (see left panel of fig. 6 in Catelan 2009). This suggests that the Oo dichotomy is intrinsic to Galactic GCs and thus might be a unique fingerprint of the Milky Way's evolution history.

In this paper, we explore the spatial structure of the Galactic bulge using RR Lyrae stars with respect to their Oosterhoff association. Galactic bulges are commonly grouped into two main types, classical (spheroidal) bulge formed through early merging events and (bar-like) pseudobulges formed through buckling disc instabilities (Kormendy & Kennicutt 2004). The Milky Way's bulge has a boxy/peanut (B/P) shape and is mainly characterized by cylindrical rotation (Howard et al. 2009). Roughly half of the edge-on disc galaxies contain B/P bulges (Lütticke et al. 2000). The B/P shape of our Galaxy is directly visible due to the fact that the structure is viewed under a non-zero angle (27 deg, Wegg & Gerhard 2013), and can be traced using red clump giants (McWilliam & Zoccali 2010; Gonzalez et al. 2011; Ness et al. 2012; Wegg & Gerhard 2013). Attempts to trace bar structure using old-population stars has been made in the past with disparate results (Dékány et al. 2013; Pietrukowicz et al. 2015). The radial velocity distribution of bulge RR Lyrae stars is inconsistent with typical B/P bulge kinematics, and overall they do not contribute to the boxy shape of the Galactic bulge (Kunder et al. 2016).

The Galactic bulge has been a target for studies of the Oosterhoff dichotomy in the past, for example, by Kunder & Chaboyer (2009). Using V-band data from the MACHO survey for RRab stars with *normal* light curves (based on the calculated deviation parameter from Jurcsik & Kovacs 1996), Kunder & Chaboyer found that the difference in pulsation periods between the bulge Oo I variables and the globular cluster OoI variables is about $\Delta \log P = 0.02$ days. In addition, in their study variables identified as Oo II stars could be on average brighter by 0.2 mag than their Oo I counterparts.

In this first paper of the series, we used data of RRab variables from the Optical Gravitational Lensing Experiment IV (from hereon OGLE-IV, Udalski et al. 2015) and the VISTA Variables in the Vía Láctea survey (VVV, Minniti et al. 2010) to study the physical and spatial properties of the Oosterhoff populations in the Galactic bulge. In the second paper of the series, Paper II (Prudil et al., in preparation), we will look at the kinematical distribution of some of the studied stars from the present paper. This paper is structured as follows. In Section 4.2 we describe how we selected our stellar sample. Section 4.3 discusses the computation of individual distances to the selected stars and the separation of the two Oost-

erhoff groups in the Galactic bulge. In Sect. 4.4 we compare the two classical Oosterhoff populations with two GCs located in the Galactic bulge and we discuss the mean physical parameters of the Oosterhoff groups. Section 4.5 discusses the spatial distribution of stars in our sample. We summarise our results in Sect. 4.6.

Sample selection

In order to study the Oosterhoff dichotomy in the Galactic bulge, we combined data from two large photometric surveys monitoring the area around the Galactic center, OGLE-IV and VVV. The OGLE survey monitors the Galactic bulge in optical wavelengths (V and I-bands), while VVV conducted observations in the near-infrared (Z, Y, H, J, and K_s-bands). Therefore, the combination of both datasets allowed us to cover a broad wavelength range.

To ensure homogeneity and detection completeness of our sample, we employed cuts to the sample of OGLE-IV variables and the resulting sample was then cross-matched with the data from the VVV survey. For the purpose of this study, we thus considered only variables with data in both surveys. In the Galactic bulge, OGLE-IV observed over 38 000 RR Lyrae stars of which more than 27 000 are fundamental-mode pulsators (Soszyński et al. 2014, 2017b). For the majority of objects the fourth OGLE release contains photometric data for individual stars, mean magnitudes in the V and I-bands, pulsation periods, peak-to-peak amplitudes and Fourier coefficients (R_{21}, φ_{21}, R_{31}, φ_{31}). To examine the Oosterhoff dichotomy in the Galactic bulge we used only RRab stars for which all aforementioned Fourier coefficients and mean magnitudes were available in both filters. We also omitted variables that belong to GCs (`gc.dat`[1]), have uncertain identification (`remarks.dat`[1]), and stars exhibiting additional periods (Smolec et al. 2016; Prudil et al. 2017). In addition, we employed cuts based on the colour-magnitude diagram (CMD) using the selection criteria suggested by Pietrukowicz et al. (2015):

$$I \leq 1.1(V-I)+16.0 \tag{4.1}$$
$$I \geq 1.1(V-I)+13.0 \tag{4.2}$$
$$V-I > 0.3 \tag{4.3}$$
$$I < 18.0. \tag{4.4}$$

These cuts were performed in order to remove stars with unreliable colours (bluer than the bulk of RR Lyrae pulsators in the Galactic bulge) and to improve the homogeneity of our selected sample (see top panel of fig. 1 in Pietrukowicz et al. 2015). In the end, 11 888 variables passed the aformentioned thresholds.

Removing stars with the Blazhko effect

As shown by Prudil et al. (2018a), the Blazhko effect can hide the existence of the Oo I and II populations in the Galactic bulge. One way to detect the Blazhko effect is the period

[1] Files provided by the OGLE-IV survey from their ftp data access.

analysis of individual stars, which in our case would be enormously time-consuming due to our sample size. Therefore, we combined two different approaches to remove stars from our sample exhibiting the Blazhko effect. First, we removed the fundamental-mode pulsators that were previously identified to show the Blazhko effect (over 40 % variables in the sample studied by Prudil & Skarka 2017, from hereon referred to as PS17). We employed a 3σ clipping based on the variables' position in the φ_{31} vs. R_{31} and φ_{21} vs. R_{31} planes using equations 5 and 6 from PS17.

Secondly, we used supervised machine learning to classify stars with Blazhko modulation. We used the data of RR Lyrae stars classified as modulated or non-modulated by PS17 (over 8 000 variables) to train various classifiers implemented in `scikit-learn` (Pedregosa et al. 2011), a library of the Python programming language. As input features we used the pulsation periods, total amplitudes, and a combination of the Fourier coefficients (R_{21}, R_{31}, φ_{21}, φ_{31}).

The classifier's performance can be hampered by under- or overfitting the training sample, which can result in poor performance on the test dataset. We can optimize the performance via cross-validation, i.e., by dividing the already classified dataset into two parts: a training sample, and the validation sample. The model's parameters are fitted to the training data, while its hyper-parameters (i.e., parameters that govern the model complexity or the fitting procedure) are optimized on the validation data. The tuning of hyper-parameters was carried out using the module `GridSearchCV` with 10-fold cross-validation by maximizing one of the metrics (Average precision), from the aforementioned library. In this procedure, the classified data from PS17 were randomly shuffled and then divided 10 times into training and validation sets with 9:1 ratio in a way that every star is used in the a validation set only once. The resulting model was then applied to the test set that was not used in building and optimizing the model in order to evaluate the performance of the classifier.

Here we provide a brief overview of the tested classifiers:

- The `Random forest` (RanForest) is a bootstrapping algorithm based on Decision tree models. Decision trees are accumulated into the final forest to determine the classification value. The Random forest builds a model with different samples and various initial variables. This process is repeated several times before the final model and prediction are made. Therefore, the final prediction is a function of the prediction of each model.
- The `Support vector machines` (SVMk) project initial variables into a high-dimensional space. Then the algorithm searches for a linear hyperplane to separate the training groups with the largest margin. Support vectors, in this case, are the data points located nearest to this hyperplane. Their removal would alter the location of the hyperplane and result in a different classification of the training data.
- The `Multi-layer perceptron` (MLP) is an artificial neural network mimicking the pattern of a biological neural network. It contains at least three layers, the input, hidden, and the output layer. The number of neurons (nodes) in each hidden layer and the number of neurons (nodes) in each of them are hyper-parameters of the model. Each individual neuron is connected to all other neurons of the surrounding layers.

We refer the interested reader to the book by Ivezić et al. (2014) for a general and more thorough overview of machine learning and the classifiers. To select which classifier would serve best for our classification problem we used several performance metrics:

- Average precision
- Precision
- Recall
- Accuracy score
- Area under curve (under receiver operating curve)

where the average precision is the area under the precision-recall curve. Precision and recall are described by the following equations:

$$\text{precision} = \frac{\text{TP}}{\text{TP} + \text{FP}}, \tag{4.5}$$

$$\text{recall} = \frac{\text{TP}}{\text{TP} + \text{FN}}, \tag{4.6}$$

where the precision stands for the ratio between true-positives (TP) and the sum of TP and false-positives (FP). The precision (sometimes referred to as purity), represents how likely the classifier will be correct in giving a positive example. The recall (or completeness/sensitivity) represents the ratio between TP and the sum of TP and false-negatives (FN) and stands for a probability that a positive example will be retrieved by the classifier. To summarise, high precision gives a lower number of false examples and high recall gives high completeness of the retrieved positive examples. The accuracy score (ACC) is given by equation:

$$\text{accuracy score} = \frac{\text{TP} + \text{TN}}{\text{P} + \text{N}}, \tag{4.7}$$

and represents the ratio between the sum of true positives and true negatives (TN) and the total population of examples (P - positive and N - negative). The area under the curve (AUC) stands for the area under receiver operating curves. The receiver operating curve (ROC) is a dependence between the true positive rate against the false positive rate (see bottom panel of Fig. 4.2.1).

In Table 4.2.1 we list various performance metrics of the tested classifiers. The highest and second highest values for a given criterion are marked by bold-face and italics, respectively. The top classifier with the best performance was MLP (red line in Fig. 4.2.1), with the following hyper-parameters[2]:

```
parameters = {Hidden layers = (100,75,50,25),
              Activation function = 'tanh',
```

[2]For a thorough documentation of individual hyper-parameters see the `scikit-learn` description of the MLP classifier at http://scikit-learn.org/stable/modules/generated/sklearn.neural_network.MLPClassifier.html

```
Learning rate = 'constant',
Solver = 'lbfgs',
Regularization term $\alpha$: 0.75}
```

Therefore, we used as a training sample stars in which the Blazhko effect was already identified by PS17 for the MLP classifier with optimized hyper-parameters to train the model that was applied to our selected sample. Stars identified by the classifier as non-Blazhko stars (8 339 RR Lyraes) remained in the sample, while stars classified as Blazhko candidates were removed. We note that the majority of the stars marked as modulated were short period variables associated with the Oo I population.

Table 4.2.1: Performance of tested classifiers. Column 1 lists the classifiers: MLP, RanForest, SVMk. Column 2 contains average precision, columns 3 and 4 provide values for the precision and recall, respectively. Columns 5 and 6 contain the accuracy score (ACC) and area under the curve (AUC), respectively. Bold and italic fonts mark values with the best and second-best performance for each tested criterion.

Classifier	⟨Prec.⟩	Prec.	Recall	ACC	AUC
RanForest	*0.828*	*0.842*	*0.944*	*0.862*	*0.911*
MLP	**0.845**	**0.863**	0.934	**0.873**	**0.921**
SVMk	0.816	0.825	**0.961**	0.856	0.911

Distance determination and separation of the Oosterhoff groups

To study the spatial distribution of the Oosterhoff groups in the Galactic bulge we first calculated their distances using period-metallicity-luminosity (P-M-L) relations, and then separated the Oosterhoff populations based on their position in the period-amplitude (*P-A*) diagram.

Metallicities and distances of RRab stars

To determine the distance of RRab stars we took advantage of our broad range in colour for individual RR Lyrae stars in estimating their extinction, and then used K_s-band mean magnitudes from the VVV survey. In the near-infrared, the period-luminosity-metallicity relations for RR Lyraes follow rather tight sequences, slightly less dependent on metallicity, and relations between absolute magnitudes and pulsation periods are known in various passbands (see Catelan et al. 2004; Alonso-García et al. 2015; Marconi et al. 2015).

For the optical data we first decomposed light curves using the Fourier series for the I-band photometric data:

$$m(t) = A_0^I + \sum_{k=1}^{n} A_k^I \cdot \cos\left(2\pi k\vartheta + \varphi_k^I\right), \tag{4.8}$$

where φ_k^I stands for phases, and A_k^I represents amplitudes. The phase function ϑ is defined as follows: $(HJD - M_0)/P$, where the time of observation is denoted by HJD (Heliocentric

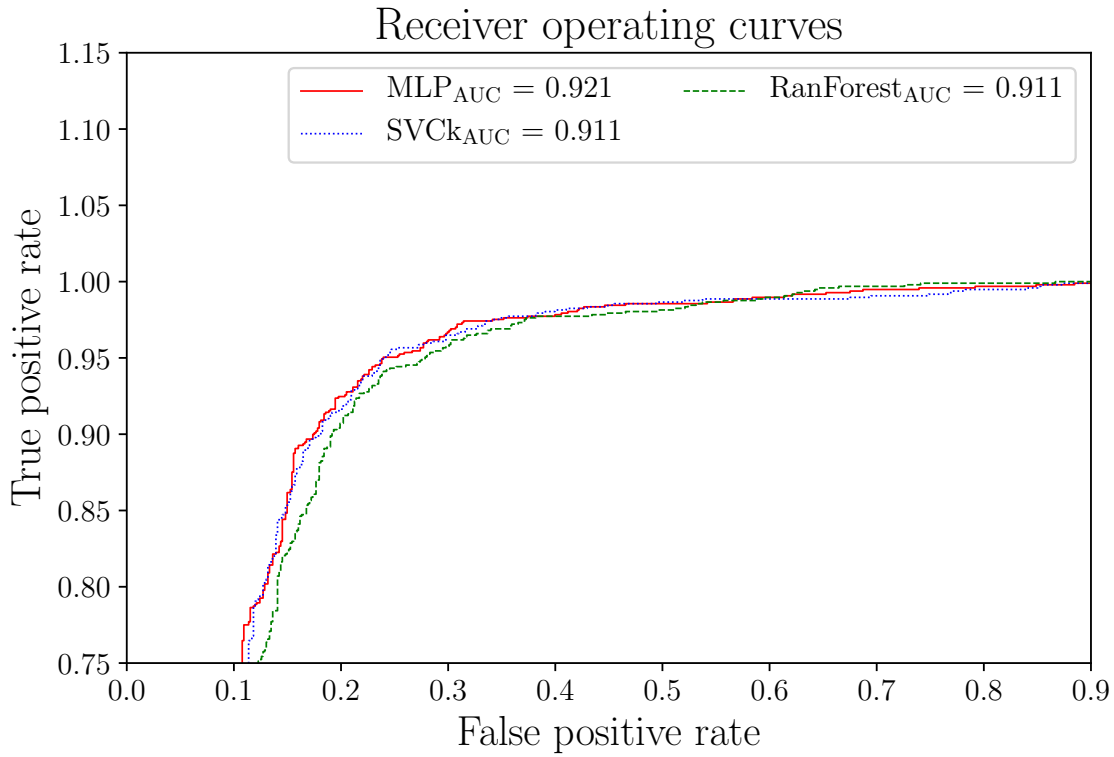

Figure 4.2.1: Comparison of tested classifiers against the test sample. To increase clarity, we choose to show only that region in which the reader can easily distinguish differences between the tested classifiers. This figure shows receiver operating curves with lines (green, red and blue) representing the RanForest (dashed), MLP(solid) and SVMk (dotted). The MLP performs better in comparison with other classifiers, which is also reflected in the AUC listed in the legend for the individual classifiers.

Julian Date), M_0 marks the time of maximum brightness and the pulsation period is represented by P. The n represents the degree of the fit and was iteratively tailored for each light curve. First, we started the calculation with the third degree and increased the degree every time when the condition $A_k/\sigma_k > 4$ was met. Once this condition was no longer valid, we removed the outliers from the residuals, detrended the data using a low-degree polynomial, and started the iteration again. Stars for which we were unable to find a light curve solution including φ_3^I was removed from the sample (198 stars). We note that the VVV survey provides only aperture photometry and not preferable point-spread function photometry. Thus, for each star, we selected an appropriate aperture based on the minimum value of a cost function for the fitted model on each light curve.

The obtained Fourier coefficients served to calculate the metallicity for the remaining

8 141 stars using equation 3 from Smolec (2005) (on the Jurcsik (1995), JK scale)[3]:

$$[\mathrm{Fe/H}]_{\mathrm{JK}} = -6.125 - 4.795P + 1.181\varphi_{31} + 7.876A_2. \tag{4.9}$$

To properly account for errors in the metallicity we re-analysed relation 3 from Smolec (2005) and calculated the covariance matrix for the three-parameter solution:

$$\mathrm{Cov} = \begin{bmatrix} 0.6914 & -0.0632 & -0.0907 & -1.1951 \\ -0.0632 & 0.0813 & 0.0024 & 0.0428 \\ -0.0907 & 0.0024 & 0.0127 & 0.1430 \\ -1.1951 & 0.0428 & 0.1430 & 3.1552 \end{bmatrix} \tag{4.10}$$

This yields errors of on average 0.06 dex. With a dispersion of $\sigma = 0.14$ dex from the Smolec (2005) relation, the resulting average error in metallicity was 0.20 dex. The calculated metallicities were rectified using a customized *pyrime*[4] code from Hajdu et al. (2018) updated for our own Oosterhoff classification (for our definition see Subsection 4.3.2). The final metallicities were then converted to $\log Z = [\mathrm{Fe/H}]_{\mathrm{JK}} - 1.772$. We used the conversion factor -1.772 based on the solar metallicity determined by Grevesse & Sauval (1998) and a helium mass fraction of $Y = 0.2485$. The $\log Z$ and [Fe/H] were subsequently used to determine absolute magnitudes in the I and K_s-bands using relations from Catelan et al. (2004) and Muraveva et al. (2018), respectively, transformed into the VVV photometric system[5]:

$$M_I = 0.471 - 1.132 \cdot \log P + 0.205 \cdot \log Z \tag{4.11}$$

$$M_{K_s} = -0.8481 - 2.5836 \cdot \log P + 0.17 \cdot [\mathrm{Fe/H}]_{\mathrm{JK}}. \tag{4.12}$$

We note that we tested several theoretical relations for the absolute magnitude in K_s band. We found, similarly to Marconi et al. (2015, their fig. 15) or Muraveva et al. (2015, their table 3), non-negligible differences between different versions of the same relation, suggesting the presence of systematic uncertainties at the ~ 0.1 mag level. In the end, we decided to use the relation from Muraveva et al. (2018), which is based on the latest (i.e. Data Release 2) parallaxes from the Gaia space telescope and is model-independent.

Absolute and apparent magnitudes then served to estimate the reddening vector. First, we omitted stars with $E(I-K_s) < 0.5$ and $E(I-K_s) > 2.5$ to limit the possible incompleteness at the bright and faint ends of our sample. We then applied an average boxcar filter on the $I - M_I$ vs. $E(I-K_s)$ distribution with varying box width (from 300 to 800 points) and a step size (from 10 to 299 points) and linearly fitted each binned distribution. We took into account errors in $I - M_I$. As weights for the fit, we used the standard deviation of the $I - M_I$ distribution in the individual bins. The final coefficients of the linear fit were selected based on the median value of the distribution for the first coefficient. The results of this procedure

[3] In the supplementary material for this paper we also provide transformed metallicities on the Carretta scale (Carretta et al. 2009) using eq. 6 from Hajdu et al. (2018).

[4] https://github.com/gerhajdu/pyrime

[5] For calculation the M_{K_s} magnitudes we transformed our metallicities to the Zinn & West (1984) metallicity scale using the relation from Papadakis et al. (2000).

are shown in Fig. 4.3.1. For a derivation of the extinction in the K_s-band, we then followed:

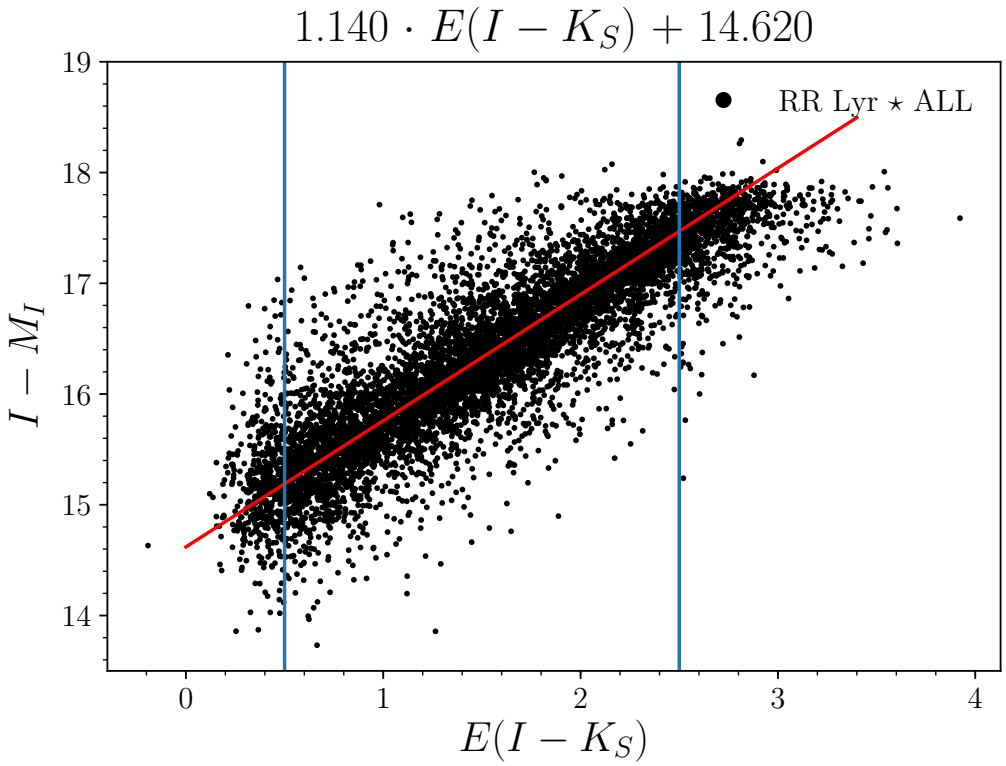

Figure 4.3.1: The linear dependence between reddening $E(I-K_s)$ and difference of apparent and absolute magnitude. The black dots represent stars from our sample together with a red line representing the reddening vector and blue lines outlining the applied boundaries.

$$E(I-K_s) = (I-K_s) - (I-K_s)_0 \tag{4.13}$$

$$A_{K_s} = 0.14 \cdot E(I-K_s)\,. \tag{4.14}$$

Lastly, the distances d (in pc) to the individual RRab stars were detemined from the distance modulus:

$$d = 10^{1+0.2\cdot(K_s - M_{K_s} - A_{K_s})}. \tag{4.15}$$

The errors in the distances were estimated as well. We assumed 0.02 mag as the average errors for the I and K_s-band light curves (Dékány et al. 2013; Udalski et al. 2015). With the individual error estimates for the metallicities, the errors in distance vary around a mean of 0.19 kpc.

Separation of Oosterhoff groups

Traditionally, the separation of the two Oosterhoff groups can be achieved in the *P-A* plane using linear/polynomial relations (see Clement & Shelton (1999) and Cacciari et al. (2005), respectively). These relations are based on the fundamental-mode RR Lyrae stars in GCs and the overall position of the Oosterhoff type I locus. As shown by Kunder & Chaboyer (2009), the locus of Oosterhoff type I variables in the Galactic bulge is shifted to lower pulsation periods approximately by 0.02 days, in comparison with the archetype of Oo I clusters, M3. This effect is due to the difference in metallicity of the aforementioned systems (-1.5 dex for M 3 and -1.0 dex for the Galactic bulge, respectively, Cacciari et al. 2005; Pietrukowicz et al. 2015). Due to this effect, we tailored our own polynomial relation based on the selected sample in the V, I, and K_s-bands.

The OGLE-IV survey provides V-band data for our sample stars, but the data in this passband are rather sparse. Specifically, more than two-thirds of the sample stars have less than 86 observations in the V-band. Therefore, we defined a relation for V-band amplitudes of RR Lyraes using the I-band photometry. We selected stars from our sample that have at least 86 observations in the V-band (in total 2 671 variables). Using a Fourier decomposition (see Eq. 4.8) of fourth degree we calculated amplitudes for the selected RR Lyraes in the passband V. The V-band amplitudes were compared with their I-band counterparts and a transformation equation was obtained in the following form:

$$\mathrm{Amp}^V = 1.6130 \pm 0.0060 \cdot \mathrm{Amp}^I, \tag{4.16}$$

where Amp^V and Amp^I stand for the amplitudes in the aformentioned passbands. We set the intercept to zero to preserve the physical representation of the calculated V-band amplitudes. We note that this relation between amplitudes can depend on metallicity since amplitudes appeared in some of the empirical relations for metallicity (e.g. see eq. 6 in Sandage 2004). We tested this in several metallicity bins and found only a negligible discrepancy between individual bins.

To define a polynomial relation that would adequately describe the locus of Oo I stars we proceeded in the following way. We binned our stellar sample based on their amplitudes, computed kernel density estimates (KDE) as a function of the period for each amplitude bin and computed the maximum in each individual bin. These maxima were then fitted with third and second-degree polynomial relations. We proceeded in the same way in all available colours to define the Oo I progression. The number of amplitude bins were manually optimized for each passband. The results of this procedure are shown in Fig. 4.3.2 and the individual coefficients are listed in Table 4.3.1 for all three passbands.

In the *P-A* diagrams, we can distinguish the Oo I locus, but an Oo II locus (expected toward the right edge of the distributions) is not visually apparent. In the bottom right panel of Fig. 4.3.2 we show the distribution of the difference between the observed and calculated pulsation periods (ΔlogP, based on the period-amplitude relations from Tab. 4.3.1). We see a sign of a bimodal distribution with a peak at zero (the Oo I locus) and an enhanced tail on the positive side (consistent with Oo II stars). Thus, we decided to apply the conditions prescribed by Miceli et al. (2008) to separate between the two Oosterhoff groups while using

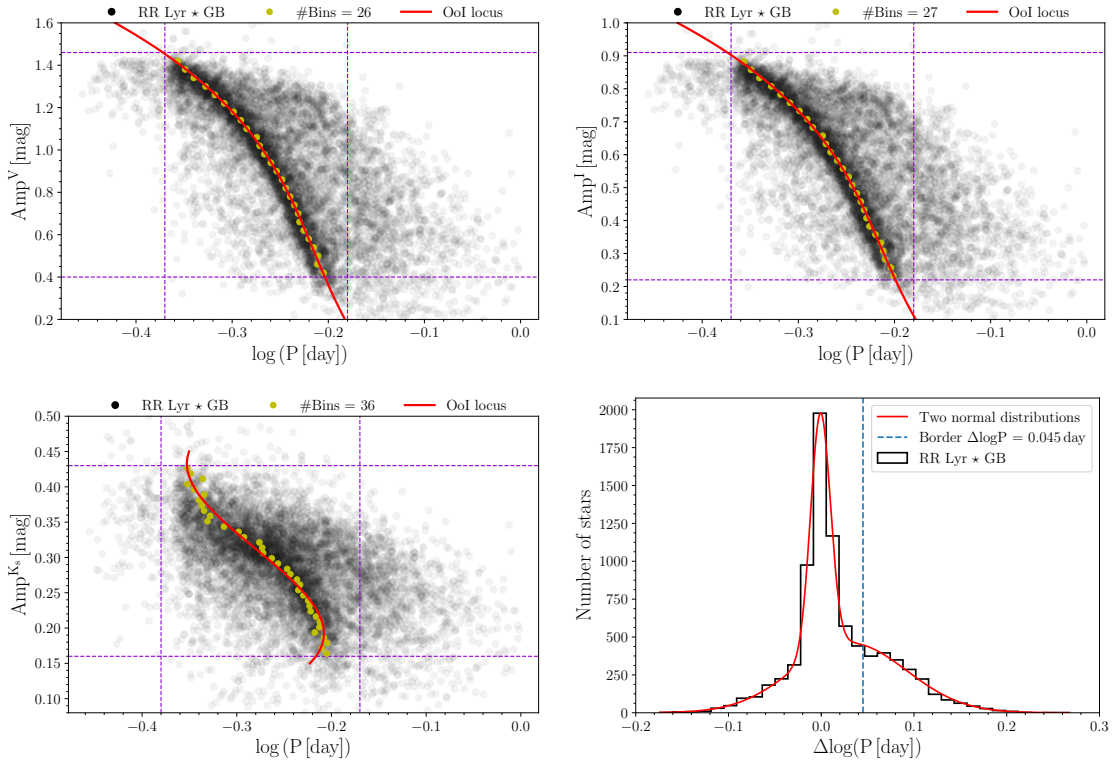

Figure 4.3.2: The *P-A* diagrams for selected filters (top left panel: V, top right panel: I, bottom left panel: K_s) of studied RR Lyrae stars in the Galactic bulge (GB), and the distribution of period differences based on the defined relation for I-band amplitudes (bottom right panel). In the *P-A* diagrams, the yellow circles stand for the binned Oo I locus. The total number of bins is listed in the legend of each plot. The violet dashed lines display a cut in order to select solely the Oo I progression in the *P-A* diagrams for each passband individually. The black dots represent fundamental-mode RR Lyraes, and the red line shows our third-degree polynomial equation for the Oo I locus. Lower right panel: The distribution of ΔlogP values, obtained using the third degree polynomial relation for the Oo I locus in the I-band amplitudes, is shown as a black line. The distribution was fitted with a sum of two Gaussian distributions (red line), the blue dashed line denotes the borderline between both Oosterhoff groups.

a fixed threshold with respect to the third-degree polynomial fitted to the I-band amplitudes:

$$\Delta P = P_{\rm ab} - P_{\rm OoI} \begin{cases} \mathrm{RRab_{OoI}} & \Delta P \leq 0.045\,\mathrm{days} \\ \mathrm{RRab_{OoII}} & \Delta P > 0.045\,\mathrm{days} \end{cases}. \tag{4.17}$$

We note that the value of 0.045 days is based on RR Lyrae stars in GCs. We tested different values for the boundaries between both Oosterhoff populations ranging in $\Delta\log P$ from 0.035 to 0.055. Values between 0.040 and 0.050 yield analogous results when compared with the separation of the two-hook structure in the top panel of Fig. 4.3.3. The uncertainty in this value is mostly due to the metallicity dependence of the Oo I locus.

The resulting separation based on I-band amplitudes yields 6 086 variables associated

Table 4.3.1: Tables of coefficients for third and second-degree polynomials describing the Oo I locus. Each table contains a list of filters (column 1). The top table contains coefficients for the third-degree polynomial (columns 2 - 5) and column 6 contains the σ of the fit. The bottom table shows the coefficients for the second-degree polynomial (columns 2 - 4) and the σ of the fit (column 5).

Filter	$\log P = a_1 \cdot \mathrm{Amp}_i^3 + a_2 \cdot \mathrm{Amp}_i^2 + a_3 \cdot \mathrm{Amp}_i + a_4$				
	a_1	a_2	a_3	a_4	σ
V	-0.084	0.129	-0.157	-0.156	0.0016
I	-0.324	0.289	-0.229	-0.160	0.0015
K_s	21.356	-20.004	5.340	-0.647	0.0066

Filter	$\log P = a_1 \cdot \mathrm{Amp}_i^2 + a_2 \cdot \mathrm{Amp}_i + a_3$			
	a_1	a_2	a_3	σ
V	-0.102	0.042	-0.209	0.0025
I	-0.253	0.051	-0.204	0.0025
K_s	-1.104	-0.003	-0.168	0.0106

with the Oo I group, and 2 055 stars with the Oo II group. A similar separation using the V passband yields almost the same classifications as the I-band data (the disagreement is around 1 %). This negligible difference was most likely caused by the transformation from I-band amplitudes into the V-band. On the other hand, the separation based on the infrared amplitudes yields different Oosterhoff classifications for 7.7 % of the sample. This discrepancy was probably caused by the large scatter in the *P-A* diagram and the lack of a pronounced Oo I locus in the K_s-band. In the following, we will work with the Oosterhoff groups separated based on the I-band *P-A* relation.

Our sample shows two-hook structures in the φ_{21} vs. R_{31} and φ_{31} vs. R_{31} planes (see Fig. 4.3.3). These structures were identified as two Oosterhoff populations in the Galactic bulge by Prudil et al. (2018a). On the other hand, in the period-amplitude diagram we do not observe the locus of the Oosterhoff type II variables, but only a pronounced Oosterhoff type I locus (top-left panel of Fig. 4.3.2).

In total, approximately 25 % of the stars in our sample belong to the Oo II group, which is almost identical to the 1:4 ratio found by Drake et al. (2013, 24 %, in a sample of 12 227 fundamental mode RR Lyraes) and Sesar et al. (2013, 25 %, in a sample of 4 067 RRab type stars) for the Galactic halo. However, the *P-A* diagrams for the Galactic bulge and Galactic halo differ. In the Galactic halo, the Oo I locus fits the polynomial relation by Cacciari et al. (2005) due to its lower metallicity. In addition, the *P-A* distribution of Galactic halo RR Lyraes shows a more pronounced Oo II locus than in the bulge.

The separation of the Oo groups by Manifold learning

The separation of the Oosterhoff groups as described in Sec. 4.3.2 is based on external information (i.e., locus positions in GCs), which might be debatable due to the fact that the Oo II locus is not apparent on the *P-A* plane for the bulge.. One can try and infer the Oo separation from the two-hook structure in $\varphi_{21}/\varphi_{31}$ vs. R_{31} using clustering algorithms, but due to their

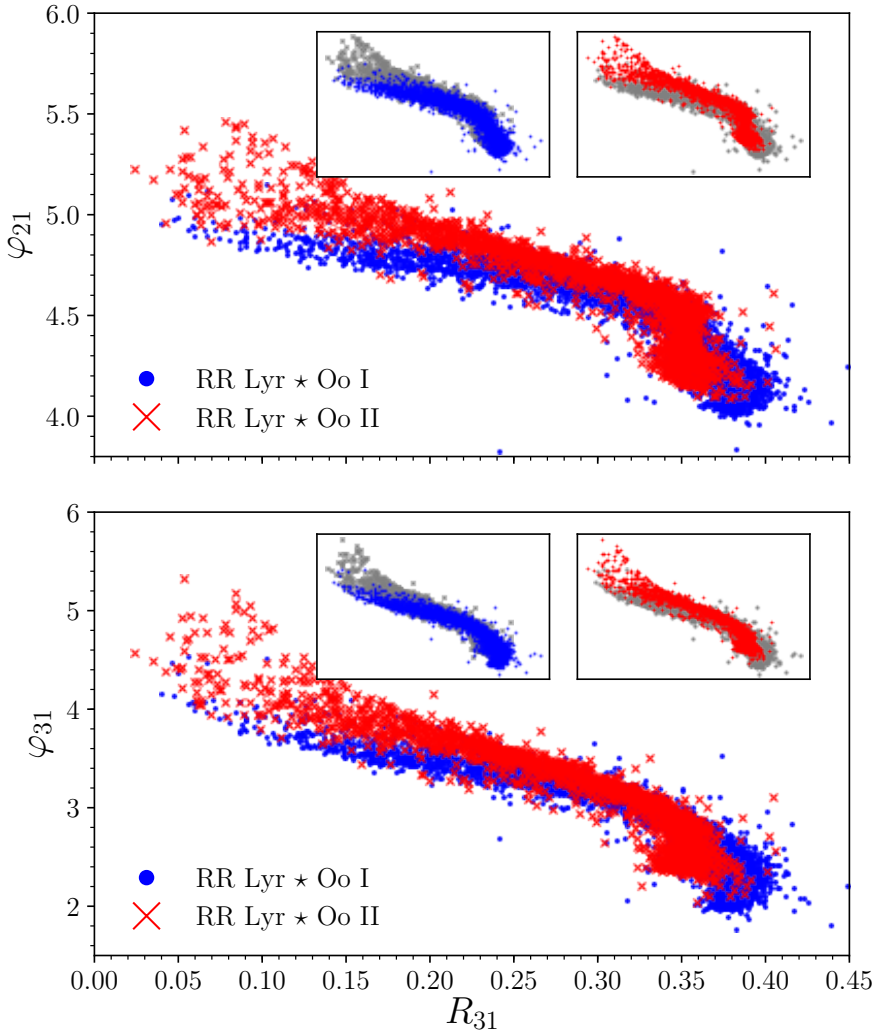

Figure 4.3.3: Distributions of our non-Blazhko bulge RRab sample on the φ_{21} *vs* R_{31} (top) and the φ_{31} *vs* R_{31} (bottom) planes. In both panels, blue dots represent Oo I stars, while red crosses stand for Oo II variables. The insets in both panels display the separated Oosterhoff groups highlighted with blue/red colours and the rest of the sample marked by gray points to enhance the visibility of the two-hook structure.

tight entanglement, this could be challenging.

Thus we decided to employ `Manifold-learning` from the `scikit-learn` library. The `Manifold-learning` is a type of unsupervised machine learning algorithms that perform non-linear dimensionality reduction and thus project data into a low-dimensional Euclidian space. We looked for the separation of the two Oosterhoff groups based on the same parameters that were used for the removal of modulated stars (i.e., pulsation periods, am-

plitudes, R_{21}, R_{31}, φ_{21}, φ_{31} see Sec. 4.2.1) and $\Delta\log P$ calculated from the third-degree polynomial relation for I-band amplitudes. We used the `scikit-learn` implementation of the `Isometric Mapping (Isomap)` algorithm (Tenenbaum et al. 2000), which searches for a lower-dimensional setup while preserving geodesic distances between data points.

The results of the `Isomap` algorithm can be seen in the left panel of Fig. 4.3.4, where we show the reduced dimensions of our RRab sample. We clearly see two rather well-separated groups in the left-hand panel of Fig. 4.3.4. To separate Oosterhoff groups, we used the implementation of the `Birch` clustering algorithm from the aforementioned library. We used the entire stellar sample associated with the two Oosterhoff groups based on the *P-A* diagram, and trained the clustering algorithm for the best performance, which separated both clusters (middle panel of Fig. 4.3.4) and divided them consistently with the aformentioned Oosterhoff groups (see Sec. 4.3.2). When compared to the original classification based on the period-amplitude diagram we found agreement in 95 % of the cases. The rest of the stars lie on the boundary between the Oo I and Oo II groups as divided on the basis of the period-amplitude diagram.

In the left-hand panel of Fig. 4.3.4 we see a small clump between the identified Oo I and II groups. Closer inspection of the period-amplitude diagram shows that stars associated with this structure fall on the low-amplitude, long-period end of the Oo I group. In this subsection we showed that it is possible to identify the Oosterhoff dichotomy and separate the two Oosterhoff groups purely on the basis of the properties of the bulge RR Lyraes and the location of the Oo I locus. This approach can be used in any system that does not show both Oo loci in the *P-A* plane.

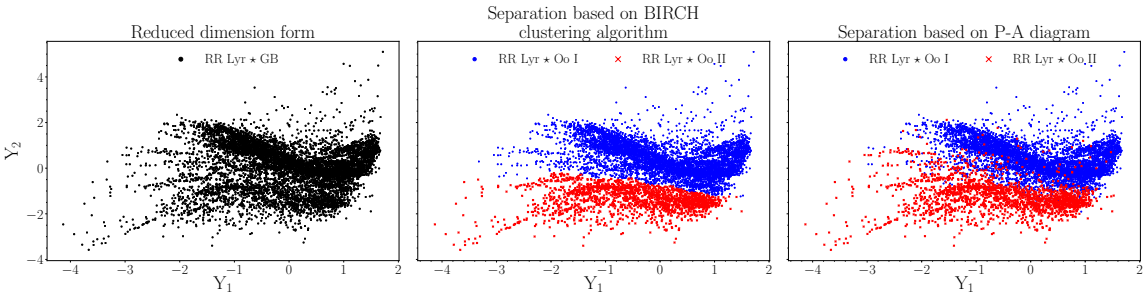

Figure 4.3.4: Reduced dimensions (Y_1 and Y_2) based on the `Manifold Isometric Mapping` algorithm. The left-hand panel displays sample stars (black points) after dimension reduction with two structures representing the Oosterhoff populations in our data. The middle panel shows separated groups based on the `Birch` clustering algorithm with blue dots representing Oo I variables and red crosses standing for Oo II pulsators. The same colour-coding applies also for the right-hand panel where both Oosterhoff groups are depicted based on the separation in the *P-A* space.

Comparison with bulge GCs and physical parameters

The OGLE-IV photometry contains information about 300 RR Lyraes that are probable members of 15 GCs (see the bottom-left panel of fig. 2 in Soszyński et al. 2014, for their spatial

distribution). We decided to compare our two Oosterhoff populations with two Galactic bulge GCs with the highest number of fundamental mode RR Lyraes in OGLE-IV data[6], NGC 6401 and NGC 6441. We excluded the globular cluster M 54 from this comparison due to its location in the Sagittarius dwarf spheroidal galaxy.

The globular cluster NGC 6401 is considered as a metal-rich globular cluster ($[Fe/H]_{JK} = -0.98$ dex, Tsapras et al. 2017). We performed Fourier analysis using the I-band light curves and estimated the metallicity of the associated RRab variables using Eq. 4.9, and removed potential modulated stars using the trained classifier (see Sec. 4.2.1). This yields a median metallicity of $[Fe/H]_{JK} = -1.02 \pm 0.05$ dex, which is in good agreement with the average metallicity of RR Lyraes in the Galactic bulge $[Fe/H]_{JK} = -1.02 \pm 0.25$ dex, (Pietrukowicz et al. 2015). Based on the positions of its RRab variables in the *P-A* diagram, the [Fe/H] vs. log$P$ dependence, and the φ_{21} vs. R_{31} distribution (orange circles in Fig. 4.4.1), the RR Lyraes in NGC 6401 clearly belong to the Oo I group with a metallicity of the old bulge population.

The globular cluster NGC 6441 is a larger system in comparison with NGC 6401. It is a known oddball in the Oosterhoff population scheme. Together with NGC 6388, these two clusters create their own group (sometimes referred to as Oosterhoff type III, Pritzl et al. 2000). The fundamental-mode pulsators in NGC 6441 cluster occupy the long-period end of the *P-A* diagram (green squares in Fig. 4.4.1), similarly to Oo II stars, yet they have a high mean metallicity of $[Fe/H]_{JK} = -0.43$ dex (Clementini et al. 2005). We performed a light curve decomposition on RRab variables associated with NGC 6441, and removed stars marked by the trained classifier as possible modulated variables. We detrended the data for individual pulsators (nearly all stars show trends in the mean brightness) and calculated their metallicities using Eq. 4.9. Their median metallicity is $[Fe/H]_{JK} = -1.19 \pm 0.23$ dex, which does not agree with the spectroscopic measurements by Clementini et al. (2005). We comment on this discrepancy later in this Section. The RRab stars associated with this cluster occupy similar regions in the *P-A* diagram as some of the stars identified as the Oo II variables. This hints at the possibility that some Oo III stars may be hidden in our bulge RRab sample. Furthermore, Kunder et al. (2018) found eight RRab stars in up to three times the distance from the tidal radius of the NGC 6441, which share similar radial velocities as RR Lyrae members of NGC 6441. This points towards the possible occurrence of stripped Oo III variables in the Galactic bulge among the Oo II variables.

In addition, the low-amplitude double-mode variables found by Smolec et al. (2016) with a dominant fundamental mode and long periods fall roughly in the region of Oo III variables. Most of these double-mode pulsators can be described using linear pulsation models with very high metallicity (around -0.5 dex). Thus, we performed a thorough analysis of the frequency spectra of fundamental-mode variables in NGC 6441. We found that the object OGLE-BLG-RRLYR-03918 exhibits an additional peak in the frequency spectrum at $f_x = 1.99974$ c/d with S/N=4.16. The period ratio of this additional peak and the dominant mode is 0.720, therefore it lies in a region of the Petersen diagram (see fig. 1 in Smolec et al. 2016) where the aforementioned double-mode pulsators occur. We did not detect any signal at the combination frequency of the dominant mode and the additional signal (f_x). The f_x is

[6] http://www.astrouw.edu.pl/ogle/ogle4/OCVS/blg/rrlyr/gc.dat

[6] Transformed from the Zinn & West (1984) scale to $[Fe/H]_{JK}$ using the relation from Papadakis et al. (2000).

Table 4.4.1: Table of physical parameters determined from the photometric data. The columns from left to right list the Oo group, and the columns 2 and 3 list the medians of the pulsation periods and the mean metallicities for the Oosterhoff groups. Columns 4 and 5 list the median effective temperatures and the rise time (RT).

	P [day]	$[Fe/H]_{JK}$ dex	T_{eff} [K]	RT
Oo I	0.536	-1.04	6522	0.153
Oo II	0.674	-1.15	6100	0.178

close to the integer value in the frequency spectra caused by Earth's rotation. Therefore, this star should be considered as merely a candidate for possible double-mode pulsators found by Smolec et al. (2016).

In the middle panel of Fig. 4.4.1, showing the [Fe/H] vs. log$P$ dependence, we see that RRab variables from NGC 6441 mostly occupy the same region as the Oo II stars in our sample. But for the RR Lyraes in a globular cluster, we would expect a very narrow distribution in metallicities. What we see here suggests that the RR Lyrae metallicity relation (Eq. 4.9) does not apply to Oo III RR Lyraes. We see a large dispersion in metallicity for RR Lyraes in NGC 6441 when compared with RRab variables in NGC 6401 (yellow circles). The bottom panel of Fig. 4.4.1 further corroborates our conclusions that the fundamental-mode pulsators from NGC 6441 coincide with the tail of the Oo II stars from our sample, and therefore some Oo III variables may be hidden in our Oo II sample.

Physical parameters

Based on the photometric data we can also estimate some of the physical parameters of the selected variables. In this analysis we assume that the calibrations are equally valid for the Oo I and Oo II groups. To calculate effective temperatures we used equation 6 from Jurcsik et al. (2018). From the Fourier analysis performed in § 4.3.1 we also estimated the rise time (time between the minimum and maximum light, from hereon RT) for individual variables. The calculated median physical parameters for both Oosterhoff groups can be found in Table 4.4.1.

We see a larger difference in pulsation periods than in GCs (see tab. 3.2 in Smith 1995) which broadcasts the difference in metallicity. The difference in the RT, on the other hand, shows that light curves of Oo II stars are less skewed than those of Oo I stars. This effect is also observed in Milky Way GCs (see fig. 10 in Sandage et al. 1981). When we look at the distribution of the RT (see Fig. 4.4.2) we see that stars with the shortest RT are solely associated with the Oo I group. These stars have the highest amplitudes and shortest pulsation periods. The vast majority of them belong to the HASP (high amplitude short period) group identified by Fiorentino et al. (2015).

The top and bottom panels of Fig. 4.4.3 show colour-magnitude diagrams (CMDs) of the stars in our sample. We compared the Oosterhoff groups with linear pulsating models (top panel) and stellar evolutionary models (bottom panel). We computed the boundaries of the instability strip (IS) using linear pulsation models (Smolec & Moskalik 2008), calculated on a grid of the following physical parameters:

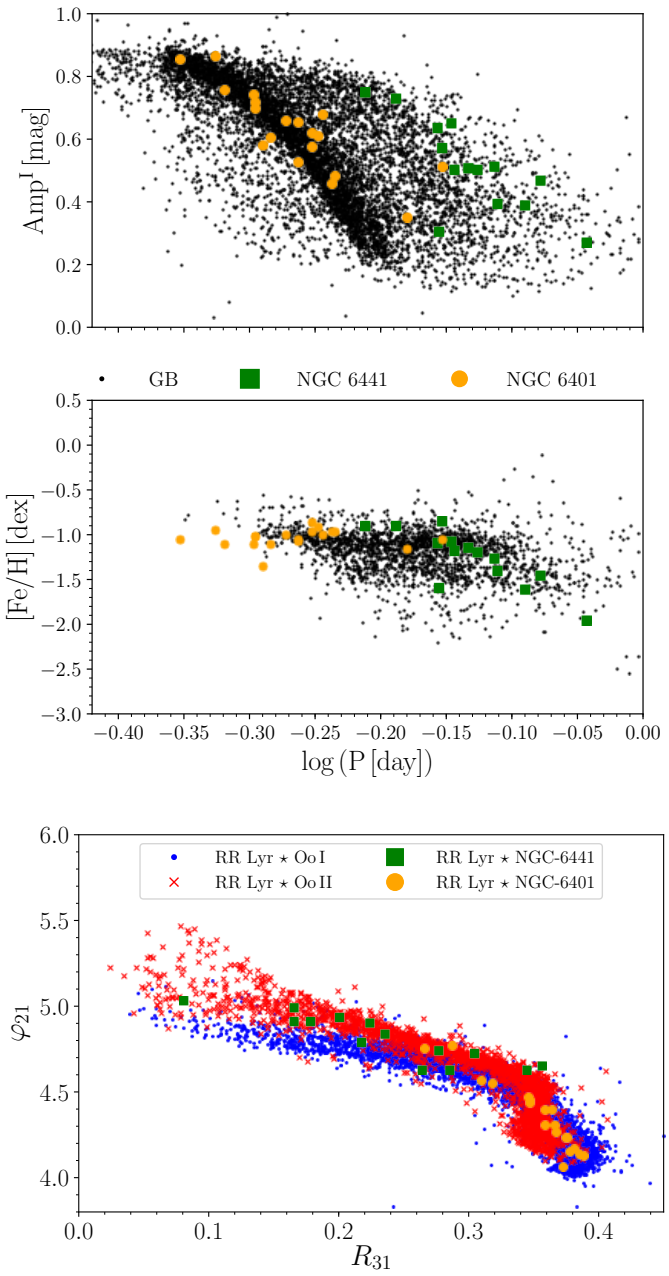

Figure 4.4.1: The *P-A* diagram (top panel), metallicity vs. period distribution (middle panel), and φ_{21} vs. R_{31} dependency (bottom panel). In all three figures, the orange circles and green squares represent RRab stars in the GCs NGC 6401 and NGC 6441, respectively. In the top panel the black dots represent all RRab variables from our selected sample while in the middle plot they stand for Oo II stars only. The bottom panel shows Oo I and Oo II variables (blue dots and red crosses, respectively).

- Masses - $0.5 < M_{\odot} < 0.8$
- Luminosities - $30 < L_{\odot} < 80$
- Temperatures - $5500\,K < T_{\rm eff} < 8000\,K$

We used OPAL opacities (Iglesias & Rogers 1996) and the solar heavy element mixture according to Asplund et al. (2009). With the linear pulsation models we also calculated lines of constant period (yellow and green lines) for the median values of the pulsation periods in both Oosterhoff groups (see Table 4.4.1). We computed the lines of constant period for the whole grid of stellar pulsation models for masses ranging from 0.5 to 0.8 $M_{\odot}$ and searched for a case where we find a similar amount of stars above and below the lines of constant period in the CMD. The lines of constant period best describe our studied Oo I and Oo II populations for masses above 0.6 $M_{\odot}$ (0.63 $M_{\odot}$ for Oo I and 0.67 $M_{\odot}$ for Oo II). We note that for this estimate we considered only stars with distances in the range from 6.4 to 10.3 kpc (see Sec. 4.5.1), thus only the stars located in the approximate volume of the Galactic bulge. Therefore, we assumed these masses also for further comparison with stellar evolutionary models.

We used the pre-computed horizontal branch tracks from the BaSTI database (Pietrinferni et al. 2004). We selected tracks for each Oosterhoff group separately. For the Oosterhoff type I stars we used horizontal branch tracks with the following parameters: $Z = 0.002$, $M = 0.63\,M_{\odot}$ and α-enhanced abundances ($[\alpha/\mathrm{Fe}] = 0.4$ dex). For the Oosterhoff type II stars we used a different set of parameters $Z = 0.001$, $M = 0.67\,M_{\odot}$ and α-enhanced abundances ($[\alpha/\mathrm{Fe}] = 0.4$ dex) due to their different median metallicity and mass from the models of stellar pulsation. We note that selecting α-enhanced or scaled solar models does not change the results significantly. Thus, Oo II variables seem to have either similar or higher masses than their Oo I counterparts. A similar difference in masses between both Oosterhoff populations has been suggested in the past (Catelan 1992; Cacciari & Bruzzi 1993; Sandage 2006). We note that for pulsation and evolutionary models the K_0 and $(V-I)_0$ magnitudes were computed using static atmosphere models (Kurucz 2005).

Our results are in agreement with a study performed by McNamara & Barnes (2014) on GCs, where they demonstrated that Oo II variables have larger radii and are brighter in comparison with the Oo I stars. They also found 4 pulsators associated with the Oo III group. Overall we see that the Oo II group is on average brighter (see the top and bottom panel of Fig. 4.4.3) by approximately 0.23 mag in the dereddened K_s band. Moreover, the mean magnitudes of stars from this group are redder (by $(V-I)_0 \approx 0.1$ mag) than those of their Oo I counterparts. Furthermore, the masses of Oo I and II seem to be different as well. At this point, it is necessary to emphasize that the estimated physical parameters are strongly correlated with the pulsation periods and metallicities. Therefore, the difference between the Oo I and II populations in both parameters will propagate into the others as well.

Spatial distribution of the Oosterhoff groups

In this section, we analyse the spatial distribution of both Oosterhoff groups in the Galactic bulge, based on their coordinates and calculated distances. We search for possible overdensi-

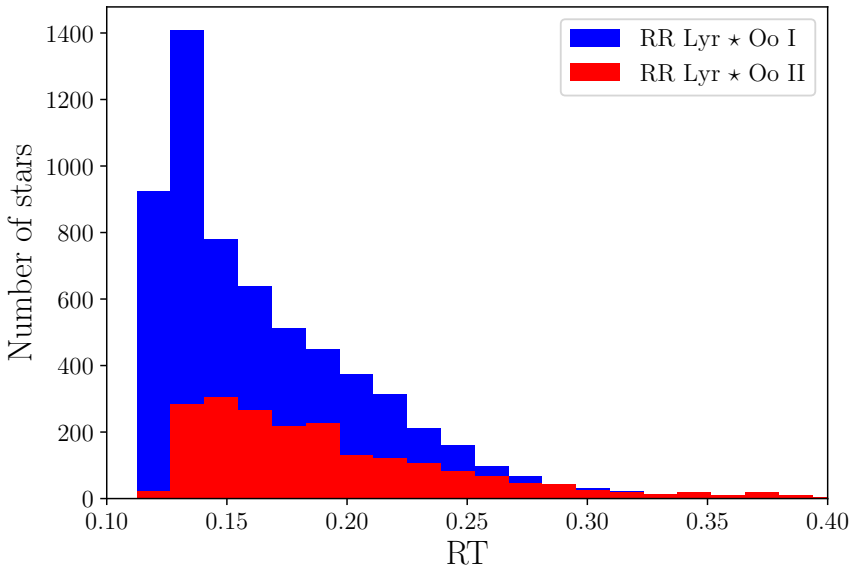

Figure 4.4.2: The distribution of rise times (RT) for Oosterhoff groups from our sample. The Oo I and Oo II groups are represented by blue and red columns, respectively.

ties within the groups, differences in their positions in the bulge, and analyse their positions with respect to the Galactic bar.

Oosterhoff variables in Galactic coordinates

For this part we used the known Galactic coordinates and distances of our sample stars. First, the distances to individual stars were projected on the Galactic plane by multiplying them with a factor of $\cos b$. Then we defined three regions: *foreground*, *center*, and *background*. As the *foreground* of the Galactic bulge we selected stars with $d \leq 6.4$ kpc and for *background* variables we applied a $d \geq 10.3$ kpc condition. These cuts were selected based on the spatial density of our sample, to median distance to the Galactic bulge of 8.3 kpc, assuming a bulge radius of approximately 2 kpc (more than 80 % of our sample confined within selected radius, see Fig. 4.5.2, 4.5.4). Subsequently, we divided the central region into 1287 cuboids with a edge length of 1.5 deg edge and a length of 0.3 kpc, and calculated the ratio of Oo I and Oo II variables in each frustum. The ranges into which we divided the central region were as follows: $l = (-8; 8.5)$ deg, $b = (-7.5; 6.0)$ deg and $d = (6.4; 10.3)$ kpc.

Then, we divided our cuboid sample into stripes based on the Galactic latitude creating nine slices, each composed of 143 cuboids. The fraction of Oo I group stars in each slice is shown in Fig. 4.5.1. This figure shows in nine panels colour maps of the fraction of Oo I stars in different slices of the central region of the Galactic bulge. Overall, we do not see any large-scale structures traced by an excess of Oo I variables as compared to the characteristic

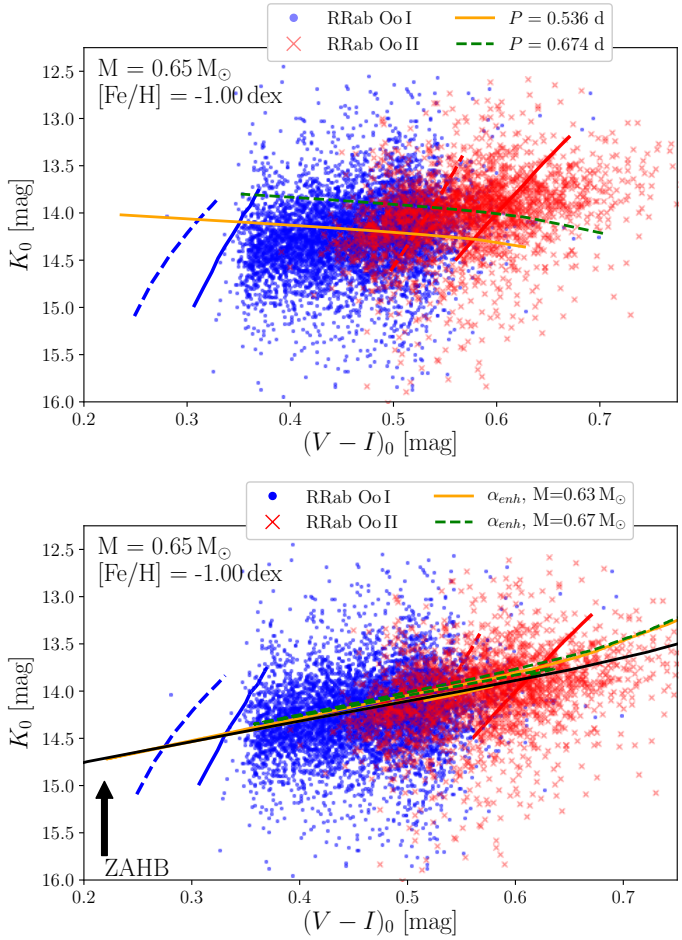

Figure 4.4.3: The colour-magnitude diagrams for the Oosterhoff groups from our sample stars compared with stellar pulsation models (top panel) and stellar evolution models (bottom panel). In the top and bottom panels red and blue lines stand for the red and blue edges of the instability strip for fundamental mode pulsators (solid lines) and the first overtones (dashed lines). In the top and bottom plots, blue dots and red crosses represent Oo I and Oo II variables, respectively. The green and orange lines in the top panel represent lines of constant period for the analysed Oosterhoff groups, calculated using stellar pulsation models. The bottom panel depicts sample stars with horizontal branch models, where orange and green lines represent evolutionary tracks form masses 0.63 M$_\odot$ and 0.67 M$_\odot$ for Oo I and Oo II, respectively.

ratio between Oo I and Oo II for the bulge as a whole (25 %; see Sec. 4.3.2). We see some small structures but when closely inspected they do not show any possible overdensity in one or the other Oosterhoff type.

In Table 4.5.1, we listed median values in d for both Oosterhoff groups in individual regions, together with their fraction in each segment. From this table we see that in almost all studied regions the median values of d are higher for Oo II stars. It is necessary to add that within the absolute-median-deviation for Oo I and II (±0.6 kpc), differences in distances are not significant. The difference in the representation of both Oosterhoff groups is the most

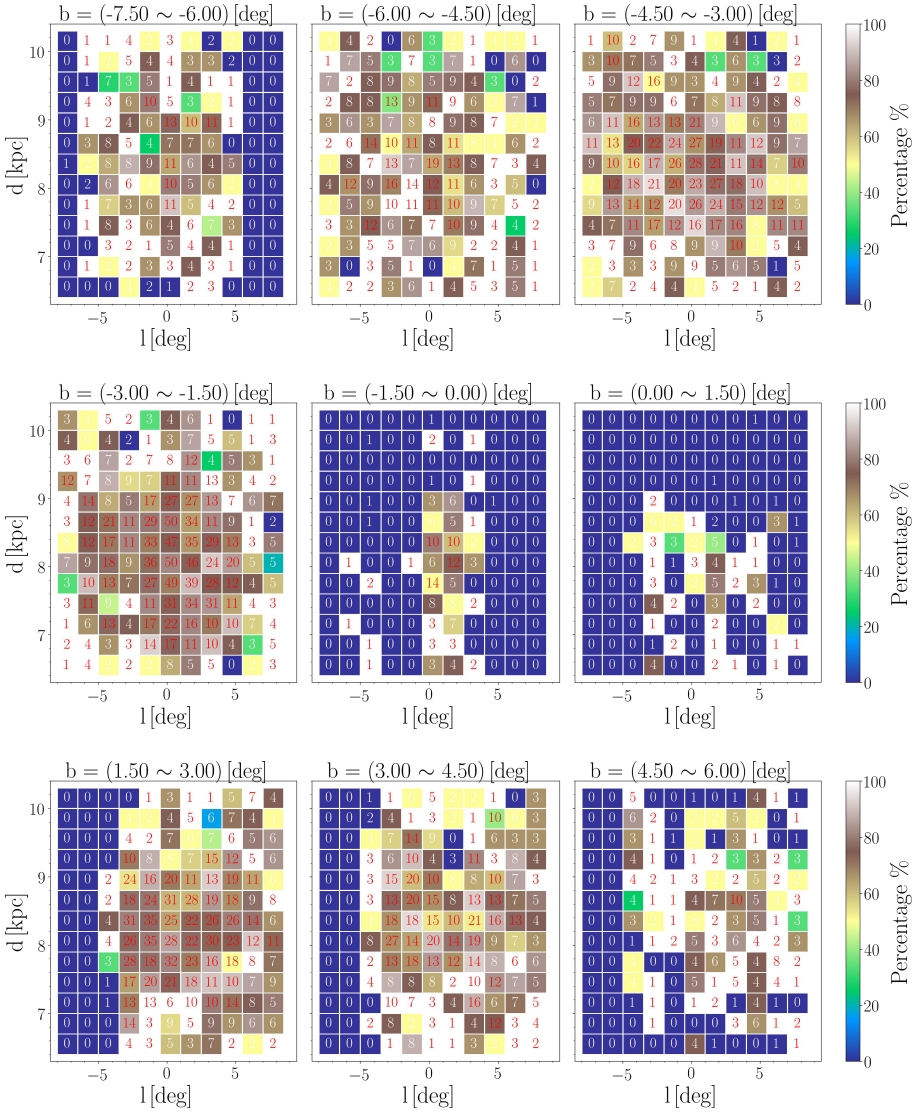

Figure 4.5.1: Colour maps for the spatial distribution of the studied RRab pulsators based on the fraction of the Oo I group using distance vs. Galactic longitude in selected stripes in Galactic latitude coordinates. From the top-left to the bottom-right panels we displayed slices going from −6.75 up to 5.25 deg with 1.5 deg steps. The white/brown colours mark the regions with the majority of Oo I variables, and green/yellow regions represent the regions with equivalent or higher number of Oo II variables. The blue regions denote in most cases the sectors with the lowest number of stars or those where the ratio between the Oosterhoff groups is more in favour of the Oo II group. These regions were in most cases not observed by the OGLE team. The numbers in each grid represent the total number of RR Lyraes that were found in that region.

striking between *foreground* and *background*. In the *foreground* more than 80 % variables are Oo I stars, while in the *background* their numbers go down to 63 %. For the central region the representation of Oo II increases up to 30 %. The discrepancy between *foreground*,

Table 4.5.1: Table for the median values of the distance in each selected segment with respect to the Oosterhoff group. Column 1 lists the studied regions, columns 2 and 3 and columns 4 and 5 mark the median values of the distance and fraction of a given Oosterhoff group, respectively.

	Oo I		Oo II	
Region	d [kpc]	%	d [kpc]	%
$foreground_{(d\leq 6.4\,\mathrm{kpc})}$	5.85	81.4	5.94	18.6
$b = \langle -6.75 \pm 0.75 \rangle$ [deg]	8.35	73.5	8.50	26.5
$b = \langle -5.25 \pm 0.75 \rangle$ [deg]	8.29	75.5	8.48	24.5
$b = \langle -3.75 \pm 0.75 \rangle$ [deg]	8.25	77.1	8.37	22.9
$b = \langle -2.25 \pm 0.75 \rangle$ [deg]	8.14	76.7	8.21	23.3
$b = \langle -0.75 \pm 0.75 \rangle$ [deg]	7.94	69.2	8.11	30.8
$b = \langle 0.75 \pm 0.75 \rangle$ [deg]	7.74	67.4	8.42	32.6
$b = \langle 2.25 \pm 0.75 \rangle$ [deg]	8.17	75.5	8.31	24.5
$b = \langle 3.75 \pm 0.75 \rangle$ [deg]	8.20	75.4	8.43	24.6
$b = \langle 5.25 \pm 0.75 \rangle$ [deg]	8.31	73.8	8.57	26.2
$background_{(d\geq 10.3\,\mathrm{kpc})}$	11.36	63.1	11.58	36.9

background and central regions might also be an incompleteness effect, since the Oo II stars are on average brighter and thus easier to detect at larger distances or in high-extinction regions.

To conclude, we do not see any major structures in the Galactic bulge formed by either of the Oosterhoff groups. We do see some small iregularities in their distributions, mainly in the front and back part of the Galactic bulge. The differences in number fraction of *foreground* and *background* regions might be connected to an observational bias, since the Oo I and II populations differ in luminosity.

Density profile of bulge RR Lyraes and the Galactic bar

For the construction of the density profile we transformed Galactic coordinates and distances of individual stars into a Galactocentric Cartesian coordinate system using the following equations:

$$x = (-d + d_{\mathrm{cen}}) \cdot (\cos b \cdot \cos b_{\mathrm{cen}} \cdot \cos(l - l_{\mathrm{cen}}) + \sin b \cdot \sin b_{\mathrm{cen}}), \tag{4.18}$$

$$y = d \cdot \cos b \cdot \sin(l - l_{\mathrm{cen}}), \tag{4.19}$$

$$z = d \cdot (\sin b \cdot \cos b_{\mathrm{cen}}) - d \cdot \cos b \cdot \sin b_{\mathrm{cen}} \cdot \cos(l - l_{\mathrm{cen}}), \tag{4.20}$$

where b_{cen} and l_{cen} denote the center of the Galactic bulge ($b_{\mathrm{cen}} = l_{\mathrm{cen}} = 0°$), The d_{cen} stands for the median of the estimated distances for stars from our sample, which we will denote as distance to the Galactic center. In our transformation, the coordinate axes correspond to each other in the following way: $x \sim d$ (increases in positive direction towards the Galactic anticenter), $y \sim l$ (positive in the direction of Galactic rotation) and $z \sim b$ (positive in the

direction to the Galactic North pole). Using the Cartesian coordinates we then calculated the radius r:

$$r = \sqrt{x^2 + y^2 + z^2}. \tag{4.21}$$

Subsequently, using the radius r we divided our sample stars, with respect to each Oosterhoff group, into individual annuli with a width of roughly 0.18 kpc except for the first bin, which had a larger width of 0.2 kpc to account for the low number of pulsators in the central region. We cut off at a radius of $r = 3.4$ kpc, due to the fact that for higher radii we would include only the stars behind the Galactic bulge at distances higher than 11.7 kpc. Furthermore, we calculated the number density of stars in individual spherical shells around the Galactic bulge. All calculated densities were normalized using the density of the first bin. This bin was afterwards removed from the density plot due to possible incompleteness because of its position close to the Galactic center. The spherical distribution was fitted with a power-law in the following form:

$$\log(\rho_r) = k + n \cdot \log(r), \tag{4.22}$$

where ρ_r stands for RR Lyrae number density, and k and n are parameters of the model. Fig. 4.5.2 depicts the resulting density profile for the RR Lyrae distribution in the Galactic bulge. The spherical distribution for both Oosterhoff populations can be described by a simple power-law.

Error bars for an individual bin in the density profile were calculated in the following way. We assumed that the distribution of $\log(r)$ for both Oosterhoff groups follows a Gaussian distribution. Using average values and the standard deviation for $\log(r)$ we randomly generated 50 000 distributions for an individual Oosterhoff population and divided them into the same bins as for the selected sample stars. Subsequently, we calculated the standard deviation in individual bins, which is depicted as the aforementioned error bar in Fig. 4.5.2. Based on the calculated deviations in the bins, we detect at some radii a statistically significant difference between the Oo I and Oo II stellar density, especially in the outer regions.

From Fig. 4.5.2 we see that in the central regions (around $r = 1$ kpc from the center) the normalized density of Oo II variables is higher than that of Oo I pulsators (although not statistically significant). This is potentially due to the fact that Oo II stars are on average brighter than their Oo I counterparts, thus it is easier to detect them at such large distances or in regions with higher extinction. As we move outward, the densities become comparable and Oosterhoff populations seem evenly distributed. In the regions with higher r (approximately from $r = 2.0$ kpc) the difference between the density of Oo II stars and their Oo I counterparts becomes equal and in some cases even higher and statistically significant, based on the calculated errors. This higher incidence rate of Oo II variables could be ascribed to a region behind the Galactic bulge (see Sec. 4.5.1).

Here it is important to address the depth of the OGLE survey and its completeness. Udalski et al. (2015) estimated the depth of dense OGLE-IV fields to reach ≈ 20.5 mag. They found OGLE-IV to be complete to ≈ 18.5 mag in the I-band for individual sources in dense fields. The completeness of OGLE-IV RR Lyraes depends on many aspects, e.g. the amplitude of changes and the brightness, the number of observations, the pulsation mode etc. For detection and correct classification of individual RR Lyrae stars the above value might not be

the true completeness of the OGLE-IV sample. Soszyński et al. (2014) used overlapping fields observed by OGLE-IV to evaluate completeness. For fundamental-mode RR Lyrae pulsators they estimate the completeness to be above 95 % for variables brighter than $I = 17$ mag.

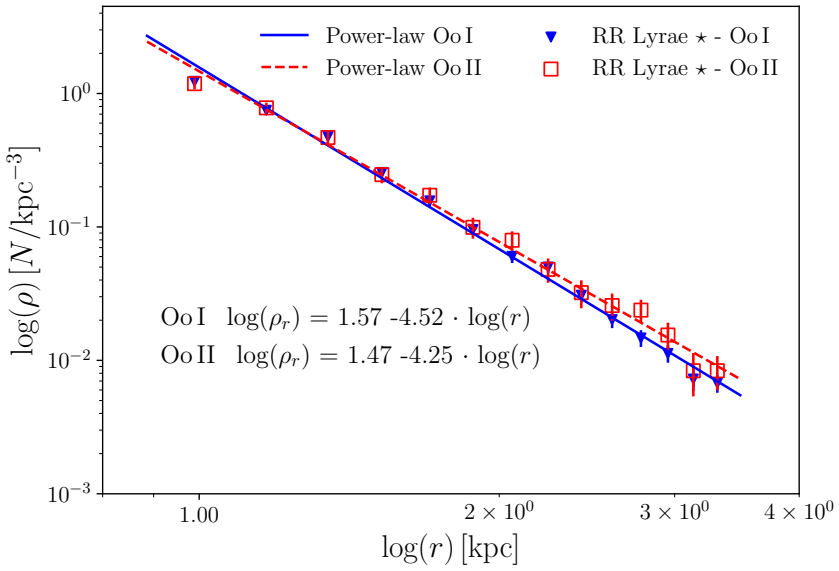

Figure 4.5.2: The density profile in the studied Oosterhoff groups in the Galactic bulge. The panel shows the density profile of RR Lyraes in the Oo I and II populations assuming a spherical model of the Galactic bulge. The blue dots and red squares represent Oo I and Oo II stars, respectively. The errors in the individual bins were calculated using a Monte Carlo simulation.

Oosterhoff groups with respect to the Galactic bar

In the past, several studies tried to use RR Lyrae stars as tracers of the Galactic bar with different results (Dékány et al. 2013; Pietrukowicz et al. 2015). From the kinematical point of view, the kinematics of old population variables is inconsistent with the kinematics expected for a B/P bulge (Kunder et al. 2016).

The position of the Galactic bar has been traced by intermediate-age stars (red clump stars; Nishiyama et al. 2005; Gonzalez et al. 2011; Wegg & Gerhard 2013). In order to explore a possible association with the Oosterhoff groups, we will use the bar positions found by Gonzalez et al. (2011). They traced the bar above and below the Galactic center (Galactic latitudes $b = \pm 1$ deg). To compare the distances of individual stars from the Galactic bar with respect to their Oosterhoff population we transformed coordinates and distances into the Cartesian coordinate system described above. We transformed the coordinates and distances from Gonzalez et al. (2011) for the Galactic bar as well. Subsequently, we calculated the Euclidian distances between individual pulsators and the Galactic bar.

In Fig. 4.5.3 we plot the cumulative fraction and normalized distributions of distances for our sample stars from the Galactic bar above (left-hand panel) and below (right-hand plot)

Table 4.5.2: Table for differences in density between the Oosterhoff groups in the Galactic bulge. Column 1 represents annuli in radius r extending from the Galactic center. The columns 2 and 3 list the normalized stellar density for the Oo I and Oo II populations, respectively. Column 4 represents absolute differences between the densities of the Oosterhoff populations in individual bins and the uncertainty of this difference. The bold-faced rows mark regions where the difference is statistically significant.

r [kpc]	$\rho_{\mathrm{Oo\,I}}$ [N$_\star$/kpc^3]	$\rho_{\mathrm{Oo\,II}}$ [N$_\star$/kpc^3]	$\lvert\rho_{\mathrm{Oo\,I}} - \rho_{\mathrm{Oo\,II}}\rvert$
0.99	1.2326	1.1851	0.0475 ± 0.1263
1.17	0.7480	0.7804	0.0324 ± 0.0832
1.35	0.4755	0.4678	0.0077 ± 0.0559
1.53	0.2559	0.2466	0.0092 ± 0.0387
1.70	0.1567	0.1728	0.0161 ± 0.0275
1.88	0.0955	0.0994	0.0038 ± 0.0198
2.06	0.0601	0.0795	**0.0194 ± 0.0147**
2.24	0.0500	0.0481	0.0019 ± 0.0110
2.42	0.0308	0.0322	0.0014 ± 0.0084
2.60	0.0202	0.0258	0.0056 ± 0.0065
2.78	0.0147	0.0238	**0.0091 ± 0.0051**
2.95	0.0113	0.0155	**0.0042 ± 0.0040**
3.13	0.0072	0.0084	0.0011 ± 0.0033
3.31	0.0068	0.0084	0.0016 ± 0.0026

the Galactic plane. We see that below and above the Galactic plane the Oo I stars peak at slightly shorter distances from the Galactic bar than the Oo II population. For Oo I stars the median values for distances from the Galactic bar are 0.75 kpc and 0.97 kpc above and below the Galactic plane, respectively. The Oo II component has a median distance of 0.77 kpc and 1.00 kpc above and below the Galactic plane, respectively. A similar effect is also seen in the inset of Fig. 4.5.3 where we see that for distances close to the Galactic bar, the probability of finding Oo I stars is higher than for Oo II variables. Once we move further away from the bar (approximately at 1.15 kpc away in radial direction) the probability of finding one or the other group becomes almost the same or higher for the Oo II group.

To further study the possible correlation between the Galactic bar and RR Lyrae stars we computed two-point correlation functions in order to quantify the clustering of stars in the vicinity of the Galactic bar. In the two-point correlation function $\omega(\theta)$ we quantify how likely it is to find two stars separated by a distance θ in a non-clustered randomly generated distribution (Peebles 1980). Over the years several estimators have been introduced by e.g., Davis & Peebles (1983) and Hamilton (1993). In this study we will use the estimator from Landy & Szalay (1993), which reads as follows:

$$\omega(\theta) = \frac{r\cdot(r-1)}{n\cdot(n-1)}\frac{DD}{RR} - \frac{(r-1)}{n}\frac{DR}{RR} + 1, \tag{4.23}$$

where the variables r and n represent total number of random points and of data points. The DD, DR, and RR acronyms are pair counts of stars in the data catalogue, data and random

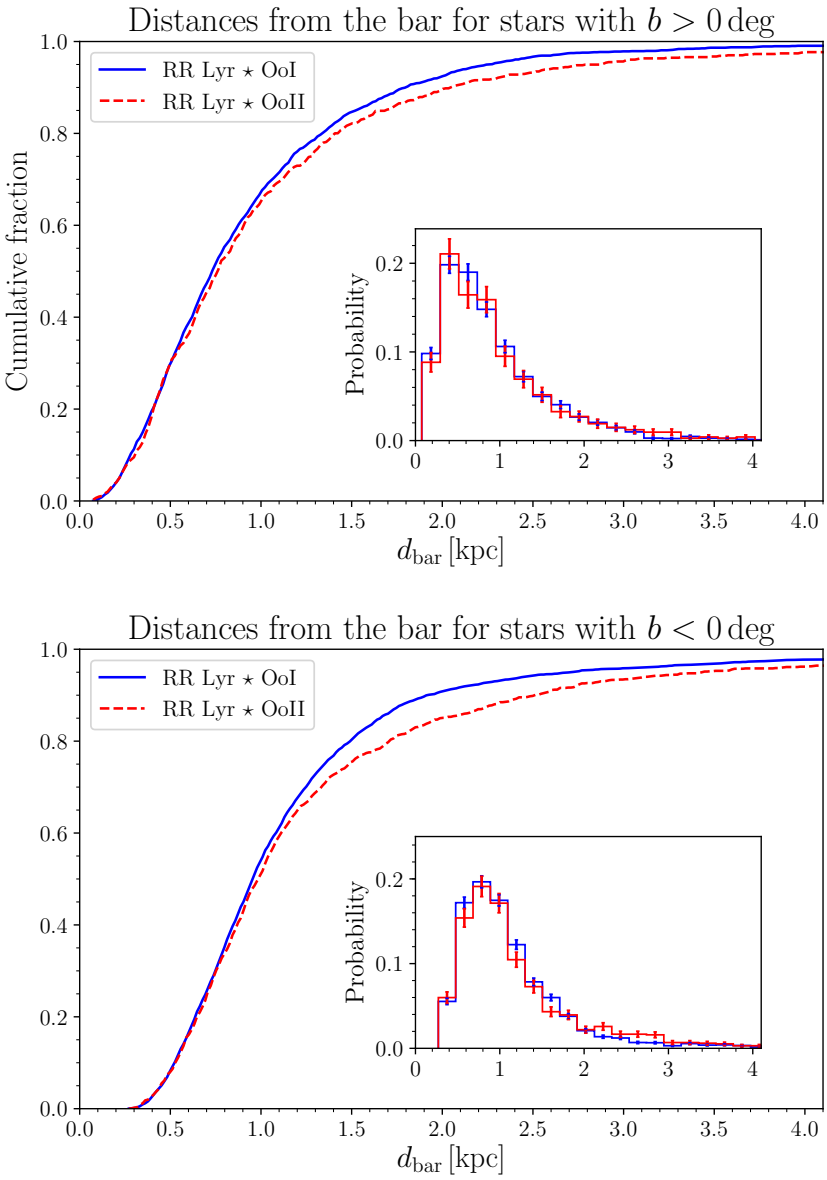

Figure 4.5.3: The cumulative fractions and distributions (in the insets) of the distances from the bar for the studied Oosterhoff groups. The left-hand plot depicts the distribution above the Galactic plane where the red dashed lines stand for the Oosterhoff type II variables and the blue lines represent Oosterhoff type I pulsators. The right-hand plot represents a similar distribution but for stars below the Galactic plane with the same colour-coding.

catalogue, and random catalogue, respectively. We selected regions around the Galactic bar in x and y coordinates above and below the Galactic plane with a range of $\pm 2\,\mathrm{kpc}$ in x direction for the position of the Galactic bar and removed stars lying outside the set borders

(see bottom panels of Fig. 4.5.4). Two random catalogues were generated and masked in the same manner.

The top panels of Fig. 4.5.4 show the resulting two-point correlation functions for both Oosterhoff groups above and below the Galactic plane with respect to the Galactic bar. For the region below the Galactic plane we see that Oo I and II stars, in the vicinity of the Galactic bar, cluster in a similar manner. Neither of the groups seems to be more clustered. On the other hand, above the Galactic plane we see that the Oo II group seems to be more clustered in comparison with the Oo I component. However, results from the Kolmogorov-Smirnov test suggests that the Oo I and II groups are drawn from the same distribution, with a p-value = 0.27. Overall neither of the groups seems to cluster at the position of the Galactic bar, which is in agreement with the previous studies done by Dékány et al. (2013) and Minniti et al. (2017) as well as seen in the study of the disc RR Lyrae stars by (Dékány et al. 2018). In addition, in the bottom panel of Fig. 4.5.4 we do not observe any major trend in RR Lyrae stars that would imply that they concentrate at the position of the Galactic bar above or below the Galactic plane.

Conclusions

In this paper, we used photometric data for RRab type stars from the OGLE-IV and VVV surveys to study the differences, in physical properties, and spatial distributions of the Oosterhoff I and II populations in the Galactic bulge. Our results can be summarised as follows:

- We identified and separated the Oo I and II populations among non-modulated RR Lyrae stars in the Galactic bulge, based on the period-amplitude space and using the manifold learning. Approximately 25 % of the analysed stars (from 8 141 fundamental-mode variables) belong to the Oo II group, which is consistent with similar studies for the Galactic halo.
- Based on the estimated physical parameters the Oo II stars are on average cooler ($\approx$ 400 K), more massive ($\approx 0.04\,M_{\odot}$), brighter (by 0.23 mag in K_s-band), and more metal-poor (≈ 0.1 dex) than the Oo I pulsators. A comparison with models of stellar pulsation and evolution showed that the Oo II variables are more massive than Oo I stars.
- Both Oosterhoff groups were compared with two GCs in the Galactic bulge, NGC 6401 and NGC 6441, identified as containing Oo I and Oo III stars, respectively. Based on the positions of individual stars in the period-amplitude or metallicity and φ_{21} or φ_{31} vs. R_{31} diagrams some stars from our Oo II group may actually belong to the Oo III group.
- We studied the spatial distribution of the Oo I and II groups in the Galactic bulge. We found that the region denoted in our work as the *foreground* (for distances $d \leq 6.4$ kpc) of the Galactic bulge contains fewer variables associated with the Oo II component (less than 19 %, in comparison with the overall distribution 25 %). On the other hand, in the central region of the Galactic bulge with one exception, we do not see any difference in

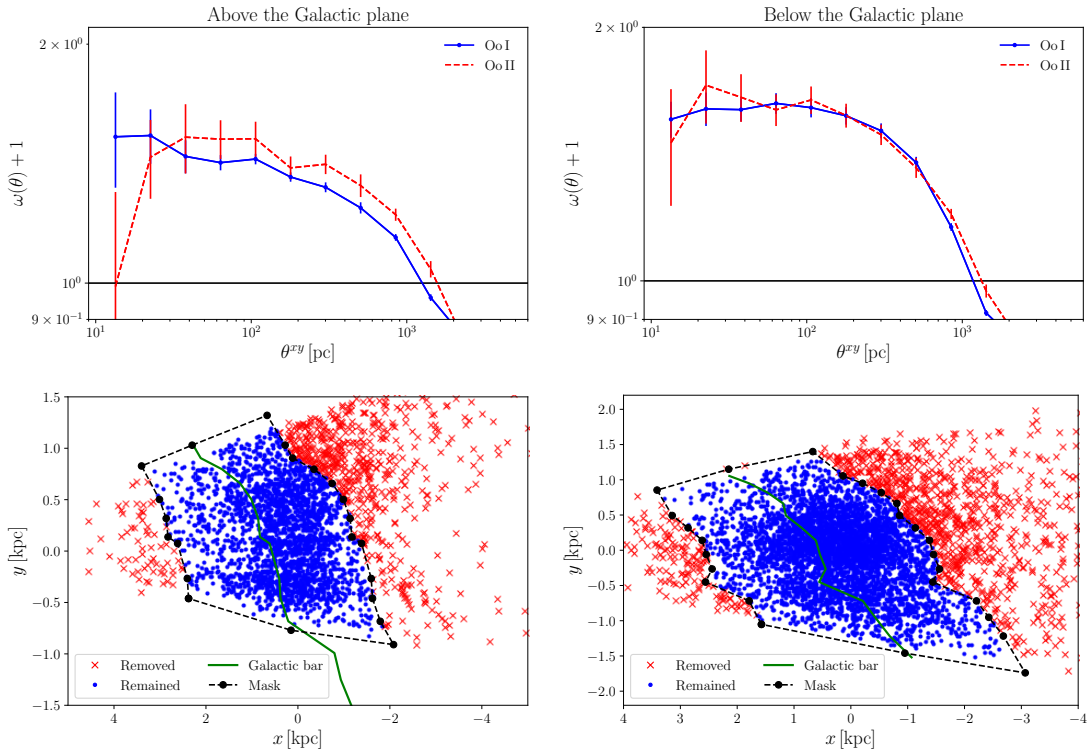

Figure 4.5.4: Two-point correlation function for the Oo I and II groups in the Galactic bulge. The two top panels show results of the two-point correlation function, $\omega(\theta)$, with blue and red lines denoting Oo I and Oo II stars, respectively, while θ represents the distance separation between the data and randomly generated points. The left-hand panel shows results for the region above the Galactic plane and the right-hand panel illustrates the region below the Galactic plane. The two bottom figures display masked regions (black dashed lines) with the Galactic bar (green solid line). The blue points stand for stars within the masked region, while red crosses lie outside the outline boundary.

the overall value of 25 %. We found an increase in the occurrence of Oo II stars (above 30 %) in the region encompassing the Galactic center in $b = (-0.75 \pm 0.75$ deg) Galactic latitude. The difference in the representation of the Oo I and II groups also appears when we progress from the Galactic center toward larger distances to the denoted *background* (for distances $d \geq 10.3$ kpc) region. Here we found a high occurrence of Oo II stars, which constitute almost one-third of the RR Lyrae stars. Both of these discrepancies may be related to the fact that Oo II stars are intrinsically brighter and redder than Oo I stars, and therefore detectable at larger distances and in regions with higher extinction.

- The density profile for both Oosterhoff groups in the Galactic bulge shows that as we move radially outward from the Galactic center the density of the Oo II stars rises. In some cases, the normalized density even exceeds the normalized density of the Oo I variables with a statistical significance (more than σ). The distribution of distances

from the Galactic bar showed that the Oo I group peaks on average on shorter distances than the Oo II populations. On the other hand, based on the two-point correlation function for the Oo I and II group below the Galactic plane, both groups are similarly distributed. Above the Galactic plane the Oo II population seems to be slightly more clustered in comparison with the Oo I population. We did not find any correlation between the Galactic bar and the Oosterhoff groups.

- In order to test our derived extinction law and subsequently our results, we decided to re-do the whole analysis for two independent distance estimations. In the first approach we used the J-band from the VVV photometry using the `pyfiner` (Hajdu et al. 2018) for our sample and extinction law derived by Majaess et al. (2016) for $E(J-K)$ to estimate A_K. In the second approach we used the extinction maps by Gonzalez et al. (2012) to gain $E(J-K)$ and equation 29 from Nataf et al. (2013) to derive A_I. In the end, we compared the results for all three methods and verified that our main conclusions remain the same regardless of the assumed extinction law.

Our main conclusions are as follows. The Galactic bulge contains mainly two Oosterhoff groups (Oo I and II) that differ in metallicities, masses, luminosities, and colours. This is in agreement with similar studies in GCs. A small portion of Oo II stars probably belong to the Oo III group. The spatial distribution of Oo I and II groups in the Galactic bulge does not show any systematic difference between both groups and the Oosterhoff populations seem to be well mixed. In the *background* and central region of the Galactic bulge we observe an increase of Oo II variables, which is probably an observational bias due to their higher brightness. We do not observe any spatial correlation with the Galactic bar for the aforementioned Oosterhoff groups, which is in agreement with Dékány et al. (2013) and Minniti et al. (2017) but in disagreement with Pietrukowicz et al. (2015). One of the possible reasons for this discrepancy is a different treatment of extinction, and that our analysis, unlike that of Pietrukowicz et al., is partly based on near-infrared data.

CHAPTER 5

ON THE OOSTERHOFF DICHOTOMY IN THE GALACTIC BULGE: II. KINEMATICAL DISTRIBUTION

"... then you gotta co-operate, right?"
"Wrong."

— Col. John Matrix, Val Verde

Abstract: We present a kinematical study of RR Lyrae stars associated with two Oosterhoff groups in the Galactic bulge. We used data published in the first paper of the series, plus proper motions from the *Gaia* Data Release 2, and radial velocities from the literature. A 6D kinematical and spatial solution was obtained for 429 RR Lyrae stars. We use a model of the Galactic gravitational potential to infer stellar orbits. We did not find a difference between the Oosterhoff groups in the individual components of the space velocity. We report that *foreground* and *background* stars with respect to the Galactic bulge stand out in the mean V velocity component, which we interpret as a sign of the Galactic rotation. The movement of the studied stars in the central region of the Galactic bulge is consistent with random motions expected for a classical bulge component. From the orbital integration, we estimate that 8 % of the RR Lyrae stars are halo interlopers currently located in the Galactic bulge. The majority of the stars' orbits are within a 3 kpc radius from the Galactic bulge. The fraction of Oosterhoff II stars increases with increasing Galactic latitude, as well as towards longer orbital periods. We found several RR Lyrae stars with high space velocities, one of which has an extremely long orbital period of ~1 Gyr. We conclude that based on their kinematics, the vast majority of the stars in our sample do not seem to contribute to the boxy/peanut component of the Galactic bulge.

This chapter is based on our published paper : **Prudil, Z.**, Dékány, I., Grebel, E. K., Catelan, M., Skarka, M., Smolec, R.: On the Oosterhoff dichotomy in the Galactic bulge: II. kinematical distribution, 2019, MNRAS, 487, 3270

Context

According to the current paradigm, galactic bulges form in two main ways: the bar-like pseudobulges through instabilities of the disc, and the spheroidal (classical) bulges through early mergers. The pseudobulges are characterized by cylindrical rotation while random motion dominates the classical bulges (e.g., Wyse et al. 1997; Kormendy & Kennicutt 2004; Barbuy et al. 2018).

The Milky Way (MW) bulge has a pronounced boxy/peanut bulge component recognized already in images from the *COBE* satellite (Weiland et al. 1994; Dwek et al. 1995) and later spatially studied using red clump giants by, e.g., McWilliam & Zoccali (2010) and Wegg & Gerhard (2013), among many others. Recent studies suggest that a pseudo- and a classical bulge component (one from secular formation, the other via mergers) can co-exist (Obreja et al. 2013), but whether our own Galaxy's bulge contains both components is still a matter of a debate (e.g., Zoccali et al. 2008), for instance, due to the possible vertical metallicity gradient (e.g., Zoccali et al. 2008; Ness et al. 2013a). Kinematically, the Galactic bulge has been studied mainly using red clump stars (The Abundances and Radial velocity Galactic Origins Survey - ARGOS, Freeman et al. 2013; Ness et al. 2013b) and using M giants (Bulge Radial Velocity Assay - BRAVA, Kunder et al. 2012). Both surveys targeted mainly the intermediate-age population of the Galactic bulge, and supported the pseudo-bulge morphology.

In this work, we will focus on tracers of the oldest bulge population, as represented by the RR Lyrae variables. They are short-period pulsating stars burning helium in their cores and are associated with Population II (Catelan & Smith 2015). They are ideal probes of the old stellar systems in the Local Group, for instance through their period-luminosity dependence (Alcock et al. 1997; Sesar et al. 2013; Dékány et al. 2013). They have been proven a useful tool in many branches of astrophysics, ranging from in-depth studies of individual stars (e.g., Guggenberger et al. 2012) to studies of Galactic structure and evolution (Dékány et al. 2013, 2018; Pietrukowicz et al. 2015).

Despite their abundance in the MW and in the Magellanic system, there are still some unanswered questions related to RR Lyrae stars, e.g. the origin of the Oosterhoff dichotomy (Oosterhoff 1939). The Oosterhoff dichotomy divides MW globular clusters that contain RR Lyrae stars into two main groups, traditionally labeled Oosterhoff I (Oo I) and Oosterhoff II (Oo II), based on the pulsation properties of the associated RR Lyrae variables. The Oosterhoff type I globular clusters contain RR Lyrae stars with short pulsation periods and are more metal-rich in comparison with globular clusters of Oosterhoff type II, which are metal-poor and contain RR Lyrae variables with longer pulsation periods. At the same time, GCs in the Magellanic Clouds and nearby dwarf galaxies do not fit into either of the two Oo groups in general, which connects the Oo dichotomy to the MW itself. In addition, two globular clusters located in the Galactic bulge, NGC 6441 and NGC 6388, constitute a third

Oo group of their own (Pritzl et al. 2000, Oo III). We point the interested reader to Catelan (2009) and Catelan & Smith (2015) for comprehensive reviews of the Oosterhoff dichotomy.

The RR Lyrae stars have been used for kinematical studies in the past, e.g. Layden et al. (1996) showed that the metal-rich ones ([Fe/H]> -1.0 dex) in the nearby Galactic field belong to the thick disc population while the rest probably originate from the halo. In addition, recent kinematic studies targeted RR Lyrae stars in the Galactic bulge (Kunder et al. 2015, 2016, 2018) concluding that they are part of a classical bulge or metal-rich inner halo/bulge component with a random orbital distribution.

In the first paper of this series (Prudil et al. 2019a), we studied the spatial distribution of RR Lyrae stars in the Galactic bulge in the context of the Oosterhoff dichotomy. We found that ≈ 25 % of the RR Lyrae variables in the Galactic bulge are associated with the Oosterhoff II group. Pulsators of the Oosterhoff II population are on average more massive, brighter, and cooler than their Oosterhoff I counterparts. We did not find any link between the individual Oosterhoff populations and the Galactic bar.

In this paper, we present a kinematical study of the Oosterhoff groups in the Galactic bulge based on several hundred RR Lyrae variables used in the previous work. In Section 5.2, we describe the selection criteria and basic statistics of our sample. In Section 5.3 we outline the process of calculating kinematical properties and discuss sources of possible contamination in our sample. Section 5.4 discusses the orbital integration of our sample using a gravitational potential model of the MW and their orbital parameters. A few particularly interesting objects are addressed in greater detail. In Section 5.5 we summarise our findings.

Data sample

We used the fundamental-mode RR Lyrae stars located toward the Galactic bulge with estimated metallicities, distances, and Oosterhoff status from Prudil et al. (2019a). The distances and metallicities were obtained using photometric data from the fourth phase of the Optical Gravitational Lensing Experiment (hereafter OGLE-IV, Udalski et al. 2015; Soszyński et al. 2017b) and the VISTA Variables in the Vía Láctea survey (VVV, Minniti et al. 2010).

In this study, we will use data from the second *Gaia* data release, the *Gaia* DR2 (Gaia Collaboration et al. 2016a, 2018a). It contains multiband photometry for 1.7 billion sources together with parallaxes and proper motions for 1.3 billion sources. From our sample, we found a match for 7 785 objects with proper motions and parallax measurements, thus nearly for all selected stars.

Some of the cross-matched variables have unreliable proper motions (with an error in proper motion higher than the proper motion itself). Thus, we removed stars in which the error in proper motion exceeds 50 % of its proper motion value. The majority of the removed pulsators have negligible proper motion either in R.A. or Dec. In the end, 6 542 variables were considered for further analysis. We investigated whether stars with different Oosterhoff classifications have different distributions of proper motion in either direction using the two-sample Kolmogorov-Smirnov test. This statistical test returns the probability p_{KS} of obtaining our sample under the null hypothesis that they have identical distributions. The null hypothesis is usually rejected if $p_{\mathrm{KS}} < 0.05$. Our test resulted in $p_{\mathrm{KS}} = 0.33$, thus we conclude

that there is no significant difference between the proper motion distributions of the tho Oosterhoff groups.

If we assume that RR Lyrae stars trace the spheroidal component of the Galactic bulge they should belong to its kinematically hot component with a minor rotation component and large velocity dispersion. The tangential velocities v^t can be used to test such an assumption through a simple equation, $v^t = 4.74 \cdot \mu \cdot d$, with the proper motion μ in mas yr^{-1} and distance d in kpc. For individual proper motion components we a get dispersion $\sigma v^t_{\alpha*} = 125\,\mathrm{km\,s^{-1}}$ and $\sigma v^t_{\delta} = 123\,\mathrm{km\,s^{-1}}$. Therefore, the tangential velocity ellipsoids are fairly symmetric and support the assumption about the RR Lyrae stars being part of the kinematically hot component of the Galactic bulge. This conclusion is in agreement with a study using the Galactic bulge Type II Cepheids (Braga et al. 2018).

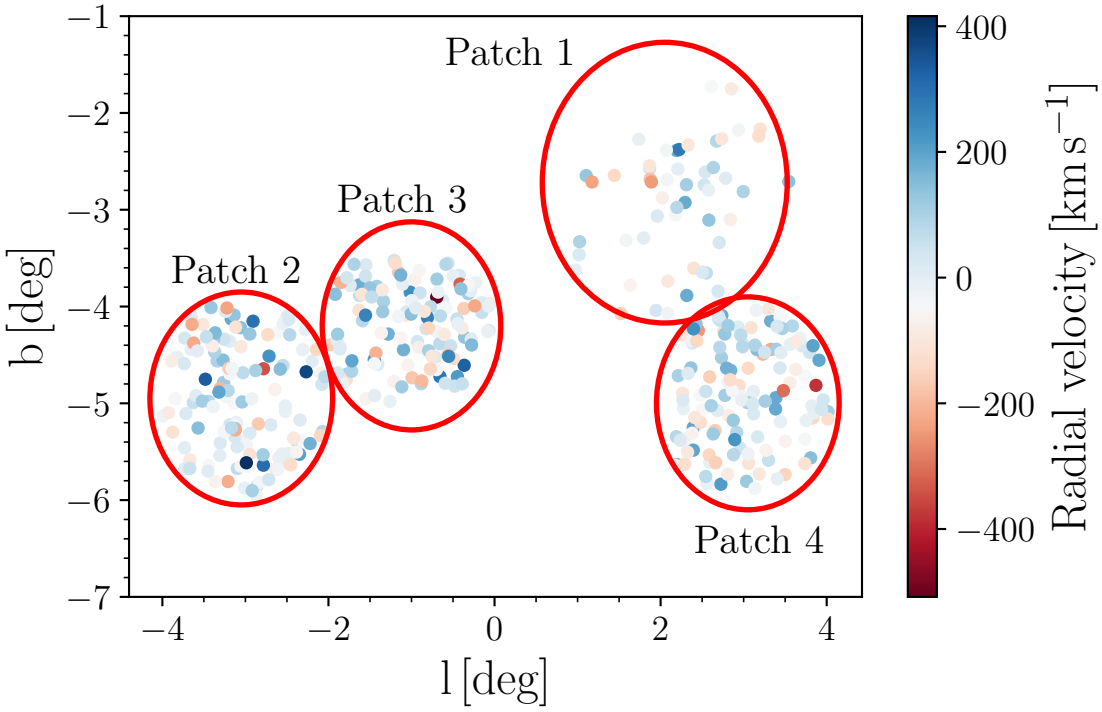

Figure 5.2.1: The spatial distribution of our sample variables in Galactic coordinates with colour-coding representing the measured radial velocity.

The full information of space velocities can hint at possible differences between stars if they differ in origin. Therefore, for the purpose of this paper, we cross-matched stars with distances and proper motions with the published catalogue of Kunder et al. (2016), consisting of radial velocities for 947 RR Lyrae pulsators in the Galactic bulge. The cross-matched sample consists of 429 variables (313 Oo I and 116 Oo II type). Figure 5.2.1 shows the distribution of radial velocities for our sample of variables in Galactic coordinates in four observed patches. The radial velocities for the Oo I variables vary from $-381\,\mathrm{km\,s^{-1}}$ to

337 km s^{-1} with a median of 8 km s^{-1}. On the other hand, Oo II stars have a broader range of values (from −508 km s^{-1} to 416 km s^{-1}) with a median of 12.5 km s^{-1}. The K-S test of the radial velocity distribution of both Oosterhoff populations yields the following values: D = 0.100 and $p_{\rm KS} = 0.344$. Therefore, the radial velocities seem to be drawn from the same distribution, and there is no difference between both groups.

We note that the selected sample of radial velocities does not contain individual errors. Therefore, we decided to assume a constant error value of 10 km s^{-1} for each star. Our assumption is based on errors in the radial velocities of variables in NGC 6441 (Kunder et al. 2018), where 40 RR Lyrae stars have been observed with the same instrument, similar exposure time (from 0.5 to 2 hours), and the same resolution as for the pulsators in Kunder et al. (2016). Their errors are on average ±7.5 km s^{-1} and only 3 stars have higher errors than 10 km s^{-1}. Thus, on average, we slightly overestimate the velocity errors.

Kinematics of the Oosterhoff populations in the Galactic bulge

In this section, we study the kinematics of the different Oosterhoff groups in the Galactic bulge.

The components of the space velocity were obtained following Johnson & Soderblom (1987) in the U, V, and W Galactic Cartesian system. We assumed a left-handed system with positive U towards the Galactic anticenter, V in the direction of Galactic rotation, and positive W in the direction to the Galactic north pole. We adopted the coordinates of the Galactic north celestial pole based on the coordinates provided by the Hipparcos satellite (ESA 1997):

$$\alpha_{GP} = 192.85948^{\circ}, \qquad \delta_{GP} = 27.12825^{\circ}, \tag{5.1}$$

$$l_{GP} = 122.93192^{\circ}, \tag{5.2}$$

where α_{GP} and δ_{GP} represent the coordinates of the Galactic north celestial pole and l_{GP} stands for the position angle between the Galactic north celestial pole and zero Galactic longitude. For the peculiar solar motion we assumed:

$$(U_{\odot}, V_{\odot}, W_{\odot}) = (-14.1 \pm 0.57, 12.24 \pm 0.47, 7.25 \pm 0.37)\ \mathrm{km\,s^{-1}} \tag{5.3}$$

from Schönrich et al. (2010); Schönrich (2012) and a local standard of rest velocity v_{LSR} = 220 km s^{-1} (Kerr & Lynden-Bell 1986; Bovy et al. 2012).

The true space velocity sv can be obtained through the simple equation:

$$sv = \sqrt{U^2 + V^2 + W^2}. \tag{5.4}$$

The median values and dispersions of the individual sv components are listed in Tab. 5.3.1. In Fig. 5.3.1 (top and side insets) we display the distributions of the space velocity and its Cartesian components. The errors for the individual velocity components were obtained through 10000 iterations of the Monte Carlo error sampling where we added Gaussian random noise to the solar motion, distances, radial velocities, and proper motions with σ made

Table 5.3.1: Statistical properties of the velocity distributions displayed in Fig. 5.3.1. The first column lists both Oosterhoff groups, while individual velocities are listed in columns 2, 4, 6, and 8 with respect to the two Oosterhoff populations. Columns 3, 5, 7, and 9 list the dispersion in the components of sv and in sv proper, respectively.

	U [km s^{-1}]	σ^U [km s^{-1}]	V [km s^{-1}]	σ^V [km s^{-1}]	W [km s^{-1}]	σ^W [km s^{-1}]	sv [km s^{-1}]	σ^{sv} [km s^{-1}]
Oo I	-20	118	-22	123	10	121	192	89
Oo II	-35	126	-25	128	15	129	203	99

equal to their uncertainties. From these four panels, we see that both Oosterhoff groups are centered at 0 km s^{-1} and that the distributions are fairly similar for the velocities in the Galactic plane U and V. A small systematic difference between the two groups can be seen in the W component, where on the positive side we see two peaks (roughly at 58 km s^{-1} and 187 km s^{-1}, marked with black arrows in Fig. 5.3.1). Closer examination of the spatial and kinematical properties of the stars responsible for this deviation did not show any sign of clustering or any preferential direction of velocities. The distribution of space velocities is depicted in the bottom-right panel of Fig. 5.3.1. As in the case of individual components, we do not see any major differences between the two Oosterhoff groups. The green dashed line represents the true space velocity found by Kunder et al. (2015) for one of the high-velocity RR Lyrae stars in the Galactic bulge. From our sample, six stars have higher velocities than the variable found by Kunder et al. (2015); two of these stars are discussed in detail in Sec. 5.4.2.

In order to test whether the distribution of space velocity components differs between Oosterhoff groups, we used the crossmatch test (CM test) for multivariate distributions (Rosenbaum 2005) using the package implementation `crossmatch` in `R`. The CM test uses the distances between observations for comparison. In our case, we calculated Mahalanobis distances (distance between a point and a distribution) instead of the commonly used Euclidian distances since our data are highly correlated. The CM test works only with distributions having an even number of values, therefore for our sample, we calculated the p-value for the entire distribution while always leaving one star out. In the end, we ran this calculation 429 times and calculated the median of the resulting p-values. The comparison for the velocity components U, V, and W in both Oosterhoff groups yields $p_{\mathrm{CM}} = 0.32$ following the same considerations as in Sec. 5.2, therefore the distribution of the velocity components for the two Oosterhoff groups in the Galactic bulge is fairly similar. In addition, we calculated the same test for the distribution of the Galactocentric Cartesian coordinates (x, y, and z) for our sample, and the resulting p-value, $p_{\mathrm{CM}} = 0.71$, suggests that the distribution of both Oosterhoff groups in the Galactic bulge is very similar.

Possible contamination

Our sample might contain some stars from the Galactic disc and/or halo that would cause contamination. In Fig. 5.3.1 we plotted dependences of individual velocities, calculated their velocity ellipsoids, and displayed the distribution of the sv with respect to the photometric metallicity. The velocity ellipsoids are quite *round*, with ratios of dispersion varying around

0.9 ~ 1.0 (see the annotations in the individual panels).

In the sv vs. metallicity plane, we see several interesting features. The upper envelope of the space velocities of RR Lyrae stars with [Fe/H] ~-1.0 dex seems to monotonically approach 400 km s^{-1} as we move towards more metal-poor variables. The bulk of the studied variables have velocities below 400 km s^{-1} with only 11 stars exceeding this value. The velocities of these 11 RR Lyrae increase with decreasing metallicity, which suggests an origin outside the Galactic bulge (i.e., in the metal-poor halo).

In addition, five stars in the bottom-left corner of this panel exhibit very low metallicity and sv values. This behaviour is in contrast with the general trend in our sample, which shows higher velocities for lower metallicities. These five stars have rather low radial velocities (average 19 km s^{-1}), and preferentially longer pulsation periods (average 0.75 days). Two out of these five stars fall into the region of the Oo III group for the globular cluster NGC 6441 in the period-amplitude diagram (see fig. 5 in Prudil et al. 2019a). If they belonged to that globular cluster, their metallicity from the photometric data would not agree with the metallicity determined from spectroscopic measurements and thus their distance, determined on basis of photometric metallicity, would be incorrect.

Some of the globular clusters in the Galactic bulge seem to be dissolving (e.g., NGC 6441, Kunder et al. 2018). Therefore, some of the stars in our sample might have been stripped from NGC 6441 in the past and have mixed with the bulge field population of RR Lyrae stars. In addition, one of these stars is a candidate for the double-mode variables found by Smolec et al. (2016), which, based on stellar pulsation models, have a high metallicity despite the low metallicity determined using photometric data. After a careful analysis of the Fourier spectra of the remaining four stars, none of them shows any sign of a double-mode behaviour.

In addition, the calculated orbits of these 5 stars show that 4 of them stay within the ≈ 3.5 kpc radius of the Galactic bulge and do not deviate more than 1 kpc from the Galactic plane during their orbits (for details on orbital integration see Sec. 5.4). Thus, they may be interesting candidates for spectroscopic follow-up studies, since they stand out in comparison with other bulge RR Lyrae stars due to their uncertain origin.

Overall, we do not see a major disc/halo contribution to our sample. Further examination with orbital solutions of the studied variables can be found in Sec. 5.4.

Distribution of velocities in space

Fig. 5.3.2 shows the spatial distribution of our stars with components of the space velocity. The space velocity components for stars in the central region of the Galactic bulge do not show any preferential direction and resemble random motions. We do not find any clumps nor groups of stars with similar location and following a preferential direction. We searched for stars with similar proper motions and radial velocities (difference in proper motion <0.1 mas yr^{-1} and radial velocity <20 km s^{-1}). For possible candidates, we calculated their orbits (see Sec. 5.4) to further investigate their possible link. In the end, we did not find any connection between the stars in our sample.

[1] We note that the calculated photometric metallicity does not agree with the metallicity determined through spectroscopy (Clementini et al. 2005). We use this metallicity to emphasize our point that slowly-moving RR Lyrae stars with large photometric metallicity may actually belong to the Oo III group (Pritzl et al. 2000).

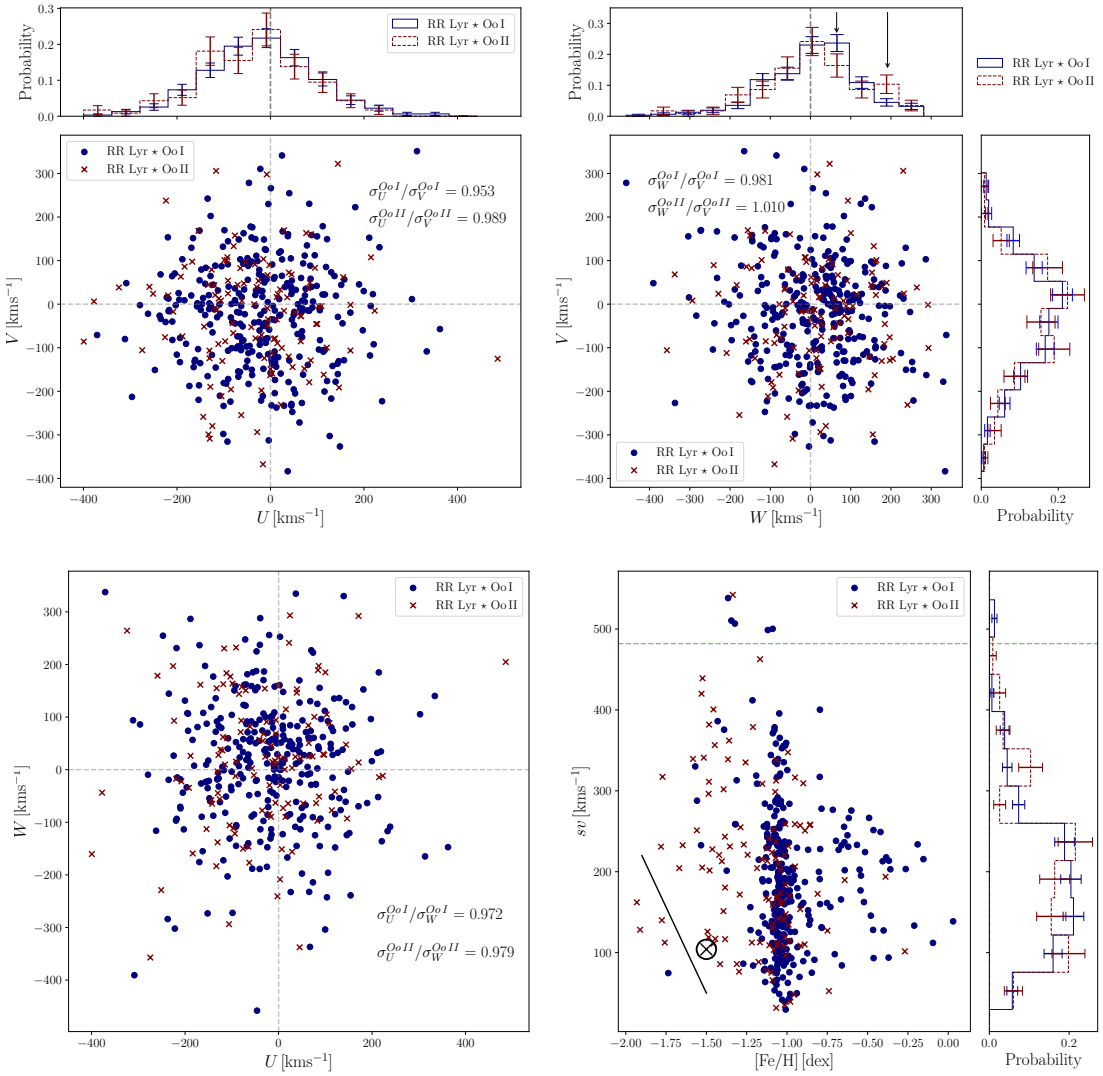

Figure 5.3.1: The dependences of individual components of the sv with respect to each other (top left and right and bottom left panels) and sv vs. [Fe/H] dependence (bottom right panel). The blue points and red crosses represent the Oo I and Oo II population, respectively. The dashed green line in the bottom right panel stands for the high-velocity bulge RR Lyrae stars ($sv = 482\,\mathrm{km\,s^{-1}}$) found by Kunder et al. (2015). The black line in the same panel separates 5 variables with very low metallicity and sv values. In addition, the black crossed circle represents the average position of RR Lyrae stars in NGC 6441 with respect to their sv and photometrically determined [Fe/H].[1]

In addition, we used a catalogue for the Milky Way globular clusters, containing their distance, average proper motions, and radial velocities (Vasiliev 2019). We inspected stars whose kinematic elements (proper motion and radial velocity) match the kinematic features of globular clusters, using the same criteria as in the search for groups of stars with similar kinematics. Using orbital integration (see Sec. 5.4) we then integrated the orbit of selected

candidates (the variables and globular clusters) forward and back in time. We did not find any sign of an association between the sample stars and retrieved globular clusters.

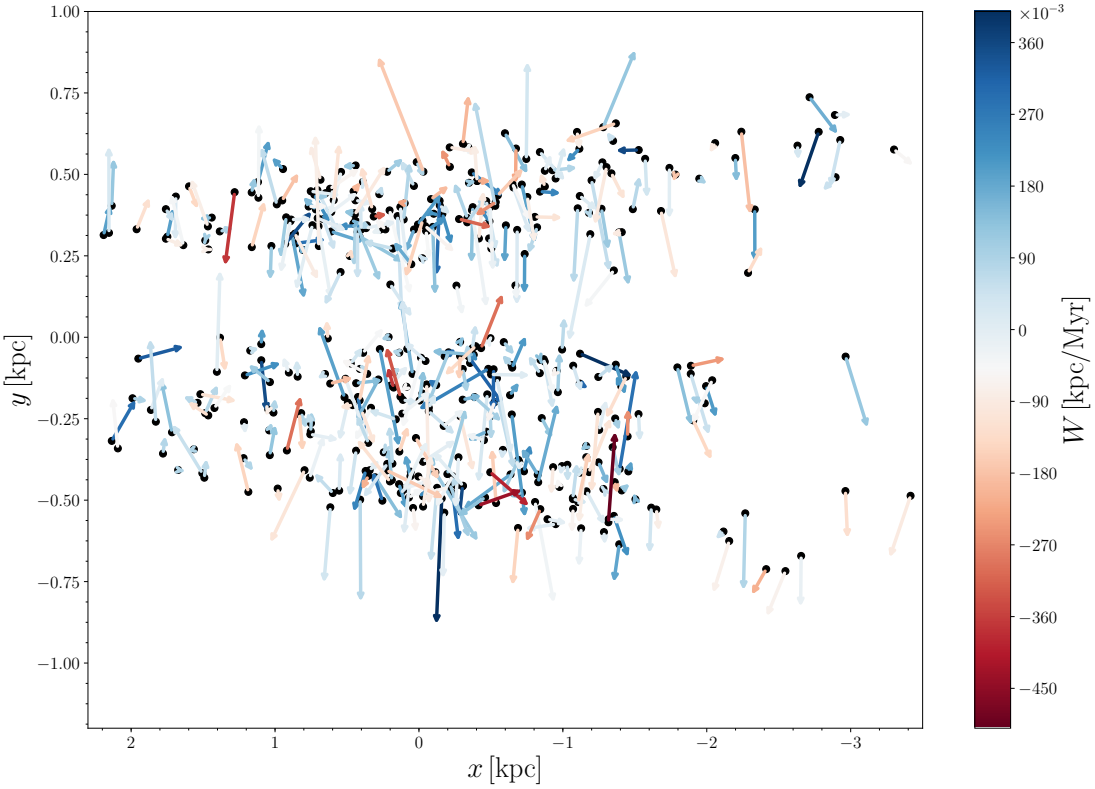

Figure 5.3.2: The spatial distribution of variables with calculated space velocities (black dots). The arrows represent the directions and values of the velocities U ($\dot{x}$ [kpc/Myr]) and V ($\dot{y}$ [kpc/Myr]) with the third component W ($\dot{z}$ [kpc/Myr]) depicted using the colour-code indicated on the right.

We do observe an opposite general direction of the space velocity component V for the foreground ($x > 1.75$ kpc) and background ($x < -1.75$ kpc) of the Galactic bulge (see Fig. 5.3.3). Regardless of the Oosterhoff group in the *foreground*, the majority of variables move in the direction of the Galactic rotation, with a median velocity $V = 97\,\mathrm{km\,s^{-1}}$. In the *background* of the Galactic bulge, irrespective of the Oosterhoff group, the majority of pulsators move in the opposite direction, with a median velocity of $V = -83\,\mathrm{km\,s^{-1}}$. This is a clear sign of the Galactic rotation in the front of and behind the Galactic bulge. Neither of the Oosterhoff groups seems to be dominant in this motion, they both contribute to this pattern equally. We note that, for RR Lyrae stars in the background of the Galactic bulge, we see in Fig. 5.3.3 two peaks and a small dip between them. Using the algorithm `Skinny-dip`[2], which is based on Hartigan's dip test of unimodality (Hartigan & Hartigan 1985), we got a p-value= 0.48 following the same considerations as in Sec. 5.2, which supports a unimodal

[2] http://www.kdd.org/kdd2016/subtopic/view/skinny-dip-clustering-in-a-sea-of-noise

distribution of V velocities behind the Galactic bulge. For these stars, assuming they rotate with the bar/disc, their Galactocentric velocity (V_{GC}) should increase with increasing Galactic longitude – l (see fig. 3 in Ness et al. 2013b). For selected variables associated with the *foreground* and *background* we do not observe such an effect, most likely due to such factors as, e.g., low width in l (for stars around 0 deg in l the V_{GC} varies around 0 km s^{-1}) and the fact that our sample contains only a few dozen objects.

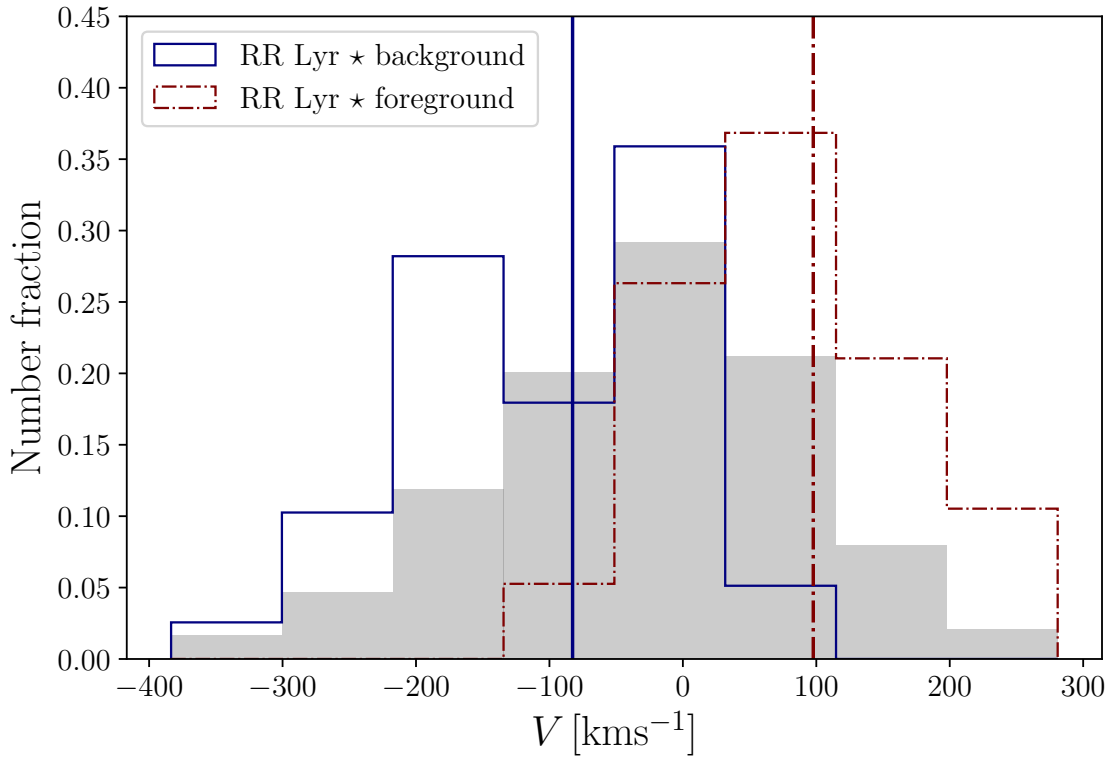

Figure 5.3.3: The distribution of the V velocity components for the studied stars (grey histogram). The red and blue histograms represent the distribution of RR Lyrae stars in the foreground and background of the Galactic bulge, respectively, with the same colour-coding for vertical lines denoting the median velocities for a given region.

Orbits of the Oosterhoff populations

To compare the orbits and orbital parameters of both Oosterhoff groups we used the `galpy`[3] library (Bovy 2015) to integrate orbits of individual stars. We utilized the axisymmetric model for the MW Galactic potential in `galpy`, `MWPotential2014`, which is composed of a power-law density profile for spherical bulges with exponential cut-off, Miyamoto-Nagai

[3] `http://github.com/jobovy/galpy`

Table 5.4.1: Median values of calculated parameter orbits for the individual Oosterhoff groups. Column 1 lists the studied components, colums 2 and 3 list values for each Oosterhoff group.

	Oo I	Oo II
z_{max} [kpc]	1.136 ± 0.295	1.280 ± 0.363
e	0.855 ± 0.052	0.817 ± 0.078
r_{apo} [kpc]	2.212 ± 0.641	2.416 ± 0.886
r_{peri} [kpc]	0.211 ± 0.122	0.304 ± 0.176

disc (Miyamoto & Nagai 1975), and Navarro-Frenk-White halo potential (Navarro et al. 1997). We also added the `KeplerPotential` for the supermassive black hole in the MW center with a mass $4 \cdot 10^6\, M_\odot$ (Gillessen et al. 2009) to account for close encounters, and the `DehnenBarPotential` for the Galactic bar (Dehnen 2000). For all of the following calculations, we assumed a rotation velocity of 220 km s^{-1} (Kerr & Lynden-Bell 1986; Bovy et al. 2012), a distance to the Galactic center of 8.2 kpc (Bland-Hawthorn & Gerhard 2016), and the same peculiar solar motion as in Sec. 5.3, and we integrated forward in time up to 1 Gyr.

The `galpy` software allows one to calculate parameters of individual orbits, including e.g. eccentricity e, maximum height above or below the Galactic plane z_{max}, and peri- and apocenter of the orbit, r_{peri} and r_{apo}, respectively. For each star, we ran a Monte Carlo simulation. We calculated 200 orbital solutions in which we varied the initial conditions (proper motions, radial velocities, and distances) within their uncertainties assuming that their distribution is Gaussian. From the resulting distribution, we calculated the median orbital parameters for both Oosterhoff groups. The results are listed in Tab. 5.4.1. In order to test the differences between the two Oosterhoff groups we used the CM test (see Section 5.3). For the entire distribution of orbital parameters z_{max}, e, r_{peri}, and r_{apo}, the CM test yields $p_{CM} = 0.68$, there is no statistical evidence that the two distributions are not identical.

Figure 5.4.1 depicts the distribution of apocentric distances for the studied RR Lyrae stars. In this diagram, we see that both Oosterhoff groups have very similar apocentric distance distributions. We also noticed a sudden decrease at ≈ 3 kpc ($\log(r_{apo} \approx 0.5$ kpc), which is roughly in agreement with the overlap between bulge, metal-weak thick disc, and inner halo (3.5 kpc; Ness et al. 2013a). In fact, the majority of the RR Lyrae stars in our sample stay inside the bulge volume during their full orbits.

Based on the negligible difference in the median value of z_{max} between the two Oosterhoff groups, we explored whether the Oo II variables could follow higher orbits from the Galactic plane and thus possibly come from the halo. Based on the distribution of apocentric distances (Fig. 5.4.1), as a nominal boundary for the Galactic bulge we chose $z_{max} > 3$ kpc (roughly above ± 20 deg at the distance of the Galactic bulge) and calculated the number of stars that fulfill this condition in at least 50 % of the iterations of the Monte Carlo simulation. In total, only 34 RR Lyrae stars fulfill the aforementioned condition. Among these 34 variables, 35 % belong to the Oo II population. This is a significant increase in comparison with the overall bulge and halo Oosterhoff population where the fraction of Oo II pulsators is around 25 % (Drake et al. 2013; Sesar et al. 2013; Prudil et al. 2019a). Furthermore, a

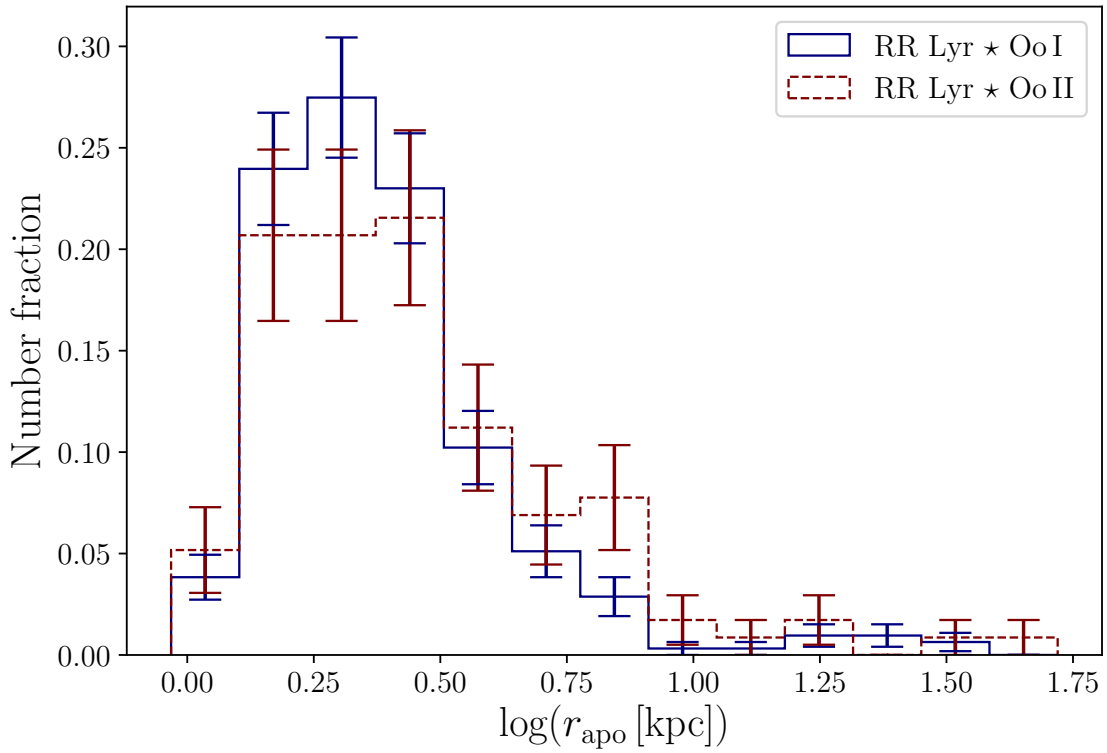

Figure 5.4.1: The distribution of apocentric distances for the studied variables. The blue and red histograms represent the Oo I and Oo II groups, respectively.

similar difference prevails even when we apply the less conservative threshold of $z_{\max} > 2$ kpc resulting in 8 % variables that exit the bulge volume on their orbits as members of the Oo II component. Therefore, if we consider stars with $z_{\max} > 3.0$ kpc as halo interlopers passing through the Galactic bulge, their contribution to the Galactic bulge RR Lyrae population would be $\sim$ 8 %, which is roughly in agreement with the 6 % estimate by Kunder et al. (2015).

To further analyse the stars with $z_{\max} > 3.0$ kpc, we used metallicity estimates for our sample of stars. The spatial distribution of these stars in Galactocentric coordinates with colour-coding according to metallicity is shown in Fig. 5.4.2. Stars with high metallicity (blue lines) are more concentrated around low $z_{\max}$ values, while metal-poor variables (red lines) reach higher $z_{\max}$.

In Fig. 5.4.3 we show the metallicity distribution of probable halo interlopers. We see a strong peak at -1.5 dex for the Oo II group suggesting that these stars probably do not pertain to the Galactic bulge but are currently looping through it, thus contributing to the Oo II population in the bulge. The median metallicity of Oo I stars in our sample exceeding the $z_{\max} \geq 3.0$ kpc is -1.09 dex (in comparison, the median metallicity of the entire Oo I

sample is −1.04 dex), while the median metallicity of Oo II is −1.47 dex, which exceeds the $z_{\max} \geq 3.0$ kpc (in contrast, the median metallicity of the entire Oo II population in our sample is −1.11 dex). Here we see a discrepancy between the metallicities of the two Oosterhoff groups in our sample, and between stars whose orbits exceed 3.0 kpc from the Galactic plane. The metallicity of the Oo I group seems to be nearly the same in both cases, and is consistent with bulge values, but the Oo II population shows a lower median metallicity that is comparable to that seen in halo stars (∼ −1.5 dex, Ivezić et al. 2008; Sesar et al. 2011).

Orbital periods

We estimated the orbital periods of our studied stars in the following way: First, we calculated 200 times the orbital solution for each star forward in time up to 3 Gyr, while varying the input parameters with respect to their uncertainties (assuming they have a normal distribution). We recorded the changes in radial distance R over this time span and used the Lomb-Scargle periodogram (Lomb 1976; Scargle 1982) to calculate the orbital period. The Lomb-Scargle periodograms are used for the analysis of time-series data to search for a potential periodic signal. In the frequency spectrum generated for each orbital solution, we looked for the highest peak and adopted its inverse value as the orbital period $P_{\rm orbit}$.

Fig. 5.4.4 shows the distribution of the resulting orbital periods for both Oosterhoff populations. The two Oosterhoff groups share a similar median orbital period (∼ 36 Myr). The shortest orbital periods are only around 21 Myr. Both distributions appear to be fairly similar on the short orbital period end. We do notice that the fraction of stars in the Oo II group increases toward longer orbital periods. At the long end of the orbital periods (over 100 Myr), 46 % of the RR Lyrae stars belong to the Oo II population, which is a significant increase with respect to their fraction in the entire bulge population (25 %). This is in agreement with the findings in Figs. 5.4.2 and 5.4.3 where the percentage of Oo II stars and fraction of metal-poor variables in general increase with distance from the Galactic center.

Notes on peculiar objects

Several stars from our sample exhibit peculiar orbits on which they pass through the bulge with high space velocities and have a long orbital period. In this subsection, we will look closely at two such examples.

Almost all of the studied stars in the two top panels of Fig. 5.4.2 reach their apocenters at 30 kpc. One exception is OGLE-BLG-RRLYR-07001 (from hereon *07001*), with $z_{\max}$ above 46 kpc which is two times larger than the second-highest distance from the Galactic plane in our sample. This star has a typical value of distance (located in the Galactic bulge at 9.5 kpc), radial velocity, proper motion component μ_δ, and belongs to the Oo I group. On the other hand, the α component of its proper motion, $\mu_{\alpha*} = 9.35 \pm 0.38$ mas yr^{-1}, stands out. Furthermore, its metallicity of [Fe/H] = -1.37 ± 0.19 dex is rather peculiar in comparison with the general metallicity of Oo I stars in the Galactic bulge. The trajectory in the Galactocentric coordinates of this star can be seen in the top and bottom panels of Fig. 5.4.2 as an almost straight line going through $x = 0$ on the horizontal axis (see the black arrows in Fig. 5.4.2). The orbital period of *07001* is above 700 Myr, which puts it in the top 5 highest orbital periods

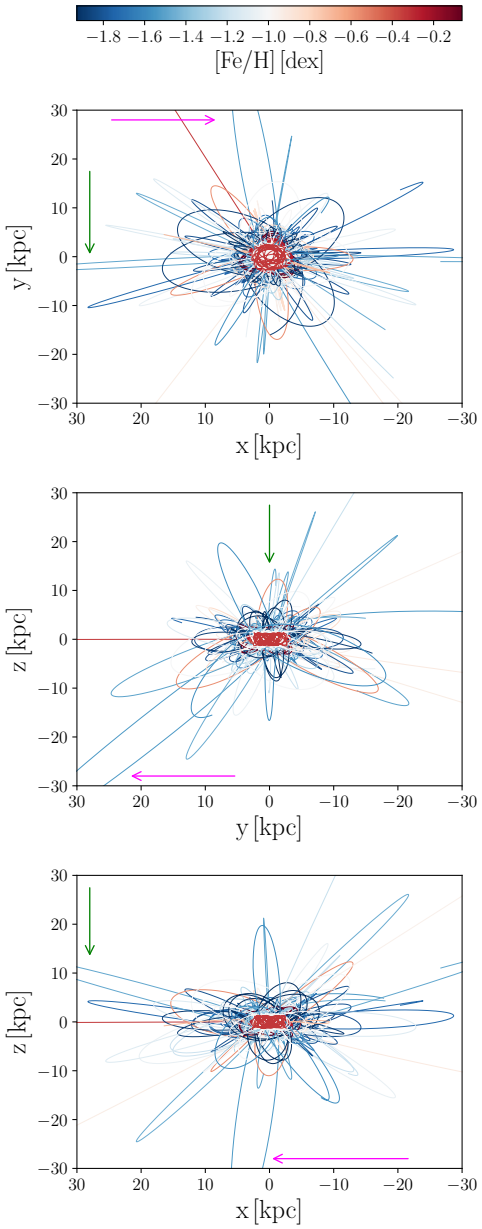

Figure 5.4.2: The Cartesian spatial distributions with outlined orbital movement colour-coded according to the metallicities of individual RR Lyrae stars, integrated over 1 Gyr. The arrows mark the high-velocity stars *07001* (magenta arrow) and *09983* (green arrow), disscussed in Sec. 5.4.2.

in our sample. This RR Lyrae star resides in the Galactic bulge for only a few million years. A closer look at the components of the space velocity shows an ordinary velocity component $U = -46 \pm 10\,\mathrm{km\,s^{-1}}$, but the V and W components stand out and amount to $278 \pm 15\,\mathrm{km\,s^{-1}}$

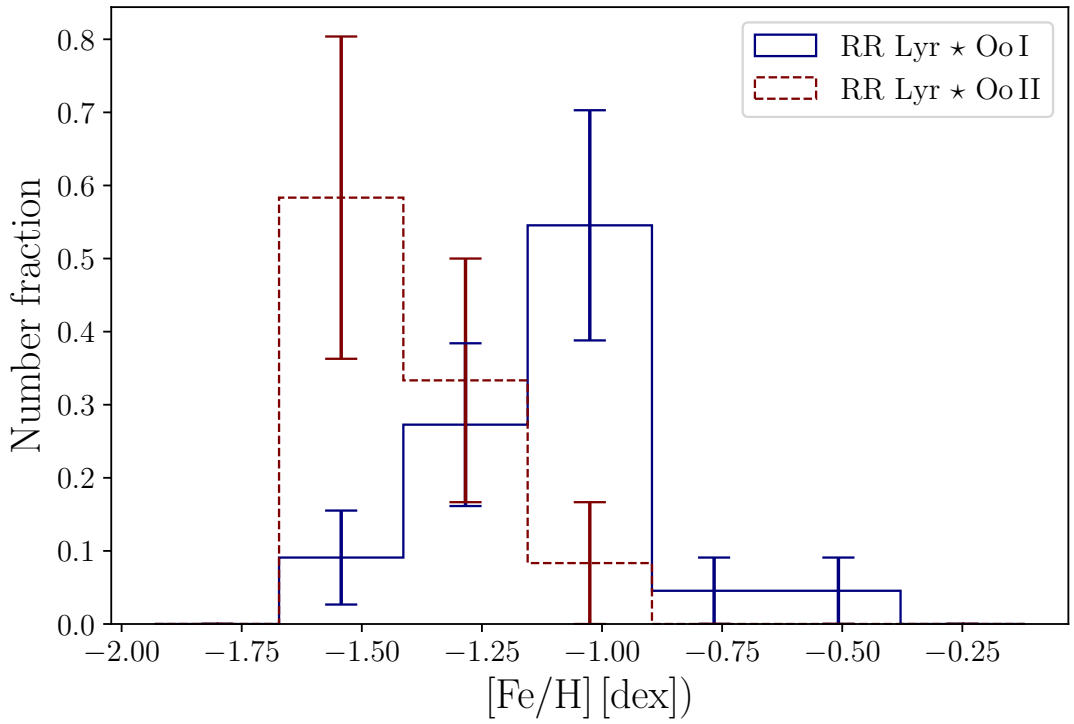

Figure 5.4.3: The metallicity distribution for variables with $z_{\max} > 3.0$ kpc. The blue and red histograms represent the Oo I and Oo II groups, respectively.

and $-458 \pm 18\,\mathrm{km\,s^{-1}}$, respectively. The true space velocity of *07001* is the second highest among the studied stars, with $sv = 538 \pm 18\,\mathrm{km\,s^{-1}}$.

Another interesting object is OGLE-BLG-RRLYR-09983 (from hereon *09983*). With $sv = 542 \pm 10\,\mathrm{km\,s^{-1}}$ it has the highest space velocity, and one of the longest orbital periods, $P_{\mathrm{orbit}} \approx 0.6$ Gyr. The astrometric properties of this star do not stand out as clearly when compared with the whole sample, but its radial velocity ($-508\,\mathrm{km\,s^{-1}}$) is the highest within our sample. Such a high radial velocity transforms into the space velocity component U as $486 \pm 10\,\mathrm{km\,s^{-1}}$, which makes it the fastest in this component. Unlike *07001*, *09983* belongs to the Oo II group, having one of the longest pulsation periods (> 0.81 day), and a low metallicity, [Fe/H]$= -1.34 \pm 0.27$ dex. In addition, its orbit is different from that of *07001* with respect to the Galactic plane. Star *09983* does not deviate from the plane by more than 15 kpc, but its apocenter lies more than 40 kpc from the Galactic center. Therefore, it crosses the inner bulge and then for most of its orbit stays fairly close to the Galactic disc in comparison with *07001* with a small excursion in the Galactic inner halo.

For a comparison, the high-velocity RR Lyrae variable, OGLE-BLG-RRLYR-10353, stud-

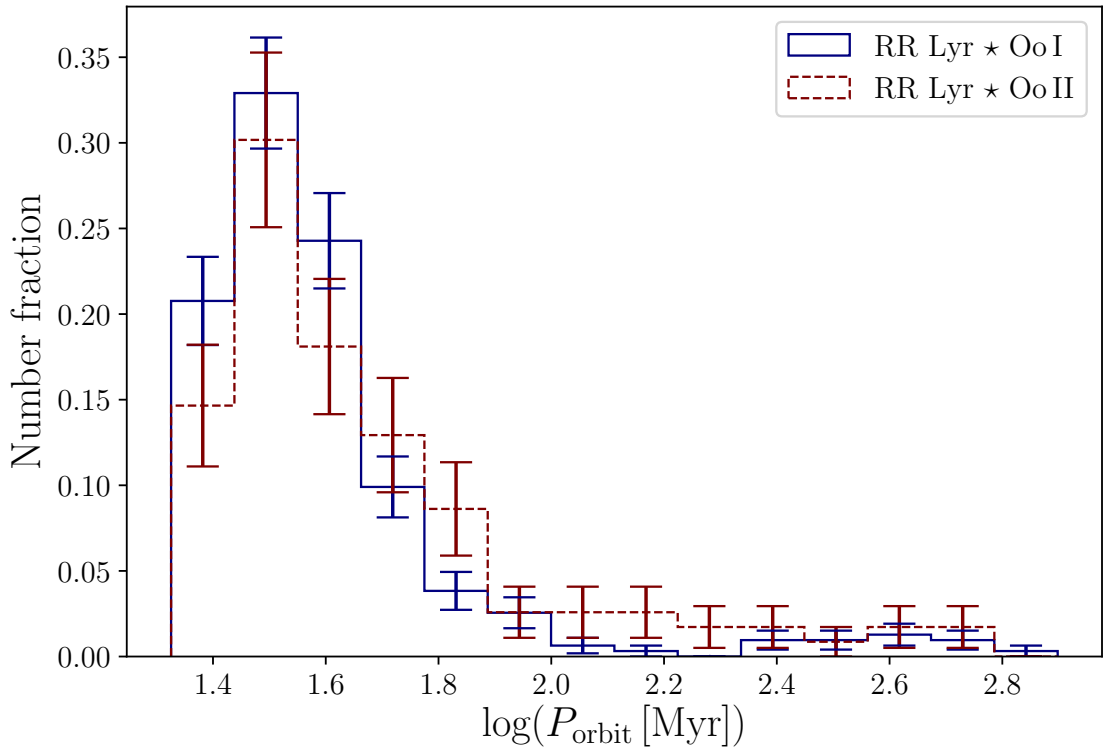

Figure 5.4.4: The orbital period distribution for the studied variables. The blue and red histograms represent the Oo I and Oo II groups, respectively.

ied by Kunder et al. (2015) and Hansen et al. (2016), has $sv = -482 \pm 22\,\mathrm{km\,s^{-1}}$, with a somewhat low metallicity (-1.32±0.19 dex from its I-band light curve[4] and -0.9±0.2 dex from spectroscopy; Hansen et al. 2016). It is necessary to emphasize that this star has been marked as modulated (Prudil & Skarka 2017) and thus might not be suitable for metallicity determination from the photometric data. We note that the escape velocity at the radius of the Galactic bulge is over $600\,\mathrm{km\,s^{-1}}$, thus *07001* and *09983* are still be confined to the MW, but based on the orbital integration they spend the majority of their orbit in halo/disc.

Summary and Conclusions

In this paper, we used RR Lyrae stars with distances from Prudil et al. (2019a), together with kinematical information from the *Gaia* DR2 (Gaia Collaboration et al. 2018a) and radial velocities from Kunder et al. (2016) to study possible differences in their kinematical properties per Oosterhoff group in the Galactic bulge. For the 429 variables in our sample,

[4]Using the same procedure as described in Prudil et al. (2019a).

we calculated 6D kinematical solution and predicted their Galactic orbits (Bovy 2015).

The RR Lyrae stars appear to be part of the kinematically hot component of the Galactic bulge based on their tangential velocities, similar to the Galactic bulge Type II Cepheids (Braga et al. 2018). The orbits of the majority of the studied RR Lyrae stars are fully confined to the bulge volume, with only 8 % of the sample (34 stars) have their apocenters more than 3 kpc from the Galactic Center. This is in agreement with the 6 % estimate by Kunder et al. (2015). Based on the orbital parameters both Oosterhoff groups seem fairly similar, with the exception of $z_{\rm max}$, where we see an increase in the Oo II population as we move away from the Galactic plane. There more than one-third belong the Oo II population, which is in contrast with 25 % ratio found by Prudil et al. (2019a) for the Galactic bulge.

We identified six high-velocity RR Lyrae stars that have higher space velocity than RR Lyrae variable studied by Kunder et al. (2015) and Hansen et al. (2016). Neither of their space velocities exceeds the escape velocity at the radius of the Galactic bulge. Nevertheless, they can serve as targers for future spectroscopic studies as probes of the Galactic bulge and halo.

In summary, the kinematics of bulge RR Lyrae stars belonging to different Oosterhoff groups is fairly similar. A small part of our sample probably consists of halo interlopers, also from a chemical perspective. Based on the kinematics and orbital solutions for our stars, the vast majority do not seem to contribute to the boxy/peanut component consisting of the bulge's intermediate-age population (McWilliam & Zoccali 2010; Wegg & Gerhard 2013); but rather they seem to be part of a primordial component of the Galactic bulge, confirming the previous findings by Dékány et al. (2013); Kunder et al. (2016).

CHAPTER 6

EVIDENCE FOR GALACTIC DISC RR LYRAE STARS IN THE SOLAR NEIGHBOURHOOD

"What happened to Buzzsaw?"
"He had to split."

— Ben Richards, helicopter pilot

Abstract: We present a kinematical study of 314 RR Lyrae stars in the solar neighbourhood using the publicly available photometric, spectroscopic, and *Gaia* DR2 astrometric data to explore their distribution in the Milky Way. We report an overdensity of 22 RR Lyrae stars in the solar neighbourhood at a pericenter distance of between 5–9 kpc from the Galactic center. Their orbital parameters and their chemistry indicate that these 22 variables share the kinematics and the [Fe/H] values of the Galactic disc, with an average metallicity and tangential velocity of [Fe/H] $= -0.60$ dex and $v_\theta = 241$ km s^{-1}, respectively. From the distribution of the Galactocentric spherical velocity components, we find that these 22 disc-like RR Lyrae variables are not consistent with the *Gaia* Sausage (*Gaia*-Enceladus), unlike almost half of the local RR Lyrae stars. Chemical information from the literature shows that the majority of the selected pericenter peak RR Lyrae variables are α-poor, a property shared by typically much younger stars in the thin disc. Using the available photometry we rule out a possible misclassification with the known classical and anomalous Cepheids. The similar kinematic, chemical, and pulsation properties of these disc RR Lyrae stars suggest they share a common origin. In contrast, we find the RR Lyrae stars associated with the *Gaia*-Enceladus based on their kinematics and chemical composition show a considerable metallicity spread in the old population (~ 1 dex).

This chapter is based on our published paper : **Prudil, Z.**, Dékány, I., Grebel, E. K., Catelan, M., Skarka, M., Smolec, R.: On the Oosterhoff dichotomy in the Galactic bulge: II. kinematical distribution, 2019, MNRAS, 487, 3270

Context

Understanding the formation and evolution of spiral galaxies, the most common type of massive galaxies, is one of the main tasks of Galactic astrophysics. The Milky Way (MW) is a very useful laboratory for studies of the chemical and dynamical history of spiral galaxies, thanks to our ability to resolve individual stars. With the rise of large-scale photometric, spectroscopic, and astrometric surveys, we are now able to probe individual MW components (Galactic halo, disc, and bulge) to great depths and in enhanced detail.

Gilmore & Reid (1983) found that the stellar number density distribution cannot be modeled by a single density profile as we move above or below the Galactic plane, but two density components are needed – called the *thin* and the *thick* disc. The bimodality of the disc is also visible in the chemical distribution of [α/Fe] vs. [Fe/H], where we can identify different stellar populations based on their chemical composition (e.g., Fuhrmann 1998; Bensby et al. 2003; Haywood 2008). This bimodality suggests a separation of the disc into a thin (α-poor) and a thick (α-rich) component. Moreover, the thin disc can be divided into an *inner* and *outer* thin disc, both with different metallicities, (e.g., Haywood et al. 2013; Hayden et al. 2015; Bland-Hawthorn et al. 2019). In addition, the inner disc (between the Sun and the Galactic center) is composed of the thick disc and metal-rich thin disc, while the outer disc consists of only the metal-poor thin disc (e.g., Bensby et al. 2013; Anders et al. 2014; Haywood et al. 2015).

One of the modern formation scenarios suggests that the thick disc formed first from a turbulent, well-mixed gas disc and that its youngest part supposedly defined the conditions for subsequent build-up of the inner thin disc (e.g., Haywood et al. 2013; Hayden et al. 2015; Bland-Hawthorn et al. 2019). On the other hand, the outer thin disc might have formed independently of the thick disc with a time scale similar to the thin disc. The Galactic disc formation timelines range from 8 – 13 Gyr for the thick disc and up to 8 Gyr[1] for the thin disc, which implies two prominent periods of star formation with the older one being associated with the thick disc (e.g., Oswalt et al. 1996; Haywood et al. 2013; Kilic et al. 2017; Gallart et al. 2019).

Many kinematical and chemical studies have been conducted over the years to study the structure of the Galactic thin and thick disc, especially using F and G dwarfs (e.g., Bensby et al. 2003; Nordström et al. 2004; Bensby et al. 2014) in addition to public surveys (Lee et al. 2011; Hayden et al. 2015; Guiglion et al. 2015; Bland-Hawthorn et al. 2019). Furthermore, some of these studies tried to separate both MW components based on their kinematical properties, although the thin and thick disc have overlapping kinematical distributions, which hampers such efforts. On the other hand, the two MW components have different velocity dispersions, the thick disc exhibiting a higher velocity dispersion in all three velocity

[1] With a few stars reaching up to 10 Gyr, see fig. 16 in Haywood et al. (2013).

components, e.g., Casagrande et al. (2011) and Haywood et al. (2013). Moreover, the thick disc population seems to lag behind the thin disc stars (e.g., Lee et al. 2011).

In this study we focus on RR Lyrae stars, which are old (age > 10 Gyr, e.g., Glatt et al. 2008; VandenBerg et al. 2013) helium-burning, pulsating horizontal branch variables. They can be divided into three types based on the pulsation mode: RRab – fundamental mode, RRc – first overtone, and RRd - double mode (fundamental and first overtone) pulsators. The RR Lyrae pulsators are often used as tracers of the properties of the old population of the Galactic halo and bulge (e.g., Dékány et al. 2013; Belokurov et al. 2018a; Prudil et al. 2019a), or nearby galaxies (e.g., Haschke et al. 2012a,b; Jacyszyn-Dobrzeniecka et al. 2017). In general, these variables are not used as probes of the Galactic disc, although they have been used successfully to put constraints on the structure of the thick disc and the mechanisms that contributed to its formation (Kinemuchi et al. 2006; Kinman et al. 2009; Mateu et al. 2012; Mateu & Vivas 2018; Dékány et al. 2018). Kinematic studies using RR Lyrae stars in the solar neighbourhood (e.g., Layden et al. 1996; Maintz & de Boer 2005; Marsakov et al. 2018) and in the Galactic bulge (Kunder et al. 2016, 2019; Prudil et al. 2019c), suggest that a small fraction of nearby RR Lyrae variables might be associated with the Galactic disc and the old spheroidal component of the Galactic bulge whereas most of them belong to the halo. Mainly the work by Layden et al. (1996) and Marsakov et al. (2018, 2019a) link some of the local RR Lyrae stars to the Galactic disc based on their kinematical and chemical properties.

In this paper, we study the kinematic distribution of fundamental mode RR Lyrae stars in the solar neighbourhood based on radial velocities and astrometric parameters (proper motions and parallaxes) from the *Gaia* space telescope (Gaia Collaboration et al. 2016a, 2018a; Lindegren et al. 2018). We report the discovery of a kinematical feature associated with the disc, which is especially apparent in the pericenter distribution of the local RR Lyrae stars. In Section 6.2 we describe the features of the collected sample. Section 6.3 discusses calculated orbital properties for individual objects, which show an apparent peak at a pericenter distance of ~7 kpc. In Section 6.4, we explore the possibility that the RR Lyrae stars in the pericenter peak originate in the Galactic disc. Section 6.6 summarises our results.

Data

We collected a sample of fundamental-mode RR Lyrae stars from various sources with spectroscopically determined metallicities, radial velocities, photometry in optical and infrared passbands, and precise astrometric solutions. We utilized data from the following sources applying several selection criteria:

- The metallicities – [Fe/H] (on the Zinn & West 1984, scale) radial velocities, and mean infrared $W1$ and K_s-band magnitudes (with their errors) of fundamental mode RR Lyrae stars were obtained from the catalogue assembled by Dambis et al. (2013). The spectroscopic properties of this catalogue come mostly from Layden (1994) (for more references see Dambis et al. 2013). The infrared photometric properties in the Dambis et al. (2013) catalogue were acquired by the *Wide-field Infrared Survey Explorer* (*WISE*, Wright et al. 2010; Cutri & et al. 2012) and *Two-Micron Sky Survey* (2MASS, Cutri et al. 2003; Skrutskie et al. 2006). From this sample, 7 stars were removed be-

cause their mean magnitudes in one of the photometric bands were unknown, which resulted in 362 variables for the following crossmatch.

- In the next step we crossmatched the sample with the *Gaia* DR2 catalogue (Gaia Collaboration et al. 2018a; Lindegren et al. 2018), in order to obtain proper motions ($\mu_{\alpha*}$ and μ_δ) and parallaxes (ϖ). The *Gaia* data release 2 (DR2) catalogue contains information about the uncertainties σ and the correlations ρ between the astrometric parameters. In addition, it includes several statistical parameters that indicate the quality of the astrometric solution, e.g. the re-normalized unit weight error (RUWE), which we used to robustly select stars with reliable proper motions. First, we constructed the covariance matrix Σ for proper motions in right ascension $\mu_{\alpha*}$ and declination μ_δ, which we then scaled by the RUWE factor:

$$\Sigma = \begin{pmatrix} \sigma^2_{\mu_{\alpha*}} & \rho_{\mu_{\alpha*}\mu_\delta}\sigma_{\mu_{\alpha*}}\sigma_{\mu_\delta} \\ \rho_{\mu_{\alpha*}\mu_\delta}\sigma_{\mu_{\alpha*}}\sigma_{\mu_\delta} & \sigma^2_{\mu_\delta} \end{pmatrix} \cdot \mathrm{RUWE}^2 \tag{6.1}$$

In order to introduce a sensible cut on the proper motions based on their errors we needed to diagonalize the covariance matrix by determining its eigenvectors and composing them in the nonsingular matrix $\boldsymbol{S}$:

$$\boldsymbol{D} = \boldsymbol{S}^{-1} \cdot \Sigma \cdot \boldsymbol{S}, \tag{6.2}$$

where the diagonal matrix $\boldsymbol{D}$ contains the eigenvalues of Σ. Using the matrix $\boldsymbol{S}$ we transformed the vector $\boldsymbol{v} = (\mu_{\alpha*}, \mu_\delta)$ containing the stars' proper motions:

$$\boldsymbol{V} = (\boldsymbol{S}^{-1} \cdot \boldsymbol{v})^2. \tag{6.3}$$

Then for the diagonalized covariance matrix $\boldsymbol{D}$ and the transformed proper motion vector $\boldsymbol{V}$ we demanded at least 5σ significance of the transformed proper motions:

$$\sqrt{\sum_{k=1}^{2} \boldsymbol{V} / \mathrm{diag}(\boldsymbol{D})} > 5. \tag{6.4}$$

In addition to the proper motion criterion, we also require the same significance for the *Gaia* DR2 parallaxes

$$\varpi / \sigma_\varpi > 5. \tag{6.5}$$

Applying these criteria, we removed over 39 stars from our sample. According to Lindegren et al. (2018) the *Gaia* DR2 parallaxes are offset from the parallaxes of quasars by -0.029 mas, so we applied this offset to our sample of RR Lyrae stars. Once the DR2 parallax offset is properly corrected for, the use of Gaia DR2 parallaxes to establish the distances of the local RRLs appears to be effective (Muraveva et al. 2018).

- The photometric light curves in the V-band were collected from the All-Sky Automated Survey for Supernovae (ASAS-SN, Shappee et al. 2014; Kochanek et al. 2017; Jayasinghe et al. 2018).

In addition to the aforementioned criteria, we removed the stars BI Tel, VX Ind, V363 Cas, V338 Pup, and SS Gru due to their uncertain classification as RR Lyrae stars (see The International Variable Star Index, VSX, about these objects[2], Watson et al. 2006). Moreover, Y Oct, VY Lib, and MS Ara were removed due to either insufficient data in ASAS-SN or due to their classification as double-mode RR Lyrae pulsators.

The mean V-band magnitude of an RR Lyrae star was computed as the intercept of a truncated Fourier series fitted to the ASAS-SN photometric data with the following form:

$$m(t) = A_0^V + \sum_{k=1}^{n} A_k^V \cdot \cos\left(2\pi k\vartheta + \varphi_k^V\right), \tag{6.6}$$

where A_k^I represents the amplitudes, n stands for the degree of the Fourier series, and φ_k^V stands for the phases. The variable ϑ describes the phase function, which is defined as $(HJD - M_0)/P$, where the HJD represents the time of observation in the Heliocentric Julian Date, and M_0 and P are the ephemerids, i.e. the time of maximum brightness and the pulsation period. Using the ASAS-SN photometry we also estimated pulsation periods for all studied variables using the Lomb-Scargle periodogram (Lomb 1976). For the errors on the mean V-band magnitudes we assumed average photometric errors for the individual variables of ≈ 0.046 mag.

We also computed amplitude ratios and generalized phase differences (R_{21}, φ_{21}, R_{31}, φ_{31}) from the Fourier decompositions:

$$R_{i1} = \frac{A_i}{A_1} \varphi_{i1} = \varphi_i - i\varphi_1 \tag{6.7}$$

The amplitude ratios R_{21} and R_{31} reflect the light curve deviation from a sinusoidal shape. With higher values of R_{21} and R_{31} the light curve is more skewed and asymmetric. The phase differences φ_{21} and φ_{31} mirror the width of the light curve. With decreasing phase differences the light curves become more acute (narrow) at the half maximum light (Simon 1988). The Fourier parameters are useful for the classification of variable stars and for separating them into subclasses. Using the classification from ASAS-SN and our analysis we removed stars that could not be classified as fundamental mode RR Lyrae stars (for more details see Sec. 6.5 where we discuss the photometric properties of the studied RR Lyrae variables).

For each individual star in our sample we determined the extinction in the $W1$, K_s, and V band using the reddening maps from Schlafly & Finkbeiner (2011) with the relations $A_{W1} = 0.065 \cdot A_V$ (Madore et al. 2013), and $A_K = 0.114 \cdot A_V$ (Cardelli et al. 1989). This allowed us to estimate the absolute magnitudes of our stars and to calculate the dereddened mean observed magnitudes in the aformentioned passbands, using *Gaia* parallaxes (incorporated in the Monte Carlo error analysis, see Sec. 6.3).

We emphasize that throughout this paper we do not use any period-metallicity-luminosity relations to estimate distances for our studied stars. We base our findings on the distance deduced from *Gaia* parallaxes.

In the end, we had a final sample of 314 RR Lyrae stars with full kinematic, spatial, and

[2] https://www.aavso.org/vsx/index.php

metallicity information, which form the basis of our study. In Fig. 6.2.1 we depict the spatial distribution of the whole RR Lyrae sample in Galactic coordinates. In Fig. 6.2.1 we see that our sample covers the majority of the sky, with the exception of the Galactic bulge and some parts of the Galactic disc. The heliocentric distances of our RR Lyrae stars range from 0.5 kpc up to 7 kpc (with over 90 % residing at distances < 3.5 kpc). The stars cover a broad range in metallicities of $-2.84 <$ [Fe/H] < 0.07 dex. In apparent magnitude space, almost 97 % of the RR Lyrae variables in our sample are brighter than 14 mag in the V passband. For comparison, the ASAS-SN survey contains 2778 fundamental mode RR Lyrae stars brighter than 14 mag covering a similar coordinate space as in our dataset. Therefore, based on the ASAS-SN catalogue, our sample contains approximately 10 % of the local RR Lyrae stars. We emphasize that our sample includes an obvious selection effect, namely the lack of stars toward very low Galactic latitudes, due to the strongly reduced completeness of the ASAS-SN catalogue toward these highly attenuated regions. However, we would expect to find more RR Lyrae stars with thin disc kinematics if our sample was complete toward the Galactic plane. Toward other sight-lines, our selection function does not have any significant non-uniformity.

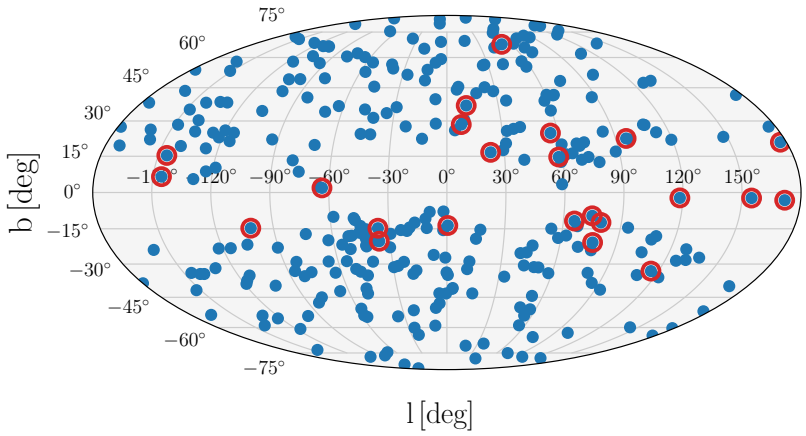

Figure 6.2.1: The spatial distribution of the studied stars (blue points) in the Galactic coordinates. The red circles encompasing some of the sample RR Lyrae stars will be explained in the following Section 6.3.

Orbits

We used the `galpy`[3] library (Bovy 2015) to study the kinematics of our sample. For the calculation of the orbital parameters we used the `MWPotential2014` provided in `galpy` as an axisymmetric Galactic potential for the MW. The `MWPotential2014` is composed of three

[3]Available at `http://github.com/jobovy/galpy`

potentials for the Galactic bulge (implemented as a power-law density profile for spherical bulges with an exponential cut-off), a Navarro-Frenk-White halo potential (Navarro et al. 1997), and a Miyamoto-Nagai disc (Miyamoto & Nagai 1975). For the Sun's position in the MW we assumed a distance to the Galactic center of $R_0 = 8.178$ kpc (Gravity Collaboration et al. 2019) and a height above the Galactic plane of $z_\odot = 25$ pc (Jurić et al. 2008). In order to correct for solar motion, we used the Sun's velocity with respect to the local standard of rest $(U_\odot, V_\odot, W_\odot) = (-11.1, 12.24, 7.25)$ km s^{-1} (Schönrich et al. 2010) and the velocity of the local standard of rest (LSR) $v_{LSR} = 235$ km s^{-1} based on R_0 (Gravity Collaboration et al. 2019) R_0, the proper motion of Sgr A* (Reid & Brunthaler 2004), and $V_\odot$.

For each star, we integrated over a 1 Gyr timespan and calculated its orbital parameters: maximum height from the Galactic plane $z_{\max}$, eccentricity e, and peri- and apocenters of its orbit, $r_{\rm per}$ and $r_{\rm apo}$, respectively (a 100 Myr, 300 Myr or 500 Myr timespan does not affect the orbital parameters significantly). Using `galpy`, we calculated the full 6D solution (spatial and kinematical) for the studied sample. With the `MWPotential2014` we also calculated the Hamiltonian action integrals of motion in an axisymmetric potential $\boldsymbol{J} = (J_R, J_\phi, J_z)$, where J_R represents the oscillation in the radial direction, J_ϕ is the azimuthal action (angular momentum in z-direction L_z), and J_z describes the vertical oscillation.

A Monte Carlo error analysis was performed for the complete calculation taking into account the covariance matrix of the *Gaia* astrometric solution, errors in radial velocities, reddening, and mean magnitudes. The resulting values and their errors were taken as the median, first, and third quartile from the generated distributions, in addition, we also obtained correlations between orbital parameters and velocities.

In the top panel of Fig. 6.3.1 we show a histogram for the distribution of the pericentric distances in our sample. In this distribution, we noticed a small peak approximately at $r_{\rm per} = 7$ kpc (marked with an arrow). To verify its existence we generated 1000 random realizations of the pericentric distribution for the studied stars using their median values and quantiles. For each generated distribution we calculated the `Gaussian mixture model` probability distribution implemented in the `scikit-learn` library (Pedregosa et al. 2011). Using the Bayesian information criterion (BIC) and the Akaike information criterion (AIC), we estimated a suitable number of Gaussian components for each distribution. For the BIC, in nearly all cases (above 90 %) the suggested number of Gaussians was 3, while for the AIC, three components were suitable in more than 42 % of the cases. In all of the pericentric variations, the peak is present in the histogram and is modeled by the Gaussian mixture model. The generated distributions were used to estimate the errors of the pericentric distribution. Using the calculated errors, the probability density of the pericentric peak (0.0813 ± 0.0065) has a 3σ significance in comparison with the neighboring valley (0.0460 ± 0.0092, marked with black arrows in Fig. 6.3.1).

It is worth noting that this overdensity in pericenter distance is also present when using the older pericenter values calculated by Maintz & de Boer (2005), but was not specifically pointed out in their or any previous studies of the local RR Lyrae stars. We also observe a peak around 3 kpc, which is modeled by one of the Gaussian components. We tentatively associate this peak with RR Lyrae stars in the Galactic thick disc.

For comparison with our sample, we calculated the orbital solution for the stars observed

in the Radial Velocity Experiment (RAVE) data release 5 (Kunder et al. 2017). RAVE is a spectroscopic multi-fiber survey of Milky Way stars in the $9 < I < 12$ magnitude range (Steinmetz et al. 2006). Because of its magnitude range, RAVE observed mainly the thick and thin disc stars (see fig. 19 in Kordopatis et al. 2013). We crossmatched the RAVE sample with *Gaia* DR2, requiring at least 5σ significance for proper motions and parallaxes. The distribution of pericentric distances in the RAVE sample is shown in the top panel of Fig. 6.3.1 in grey colour. From these two distributions, we see that RR Lyrae stars at $r_{\rm per} \approx 7\,$kpc fall into the region where the majority of the RAVE disc sample lies.

This small overdensity is visible also in other orbital parameters, e.g., in e and $z_{\rm max}$ (see the bottom panel of Fig. 6.3.1), where the majority of stars with $r_{\rm per} \approx 7\,$kpc clump at low values of eccentricity ($e < 0.4$) with rather small excursions above the Galactic plane ($z_{\rm max} < 2\,$kpc) is located. The low values of e together with marginal $z_{\rm max}$ suggest rather circular orbits confined to the Galactic disc. Including another dimension in the form of metallicity in the bottom panel of Fig. 6.3.1 reveals that the majority of the most metal-rich RR Lyrae stars from our sample show low eccentricities and $z_{\rm max}$ around the pericentric distance of this peak. We note that RR Lyrae stars with pericentric distances between 5-9 kpc and eccentricity above 0.5 contribute partially to the pericenter peak shown above, however, the peak is still significant after their removal.

To further isolate RR Lyrae stars sharing the same kinematics and possibly contributing to the pericenter peak, we used two criteria:

$$\begin{aligned} e &< 0.2 \\ z_{\rm max} &< 0.9\,{\rm kpc}. \end{aligned} \tag{6.8}$$

The additional condition on eccentricity e narrows the sample to circular orbits common for stars in the Galactic disc (Hayden et al. 2019)[4]. The criterion on the excursion from the Galactic plane $z_{\rm max}$ is consistent with the MW thick disc scale height $H \approx 0.9\,$kpc (Jurić et al. 2008; Bland-Hawthorn & Gerhard 2016). We did not employ any criteria for pericentric and apocentric distances. These two conditions yield 22 possible disc-like RR Lyrae stars, which are denoted by red circles in the Fig. 6.2.1. We note that almost 90 % of the stars in the RAVE sample fulfill these conditions as well.

The full orbital solution using `MWPotential2014` is examined in Fig. 6.3.2, where we show the distribution of orbits of the whole sample (blue solid lines) in rectangular Galactocentric coordinates. RR Lyrae variables fulfilling Eq. 6.8 (red dotted lines) are concentrated at small heights above the plane with almost circular orbits. This implies their association with the Galactic disc, which will be examined in the following chapters. We emphasize that throughout the paper, we refer to these 22 RR Lyrae stars as disc stars, as their association with either the thin or thick disc is not clear when based on orbital parameters alone. In Section 6.4, their association with these disc components is explored. The conditions in Eq. 6.8 lead to a sample of disc-like RR Lyrae stars with almost identical orbits (see Fig. 6.3.2). With

[4] More than 70 % of stars from their sample in the solar neighbourhood ($d < 500\,$pc) have an eccentricity $e < 0.2$.

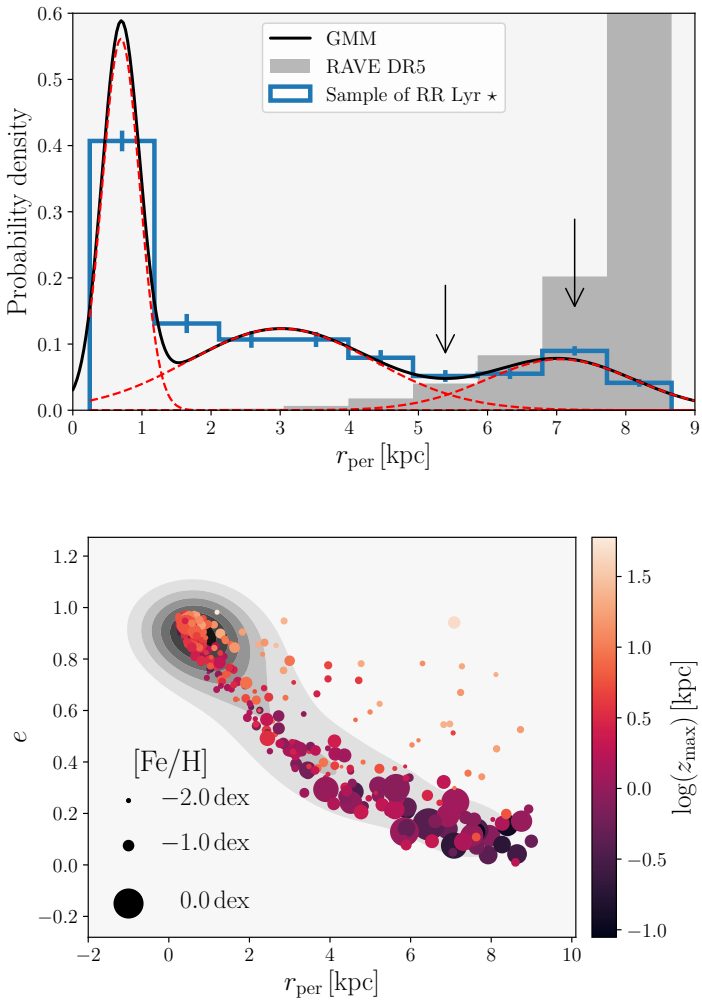

Figure 6.3.1: Distribution of pericentric distances $r_{\rm per}$ (top panel) and eccentricity e vs. $r_{\rm per}$ dependence (bottom panel) for our sample. In the top panel, the black solid line depicts the `Gaussian mixture model` with individual components denoted by red dashed lines. The grey distribution represents stars from the RAVE survey, while the blue columns stand for our sample of RR Lyrae variables. The black arrow points toward the pericentric peak of the local RR Lyrae stars. The error bars on individual columns were calculated from the Monte Carlo simulation with a fixed bin size. The bottom panel shows e vs. $r_{\rm per}$ with a colour-coding based on $z_{\rm max}$. The sizes of each point indicate the metallicity of individual RR Lyrae stars. The grey background shading represents the kernel density estimates (KDE) of the overlay points.

regard to the apocentric distances $r_{\rm apo}$, the selected disc RR Lyrae stars vary between $\approx$ 7.9 – 11.5 kpc, which is expected due to our condition on the eccentricity of the orbits, where

eccentricity is connected with r_{apo} through following relation:

$$e = \frac{r_{\mathrm{apo}} - r_{\mathrm{per}}}{r_{\mathrm{apo}} + r_{\mathrm{per}}}. \tag{6.9}$$

The 22 RR Lyrae stars selected based on Eq. 6.8 will be examined for their possible disc association in the following Section.

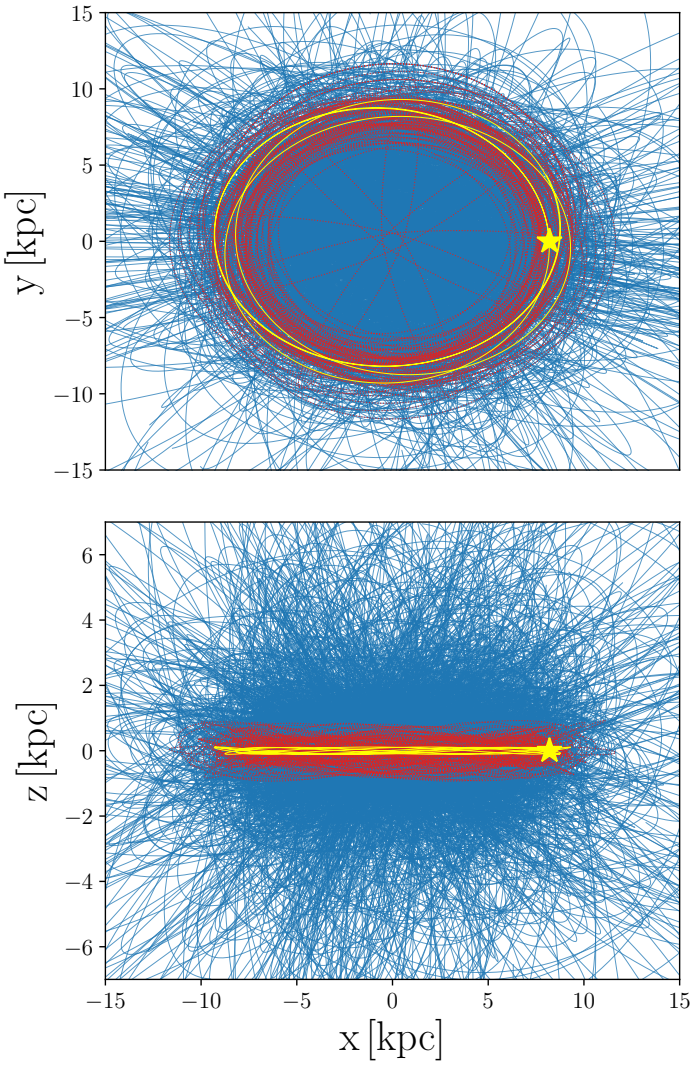

Figure 6.3.2: The spatial distrbution of the studied stars in Cartesian rectangular Galactocentric coordinates, with the top panel depicting the y vs. x and the bottom panel showing the z vs. x distributions, respectively. The blue lines stand for orbits of the sample stars, while the red dotted lines represent RR Lyrae stars based on the conditions in Eq. 6.8. The yellow stars and lines mark the position and orbit of the Sun, respectively.

RR Lyrae stars in the Galactic disc

The idea that some of the RR Lyrae stars in the solar neighbourhood originated in the Galactic disc is not new. Layden et al. (1996) suggested that some field RR Lyrae stars belong to the Galactic thick disc, as did Marsakov et al. (2018). Layden et al. (1996) suggested several approaches to separate disc and halo RR Lyrae stars based on their kinematics (see below) and metallicities, suggesting that disc and halo separate at [Fe/H]$= -1$ dex for RR Lyrae stars. Here the chemodynamics of the pericenter peak RR Lyrae are explored.

Kinematic tests

Although we are using almost the identical sample as used by Layden et al. (1996), *Gaia* DR2 affords a more precise astrometric solution, and thus better constrained orbits for individual stars. In Fig. 6.4.1 we show the tangential velocity v_θ vs. metallicity [Fe/H] distribution, where v_θ represents the Galactocentric cylindrical velocity, positive in the direction of the Galactic rotation. Using definition 1 in table 3 from Layden et al. (1996) (black solid line in Fig. 6.4.1), we separated our star sample into disc and halo RR Lyrae variables. We see that the stars in the pericenter peak (Eq. 6.8) all fall in the *disc* region in v_θ vs. [Fe/H] space. We note that other stars identified by Layden et al. as the Galactic disc RR Lyrae variables show resemblence to the stars identified using the criteria in Eq. 6.8, but they fail our criteria mainly on the basis of $r_{\rm per}$ and e, where approximately half of the stars have $e > 0.2$.

We note that $\approx 39\,\%$ of the studied variables have retrograde rotation ($v_\theta < 0\,{\rm km\,s^{-1}}$) and nearly all stars on retrograde orbits have metallicities of [Fe/H]< -1 dex. We can crudely distinguish RR Lyrae stars formed in-situ from accreted stars based on their prograde/retrograde motion in the Galaxy. In our RR Lyrae dataset, retrogradely moving variables exhibit on average higher values for $r_{\rm apo}$, e, and $z_{\rm max}$ in comparison with the rest of the variables (see Fig. 6.4.2). This is probably due to the presence of disc RR Lyrae stars in the prograde part of our sample. Together with their on average lower $r_{\rm per}$ (with respect to the remaining pulsators) this supports their possible extragalactic origin (Villalobos & Helmi 2009; Qu et al. 2011).

Velocity components

The pericenter peak RR Lyrae variables are also distinguishable in the distribution of their velocity components (see Fig. 6.4.3). Here disc stars (roughly marked with a blue ellipse) would reside in the top part of the v_θ vs. $v_{\rm R}$ distribution. The average values and dispersion for the depicted disc RR Lyrae stars in Fig. 6.4.3 are $v_{\rm R} = 4 \pm 30\,{\rm kms^{-1}}$ and $v_\theta = 241 \pm 14\,{\rm kms^{-1}}$. From Fig. 6.4.3 we also see that the transversal velocity $v_{\rm z}$ for disc stars varies around $0\,{\rm km\,s^{-1}}$, which is expected based on our cut in the $z_{\rm max}$.

The *Gaia*-Enceladus or *Gaia* Sausage (Belokurov et al. 2018b; Helmi et al. 2018; Gallart et al. 2019), is clearly seen among the local RR Lyrae stars. This remnant of a massive merger of a Small Magellanic Cloud-like galaxy in the local stellar halo contains rather metal-poor RR Lyrae stars ([Fe/H]> -1.5 dex) with a highly non-Gaussian velocity ellip-

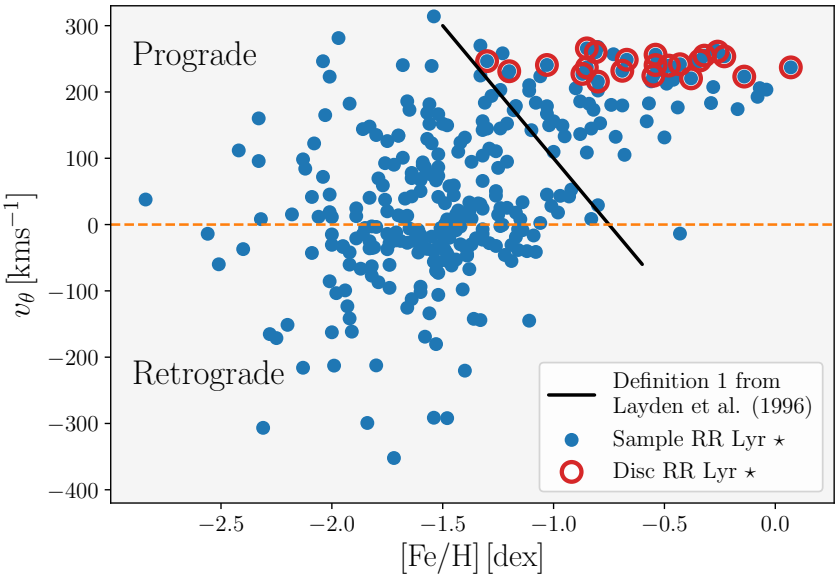

Figure 6.4.1: The tangential velocity v_θ vs. metallicity [Fe/H] for the studied variables (blue points). The variables associated with the pericenter peak (based on our criteria in Eq. 6.8) are highlighted with red circles. The black solid line represents definition 1: $v_\theta = -400 \cdot [\mathrm{Fe/H}] - 300$ listed in table 3 of Layden et al. (1996), and the dashed orange line represents the separation of stars with prograde/retrograde motion based on their v_θ.

soid. There have been several studies linking some of the MW stars and globular clusters with *Gaia*-Enceladus, e.g. Helmi et al. (2018); Myeong et al. (2018). These studies have an approximately common range of angular momenta in z-direction, L_z, with values $-1500\,\mathrm{kpc\,km\,s^{-1}} < L_z < 150\,\mathrm{kpc\,km\,s^{-1}}$. The majority of the stars with values of L_z within the aforementioned boundaries are located in the blue shaded region of Fig. 6.4.3. Some of the MW RR Lyrae stars have already been associated with *Gaia*-Enceladus by Simion et al. (2019) while studying the Hercules-Aquila Cloud and Virgo Overdensity (Vivas et al. 2001; Newberg et al. 2002; Belokurov et al. 2007). This is the first time we can link *Gaia*-Enceladus with the local RR Lyrae stars (based on L_z and the region covered by ellipse in v_θ vs. v_R defined by Belokurov et al. 2018b)

Furthermore, using the `galpy` potential for the MW, `MWPotential2014`, we calculated the asymmetric drift of the RR Lyrae variables associated with the Galactic disc concerning the circular velocity. We found that the studied subpopulation of the local RR Lyrae stars lags behind the Galactic rotation with an asymmetric drift equal to $-5\,\mathrm{kms^{-1}}$, which in agreement with the asymmetric drift assumed for the thin disc stars (see e.g., Bensby et al. 2003; Golubov et al. 2013; Sysoliatina et al. 2018). In addition, pericenter peak RR Lyrae stars appear to be kinematically cold, with a vertical velocity dispersion $\sigma_{v_z} = 16\,\mathrm{kms^{-1}}$ and a total velocity dispersion[5] equal to $\sigma_s = 37\,\mathrm{kms^{-1}}$, which agrees with their possible thin disc association.

Here we would like to add a note on high-velocity RR Lyrae stars in our sample. RR Lyrae

[5] $\sigma_s = \sqrt{\sigma^2_{v_\theta} + \sigma^2_{v_\mathrm{R}} + \sigma^2_{v_z}}$

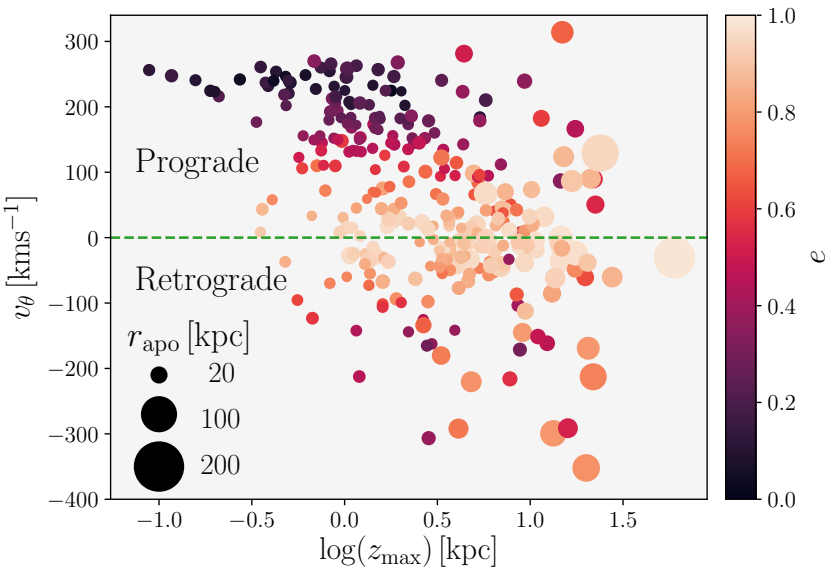

Figure 6.4.2: The tangential velocity v_θ vs. maximum height from the Galactic plane $z_{\rm max}$ for the studied RR Lyrae stars. The colour-coding of the individual points is based on e, and size of each point coresponds to the $r_{\rm apo}$.

variables with high space velocity have been reported in the Galactic bulge (see e.g., Kunder et al. 2015; Hansen et al. 2016). One example of a high-velocity RR Lyrae star is seen in the top left corner of Fig. 6.4.3 (dark point, $v_\theta = 415\,{\rm kms}^{-1}$ and $v_{\rm R} = -224\,{\rm kms}^{-1}$), AO Peg, with [Fe/H]$= -0.92$ dex and a space velocity $sv = 512\,{\rm km\,s}^{-1}$. In general, for only 2 % of the RR Lyrae pulsators from our sample the sv exceed $400\,{\rm km\,s}^{-1}$, which is similar to RR Lyrae stars in the Galactic bulge sample (Prudil et al. 2019c) where we found roughly 3 % of the RR Lyrae stars to show sv above $400\,{\rm km\,s}^{-1}$.

Association based on relative probabilities

A probabilistic approach to separate stars in the MW components (thin and thick disc and halo) was proposed by Bensby et al. (2003). The selection is done strictly on a kinematic basis using the Galactocentric rectangular velocities relative to the local standard of rest (LSR) – $U_{\rm LSR}, V_{\rm LSR}, W_{\rm LSR}$, while $U_{\rm LSR}$ in the left-handed system is positive in the Galactic anticenter direction, $V_{\rm LSR}$ increases in direction of the Galactic rotation, and the positive direction toward the Galactic north pole is described by increasing $W_{\rm LSR}$. The method introduced by Bensby et al. (2003) assumes that the aforementioned velocities for stars in the MW components follow Gaussian distributions:

$$f = \frac{1}{(2\pi)^{3/2}\,\sigma_{U_{\rm LSR}}\sigma_{V_{\rm LSR}}\sigma_{W_{\rm LSR}}} \cdot \exp\left(-\frac{U_{\rm LSR}^2}{2\sigma_{U_{\rm LSR}}^2} - \frac{\left(V_{\rm LSR} - V_{\rm asym}\right)^2}{\sigma_{V_{\rm LSR}}^2} - \frac{W_{\rm LSR}^2}{2\sigma_{W_{\rm LSR}}^2}\right), \tag{6.10}$$

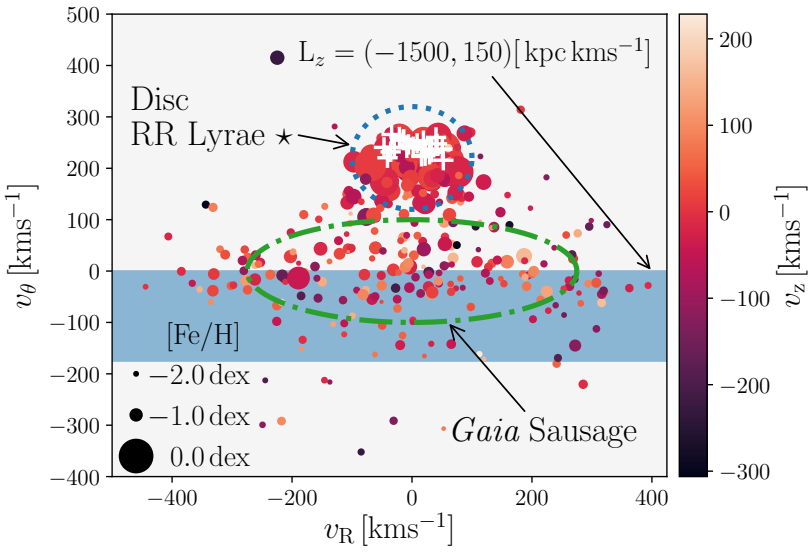

Figure 6.4.3: The distribution of the velocity components v_θ vs. v_R for the studied RR Lyrae stars. The colour-coding of the individual points is based on their transversal velocity v_z. The point sizes reflect their metallicity with decreasing size for decreasing metallicity. The white crosses mark the positions of pericenter peak RR Lyrae variables. The area of their occurrence is also highlighted with a blue dotted line. The green dashed line represents the approximate region for stars associated with the *Gaia*-Sausage in v_θ vs. v_R space based on Belokurov et al. (2018b). In addition, the blue stripe covers the region where the vast majority of our sample RR Lyrae stars fulfill the condition $-1500\,\mathrm{kpc\,km\,s^{-1}} < L_z < 150\,\mathrm{kpc\,km\,s^{-1}}$ (from Helmi et al. 2018), as discussed below.

where V_{asym} is the velocity of the asymmetric drift and the $\sigma_{U_{\mathrm{LSR}}}$, $\sigma_{V_{\mathrm{LSR}}}$, $\sigma_{W_{\mathrm{LSR}}}$ represent the velocity dispersions. Our assumed velocity dispersions and velocities of the asymmetric drift for the individual MW components are listed in Tab. 6.4.1 (Holmberg & Flynn 2000; Bensby et al. 2003). We emphasize that our sample of variables are Population II stars with ages above 10 Gyr, while studies of the MW thin disc propose ages from 0 to 8 Gyr, e.g., (Haywood et al. 2013). Therefore, based on that age range we do not have a reasonable priors for the probability of RR Lyrae stars emerging from the thin disc population, since they are believed to be older than 10 Gyr (e.g., Glatt et al. 2008; VandenBerg et al. 2013). Thus, for this analysis we will assume only two MW components: disc – D and halo – H, where for the disc we will assume priors used for the thick disc in Bensby et al. (2003). For each star from our sample we solve Eq. 6.10 and get probabilities for disc and halo membership: f_{D} and f_{H}.

The results of this analysis can be seen in the Toomre diagram depicted in Fig. 6.4.4. Here, our sample of RR Lyrae stars is colour-coded based on the logarithm of the disc to halo probability ratio $\log(f_{\mathrm{D}}/f_{\mathrm{H}})$. We note that $f_{\mathrm{D}}/f_{\mathrm{H}} < 1$ for over two-thirds of the sample, thus for clarity of Fig. 6.4.4, we included stars with $f_{\mathrm{D}}/f_{\mathrm{H}} < 1$ only as black dots in the aforementioned figure. In the same figure, we see that stars with a high probability ratio ($f_{\mathrm{D}}/f_{\mathrm{H}} > 10$) are concentrated around $V_{\mathrm{LSR}} = 0$ where one would expect to find the disc population. All of the disc RR Lyrae stars have a high disc to halo probability ratio (all above $f_{\mathrm{D}}/f_{\mathrm{H}} > 42$), which

Table 6.4.1: The adopted velocity dispersions and asymmetric drifts based on Bensby et al. (2003). Column 1 lists two MW components (halo – H, thick disc – TD) and column 2 contains the assumed velocities for the asymmetric drift. Columns 3, 4, and 5 provide values for the velocity dispersions for the thick disc and halo.

MW	$V_{\rm asym}$ [km s^{-1}]	$\sigma_{U_{\rm LSR}}$ [km s^{-1}]	$\sigma_{V_{\rm LSR}}$ [km s^{-1}]	$\sigma_{W_{\rm LSR}}$ [km s^{-1}]
H	-15	160	90	90
TD	-46	67	38	35

further corroborates their association with the MW disc population. One could argue that we did not use the observed fraction of stars in the solar neighbourhood as in Bensby et al. (2003) for our probability ratio. As a sanity check, we tested various values for the observed fraction of disc and halo stars in the solar neighbourhood, e.g., from Bensby et al. (2003) and Jurić et al. (2008). In the end, the pericenter peak RR Lyrae variables still had the highest probability ratios among the stars in our sample.

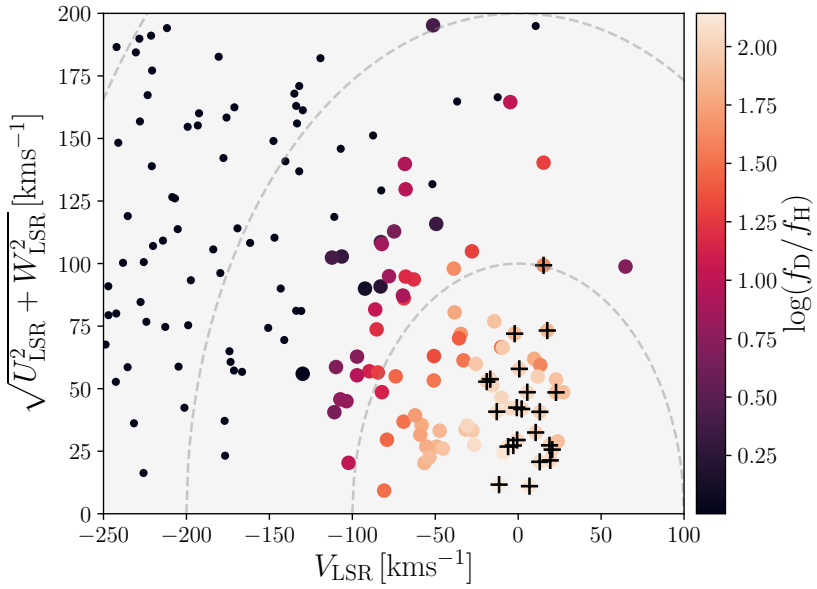

Figure 6.4.4: Toomre diagram for our studied RR Lyrae stars constructed using the Galactocentric rectangular velocities. The colour-coding is based on the logarithm of the probability ratio between disc and halo. We note that we removed from the colour-coding stars with $f_{\rm D}/f_{\rm H} < 1$ and denoted them only as black dots since they are not a target of our analysis. The pericenter peak RR Lyrae stars are marked with black crosses. The same notation applies also for the enlarged inset panel. The grey dashed lines represent lines of constant space velocity with a step size of 50 km s^{-1}.

The majority of the local RR Lyrae stars are associated with the Galactic halo (Maintz & de Boer 2005; Mateu et al. 2012; Mateu & Vivas 2018; Marsakov et al. 2018), but the stars

in the pericenter peak are consistent with the Galactic disc.

Chemical test

Here we use chemical information together with kinematics to explore the pericenter peak RR Lyrae stars. A search of the literature was carried out to collect information on the elemental abundances of the pericenter peak RR Lyare stars. We found 61 RR Lyrae stars with determined [Ca/Fe] in our sample from the following studies: Chadid et al. (2017); Liu et al. (2013); Pancino et al. (2015); Lambert et al. (1996). Calcium is an element resulting from helium burning via α particle capture and is synthesized in massive stars. Therefore, it can serve as a proxy for [α/Fe]. Fig. 6.4.5 shows [Ca/Fe] vs. [Fe/H] for the collected data overplotted over the distribution of non-variable MW stars (Edvardsson et al. 1993; Reddy et al. 2003; Bensby et al. 2003; Roederer et al. 2014; Bensby et al. 2014).

In Fig. 6.4.5 we combined the chemical abundance information with the kinematic properties: The point sizes vary with e and the colour-coding is based on $z_{\rm max}$. Stars in the pericenter peak defined by the conditions of Eq. 6.8 are located at low values of [Ca/Fe] typical for thin disc stars (in other words, consistent with the α-poor disc, Adibekyan et al. 2011, 2013; Bland-Hawthorn et al. 2019)[6]. The remaining stars are located at the α element knee and further close to the region typical for thick disc stars (the α-rich disc, Bland-Hawthorn et al. 2019), and Galactic halo stars. It is striking that the pericenter peak RR Lyrae stars reside in a different [Ca/Fe] - [Fe/H] space from the rest of the local RR Lyrae stars.

In addition, the majority of the RR Lyrae variables (14 out of 17) associated with *Gaia*-Enceladus based on L_z, v_θ, and $v_{\rm R}$ with published [Ca/Fe] abundances seems to fall beyond the *knee*, on α-poor sequence discovered by Nissen & Schuster (2010). This is in agreement with the studies of *Gaia*-Enceladus where stars associated with *Gaia*-Enceladus exhibit low α abundances at low metallicities (Hayes et al. 2018; Haywood et al. 2018; Helmi et al. 2018). The RR Lyrae stars associated with *Gaia*-Enceladus also exhibit a considerable metallicity spread in the old population (more than 1 dex)

Possibility of misclassification

We carefully examined the possibility that the pericenter peak RR Lyrae stars are misclassified variables. Using the Fourier coefficients determined based on the ASAS-SN photometry, we compared the properties of the stars selected from Eq. 6.6 and 6.7 with other pulsating variable stars (Fig. 6.5.1).

For this comparison we used the V-band photometry from the fourth data release of the Optical Gravitational Lensing Experiment (hereafter OGLE-IV, Soszyński et al. 2014, 2017b) for the Galactic bulge RR Lyrae stars. The decision to use the bulge RR Lyrae variables was based on their assumed metallicity (similar to the metallicity of the pericenter peak RR Lyrae stars [Fe/H] = −1.02 dex, Pietrukowicz et al. 2015), and high-quality photometry for over 27 000 fundamental mode RR Lyrae stars. The pericenter peak RR Lyrae stars fall into the

[6] We note that the blue line separating the thick and thin disc was derived for [α/Fe] while in our case we have only [Ca/Fe]. The overall difference is negligible.

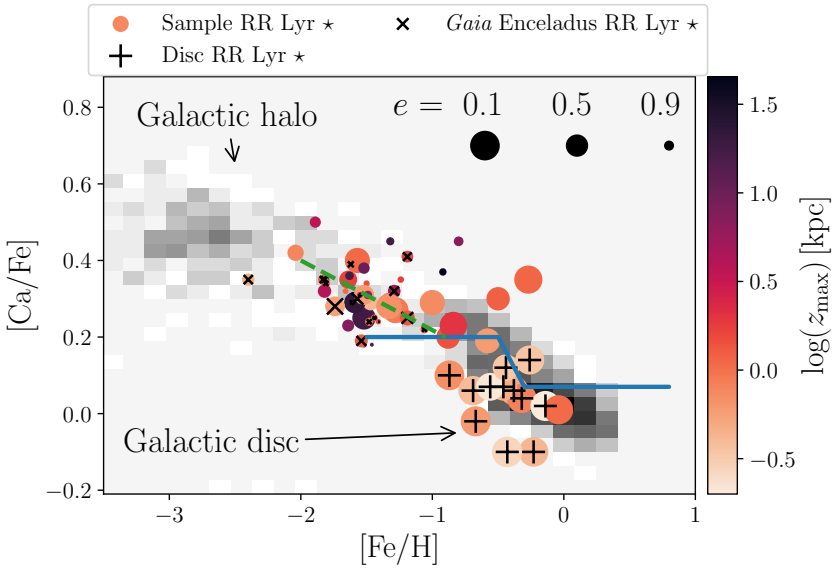

Figure 6.4.5: The [Ca/Fe] vs. [Fe/H] dependence for the studied RR Lyrae stars with determined calcium abundance from the literature, colour-coded based on the excursion from the Galactic plane $z_{\rm max}$, and marker sizes based on the orbital eccentricity e. RR Lyrae stars associated with the pericenter peak based on our set of conditions are marked with a black plus sign. The RR Lyrae variables possibly associated with the *Gaia*-Enceladus ($-1500\,{\rm kpc\,km\,s^{-1}} < L_z < 150\,{\rm kpc\,km\,s^{-1}}$ and falling in the green ellipse in Fig. 6.4.3) are marked with black crosses. The green dashed line stands for the boundary between α-rich and α-poor populations from Hayes et al. (2018). The blue solid line represents the approximate separation of the thin and thick disc stars (Adibekyan et al. 2011). The underlying gray distribution comes from the spectroscopic studies of non-variable stars in the MW disc and halo.

regions typical for the fundamental mode RR Lyrae stars with short pulsation periods and asymmetric light curves. In the period-amplitude diagram they can be all clearly associated with the Oosterhoff type I group (Oosterhoff 1939) identified in the Galactic bulge (Prudil et al. 2019a). Moreover, a large fraction of the pericenter-peak RR Lyrae stars occupy the regions of high-amplitude short-period (from hereon referred to as HASP, Fiorentino et al. 2015) RR Lyrae stars, which are found mainly in the most metal-rich systems (cf. Fig.6.4.1). This further supports that their origin is intrinsic to the MW, since apart from the MW, HASP stars reside in metal-rich environments, and it is unlikely that a merger with a massive dwarf galaxy would result in circular orbits of the accreted stars. A colour-magnitude diagram (Fig. 6.5.1, bottom-right panel) shows that the pericenter peak RR Lyrae variables are slightly dimmer than the studied RR Lyrae stars. This is mainly due to their high metallicity, which results in two effects in the stellar structure: an increase in the radiative opacity in the stellar atmosphere and a reduced mass of the helium core.

In the panels for the Fourier coefficients of Fig. 6.5.1, we also included data for the first-overtone classical Cepheids, which can have a similar pulsation period as the fundamental mode RR Lyrae stars. The classical Cepheids are Population I variables with ages up to a few

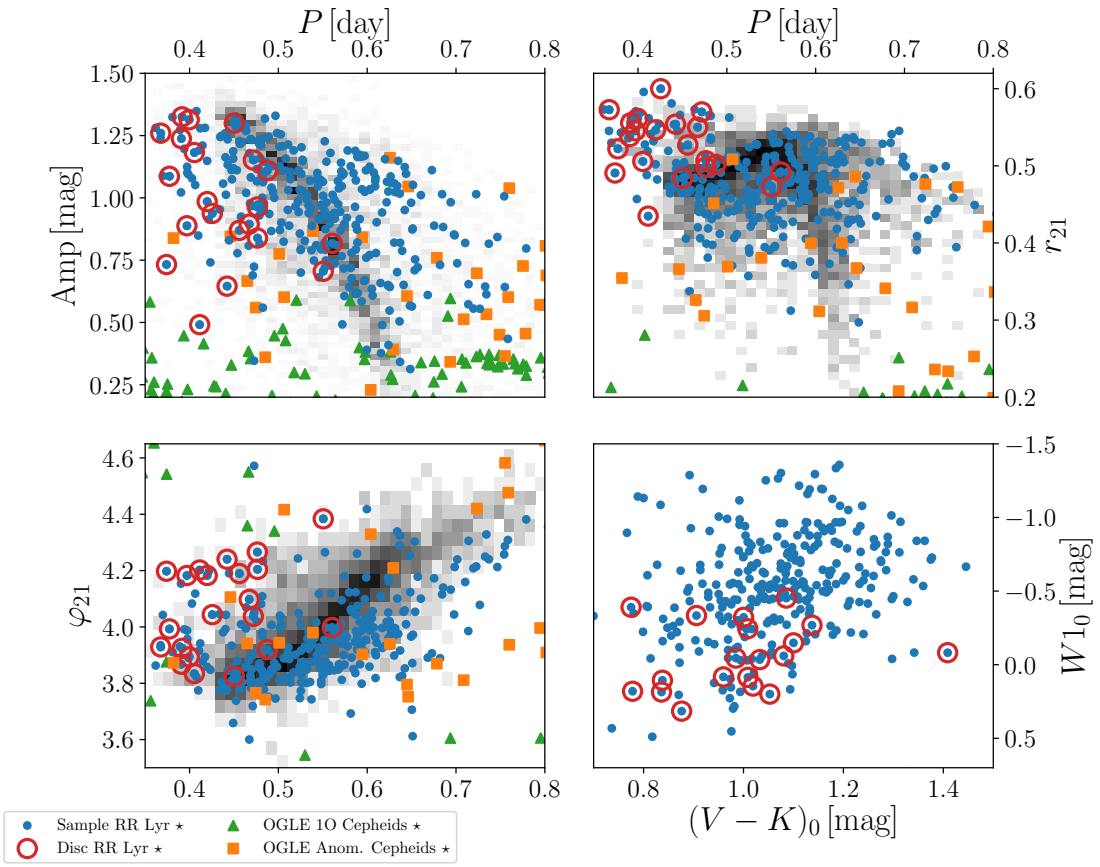

Figure 6.5.1: A mosaic of pulsation properties and a colour-magnitude diagram (right-hand bottom panel) for our sample of RR Lyrae stars represented by the blue points. Our pericenter peak RR Lyrae variables are marked with red circles. The two top panels depict the period-amplitude diagram (left-hand panel) and amplitude ratio r_{21} vs. pulsation period (right-hand panel). The bottom left-hand panel shows a phase difference φ_{21} vs. pulsation period diagram. The bottom right-hand panel shows the colour-magnitude diagram for our sample of RR Lyrae stars with the same colour-coding as in the previous three panels. In the three panels depicting the pulsation properties, the green triangles represent classical first overtone Cepheids from the Galactic bulge and Large Magellanic Cloud, and squares stand for anomalous Cepheids from the Large Magellanic Cloud (Soszyński et al. 2015a). The underlying gray distribution in the panels represents the pulsation parameters from the OGLE-IV V-band photometry (Soszyński et al. 2014, 2017b) for RR Lyrae stars.

hundred million years. We used the V-band photometry for the sample of classical Cepheids identified by OGLE-IV in the Galactic bulge and Large Magellanic Cloud (Soszyński et al. 2015b, 2017b). Using the Eqs. 6.6 and 6.7, we estimated their Fourier coefficients. In the period-amplitude diagram we see that classical Cepheids have similar pulsation periods as our pericenter peak RR Lyrae stars, but much lower amplitudes. In addition, the r_{21} vs. pulsation period dependence shows that the identified pericenter peak RR Lyrae stars have very asymmetric light curves, unlike classical Cepheids. In general, we see that pericenter peak

RR Lyrae stars deviate from the general sample population in all four panels of Fig. 6.5.1.

We performed a similar test using the anomalous Cepheids observed by OGLE-IV in the Large Magellanic Cloud (Soszyński et al. 2015a). They are metal-deficient helium-burning variables with higher masses than RR Lyrae stars (between $1.3-2.2\,M_\odot$, Marconi et al. 2004), with uncertain origin[7]. They occur usually in nearby dwarf galaxies, but very rarely in globular clusters (see Kinemuchi et al. 2008; Bernard et al. 2009). In the panels for pulsation properties, we see that anomalous Cepheids occupy similar regions as our pericenter peak RR Lyrae stars. But the major difference between anomalous Cepheids and our pericenter peak RR Lyrae stars is in the absolute magnitudes where anomalous Cepheids are intrinsically brighter ($M_V \approx (0.2; -1.5)$ mag), while the majority of the pericenter peak RR Lyraes are no brighter than 0.45 mag. The exceptions are AR Per and SW Cru. Their absolute magnitude in the V-band is higher than -0.7 mag, and therefore brighter than 95 % of our entire sample. On the other hand, both stars do not stand out in their absolute magnitudes in the K_s, and $W1$ passbands, where they fall on the faint end of the absolute magnitude distribution. In addition, both variables lie close to the Galactic plane, $|b| < 2.5$ deg, thus we believe that the correction for the extinction is responsible for this discrepancy. Therefore, based on this simple comparison, we presume that our pericenter peak variables are truly RR Lyrae stars.

We note that we did not compare our stars with other variables, e.g. eclipsing binaries, spotted stars, non-radial pulsators, Mira variables, and δ Scuti pulsators. Since our pericenter peak RR Lyrae stars occupy the instability strip in the CMD (see the bottom right-hand panel of Fig. 6.5.1) and exhibit asymmetric light curves without any sign of additional radial or non-radial modes we believe that they belong to none of the aforementioned variable classes. Some of the pericenter peak RR Lyrae stars even exhibit a modulation of their light curves (6 out of 22 stars are marked as modulated in the database of Blazhko stars[8], Skarka 2013), which points toward the Blazhko effect (Blažko 1907), a typical phenomenon observed among all RR Lyrae subtypes[9]. Moreover, in the period-amplitude diagram, they lie in a region occupied by the fundamental-mode RR Lyrae stars.

Another explanation of their disc association can be erroneous proper motions due to their binary nature. Binary systems with an RR Lyrae component are very rare; to this day only TU UMa seems to be bound in a binary system (e.g., Wade et al. 1999; Liška et al. 2016). Another 105 RR Lyrae stars are potential candidates for a binary system, based on the RRLyrBinCan database[10] (Hajdu et al. 2015; Liska & Skarka 2016; Liška et al. 2016; Prudil et al. 2019b). From our 22 RR Lyrae stars, four (RS Boo, XZ Dra, CN Lyr, DM Cyg) are considered to be binary candidates and their proper motion could have been affected by the unknown second component. For an assessment of the astrometric solution for the studied stars, we can use the RUWE parameter provided in the *Gaia* DR2. Of the aforementioned 4 RR Lyrae stars only DM Cyg has a RUWE parameter higher than 1.4 – (1.5, respectively).

[7] They are believed to be either intermediate-age variables (1 – 6 Gyr, Norris & Zinn 1975; Demarque & Hirshfeld 1975) or a product of mass transfer in binary systems with ages above 10 Gyr (Renzini et al. 1977).

[8] The online version can be found here `https://www.physics.muni.cz/~blasgalf/`

[9] For more information about the Blazhko effect see Szabó (2014) and Catelan & Smith (2015).

[10] The online version of the database can be found here: `https://rrlyrbincan.physics.muni.cz/`

The RUWE parameter of the remaining three stars is below 1.2, therefore a reasonably good astrometric solution, hence these stars are most likely not affected by a possible second object in their system.

For these reasons, we consider our disc variables as fundamental-mode RR Lyrae stars.

Conclusions

We report the detection of a peak in the pericenter distance distribution in the local RR Lyrae star sample. The majority of these stars 22 have kinematics, abundances and pulsation properties that link them to the Galactic disc. It is important to note that our sample does not contain RR Lyrae stars found independently in the Galactic disc based on a spatial distribution study (using the Vía Láctea survey Minniti et al. 2010; Dékány et al. 2018) nor in the direction of the Galactic bulge (Soszyński et al. 2014, 2017b). This may have, to some extent, affected the selection function of our sample and the observed peak in the pericenter distance distribution. For RR Lyrae stars located close to the Galactic plane ($|b| < 5$ deg), we would expect to have similar $z_{\rm max}$ and e but not necessarily the same $r_{\rm per}$.

These 22 pulsators pass the various tests of their association with the Galactic disc, e.g., based on their angular velocities and metallicities (Layden et al. 1996) and velocities in the local standard of rest Bensby et al. (2003). They also show the orbital properties associated with the disc RR Lyrae stars described earlier by Maintz & de Boer (2005). The pericenter peak RR Lyrae pulsators have an average angular velocity $v_\theta = 241\,{\rm km\,s^{-1}}$ and an average [Fe/H] $= -0.60$ dex. They also stand out in their distribution of velocity components and are clearly distinct from the halo RR Lyrae stars in our sample as well as from the RR Lyrae stars that we find to be associated with the *Gaia*-Enceladus (or *Gaia* Sausage, Belokurov et al. 2018b; Helmi et al. 2018). For some of the studied variables, we were able to find additional chemical information about their [Ca/Fe] ratio, which serves as a proxy for the α abundance. Our stars fall in the region occupied by α-poor metal-rich stars (e.g., Edvardsson et al. 1993; Reddy et al. 2003; Bensby et al. 2003; Roederer et al. 2014). Their chemical similarity in [Ca/Fe], as well as their very similar orbital parameters, suggest that the pericenter peak RR Lyrae stars have a common origin. The RR Lyrae stars associated with the *Gaia* Sausage, on the other hand, are located at the metal-poor end ([Fe/H] between -1.2 to -1.8 dex) with a large metallicity spread while overlapping with the α-poor population discovered by Nissen & Schuster (2010).

The pericenter peak RR Lyrae stars have an asymmetric drift equal to $-5\,{\rm km\,s^{-1}}$, therefore similar to the asymmetric drift estimated for the thin disc stars (e.g., Bensby et al. 2003; Golubov et al. 2013; Sysoliatina et al. 2018). Moreover, the RR Lyrae variables associated with the Galactic disc exhibit a total and vertical velocity dispersion equal to $\sigma_{\rm s} = 37\,{\rm km\,s^{-1}}$, and $\sigma_{\rm z} = 16\,{\rm km\,s^{-1}}$, respectively. Low velocity dispersion is expected for the kinematically cold thin-disc stars Hayden et al. (2017, see their fig. 4) or Casagrande et al. (2011, see their fig. 17), although we note that the pericenter peak variables should have a higher velocity dispersion based on their age if they had typical RR Lyrae ages > 10 Gyr.

The 22 RR Lyrae stars seem to be clearly associated with the Galactic disc in the solar neighbourhood, based on their orbital and chemical properties for stars with available

[Ca/Fe] abundance, and their pulsation characteristics rule out a confusion with the other variable stars such as classical and anomalous Cepheids. Their possible association with the thin disc (in the case of those with known [Ca/Fe]) is in agreement with the spatial and kinematical studies focusing on the RR Lyrae stars identified in the Galactic disc (e.g., Dékány et al. 2018; Marsakov et al. 2018). To corroborate our results for the remaining pericenter peak RR Lyrae stars we would need information about their α-element abundances (e.g., [Ca/Fe] or [Mg/Fe]).

Generally, if we were dealing with stars of ages younger than 8 Gyr (Haywood et al. 2013), and with the same kinematics and chemical properties as our pericenter peak stars, we would assign them to the Galactic thin disc (or α-poor disc, Adibekyan et al. 2013; Hayden et al. 2015; Bland-Hawthorn et al. 2019). On the other hand, the ages of RR Lyrae stars are well constrained between 10 – 13 Gyr, based on the youngest and oldest globular clusters in which RR Lyrae stars were detected (Catelan 2009; VandenBerg et al. 2013). This seems to be in contradiction to the studies of the stellar ages of the thin disc as derived by, e.g. Haywood et al. (2013) and many others. Theses boundaries are somewhat diffuse; we note that several stars in their sample, assigned to the metal-poor thin disc, have ages around 10 Gyr (see fig. 8 in Haywood et al. 2013). The pericenter peak RR Lyrae stars then possibly belong to the chemical and kinematical distribution of the thick disc overlapping the region occupied by the thin disc stars. However, their [Fe/H] and [α/Fe] values are consistent with young thin disc stars, which remains a conundrum (see also the discussion in Marsakov et al. 2018, 2019a,b).

We suggest that the 22 pericenter peak RR Lyrae stars may be the metal-rich alpha-poor extreme of the Galactic thick disc RR Lyrae population since our sample covers only $\approx 10\,\%$ of the local RR Lyrae stars. Hopefully, with future spectroscopic surveys we can expand our sample and shed more light on the Galactic disc RR Lyrae population.

CHAPTER 7

CANDIDATES FOR RR LYRAE IN BINARY SYSTEMS FROM THE OGLE GALACTIC BULGE SURVEY

"Look at your Sub-Zero, now plain zero!"
— Ben Richards, helicopter pilot

Abstract: We present 20 newly discovered candidates for binary systems with an RR Lyrae companion. Using the photometric data from the Optical Gravitational Lensing Experiment (OGLE) and Korea Microlensing Telescope Network (KMTNet) for the Galactic bulge, we searched for binary candidates among non-modulated fundamental-mode RR Lyrae variables. We constructed and investigated over 9000 $O-C$ diagrams for individual pulsators, in order to find signs of the light-travel time effect. We found 20 variables exhibiting cyclic variation in the $O-C$ (time of the observed minus calculated brightness maximum) diagram, which can be associated with a second component in the system, but for confirmation of binarity, a long-term radial velocity study is necessary. The modeling of the $O-C$ diagrams yields orbital parameters, estimates of the semi-amplitude of the radial velocity curve, and the mass function. The orbital periods of our candidates range from 3 to 15 years. Two of the binary candidates display a minimum mass higher than the assumed mass of the RR Lyrae component, which points towards an evolved companion that can under some circumstances contribute significantly to the total light of the system.

This chapter is based on our published paper : **Prudil, Z.**, Skarka, M., Liška, J., Grebel, E. K., Lee, C. -U.: Candidates for RR Lyrae in binary systems from the OGLE Galactic bulge survey, 2019, MNRAS, 487, L1

Context

Pulsating stars of RR Lyrae type (hereafter RRL) have played a prominent role since their discovery (Pickering & Bailey 1895). As one of the fundamental distance indicators, they help to map the Milky Way and its formation history (Drake et al. 2013; Sesar et al. 2013; Hernitschek et al. 2019) and close galactic systems (Haschke et al. 2012a,b; Jacyszyn-Dobrzeniecka et al. 2017).

Knowledge of the luminosity of RRL is, therefore, crucial. The luminosity of an RRL is mainly defined by the helium and heavy-element abundances and by the mass of the star. The latter one is still poorly known and can be deduced only indirectly from stellar evolutionary and pulsation models (Sweigart 1987; Lee & Demarque 1990; Popielski et al. 2000). An independent determination of the mass would constrain the accuracy of the theoretical predictions and will have a large impact on all topics employing RRL stars. This motivates the search for RRL stars in binary systems, as binaries offer an excellent means of accurate stellar mass determinations, but very few such candidate systems have been found so far (Saha & White 1990; Soszyński et al. 2009, 2011; Li & Qian 2014; Hajdu et al. 2015; Liška et al. 2016; Kervella et al. 2019a). Identification of binary systems will also help to answer the question why binaries with an RRL companion are so rare. Currently, we know about 150 000 RRL stars in the Milky Way. Even if we assume that only a few percent of these RRL stars are in binary systems (Hajdu et al. 2015), we should detect a large number of binaries. The shortcomings of the detection caused by the evolutionary status of RRL stars are discussed in Skarka et al. (2016).

Stellar dynamical mass can be derived when a star is bound in an eclipsing binary system. However, here comes the issue: to our current knowledge, no eclipsing binary containing an RRL star has been discovered and verified. There are over one hundred candidates (see the online version of the database[1], Liska & Skarka 2016), and Kervella et al. (2019a,b), but only TU UMa is bound in a binary system with high confidence (Wade et al. 1999; Liška et al. 2016; Kervella et al. 2019a). The binarity is mostly inferred from the cyclic period variations (mostly with years-long periods) as a consequence of the light-travel time effect[2] (hereafter LiTE, for example, Olah & Szeidl 1978; Hajdu et al. 2015; Li et al. 2018, just to mention some studies). A comprehensive review of the binary RRL candidates can be found in Liška et al. (2016).

Karczmarek et al. (2017) found that among binary stars with orbital periods below 2000 d, mass transfer can occur and binary evolution pulsators, which only mimic RRL type stars, can be formed (Pietrzyński et al. 2012; Smolec et al. 2013). Thus, only wide systems give a good chance to reveal a real RRL in a binary system. At the same time, the large size of the semi-major axis of wide binaries decreases the chance to observe eclipses. The observation of the cyclic pulsation period variations itself cannot give an unambiguous proof of binarity. Skarka et al. (2018) showed for Z CVn that the years-long spectacular pulsation pe-

[1] https://rrlyrbincan.physics.muni.cz/

[2] The LiTE hypothesis is based on the possible existence of an additional hidden object in the system. The RRL and the companion move around a common barycenter, and the times of brightness maxima of the pulsator's changes occur earlier or later, based on its orbital position relative to the observer.

riod variations can have a different origin than LiTE. This shows that some of the candidates are probably false positives.

Obtaining radial velocity measurements over several years is, therefore, highly desired (e.g., Fernley & Barnes 1997; Solano et al. 1997). There have been a few ongoing projects for monitoring the candidates (Guggenberger et al. 2016; Poretti et al. 2018). Probably the most promising results can be expected from Hajdu et al. (2018), who have observed candidates from the Galactic bulge and who detected the expected differences in radial velocities for two of their sample stars in two different seasons.

In this paper, we identify 20 new binary candidates using an analysis of their pulsation period variations. We describe our sample and methods in Section 7.2 and discuss the results in Section 7.3.

Data selection and analysis

For the purpose of this study, we used I-band photometric data of RRLs from the OGLE Galactic bulge (OGLE GB) survey (Soszyński et al. 2011, 2014, 2017b). Our search was aimed at the LiTE manifestation in the $O-C$ diagram (O – observed, C – calculated time of the brightness maximum based on the star's ephemerides, Irwin 1952a; Sterken 2005), which may hint towards an unseen companion of a variable star. In order to avoid confusion with modulated Blazhko stars (Blažko 1907), we investigated only the non-modulated fundamental mode variables from studies focused on the occurrence rate of the Blazhko effect (Prudil & Skarka 2017; Prudil et al. 2019a). We did not make any additional cuts based on the data quality or quantity, and in the end we analysed more than 9000 stars, in order to increase the chances of finding candidates. We note that in the end we identified almost 200 stars with a peculiar change in the $O-C$ diagram, but for our current study, we chose only those with strong signs of the LiTE.

In the first step of the analysis, we constructed the light curve templates for individual variables based on the entire OGLE GB photometry using a Fourier decomposition of high degree n:

$$m(t) = A_0^I + \sum_{k=1}^{n} A_k^I \cdot \cos\left(2\pi k\vartheta + \varphi_k^I\right), \tag{7.1}$$

where A_k^I and φ_k^I represent amplitudes and phases, respectively, and A_0^I stands for the mean magnitude. The ϑ stands for the phase function defined as:

$$\vartheta = \frac{HJD - M_0}{P}, \tag{7.2}$$

where the HJD represents the time of observation in Heliocentric Julian Date, M_0 denotes the time of zero epoch (in our case for maximum brightness), and P is the pulsation period.

We note that the photometric data from OGLE GB phases III and IV differ by an offset in their mean magnitudes (by ≈ 0.01 mag). In order to compensate this effect, we shifted the OGLE III data by the difference in the mean apparent magnitudes, A_0^I, between the aforementioned data releases. In the second step, we binned the OGLE photometry based

on the observational seasons (where each bin represents a point in the $O-C$ diagram), and in some cases, where sufficient data were available (more than 300 observations per season), we divided each season into two bins since the data were sufficient in a given observing season.

The data in each bin were phased using the ephemerides (pulsation period P and time of brightness maximum M_0) provided by the OGLE team, and fitted with a light curve template created using the whole sample. The $O-C$ was calculated for each binned phased curve as a shift in phase of the maximum brightness from the zero point, and multiplied by the pulsation period. Using a bootstrap resampling of each bin we estimated the errors of the individual points in the $O-C$ diagram. An example of the $O-C$ diagram is shown in Fig. 7.2.1.

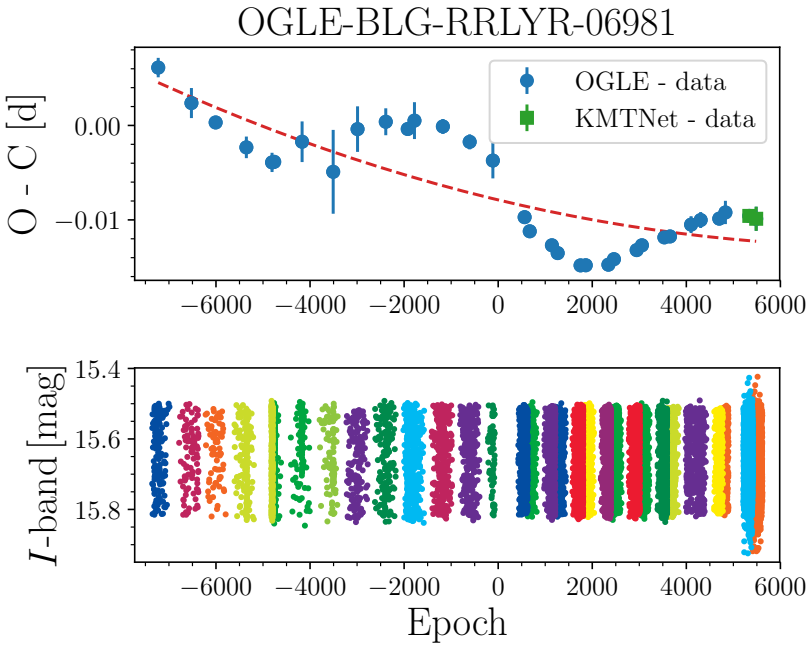

Figure 7.2.1: The analysis of the $O-C$ diagram for one of the candidate stars. In the top panel, the blue points represent the time difference between the observed and calculated time of the maxima ($O-C$) and the red dashed line represents the secular variation in the pulsation period with blue points indicating data from the OGLE survey and green squares standing for the photometry from the Korea Microlensing Telescope Network (KMTNet, Lee et al. 2014b; Kim et al. 2016). In the bottom panel, we show the available photometric data, colour-coded based on the data bins for the $O-C$ diagram.

For the subsequent visual examination, each $O-C$ diagram was corrected for the changes in the pulsation period using the following equation:

$$O-C = a_0 + a_1 \cdot E + a_2 \cdot E^2, \tag{7.3}$$

where E represents the number of cycles that elapsed since the M_0, and $a_{0,1,2}$ represents

free parameters of the parabolic fit, with a_2 denoting the pulsation period change rate. Such corrected $O-C$ diagrams were visually inspected for possible binary patterns (sinusoidal like waves). In doing so, we independently re-discovered candidates found by Hajdu et al. (2015) and Hajdu et al. (2018), thus verifying our approach. For variables that were selected for further analysis we used data uncorrected for period variation and fitted them using the combination of Eq. 7.3 and eq. 2 from Irwin (1952a):

$$O-C = a_0 + a_1 E + a_2 E^2 + A\left[\left(1-e^2\right)\frac{\sin(\nu+\omega)}{1+e\cos\nu} + e\sin\omega\right]. \tag{7.4}$$

In this relation, ν is the true anomaly, ω is the argument of periastron, e is the numerical eccentricity, and A is the shift in radial position in light days. We refer the interested reader to the appendix A in Liška et al. (2016) for a thorough description of the individual parameters.

For stars with $O-C$ diagrams that can be described by Eq. 7.4 we also further tested whether they exhibit the Blazhko modulation. We utilized the binned data and searched for an amplitude A_1 variation (derived from Eq. 7.1) similar to the trend in the $O-C$ diagram. Furthermore, we tested our stars for the Blazhko effect using the method from Shibahashi (2017), but the results were inconclusive with the available data. In total, for 20 stars, which were visually selected, Eq. 7.4 is valid and we will refer to them from here on as our binary candidates.

In order to increase the observational time span and to verify our binary candidates, we utilized data from the Korea Microlensing Telescope Network (KMTNet; Lee et al. 2014b; Kim et al. 2016) collected in 2018. The photometry was processed in a similar manner as the OGLE dataset and incorporated in our calculated $O-C$ diagrams. The orbital parameters were then determined iteratively in the following way: the $O-C$ diagrams of the selected candidates were modeled using Eq. 7.4, their light curves were then corrected for the LiTE effect, and in a next step served as a dataset for obtaining a light curve template, which is more accurate than the raw one. Using the new more accurate templates, we then derived new $O-C$ diagrams and subsequently the new orbital parameters.

Orbital parameters of candidates

In this subsection, we discuss the characteristics of 20 newly discovered binary candidates with an RRL component. In Fig. 7.2.2 we show a mosaic of the $O-C$ diagrams for all of the candidates with a model based on the Eq. 7.4. Using this model, we derived some of the orbital and physical properties of our candidate variables. In addition, we estimated the semi-amplitude of the radial velocity of RRL component K in km s^{-1} using the modified relation from Irwin (1952b):

$$K = \frac{2\pi\, a\sin i\cdot \mathrm{au}}{8.64\cdot 10^7 P_{\mathrm{orbit}}\sqrt{\left(1-e^2\right)}}. \tag{7.5}$$

where P_{orbit} represents the orbital period, a is the semi-major axis of RRL component, au is astronomical unit, and i is the inclination angle of the orbit. Furthermore, through the third

Kepler law, we can calculate the mass function $f(\mathfrak{M})$ as:

$$f(\mathfrak{M}) = \frac{4\pi^2 \, (a \sin i)^3}{\mathrm{G} \cdot P_{\mathrm{orbit}}^2}. \tag{7.6}$$

The list of candidates with their physical and orbital properties from the $O-C$ modeling can be found in Tab. 7.2.1.

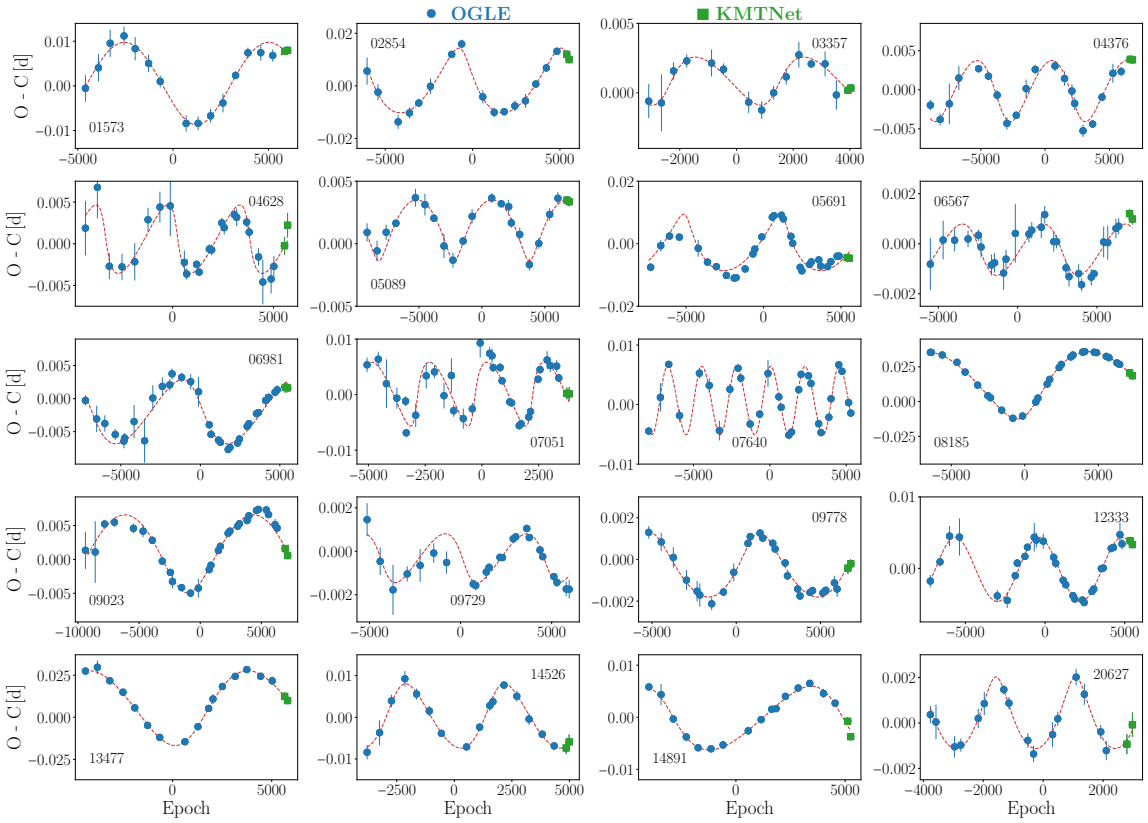

Figure 7.2.2: The $O-C$ diagrams for all of the candidates with the red dashed line representing the binary model based on Eq. 7.4 with subtracted trend for the period change. The blue points stand for photometry from the OGLE survey and green squares represent data from the KMTNet. The legend for each $O-C$ diagram contains the OGLE ID in the form OGLE-BLG-RRLYR-ID.

Using the mass function, we can estimate the minimum mass (M_*) of the companion, under certain assumption on the mass of the RRL component ($M_{\mathrm{RRL}} = 0.65$ M$_\odot$, Prudil et al. 2019a) and inclination angle $i = 90$ deg:

$$f(\mathfrak{M}) = \frac{M_*^3 \cdot \sin^3 i}{(M_{\mathrm{RRL}} + M_*)^2}. \tag{7.7}$$

We note that a difference of 0.1 M$_\odot$ in the assumed mass of the RRL variable only marginally

Table 7.2.1: Table of derived model parameters for the binary candidates. Column 1 contains the ID of the star in the form OGLE-BLG-RRLYR-ID. Columns 2 and 3 list the orbital period and semi-major axis in au. The numerical eccentricity and the argument of periastron in degrees are listed in columns 4 and 5. The columns 5 and 6 list the semi-amplitude of the radial velocity and period change rate. The column 7 and 8 contain the mass function, and minimum mass of a possible companion for an (adopted fixed mass of the RRL component of 0.65 $M_\odot$).

#ID	$P_{\rm orbit}$ [d]	$a \sin i$ [au]	e	ω [deg]	K [km s^{-1}]	β [d Myr^{-1}]	$f(\mathfrak{M})$ [$M_\odot$]	M_* [$M_\odot$]
01573	4191 ± 90	1.600 ± 0.102	0.054 ± 0.058	272 ± 93	4.16	0.59 ± 0.05	0.03108	0.305
02854	3517 ± 29	2.199 ± 0.079	0.452 ± 0.021	122 ± 9	7.62	0.08 ± 0.02	0.11458	0.548
03357	3163 ± 117	0.318 ± 0.036	0.356 ± 0.120	-20 ± 27	1.17	0.40 ± 0.03	0.00043	0.060
04376	2869 ± 43	0.688 ± 0.049	0.227 ± 0.151	-142 ± 10	2.68	0.07 ± 0.01	0.00528	0.150
04628	2088 ± 34	0.891 ± 0.086	0.609 ± 0.078	171 ± 11	5.86	0.04 ± 0.03	0.02165	0.262
05089	2874 ± 23	0.422 ± 0.018	0.453 ± 0.053	-91 ± 13	1.79	0.11 ± 0.01	0.00121	0.087
05691	3682 ± 66	1.639 ± 0.091	0.585 ± 0.043	120 ± 13	5.97	-0.10 ± 0.04	0.04330	0.352
06567	2368 ± 57	0.183 ± 0.021	0.250 ± 0.178	-174 ± 26	0.87	0.08 ± 0.01	0.00015	0.041
06981	4260 ± 107	0.883 ± 0.056	0.318 ± 0.071	165 ± 16	2.38	0.04 ± 0.02	0.00505	0.148
07051	2197 ± 27	1.200 ± 0.090	0.589 ± 0.009	-19 ± 5	7.35	0.42 ± 0.04	0.04772	0.367
07640	1243 ± 02	1.000 ± 0.015	0.109 ± 0.001	-362 ± 3	8.80	0.05 ± 0.01	0.08626	0.479
08185	5041 ± 22	4.281 ± 0.025	0.338 ± 0.004	-53 ± 2	9.82	-0.35 ± 0.01	0.41182	1.067
09023	5001 ± 133	0.998 ± 0.045	0.184 ± 0.051	-101 ± 17	2.21	0.51 ± 0.02	0.00530	0.150
09729	2211 ± 53	0.208 ± 0.027	0.367 ± 0.197	194 ± 15	1.10	-0.17 ± 0.01	0.00025	0.049
09778	3177 ± 52	0.269 ± 0.011	0.292 ± 0.044	69 ± 2	0.96	0.12 ± 0.01	0.00026	0.050
12333	3183 ± 25	0.778 ± 0.024	0.045 ± 0.046	74 ± 49	2.66	0.05 ± 0.01	0.00620	0.160
13477	4609 ± 160	3.882 ± 0.231	0.173 ± 0.021	-37 ± 11	9.30	-0.13 ± 0.19	0.36721	1.000
14526	2870 ± 27	1.363 ± 0.048	0.257 ± 0.074	38 ± 3	5.35	0.23 ± 0.01	0.04104	0.343
14891	4928 ± 89	1.121 ± 0.055	0.331 ± 0.060	167 ± 8	2.62	-0.06 ± 0.06	0.00774	0.174
20627	1180 ± 12	0.273 ± 0.016	0.345 ± 0.049	90 ± 17	2.68	0.14 ± 0.02	0.00194	0.103

affects the estimated minimum mass (less than 0.07 $M_\odot$ for a companion with the highest mass function). High uncertainty is in the unknown inclination angle.

In Fig. 7.2.3 we show a comparison of orbital parameters from our study and from studies by Hajdu et al. (2015); Liška et al. (2016); Li et al. (2018). We compare orbital periods, eccentricity, and semi-major axes of the candidates from the aforementioned studies. In these two panels, we see a gap in the orbital periods between our study and the study by Hajdu et al. (2015), and the orbital period from Liška et al. (2016); Li et al. (2018). This is most likely due to the limited time span of the OGLE GB survey, which reaches up to 25 years while the studies by Liška et al. (2016) and Li et al. (2018) consist of stars with more than a hundred years of observation. The eccentricity seems to be independent of the orbital period even though we detected a small correlation during the $O-C$ modeling for some of our sample stars. The connection between the semi-major axis and orbital period comes from the third Kepler law. We note that we do not detect any evident connection between the orbital parameters and pulsation periods.

Discussion and Conclusion

In our study, we found 20 binary candidates among more than 9000 non-modulated RRL stars from the Galactic bulge. The low number of candidates further supports a low occurrence of RRL variables in binary systems. Regarding a possible confirmation of binary

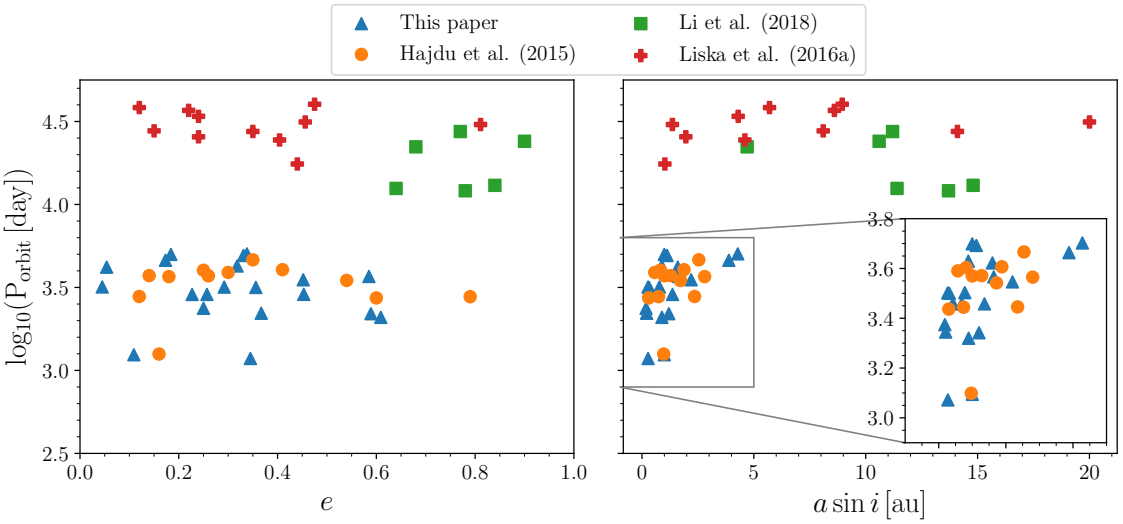

Figure 7.2.3: Comparison of orbital parameters for binary candidates in our study (blue triangles) and studies by Hajdu et al. (2015, orange points), Liška et al. (2016, red plus signs), and Li et al. (2018, green squares). In both panels, we show the orbital period on the horizontal axes, and on the vertical axes eccentricity (left-hand panel), and semi-major axis (right-hand panel).

candidates, we rely mainly on the orbital periods and semi-amplitude of the radial velocity of RRL component orbit, K, which can highlight feasible candidates for spectroscopic follow-up.

The orbital periods range from ≈ 3 years up to 14 years. This is comparable with the study by Hajdu et al. (2015) of a similar dataset, but when compared with the studies by Liška et al. (2016) and Li et al. (2018), our candidates lie on the short end of the orbital period distribution. The semi-amplitudes of the radial velocity for our candidates lie on a boundary for detection in studies of radial velocities among the bulge RRL stars (Kunder et al. 2016, radial velocities with errors between 5-10 km s^{-1}). Therefore, with current instruments, it is possible to follow-up and possibly confirm binary candidates as shown in Hajdu et al. (2018), although several years of spectroscopic observations are a necessity.

Suitable candidates for such spectroscopic radial-velocity follow-up are e.g. OGLE-BLG-RRLYR-02854, 07051, and 07640 with a rather high semi-amplitude of the radial velocity (above 7 km s^{-1}) and rather short orbital periods (less than 10 years). All three RRL stars should have a companion with a minimum mass close to the assumed mass of the RRL component. Two of the binary candidates from our sample (OGLE-BLG-RRLYR-08185 and 13477) should have a companion that is more massive than the RRL component. If the more massive companion is at the asymptotic giant branch, it can contribute to the total brightness of the system, and with a sufficiently long major axis with appropriate inclination might be detectable using the *Gaia* space telescope (Gaia Collaboration et al. 2016a, 2018a). In addition, anomalies in proper motions can help to identify potential candidates (Kervella et al. 2019a,b).

The OGLE survey has been proven in the past to suffice for a binarity search among RRL

stars, but in order to confirm the found candidates as binary systems, the combination of spectroscopic measurements with photometry is obligatory.

CHAPTER 8

HUMPS AND BUMPS: THE EFFECTS OF SHOCKS ON THE OPTICAL LIGHT CURVES OF FUNDAMENTAL-MODE RR LYRAE STARS

"Groovy..."

— Ashley 'Ash' J. Williams, clerk at S-Mart

Abstract: We present the most extended and homogeneous study carried out so far of the main and early shocks in 1485 RR Lyrae stars in the Galactic bulge observed by the Optical Gravitational Lensing Experiment (OGLE). We selected non-modulated fundamental-mode RR Lyrae stars with good-quality photometry. Using a self-developed method, we determined the centers and strengths of main and early shock features in the phased light curves. We found that the position of both humps and bumps are highly correlated with the pulsation properties of the studied variables. Pulsators with a pronounced main shock are concentrated in the low-amplitude regime of the period-amplitude diagram, while stars with a strong early shock have average and above-average pulsation amplitudes. A connection between the main and early shocks and the Fourier coefficients is also observed. In the colour-magnitude diagram (CMD), we see a separation between stars with strong and weak shocks. Variables with a pronounced main shock cluster close to the fundamental red edge of the instability strip (IS), while stars with a strong early shock tend to clump in the center and near the fundamental blue edge of the IS. The appearance of shocks and their properties seem independent of the direction of evolution estimated from the period change rate of the studied stars. In addition, the differences in the period change rate between the two

main Oosterhoff groups found in the Galactic bulge suggest that stars of Oosterhoff type I are located close to the zero-age horizontal branch while Oosterhoff type II variables are on their way toward the fundamental red edge of the instability strip, thus having already left the zero-age horizontal branch.

This chapter is based on our published paper : **Prudil, Z.**, Dékány, I., Smolec, R., Catelan, M., Grebel, E. K., Kunder, A.: Humps and bumps: The effects of shocks on the optical light curves of fundamental-mode RR Lyrae stars, 2020, accepted for publication in A&A

Context

RR Lyrae stars are dominantly radial pulsators. These horizontal branch stars are tracers of the old population. They are utilized in various fields of astronomy, mainly in studies focused on stellar pulsations (e.g., Szabó et al. 2010; Kolláth et al. 2011; Smolec et al. 2015a), on the Milky Way (MW) subcomponents such as the Galactic disc (e.g., Dékány et al. 2018; Mateu & Vivas 2018), the Galactic bulge (e.g., Dékány et al. 2013; Pietrukowicz et al. 2015), and the Galactic halo (e.g., Drake et al. 2013; Belokurov et al. 2018b; Hernitschek et al. 2018), globular clusters (e.g., Cacciari et al. 2005; Catelan 2009), and the local extragalactic neighbourhood such as the Magellanic Clouds (e.g., Haschke et al. 2012a,b; Jacyszyn-Dobrzeniecka et al. 2017) and neighboring dwarf galaxies (e.g., Pietrzyński et al. 2008; Karczmarek et al. 2015, 2017). They are divided into three categories based on their radial pulsation mode, namely RRab – fundamental mode, RRc – first overtone and RRd – double-mode RR Lyrae stars, which are simultaneously pulsating in the first overtone and fundamental mode (see, e.g., Catelan & Smith 2015).

Despite their plentitude in the MW (over 100 000 stars in Gaia DR2; Clementini et al. 2019b); several open issues hamper their full potential as e.g. stellar tracers. Some examples include the Blazhko effect (Blažko 1907), causing a modulation of the light curves, and the scarcity of RR Lyrae stars in binary systems (Hajdu et al. 2015; Liška et al. 2016; Prudil et al. 2019b) and therefore the absence of accurate mass determinations. Also, the origin of the Oosterhoff dichotomy (Oosterhoff 1939), which divides globular clusters that contain RR Lyrae variables into two groups based on their pulsation properties, is far from being resolved. Several possible solutions emerged over the past decades, e.g., increased helium abundance for RR Lyrae stars in Oosterhoff typeİI (Oo II) clusters (Sandage et al. 1981; Sandage 1981) or a different direction in crossing the instability strip (van Albada & Baker 1973). In more recent years some progress has been made suggesting that population and/or metallicity effects might be the cause of the Oosterhoff dichotomy, e.g., Catelan (2009); Lee et al. (2014a); Fabrizio et al. (2019), especially among field RR Lyrae variables.

In this study, we focus on shock phenomena in RR Lyrae stars. In their pioneering work, Struve & Blaauw (1948) observed line doubling and line emissions of hydrogen in the spectrum of the prototype of RR Lyrae stars, RR Lyr itself, during certain pulsation phases. Further spectroscopic studies (e.g. Preston & Paczynski 1964; Preston et al. 1965) confirmed the findings of Struve & Blaauw (1948) and added more features that appear at certain phases of a pulsation cycle. Today we associate these aspects with shock waves propagating through

the atmospheres of RR Lyrae stars. The Balmer lines forming in the upper layers of atmospheres are mainly affected (Hill 1972; Gillet & Crowe 1988), although some of the metallic lines are distorted through line broadening and absorption line doubling (Chadid & Gillet 1996a,b). Recently, Preston (2009) reported helium emission and absorption lines observed during the shock events in some of the RR Lyrae stars. Also, Chadid et al. (2017) showed that in the upper atmosphere the main shock intensity is larger among metal-poor RR Lyrae stars than in metal-rich RR Lyrae variables.

These shock waves correlate with features of the RRab light curves known as the hump and bump (Christy 1966). The shock waves are a consequence of rapid compression events in the atmospheres of RR Lyrae stars that oscillate with large amplitudes due to the opacity mechanism. The hump is a result of a sudden stop of the infalling photosphere and immediate outward expansion, while the bump is connected with the collision of the infalling material before reaching the minimum radius (e.g., Hill 1972; Fokin 1992).

In this paper, we study the impact of humps and bumps on the phased light curves of non-modulated fundamental mode RR Lyrae stars. In Sec. 8.2 we describe the selection criteria for the studied sample. Section 8.3 outlines the adopted procedure to estimate the strength of individual humps and bumps in the light curves. Sec. 8.4 discusses the positions of the centers of the humps and bumps, and the effect of main and early shocks on the light curves of RR Lyrae stars. In Sec. 8.5 we compare how our findings relate to the stars' positions in the colour-magnitude diagram and their evolutionary direction. In the last Section 8.6 we summarise our results.

Sample selection

To study small features in the light curve shapes of RR Lyrae stars, e.g. humps and bumps, one needs precise, homogeneous, and well-sampled photometry. Moreover, information about any alterations in the shapes of the light curves, e.g. modulation (Blažko 1907), additional modes, or possible binarity, is necessary since they would inevitably complicate the analysis and overall results.

The aforementioned criteria are fulfilled by the sample collected by the OGLE-IV survey (Udalski et al. 2015) of more than 38000 RR Lyrae stars in the Galactic bulge (Soszyński et al. 2014, 2017b). OGLE-IV provides photometry in two passbands V and I, where the latter contains substantially more measurements. The number of epochs collected for individual variables ranges from dozens up to tens of thousands. For the purpose of our study, we used the light curves of fundamental-mode RR Lyrae stars without any sign of modulation, additional modes, or binarity (Hajdu et al. 2015; Prudil et al. 2019b). We used a sample of non-modulated RR Lyrae stars collected in a study by Prudil et al. (2019a). In addition to the information provided by OGLE, this sample contains the following additional information for individiual objects: estimates of the metallicity based on the photometric data, absolute magnitudes, distances, amplitudes, and mean apparent magnitudes in the K_s-band from the VVV photometric survey (with a crossmatch radius $\approx 0.5''$, Minniti et al. 2010). Furthermore, each star is associated with one of the two Oosterhoff groups (Oosterhoff 1939) in the Galactic bulge (Prudil et al. 2019a).

To address the criteria for precision in photometry and sufficient phase coverage of the light curves, we removed stars fainter than 16.5 mag[1] and stars with less than 1000 epochs in the I-band. The data in the aforementioned passband served as a primary source of photometry for this study. The remaining variables that surpass the prior criteria were visually examined on the basis of their phased light curves. Stars with large scatter and/or with a high number of outliers were removed. In the end, from the original sample containing 8141 RR Lyrae stars, 1485 variables remained, and serve as the studied sample for the remainder of this paper.

Analysis of the impact of humps and bumps

Our initial approach to estimate the significance of humps and bumps in the phased diagrams of RR Lyrae stars was strictly subjective. We visually classified all RR Lyrae phase-folded light curves into four categories (1 - 4) based on the visual prominence of the aforementioned phase curve features (with 4 standing for a strong and 1 for a weak shock effect on the phased light curve). We note that this categorization was purely informative and in the following analysis served only for the assessment of the calculated values, in order to decide which of them best describes the impact of the humps and bumps on the phased light curves.

In order to quantitatively estimate the strength of the humps and bumps, we developed two analogous approaches (described in following subsections) using the Fourier decomposition of the phased light curves and the Gaussian fitting of the residual.

The initial steps for both approaches were similar in phasing the light curves and normalizing the magnitudes from the observed data. This way we scaled the time (Heliocentric Julian Date) and magnitude component of the data to encompass a range of $\approx \pm 0.5$ for all stars and both parameters become unitless (see the top and bottom panels of Fig. 8.3.1).

For each phased light curve we then visually marked the approximate center of the hump and bump $(x_{\mathrm{HUMP}}, y_{\mathrm{HUMP}}, x_{\mathrm{BUMP}}, y_{\mathrm{BUMP}})$ on the descending/ascending branch light curve sections (see red squares in the left-hand panels of Fig. 8.3.1). We note that we center our phased light curves at zero (maximum brightness), thus all values of x_{HUMP} and x_{BUMP} are negative. The positions for humps and bumps on the phased light curves are discussed in the Sec. 8.4.1.

Strength of a hump

For the study of the main shock (hump) in the atmospheres of RR Lyrae stars, we proceeded in the following way. First, we fitted the I-band light curves with a truncated Fourier series:

$$m(t) = A_0^I + \sum_{k=1}^{n} A_k^I \cdot \cos\left(2\pi k\vartheta + \varphi_k^I\right), \tag{8.1}$$

where the A_k^I stand for amplitudes and φ_k^I represent phases. The ϑ is a phase function, which is described as the ratio between the time difference of the Heliocentric Julian Date

[1] Stars brighter than 16.5 mag in the I-band have mean photometric errors below 0.01 mag in OGLE-IV.

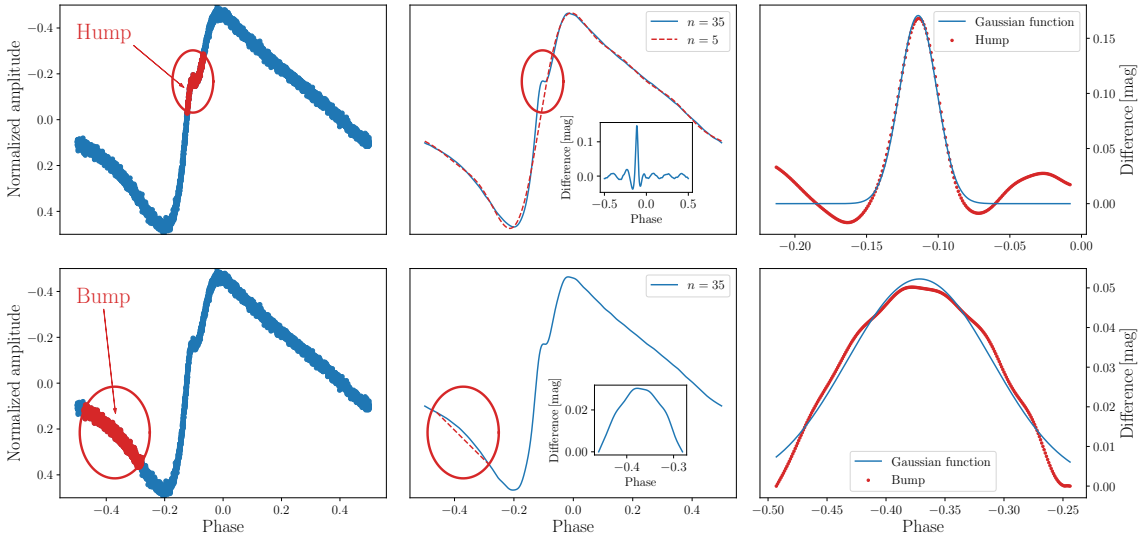

Figure 8.3.1: Visual description of the analysis of the hump (top panels) and bump (bottom panels) features in one of the sample stars. The left panels depict the phased light curve of a selected star with I-band photometric data represented with blue dots. The red ellipse denotes the shock features: hump (top left panel) and bump (bottom left panel). The red dots denote the removed portions of the phased light curve. The middle panels show the model light curve described by a high-order Fourier ($n = 35$ in the legend of the panels) fit as given by Eq. 8.1 (blue solid line). The dashed red line in the top middle panel represents a low-order Fourier fit ($n = 5$ in the legend of the panel) to the phased light curve with the hump region removed (i.e., the section of the light curve encompassed by the red ellipse), and the inset in the same panel shows the difference between the high- and low-order fits. The bottom middle panel shows a linear fit (red dashed line) for the area around the bump, and the inset shows the difference between the fit of a high-order Fourier series and the linear fit in the vicinity of the bump. The right-hand panels show the result of subtracting the linear fits from the Fourier models (red dots), as fitted with a Gaussian (blue solid line).

and time of maximum brightness $HJD - M_0$, and pulsation period P: $\vartheta = (HJD - M_0)/P$. In order to properly describe small features between brightness minimum and maximum, we chose for all stars a high order of the Fourier fit of $n = 35$ (blue solid line in the middle panels of Fig. 8.3.1). This high degree thoroughly described the region between the brightness minima and maxima where the hump occurs. We emphasize that pulsation properties like total amplitude and Fourier parameters were determined based on observed, unnormalized data.

Secondly, using the provisional centers of the hump in the normalized light curves space we removed the portion of the phased light curve containing the hump (red ellipse in the top left-hand panel of Fig. 8.3.1). The size of the removed portion was 0.15 wide in phase, and 0.3 high in normalized magnitude (denoted by the red ellipses in Fig. 8.3.1)[2]. This trimmed phased light curve was again decomposed using the low-order Fourier series (in the majority of the cases, orders from four up to fifteen were used) tailored for each phased light curve

[2]The cut out region was based on the center of the hump and bump $(x_{\mathrm{HUMP}}, y_{\mathrm{HUMP}}, x_{\mathrm{BUMP}}, y_{\mathrm{BUMP}})$ fulfiling following criteria $x \pm 0.075$ and $y \pm 0.15$.

individually (red dashed line in the top middle panel of Fig. 8.3.1).

In the next step, we subtracted both Fourier models (red and blue lines in top middle panel of the Fig. 8.3.1) and fitted the hump region using a Gaussian function (see top right-hand panel of Fig. 8.3.1). We integrated the area under the Gaussian function to obtain the amplitude (height of the hump), the full width half maximum (FWHM) of the hump, and the area under the Gaussian curve. An example of a fitted Fourier difference is shown in the top right-hand panel of Fig. 8.3.1.

Strength of a bump

In the case of the early shock, i.e., the bump, we proceeded in a similar way as for the main shock.

First, we decomposed the full phased light curve with a low degree Fourier series, since the area prior to the brightness minimum is more sensitive to overfitting. Subsequently, we removed the area around the bump, using the bump's approximate center and width in phase space ± 0.125 for each light curve separately. Since the Fourier decomposition of the light curve with a large phase gap led to unrealistic results we adopted a different approach than in the case of the hump using solely the removed region of the Fourier model. For this clipped region, we determined the line connecting the beginning and end points. Then, we subtractred this straight line from the Fourier model of the bump in the relevant phase range – ± 0.125 (see the inset in the bottom middle panel of Fig. 8.3.1). We then fitted the resulting difference using a Gaussian function (see bottom right-hand panel of Fig. 8.3.1) and integrated over it, obtaining, as in the case of the hump, its amplitude (height of the bump), the FWHM of the bump, and the area under the Gaussian curve.

In the last step, we compared the visually analysed sample (classified into four groups, see Sec. 8.3) with the obtained Gaussian properties of the humps and bumps. We conclude that the amplitude of the Gaussian curves describes the strength of the bump/hump features best, as it correlates well with the four categories we assigned to the light curves based on the visual prominence of hump/bump features, where classes 1 and 2 (denoting a negligible hump/bump) have small amplitudes and vice versa for classes 3 and 4 where we observe a prominent distortion and high amplitudes ($r_{\rm vis}^{\rm amp} = 0.86$ and $r_{\rm vis}^{\rm amp} = 0.72$, for hump and bump, respectively). Thus, for the remainder of this study, we will use it as a qualitative estimate of the shock impact on the phased light curve. We note that the amplitudes of humps and bumps are more than three times larger than the photometric errors of the dataset, therefore all amplitude detections are significant.

Humps and bumps in the phased light curves

In this section, we will discuss the positions and effects of humps and bumps on the phased light curves. We use the determined centers of humps and bumps ($x_{\rm HUMP}, y_{\rm HUMP}, x_{\rm BUMP}, y_{\rm BUMP}$) which represent the position in the phase x and in the normalized magnitudes y.

Timing of the hump and bump

In RR Lyrae stars, we observe that bumps occur on the descending branch of the light curve before the brightness minima, while the hump occurs on the ascending branch between the brightness minima and maxima. Using the centers of the humps and bumps for the stars in our sample we tested whether the positions of the shock features change with the pulsation properties.

In Fig. 8.4.1 we displayed dependences between the coordinates of the humps (top panels) and bumps (bottom panels) in the normalized phased light curves. The colour-coding of individual points is with respect to the pulsation period (left-hand panels), total amplitude of brightness changes (middle panels), and rise time (right-hand panels). The rise time (from here on referred to as RT) indicates the phase interval between the brightness minima and maxima on the phase curve. In these diagrams, we see that the centers of the humps occur on the ascending branch above the mean magnitude (negative values in y_{HUMP}), contrary to bumps, where the centers appear on the descending branch below the mean magnitude (positive values in y_{BUMP}).

In the top panels, we see a correlation between the humps' center and the pulsation properties. The RRab variables follow the period-amplitude relation (albeit with scatter caused, e.g. by the Oosterhoff dichotomy, Oosterhoff 1939), thus the correlations with pulsation period and amplitude are most likely not independent. The location of the hump changes with pulsation period and amplitude: as we move from minimum periods and amplitudes toward the average ones, the hump moves toward the brightness maximum. An even stronger correlation with the pulsation properties is noticeable in the location of the bump. In this case, the bump moves toward the brightness minimum with increasing amplitude and decreasing pulsation period.

In the case of the horizontal coordinate x_{HUMP} and x_{BUMP} we used the RT (phase interval) for comparison. In the case of the x_{HUMP} we see a strong anti-correlation with the RT, with a Pearson correlation coefficient $r \approx -0.97$. The ratio of the two parameters clusters around 0.5, thus the hump occurs almost midway between the phases of brightness minimum and maximum. As in the case of the hump, we found a strong correlation between RT and x_{BUMP} for the early shock, with a Pearson correlation coefficient of $r \approx -0.89$ (for reference see right-hand panels of Fig. 8.4.1). Thus, from Fig. 8.4.1 and from the aforementioned correlation coefficient we see that the pulsation properties are mainly correlated with the horizontal coordinate x_{HUMP} and x_{BUMP}.

For the studied RR Lyrae stars, we found that the location of the early and main shock on the phased light curves is connected with the pulsation properties of a given star. Although we note that pulsation period, amplitude, and RT are closely correlated; $r = -0.68$ for the pulsation period and amplitude, $r = -0.90$ for the amplitude and RT, and $r = 0.74$ for the pulsation period and RT. Therefore, the connection between the location of the humps and bumps with the pulsation parameters can stem from the correlation between individual pulsation parameters.

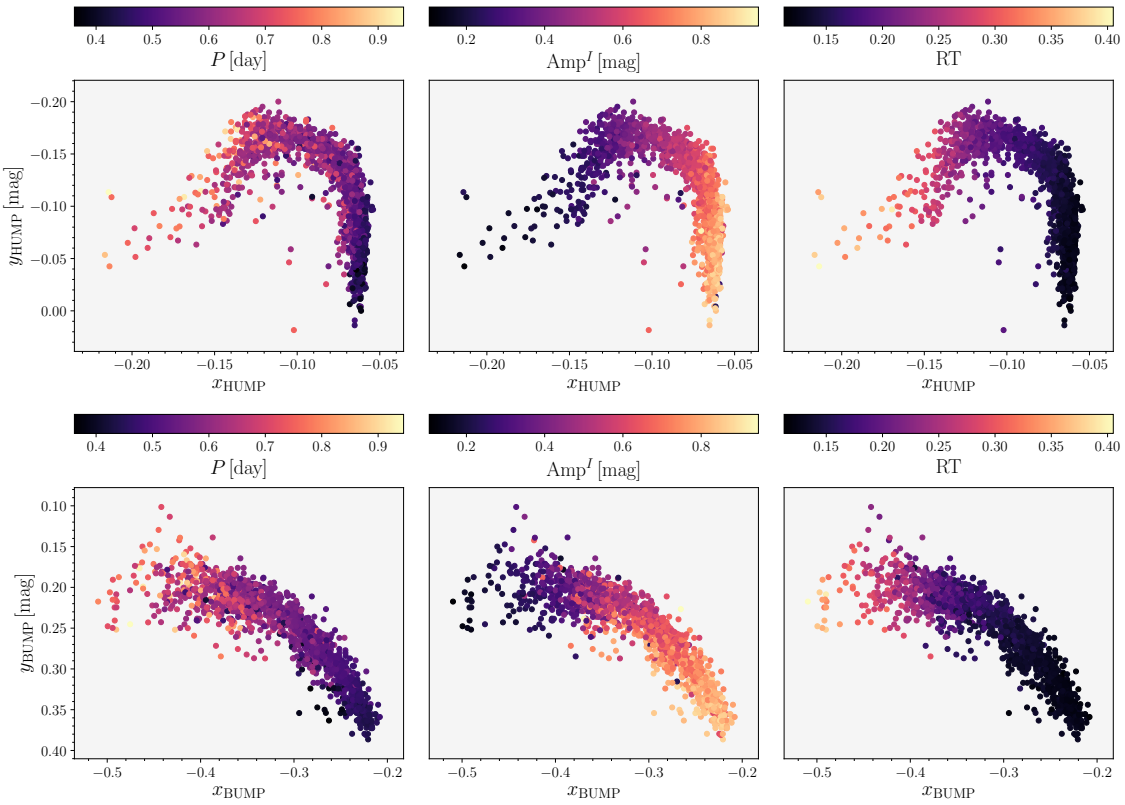

Figure 8.4.1: The relations between the coordinates of the centers for the main and early shock features in the phased light curves. The top panels display $x_{\rm HUMP}$ vs. $y_{\rm HUMP}$ and the bottom panels show the same dependence but for the bump, $x_{\rm BUMP}$ vs. $y_{\rm BUMP}$. The colour-coding is based on the pulsation period (left-hand panels), total amplitude (middle panels), and RT (right-hand panels) of the individual stars.

Relationships between shocks and light curve parameters

In this section, we will explore the relationships between the humps and bumps and the light curve properties of RR Lyrae stars.

One of the most important diagrams in studies focused on the RR Lyrae stars is the period-amplitude (hereafter *P-A*) diagram, which relies on reddening-free quantities and serves for, e.g., the separation of RR Lyrae subtypes, identification of Oosterhoff populations, and rough estimates on the metallicity of their host stellar system. Fig. 8.4.2 shows the *P-A* diagram with colour-coding for the amplitude of the hump. Stars with the most pronounced main shock (hump) are located in the lower part of the *P-A* diagram. We see a significantly less pronounced hump in the high-amplitude regime. The hump almost disappears at the very low-amplitude end of the *P-A* diagram. The light curves of these stars do not appear to be affected at all by the main and early shocks (see Fig. 8.4.3). The main shock has a negligible effect on the light curves of high-amplitude, short-period (from here on referred to as HASP; Fiorentino et al. 2015) RR Lyrae stars. These regions in the diagram are marked by grey

grid lines, and the arrows show to which region each of the insets around the *P-A* diagram belong. The examples of phased light curves were chosen based on the average size of the amplitude of the hump in a given grid region of the *P-A* diagram.

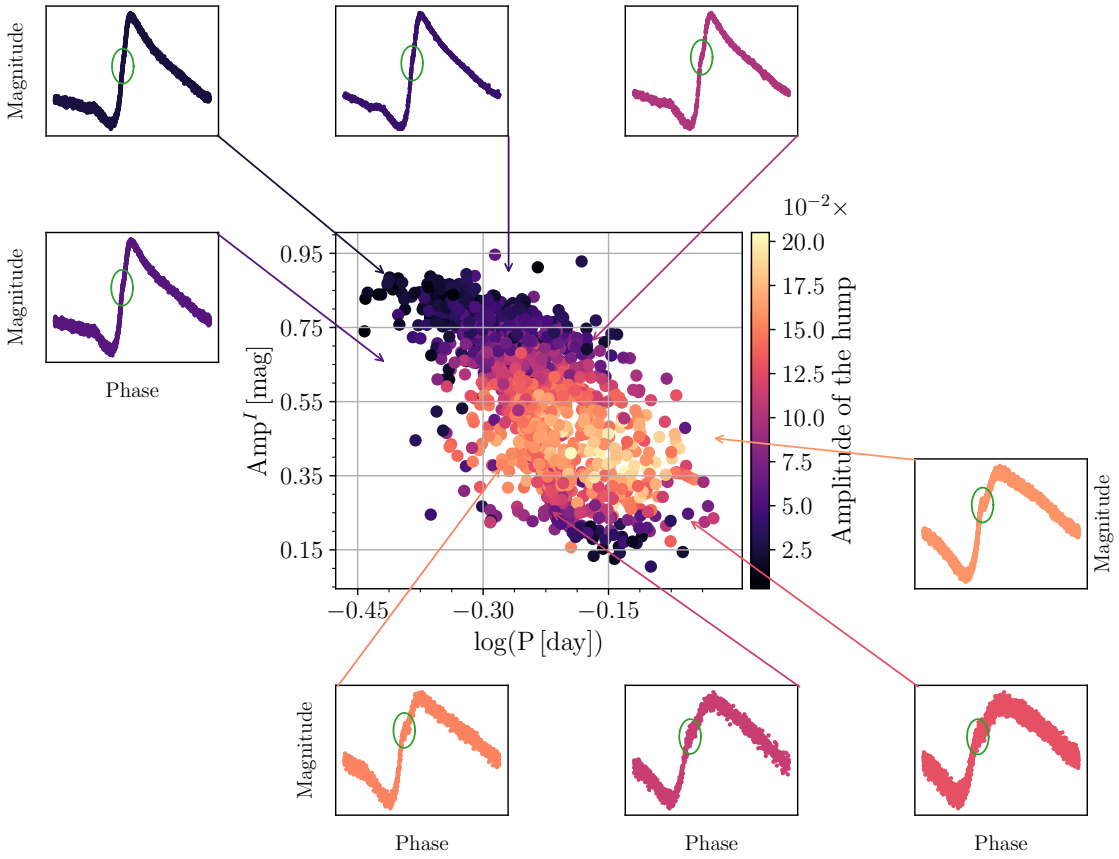

Figure 8.4.2: The *P-A* diagram for our studied stars with a colour-coding based on the amplitude of the hump for the individual objects. The insets depict examples of phased light curves for a given region (grey grid) in the *P-A* diagram indicated by the arrows. The green ellipses approximately denote the location of the hump.

The situation for the bump in Fig. 8.4.3 is different. The effect of the early shock is stronger for stars with an amplitude higher than 0.4 mag in the I band. The HASP RR Lyrae stars, contrary to the case of the main shock, show a pronounced effect of the early shock on the light curve. We see a nearly linear decline of the size of the bump with the decreasing amplitude and increasing pulsation period. A similar linear decrease is also visible if we move toward the HASP stars but variables in this region of the *P-A* diagram still show a considerable hump size. Bumps among the low-amplitude (around 0.2 mag in I band) RR Lyrae stars have almost no sign of an early shock in their light curves, similarly to the humps in Fig. 8.4.2.

In the top panels of Fig. 8.4.4 we show the amplitude vs. RT dependence with the amplitude of the hump and bump colour-coded. In the case of the hump, we see that variables

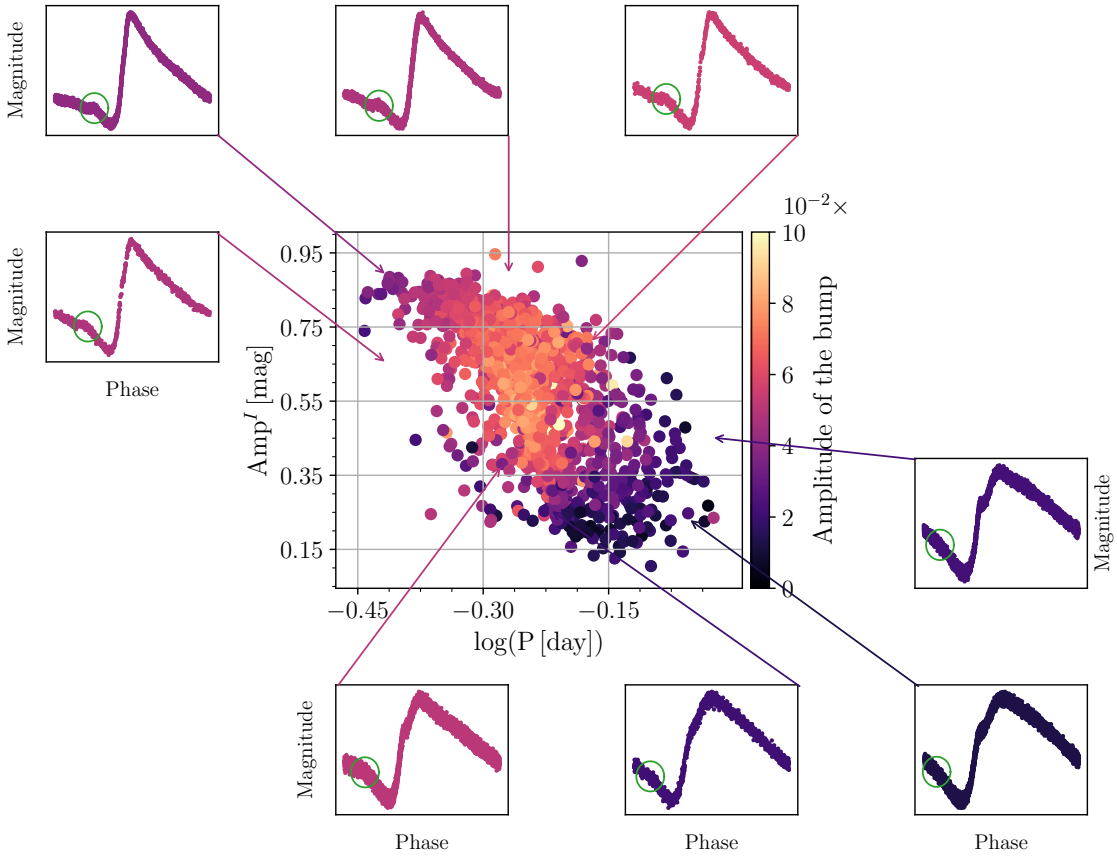

Figure 8.4.3: Similar as Fig. 8.4.2 but the colour-coding of the individual points is based on the amplitude of the bump, and the green ellipses approximately denote the location of the bump.

with a pronounced hump (hump amplitude larger than 0.12) concentrate below the average value for the amplitude (0.6 mag). As we move outward from the center the strength of the main shock decreases. Similarly to the case of the *P-A* diagram we see that stars with a swift (small RT) or rather slow (high RT) change between minimum and maximum brightness tend to have smaller values for the amplitude of the hump than the stars with average RT. In the case of the bump (the right-hand top panel of Fig. 8.4.4) we see a different dependence. Stars with a pronounced early shock have a short RT and large amplitude (as shown in the case of the *P-A* diagram).

The bottom panels of Fig. 8.4.4 show φ_{31} vs. R_{31} dependencies with a colour-coding based on the strength of the hump (left-hand panels) and bump (right-hand panels). These diagrams can be used to identify modulated fundamental-mode RR Lyrae stars (Prudil & Skarka 2017) or to identify signatures of the two Oosterhoff populations (Prudil et al. 2019a). In the left-hand panel, we see that a large number of stars, with significant hump, is concentrated on the tail of the Oosterhoff II locus (cf. top panel of fig. 4 in Prudil et al. 2019a).

In the right-hand panels the situation is different: stars with pronounced early shock are concentrated in the lower values of φ_{31}. The lower right panel shows that the increasing size of the bump is followed by an increase in R_{31} and a decrease in φ_{31}. A more detailed analysis of the physical properties (e.g. metallicity, absolute magnitude, and effective temperatures) and association with Oosterhoff populations can be found in Sec. 8.5. It is important to point out that pulsation period, amplitude, RT, and other light curve parameters are strongly correlated, therefore it is expected to find correlations with other parameters as well.

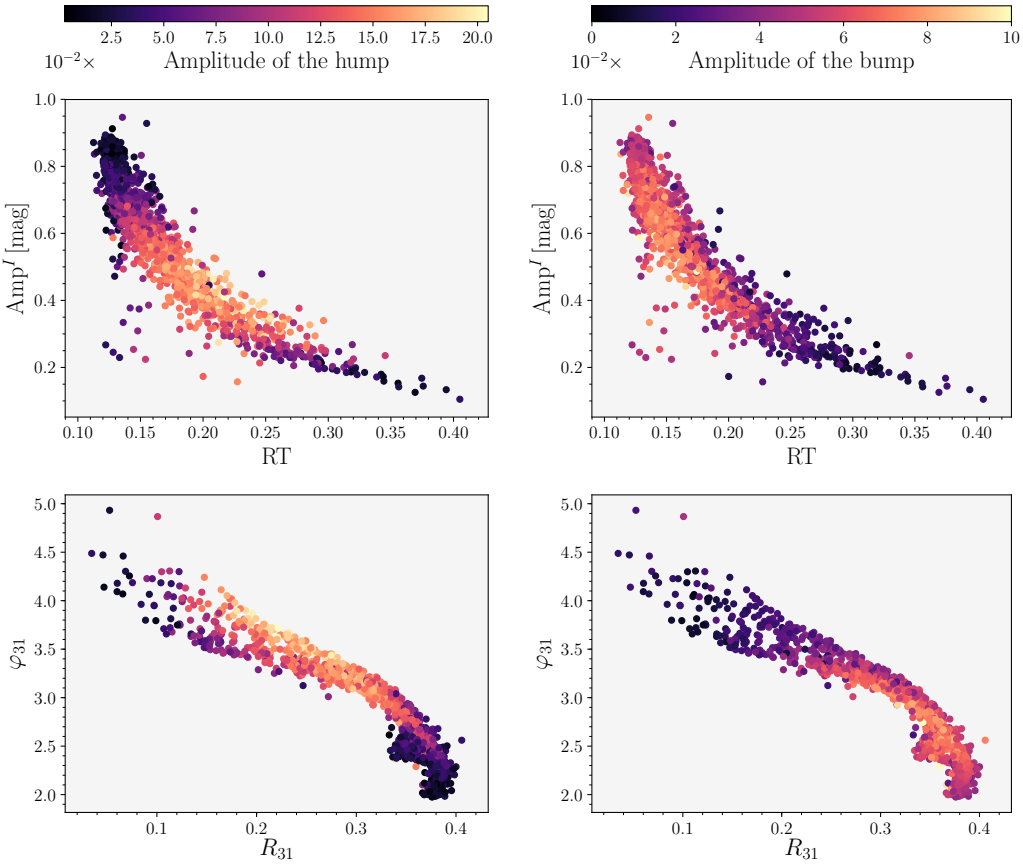

Figure 8.4.4: The RT vs. pulsation amplitude (top panels) and φ_{31} vs. R_{31} (bottom panels), colour-coded with respect to the size of the amplitude of the shock event.

In Table 8.4.1 we list the Pearson correlation coefficients, r, between the hump/bump sizes and pulsation properties of the studied stars. We highlight the strong correlations and anti-correlations between pulsation parameters and shock events. We note that the size of a hump is linked with some of the pulsation properties, namely the phase differences φ_{21}, φ_{31}, and I band amplitude. Furthermore, for the amplitude ratios R_{21} and R_{31} we observe negligible anti-correlations with the main shock. For the early shock, we observe strong and moderate correlations between the prominence of the bump and most of the pulsation

Table 8.4.1: Table for the Pearson coefficients r between various pulsation properties and the effect of the main and early shock on the phase curves. The columns from left to right list the pulsation features, columns 2 and 3 list Pearson coefficients. Strong correlations ($|r| > 0.7$) are highlighted in boldface fonts.

	r^{HUMP}	r^{BUMP}
R_{21}	−0.182	**0.709**
R_{31}	−0.390	**0.717**
φ_{21}	0.667	−0.560
φ_{31}	0.641	−0.563
P [day]	0.537	−0.466
Amp^{I} [mag]	−0.630	0.449
Amp^{K} [mag]	−0.388	0.389
RT	0.425	−0.661

properties. We also notice that in almost all cases we observe an anti-correlation between the sizes of a hump and bump for individual pulsation properties. In cases where we observe a positive correlation with the hump and the pulsation feature, we observe a negative correlation for the bump. We searched for correlations among higher orders of the Fourier amplitude ratios (up to R_{151}) and found that the strongest correlations with the main shock are for R_{61}, R_{131}, and R_{141}, while the early shock is more correlated with lower orders – R_{21}, R_{31}. To summarise, several of the pulsation properties of the studied RR Lyrae stars seem to be closely connected with the shock effects on the phased light curves.

We note that, in the available light curves, we do not see other shock events (e.g., a *jump*, or *lump*; Chadid et al. 2014), but in a handful of cases we notice a feature before the bump that can be ascribed to the post-maximum shock wave or rump (Chadid et al. 2014).

The link between the pulsation parameters and the sizes of the hump and bump is also visible in Fig. 8.4.5, where we compare the sizes of the humps and bumps in our RR Lyrae sample. We see that stars with the highest amplitudes (brighter points) and short periods (smaller points) have an average size early shock and almost no main shock feature in their phased light curves. On the other hand, we see that the majority of the stars with the lowest amplitudes (below 0.2 mag) have very little signs of both shocks. Unlike for short period RR Lyrae stars, the pronounced main shock seems to be concentrated among the average and long-period RR Lyrae variables.

Shocks in the colour-magnitude diagram

This section is focused on the connection between the sizes of the main and early shock with general properties of the studied stars from Prudil et al. (2019a) (metallicities, Oosterhoff associations, colour indices and dereddened magnitudes).

For the purpose of this paper, we used the Oosterhoff identification provided by Prudil et al. (2019a); from our studied RR Lyrae sample, 1101 objects are associated with the Oosterhoff group I (Oo I) and 384 belong to the Oosterhoff group II (Oo II). We compared

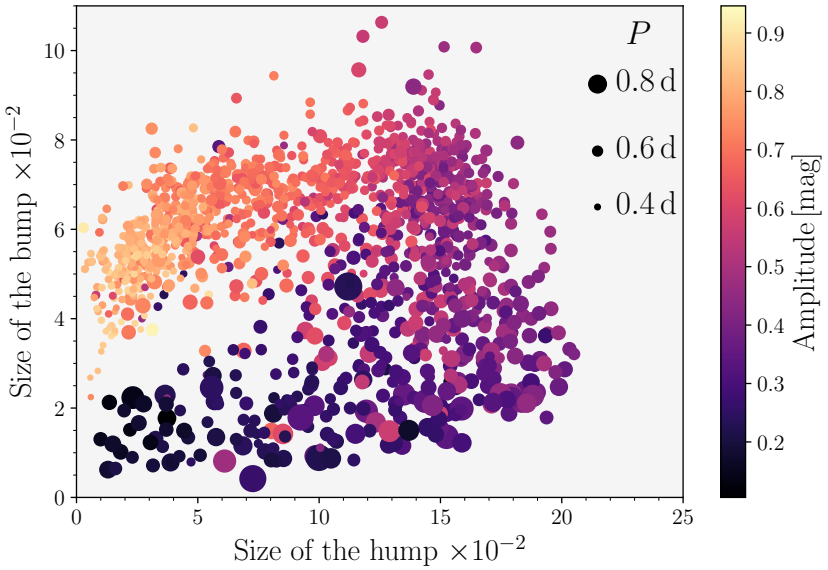

Figure 8.4.5: The size distribution of main and early shock. The colour-coding and point size are based on the amplitude and pulsation period of the individual objects as shown in the legend.

whether the appearance of humps and bumps in the two Oo populations is different. We noticed that the size of the main shock is the same within the errors for both Oosterhoff groups. For the Oo II group the median value of the amplitude of the hump is equal to $(12 \pm 5) \cdot 10^{-2}$, and for the Oo I population its value is $(10 \pm 5) \cdot 10^{-2}$. The median value for the amplitude o the bump is again similar for both Oo types, $(6 \pm 1) \cdot 10^{-2}$ (Oo I stars) and $(5 \pm 2) \cdot 10^{-2}$ (Oo II stars), which is in agreement with the population effect of the Oosterhoff dichotomy as suggested by Fabrizio et al. (2019).

The colour-magnitude diagram (from here on CMD), especially the fundamental mode instability strip (IS) of the studied stars, Fig. 8.5.1, shows very interesting features. Stars with a strong hump are concentrated on the cooler side of the IS, and as we move toward the blue edge of the IS, the hump becomes less pronounced and almost vanishes around $(I-K)_0 \approx 0.55$ mag. Stars that we find close to the blue edge of the fundamental-mode IS are stars with high amplitudes and short pulsation periods (see *P-A* diagram in Fig. 8.4.3). We note that we find stars with very little sign of the hump at the red edge of the IS, but they are scarce. For the bump the situation is almost the opposite, we see stars with a pronounced bump in the blue and central part of the IS. As we move toward the fundamental red edge, the effect of the bump on the phased light curve decreases, and almost vanishes once we cross $(I-K)_0 \approx 0.7$ mag. This correlation between the position in the CMD and the shocks is most likely not connected with the metallicity, since we detect no correlation between [Fe/H] and the shocks ($r = -0.05$ for humps and $r = -0.08$ for bumps, respectively, see Fig. 8.5.2), but appears to be connected with the pulsation periods (for correlation coeficients see Tab. 8.4.1). In the CMDs we noticed a smooth gradient of the bump strength, unlike in the case of the hump.

This is most likely due to the higher intrinsic scatter of the hump properties, and stars that have a pronounced hump (e.g., 0.14 and higher) are much less numerous than stars that have pronounced bump (e.g., 0.05 and higher) by at least a factor of 2. We simply do not have that many stars with amplitudes around 0.45 mag, and periods of 0.7 days (where the hump is large), but we have plenty of stars with amplitudes around 0.55 mag and periods around 0.55 days (where the bump is large).

In addition, the strong correlation with colours and amplitudes suggests that we are looking at the combination of these effects in the CMD. The horizontal axis of the CMDs in Fig. 8.5.1 is based on the period metallicity luminosity relations; (Catelan et al. 2004; Muraveva et al. 2018); furthermore, the same relations were used to estimate the extinction in the direction of the studied stars. Thus these assumptions enter into our analysis and the general properties from the *P-A* diagram transfer into the CMD distribution of the RR Lyrae stars.

We note that the lines in Fig. 8.5.1 (blue and red) depicting the boundaries of the IS for the fundamental mode pulsators were calculated using linear pulsation models from Smolec & Moskalik (2008) with a mixture of heavy elements based on Asplund et al. (2009) and OPAL opacities (Iglesias & Rogers 1996). We used the same grid of physical parameters as in Prudil et al. (2019a).

The period change rate

In the left panel of Fig. 8.5.1 we see that some stars without observable hump are present close to the red edge of the IS, therefore in a region where we also find stars with a rather pronounced hump (0.5 – 0.7 mag range on the horizontal axes). To gain further insight into this phenomenon, we have investigated whether the prominence of the hump and bump features may be connected with the direction of the evolution of the star in the CMD. At least in principle, one may assess the evolutionary direction of a pulsating star by means of the secular rate of change of its period, a phenomenon that is caused by the slow change in the star's mean density as it crosses the IS. In general, an RR Lyrae star that crosses the IS on its way to the asymptotic giant branch (i.e., redwards) is expected to show a positive period change rate and vice-versa for those evolving away from the zero-age horizontal branch (ZAHB) in blueward direction.

In order to explore the possible connection between shocks in RR Lyrae atmospheres and their evolutionary status, we used the data from previous releases of the OGLE survey of the Galactic bulge (Udalski et al. 1994, 1995b,a, 1996, 1997; Soszyński et al. 2011, 2014). The OGLE photometry spans up to 25 years for some objects, which provides a more or less sufficient baseline to study changes in the pulsation period. Some of our sample stars were not observed during the previous phases of the OGLE survey, therefore they have a substantially smaller baseline (≈ 7 years), and we omitted them from the subsequent analysis (46 objects).

For the purpose of constructing the $O-C$ diagrams (observed minus calculated) for the studied RR Lyrae stars, we utilized the whole light curves using the method proposed by Hertzsprung (1919), where we create a phased light curve template that we used to estimate the phase shift between individual observational seasons. We binned the available photome-

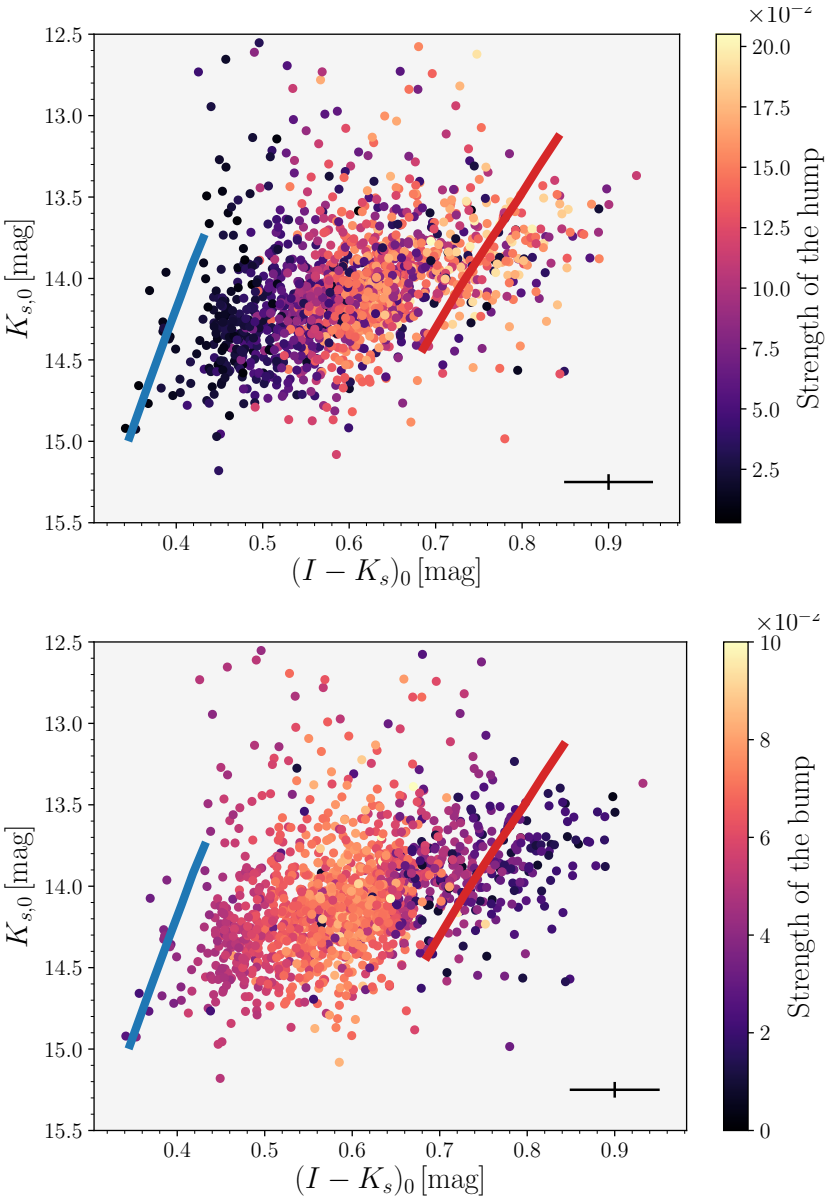

Figure 8.5.1: The CMD for the studied stars with colour-coding representing the effect of the hump (left-hand panel) and bump (right-hand panel). The edges of the fundamental-mode IS are marked with blue and red solid lines that were calculated using the linear pulsation models from Smolec & Moskalik (2008). The median of the errors on colour and mean magnitude are depicted with black lines in the bottom right corner of each panel.

try based on the observational seasons (colour-coding in the bottom panel of Fig. 8.5.3). For each subsample we phased the photometric data using the pulsation ephemerides from the OGLE-III data release. Each phased subsample was then fitted with a light curve template. The shift in phase of the brightness maximum was estimated and multiplied by the pulsation

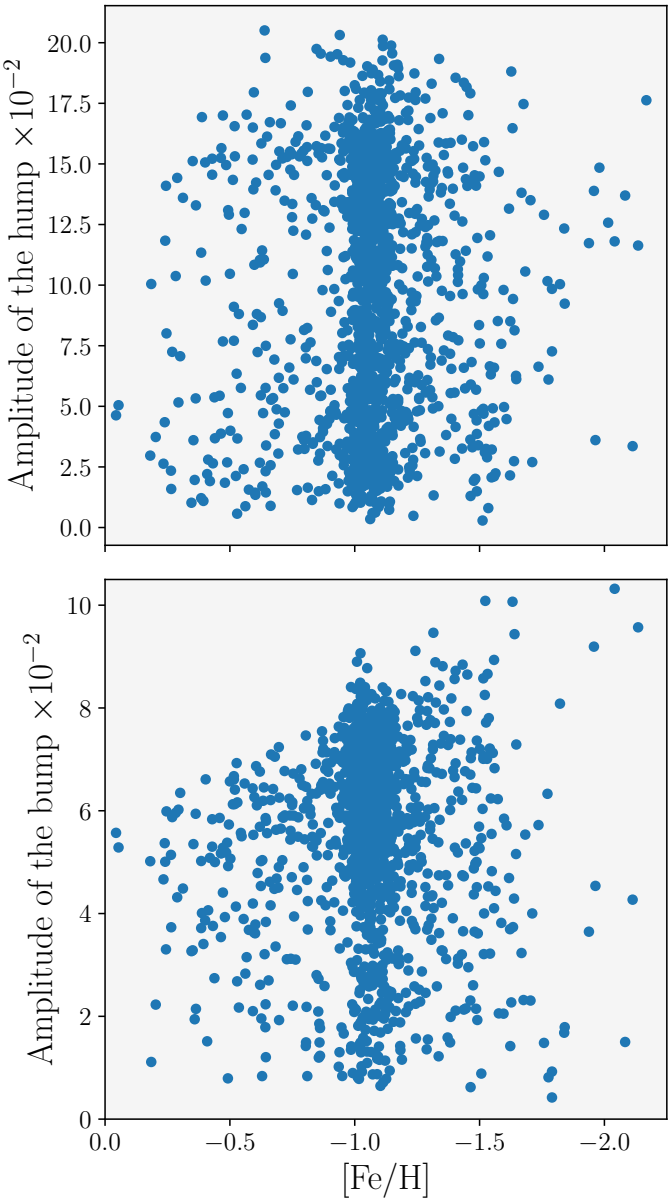

Figure 8.5.2: The photometric metallicity [Fe/H] is shown as a function of the hump (top panel) and bump (bottom panel) strength for all studied RR Lyrae stars.

period in order to get the $O-C$ value (depicted in the top panel of Fig. 8.5.3 with respect to the time span).

The $O-C$ diagrams of RR Lyrae stars can show various trends. The most common ones are a linear trend across the epochs (inaccurate ephemerides) or a parabolic trend that suggests

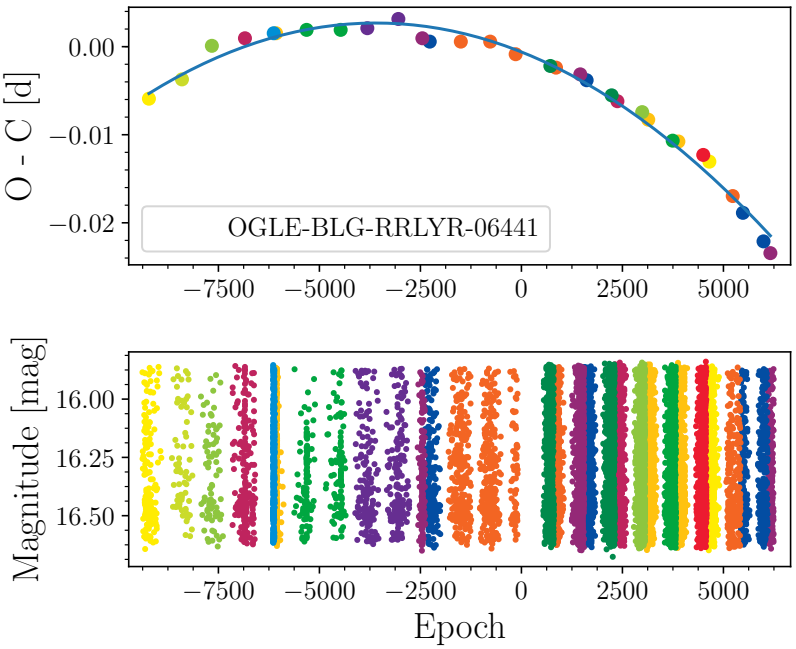

Figure 8.5.3: An example of an $O-C$ diagram for one of the stars from our sample (top panel) with all available photometry in the bottom panel. The photometry in the bottom panel is colour-coded based on the data bins for the construction of the $O-C$ diagram.

a change in the pulsation period. To estimate possible changes in the pulsation periods, the data in the $O-C$ diagram are fitted with the following quadratic equation:

$$O-C = a_0 + a_1 \cdot E + a_2 \cdot E^2, \tag{8.2}$$

where a_n are coefficients of the polynomial function of degree n, and E is the number of epochs that elapsed from M_0 (in our case M_0 corresponds to an initial time of maximum brightness from the OGLE-III survey). The period change rate β is calculated via:

$$\beta = \frac{2 \cdot a_2}{P}. \tag{8.3}$$

Not all of the stars from our sample undergo a period change; some have simply incorrectly determined ephemerides. In order to separate stars with changing pulsation periods from those with constant periods, we employed the same criterion as used by Jurcsik et al. (2001):

$$|a_2| / \sigma_{a_2} > 2. \tag{8.4}$$

Stars that fulfill this condition were considered as pulsators undergoing an increase/decrease in their pulsation periods. For 956 stars from our sample, we detected changes in the

pulsation periods. It is important to add that the use of the period-change rate as an evolutionary clock for RR Lyrae stars is hampered by the period change noise (for more details see Subsection 8.5.1).

In Fig. 8.5.4 we show the dependences of the period change rate on the strength of humps (top panel) and bumps (bottom panel) and their colour, $(I-K_s)_0$. In both panels we see that the majority of the stars cluster inside the $\pm 0.5\,\mathrm{d\,Myr^{-1}}$ range and approximately 10 % of the stars have a higher period change rate β, of which 66 % show an increase in pulsation periods (similar to the previous studies of period changes in RR Lyrae stars; e.g., Le Borgne et al. 2007; Kunder et al. 2011). We do not observe any differences in β in stars close to the red edge of the IS with different shock sizes. What we see in general, especially in the bottom panel, is that stars located near the red edge of the IS have on average a larger β in comparison with stars in the middle or close to the blue edge of the IS. Stars with large positive β in the red part of the IS are probably leaving the IS (marked with a dashed blue rectangle in Fig. 8.5.4), while stars with large negative β are probably just arriving at the IS and ZAHB (Silva Aguirre et al. 2008) or are undergoing sudden structural instabilities before leaving the IS (e.g., Sweigart & Renzini 1979; Koopmann et al. 1994). We do not observe any relation between the period change rate and the strength of the hump or bump with respect to their position in the IS.

Note on the period change rate with respect to the Oosterhoff groups

One of the possible explanations of the Oosterhoff dichotomy is the hysteresis mechanism, which suggests that Oo I stars evolve from the red edge toward the blue edge of the IS while Oo II stars evolve in the opposite direction (van Albada & Baker 1973). This hypothesis has been tested by, e.g., Kunder et al. (2011), who calculated the period change rate for RR Lyrae stars in IC 4499 and found no correlation between β and the Oosterhoff population. In general, we observe a positive period change rate among RR Lyrae stars in various globular clusters. Therefore, we used our large sample to test this hypothesis based on the determined period change rates and association with the Oosterhoff groups for individual pulsators. We found that 59 % of the stars from our sample exhibit a positive period change, which is in agreement with the observations of MW globular clusters, see fig. 15 in Catelan (2009) or fig. 6.16 in Catelan & Smith (2015). Both Oosterhoff groups exhibit on average a positive period change rate, $0.02\,\mathrm{d\,Myr^{-1}}$ and $0.16\,\mathrm{d\,Myr^{-1}}$ for Oosterhoff I and Oosterhoff II, respectively. We find that 68 % of the Oo II and 55 % of the Oo I RR Lyrae stars have a positive period change rate. In addition, the vast majority of stars with significant period change rates (positive and negative) are associated with the Oo II group and are located close to the red edge of the IS.

We note that the findings above can be affected by the presence of peculiar period changes (period change noise) with respect to the theoretical predictions. For RR Lyrae stars with the largest observed period change rates, deviations with respect to theoretical predictions can reach up to an order of magnitude or more (see also Jurcsik et al. 2012). Furthermore, some RR Lyrae undergo large, sudden changes in their pulsation periods, the latter sometimes increasing but others decreasing (see, e.g., Catelan & Smith 2015), and there is at least one known case of a double-mode RR Lyrae star (V53 in M15) whose fundamental and

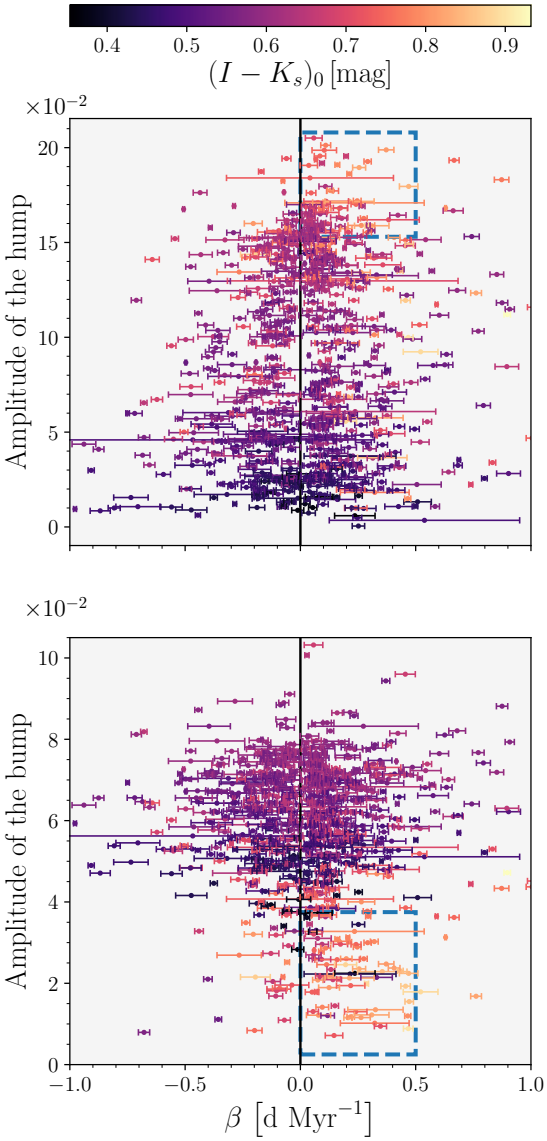

Figure 8.5.4: The period change rate β is shown as a function of the size of the amplitude of the hump (top panel) and bump (bottom panel). The colour coding is based on the colour $(I-K_s)_0$. The two blue dashed rectangles in both panels mark the positions of two groups that lie close to the red edge of the IS.

first overtone components have period change rates of different signs (Paparo et al. 1998). There have been several attempts to explain the presence of period change noise, invoking, e.g., large mass loss episodes (Laskarides 1974), discrete mixing events (Sweigart & Renzini 1979), the difference in the helium composition below the convective zone (Cox 1998). Considering the timespan of our sample, some of the studied stars may be affected by the

aforementioned abrupt changes in pulsation periods and affect the overall conclusions.

Summary and conclusions

In this paper, we provide the most extensive study of the effects of the main and early shock on the light curves of RR Lyrae stars. We used photometric data from the fourth data release of the OGLE Galactic bulge survey for fundamental mode RR Lyrae variables. We selected only non-modulated variables with abundant and good quality photometry studied in Prudil et al. (2019a). In the end, we analysed 1485 RR Lyrae stars and estimated the location and size of the humps and bumps in the phased light curves.

We found that the positions of the humps and bumps in the phased light curves are related to the pulsation properties (pulsation period, amplitude, RT) of the studied stars. Main and early shocks are most pronounced in different regions of the *P-A* diagram. Stars with a pronounced hump are centered around average and below-average amplitudes at longer pulsation periods. As we move toward variables with rather low/high amplitudes, the main shock weakens and eventually disappears from the phased light curves, especially for HASP variables (Fiorentino et al. 2015). The pulsators with a pronounced early shock are, on the other hand, located in the high amplitude regime. With decreasing amplitude, the effect of the bump declines. Overall, the bump size seems to strongly correlate with the amplitude ratios of the studied stars.

The CMD of the studied stars revealed a dichotomy between stars with and without strong shock features. This dichotomy is probably caused by the correlation between pulsation periods and amplitudes with colours and dereddened magnitudes, which are based on period-metallicity-luminosity relations. Further examination using the photometry from the TESS and *Kepler* space telescopes in combination with *Gaia* parallaxes could shed some light on the structure of the IS based on the humps and bumps.

Several of our studied stars stand out in the CMD with their weak shock feature while being located in a region with a rather pronounced hump or bump. In order to investigate their evolutionary status, we calculated the period change rate β from constructed $O-C$ diagrams. We found that the majority of the stars clump around period change rates of $\pm 0.5\,\mathrm{d\,Myr^{-1}}$ and only 10 % of the stars exceed this period change rate (which is in agreement with previous studies of the period-change rate, e.g., Le Borgne et al. 2007; Kunder et al. 2011; Jurcsik et al. 2012). We do not observe a difference in period change rate among stars with different strengths of the main and early shock. In general, the majority of the analysed stars show positive β, which is especially evident close to the red edge of the IS, where stars that are most likely leaving the IS are expected.

This is also reflected in the period change rate among the two Oosterhoff groups in our sample. In the Oosterhoff population II, 68 % of the stars have a positive period change, while in Oosterhoff group I, 55 % exhibit a period increase. This suggests that stars of Oosterhoff group I are located close to the ZAHB, while Oosterhoff population II variables already left the ZAHB and are moving toward the red side of the instability strip (a similar effect was also observed in M3 by Jurcsik et al. 2012).

A dedicated spectroscopic survey in parallel with precise photometry optimized for shocks

and their effects over a large spectral range should provide deeper insight into this phenomenon.

CHAPTER 9

SUMMARY AND OUTLOOK

"I think this just might be my masterpiece."
— Lt. Aldo Raine, front line

The presented thesis covers a broad range of topics ranging from the stellar astrophysics (shocks in RR Lyrae stars, and modeling the orbital motion) to Galactic archaeology (structure and kinematics of Galactic bulge, disc, and SMC). The core element connecting all of the described projects are the RR Lyrae stars, and submitted thesis hopefully conveys their usefulness across the various astrophysical fields. In the ensuing chapter, we will summarise our results and provide a possible outlook for future projects. Chapters related to individual projects like; 3, 4, 5, 6, 7, and 8 provide more extensive conclusions, thus for more detail discussion we refer interested reader to those chapters.

The initial project (see § 3) described in this thesis address the origin of the SMCNOD found north from the SMC (Pieres et al. 2017). We used publicly available photometric data (from the OGLE survey of the Magellanic Clouds Soszyński et al. 2015a; Udalski et al. 2015; Soszyński et al. 2016a) for the variable stars in the SMC and its outskirts that conveniently encompassed the SMCNOD. We found 4 anomalous Cepheids and 8 RR Lyrae stars spatially coinciding with the position of the SMCNOD. Found variable stars share physical properties, i.e., age (for anomalous Cepheids) and metallicity (for RR Lyrae stars) with variables associated with the SMC. Thus, we place the origin of the SMCNOD within the SMC itself.

The following two chapters (see chapters 4 and 5) discuss the two Oosterhoff populations of RR Lyrae stars in the Galactic bulge identified by the OGLE survey (Soszyński et al. 2014, 2017b). The Galactic bulge has been a target for similar studies in the past (e.g., Kunder & Chaboyer 2009), but we have for the first time, clearly identified and separated two Oosterhoff groups previously found only in the MW globular clusters (Oosterhoff 1939) based on the Fourier parameters of the studied RR Lyrae stars. When we compared both Oosterhoff groups with pulsation and evolutionary models (Smolec & Moskalik 2008; Pietrinferni

et al. 2004) two groups differ on average in luminosity, temperature, and mass. Neither of the two groups seems to be spatially associated with the Galactic bar, and two Oosterhoff groups seem to be evenly distributed in the Galactic bulge. From the kinematical point of view, both Oosterhoff groups share almost identical velocity distribution, and random orbits supporting the idea that they are part of the classical bulge (Kunder et al. 2016). Using the *Gaia* proper motions and publicly available systemic velocities for a subsample of RR Lyrae stars we were able to determine their orbits in the Galactic bulge and we found that approximately 8 % of them are halo interlopers currently passing through the Galactic bulge.

The fourth project (see § 6) involved RR Lyrae stars in the solar neighbourhood, where we studied their kinematical distribution with respect to the formation of the Galactic thick and thin disc. Using the *Gaia* astrometric products (coordinates, proper motions, and parallaxes) together with their systemic velocities we acquired 6D kinematical distribution for studied stars (314 RR Lyrae variables). We found that subsample of studied stars (22 in total) kinematically exhibits the properties characteristic for the thin disc stars. Available chemical information for some of these 22 stars revealed that based on their [Ca/Fe] and [Fe/H] they coincide with the Galactic thin disc stars, furthermore corroborating their association to the Galactic thin disc. This raises a question about the timescale of the Galactic thin disc formation, where we believe based on the current observations (e.g., Haywood et al. 2013; Kilic et al. 2017), and since RR Lyrae stars are assumed to be older than 10 Gyr (Catelan 2009; VandenBerg et al. 2013) their presence in the Galactic thin disc seem in contradiction.

The last two studies (see chapters 7 and 8) tackle two known problems in RR Lyrae stars which affect their use in Galactic archaeology. In the first one, we discuss the lack of known RR Lyrae stars in binary systems, and search for possible candidates among RR Lyrae variables in the Galactic bulge. Based on our search we found 20 RR Lyrae stars possibly residing in binary systems. We modeled their phase variations using $O-C$ models (Irwin 1952a) and estimated some of the physical properties of the system. Together with our candidates, the list of RR Lyrae stars suspected for binary grown over one hundred (see, Liska & Skarka 2016). The shocks in stellar atmospheres of RR Lyrae stars occurring during the pulsation cycle have been extensively studied in the past, using spectra of RR Lyrae stars. In our project we had, for the first time, performed the analysis of the shocks on the phased photometric light curves of fundamental-mode RR Lyrae stars. Shocks can be identified in photometry of RR Lyrae variables with two prominent features; humps and bumps. We developed a method on how to estimate their prominence and analysed almost 1500 RR Lyrae stars in the Galactic bulge. We found that shocks correlate with the pulsation parameters of the studied stars, and the CMD of examined stars shown a peculiar gradient concerning the size of the shocks. The shocks also do not seem to be connected to the evolutionary status of a given RR Lyrae star based on their period change rate.

Outlook

The projects outlined in this thesis provide many paths that can be followed in future research using RR Lyrae stars. Perhaps the most natural way how to define these paths would be on *photometric* and *spectroscopic*.

In the former path, the so-called *low hanging fruits* are RR Lyrae stars associated with the Galactic thin disc. Quite recently OGLE survey published photometric data on the Galactic disc viewed from the southern hemisphere for more than 10 000 RR Lyrae stars (Soszyński et al. 2019). This dataset in combination with the VVV survey (Minniti et al. 2010) and *Gaia* DR2, provides an interesting probe to the Galactic disc. One could use the *Gaia* astrometric information for these stars and calculate their tangential velocities, these could be compared with the tangential velocities of disc stars found in Prudil et al. (2020), for a small fraction of these stars *Gaia* DR2 also provides a radial velocity measurement (although without taking into account the pulsation of a star). As a proxy for [Fe/H], one can use the period-metallicity relation (Smolec 2005), and gain more insight into the dataset chemistry. Another photometric path that can be taken is related more to the stellar astrophysics, and shock in RR Lyrae stars. There are publicly available multi-colour photometric data on several MW globular clusters rich on RR Lyrae stars (e.g., M3, M5) this data can be utilized in the analysis of the humps and bumps and could potentially shed light on their structure in the CMD that we see for bulge RR Lyrae variables. This can be accompanied by data for field RR Lyrae stars from the *Kepler* and TESS space telescopes, which provide hundreds of RR Lyrae stars with exceptionally described light curves. An interesting stellar astrophysical project with shocks in RR Lyrae stars would be focused on RR Lyraes with the Blazhko effect (Blažko 1907). One could examine how the prominence of hump and bump changes in different phases of the Blazhko effect for stars with differnt prominence of the Blazhko effect. In addition, regarding the binarity among RR Lyrae stars one can always find more candidates, i.e., using extensive OGLE photometry for the LMC and SMC.

The later path provides a more urgent and pressing matter. The high-quality spectra of RR Lyrae stars have always been hard to get, partially due to shocks that temper the spectral lines, but mainly due to the pulsation that can cause asymmetries in the spectral lines (as a rule of thumb it is recommended not to integrate over 30-minute exposures). To this day, we do not have an extensive catalogue of RR Lyrae stars spectra (with one exception for Layden 1994) despite studies focused on atmospheric shocks among RR Lyrae stars (Gillet & Crowe 1988; Chadid & Gillet 1996b; Preston 2009). This then results in poorly constrained period-metallicity and period-metallicity-luminosity relations, and thus imperfect distance estimates. Facilitating a project on calibrating aforementioned relations using the high-resolution spectra for a several hundred nearest RR Lyrae stars with medium-size telescopes (any 2 m telescope with 20 minutes exposures should suffice) appears to be a prevailing problem. Based on projects described in this thesis, one can focus on the Galactic bulge population of RR Lyrae stars, especially the origin of two Oosterhoff groups identified in one of our projects (Prudil et al. 2019a). Spectroscopic follow-up of these stars dedicated to their chemistry could reveal potential differences between both groups, and hint toward their origin. Spectroscopic follow-up based on our analysis of photometric prominence of shocks is already on its way (based on our proposal for FEROS 0103.A-9029(A) DDT) we targeted 6 RR Lyrae stars observe by the TESS mission. This project aims at linking the size of humps and bumps with the spectroscopic properties of analysed stars.

Of course one could go like this forever, never reaching an end, bouncing from more to less feasible projects. Luckily, we are living in the *Gaia* era, with the upcoming multi-

object spectrographs like 4MOST (de Jong et al. 2014) and *Weave* (Dalton et al. 2014), and already running photometric missions like *Kepler* and TESS some of these projects will become possible. The following decade will hopefully tell us more about RR Lyrae stars and provide new paths to explore within and beyond the Milky Way.

Now comes the mystery ...

REFERENCES

Adibekyan V. Z., Santos N. C., Sousa S. G., Israelian G., 2011, A&A, 535, L11

Adibekyan V. Z., et al., 2013, A&A, 554, A44

Alcock C., et al., 1997, ApJ, 474, 217

Alonso-García J., Dékány I., Catelan M., Contreras Ramos R., Gran F., Amigo P., Leyton P., Minniti D., 2015, AJ, 149, 99

Anders F., et al., 2014, A&A, 564, A115

Armandroff T. E., Zinn R., 1988, AJ, 96, 92

Asplund M., Grevesse N., Sauval A. J., Scott P., 2009, ARA&A, 47, 481

Baade W., 1946, PASP, 58, 249

Bailey S. I., 1902, Annals of Harvard College Observatory, 38, 1

Bailey S. I., Pickering E. C., 1913, Annals of Harvard College Observatory, 78, 1

Balick B., Brown R. L., 1974, ApJ, 194, 265

Barbuy B., Chiappini C., Gerhard O., 2018, ARA&A, 56, 223

Bechtol K., et al., 2015, ApJ, 807, 50

Becklin E. E., Neugebauer G., 1968, ApJ, 151, 145

Beers T. C., et al., 2012, ApJ, 746, 34

Belokurov V., et al., 2007, ApJL, 657, L89

Belokurov V., Erkal D., Deason A. J., Koposov S. E., De Angeli F., Evans D. W., Fraternali F., Mackey D., 2017, MNRAS, 466, 4711

Belokurov V., Deason A. J., Koposov S. E., Catelan M., Erkal D., Drake A. J., Evans N. W., 2018a, MNRAS, 477, 1472

Belokurov V., Erkal D., Evans N. W., Koposov S. E., Deason A. J., 2018b, MNRAS, 478, 611

Benkő J. M., 2018, MNRAS, 473, 412

Benkő J. M., et al., 2010, MNRAS, 409, 1585

Benkő J. M., Plachy E., Szabó R., Molnár L., Kolláth Z., 2014, ApJS, 213, 31

Benkő J. M., Jurcsik J., Derekas A., 2019, MNRAS, 485, 5897

Bensby T., Feltzing S., Lundström I., 2003, A&A, 410, 527

Bensby T., et al., 2013, A&A, 549, A147

Bensby T., Feltzing S., Oey M. S., 2014, A&A, 562, A71

Bensby T., et al., 2017, A&A, 605, A89

Bernard E. J., et al., 2009, ApJ, 699, 1742

Bland-Hawthorn J., Gerhard O., 2016, ARA&A, 54, 529

Bland-Hawthorn J., et al., 2019, MNRAS,

Blažko S., 1907, Astronomische Nachrichten, 175, 325

Bond N. A., et al., 2010, ApJ, 716, 1

Bono G., Caputo F., Castellani V., Marconi M., 1996, ApJL, 471, L33

Bovy J., 2015, ApJS, 216, 29

Bovy J., et al., 2012, ApJ, 759, 131

Braga V. F., et al., 2015, ApJ, 799, 165

Braga V. F., Bhardwaj A., Contreras Ramos R., Minniti D., Bono G., de Grijs R., Minniti J. H., Rejkuba M., 2018, A&A, 619, A51

Bruck M. T., 1980, A&A, 87, 92

Cacciari C., Bruzzi A., 1993, A&A, 276, 87

Cacciari C., Corwin T. M., Carney B. W., 2005, AJ, 129, 267

Cardelli J. A., Clayton G. C., Mathis J. S., 1989, ApJ, 345, 245

Carollo D., et al., 2007, Nature, 450, 1020

Carollo D., et al., 2010, ApJ, 712, 692

Carretta E., Bragaglia A., Gratton R., D'Orazi V., Lucatello S., 2009, A&A, 508, 695

Carroll B., Ostlie D., 2007, An Introduction to Modern Astrophysics. Pearson Addison-Wesley, https://books.google.de/books?id=M8wPAQAAMAAJ

Casagrande L., Schönrich R., Asplund M., Cassisi S., Ramírez I., Meléndez J., Bensby T., Feltzing S., 2011, A&A, 530, A138

Catelan M., 1992, A&A, 261, 457

Catelan M., 2004, ApJ, 600, 409

Catelan M., 2009, Ap&SS, 320, 261

Catelan M., Smith H. A., 2015, Pulsating Stars. Wiley, New York

Catelan M., Pritzl B. J., Smith H. A., 2004, ApJS, 154, 633

Chadid M., Gillet D., 1996a, A&A, 308, 481

Chadid M., Gillet D., 1996b, A&A, 315, 475

Chadid M., et al., 2014, AJ, 148, 88

Chadid M., Sneden C., Preston G. W., 2017, ApJ, 835, 187

Chiba M., Beers T. C., 2000, AJ, 119, 2843

Christy R. F., 1966, ApJ, 144, 108

Cignoni M., Cole A. A., Tosi M., Gallagher J. S., Sabbi E., Anderson J., Grebel E. K., Nota A., 2013, ApJ, 775, 83

Cioni M. R. L., Habing H. J., Israel F. P., 2000, A&A, 358, L9

Clement C. M., Shelton I., 1999, ApJL, 515, L85

Clementini G., Held E. V., Baldacci L., Rizzi L., 2003, ApJL, 588, L85

Clementini G., Gratton R. G., Bragaglia A., Ripepi V., Martinez Fiorenzano A. F., Held E. V., Carretta E., 2005, ApJL, 630, L145

Clementini G., et al., 2019a, A&A, 622, A60

Clementini G., et al., 2019b, A&A, 622, A60

Connors T. W., Kawata D., Gibson B. K., 2006, MNRAS, 371, 108

Cox J. P., 1958, ApJ, 127, 194

Cox A. N., 1998, ApJ, 496, 246

Cox J. P., Whitney C., 1958, ApJ, 127, 561

Cutri R. M., et al. 2012, VizieR Online Data Catalog, 2311

Cutri R. M., et al., 2003, VizieR Online Data Catalog, p. II/246

D'Onghia E., Fox A. J., 2016, ARA&A, 54, 363

D'Onghia E., Besla G., Cox T. J., Hernquist L., 2009, Nature, 460, 605

Dalton G., et al., 2014, in Ground-based and Airborne Instrumentation for Astronomy V. p. 91470L (arXiv:1412.0843), doi:10.1117/12.2055132

Dambis A. K., Berdnikov L. N., Kniazev A. Y., Kravtsov V. V., Rastorguev A. S., Sefako R., Vozyakova O. V., 2013, MNRAS, 435, 3206

Davis M., Peebles P. J. E., 1983, ApJ, 267, 465

Debattista V. P., Mayer L., Carollo C. M., Moore B., Wadsley J., Quinn T., 2006, ApJ, 645, 209

Dehnen W., 2000, AJ, 119, 800

Dékány I., Minniti D., Catelan M., Zoccali M., Saito R. K., Hempel M., Gonzalez O. A., 2013, ApJL, 776, L19

Dékány I., Hajdu G., Grebel E. K., Catelan M., Elorrieta F., Eyheramendy S., Majaess D., Jordán A., 2018, ApJ, 857, 54

Demarque P., Hirshfeld A. W., 1975, ApJ, 202, 346

Diaz J., Bekki K., 2011, MNRAS, 413, 2015

Diaz J. D., Bekki K., 2012, ApJ, 750, 36

Dorfi E. A., Feuchtinger M. U., 1999, A&A, 348, 815

Drake A. J., et al., 2013, ApJ, 763, 32

Drlica-Wagner A., et al., 2015, ApJ, 813, 109

Drlica-Wagner A., et al., 2016, ApJL, 833, L5

Dwek E., et al., 1995, ApJ, 445, 716

ESA ed. 1997, The HIPPARCOS and TYCHO catalogues. Astrometric and photometric star catalogues derived from the ESA HIPPARCOS Space Astrometry Mission ESA Special Publication Vol. 1200

Eddington A. S., 1926, The Internal Constitution of the Stars. Cambridge University Press

Edvardsson B., Andersen J., Gustafsson B., Lambert D. L., Nissen P. E., Tomkin J., 1993, A&A, 275, 101

Erwin P., et al., 2015, MNRAS, 446, 4039

Evans D. W., et al., 2018, A&A, 616, A4

Fabrizio M., et al., 2019, ApJ, 882, 169

Fernley J., Barnes T. G., 1997, A&AS, 125, 313

Fiorentino G., Monelli M., 2012, A&A, 540, A102

Fiorentino G., et al., 2015, ApJL, 798, L12

Fokin A. B., 1992, MNRAS, 256, 26

Freeman K., et al., 2013, MNRAS, 428, 3660

Fuhrmann K., 1998, A&A, 338, 161

Gaia Collaboration et al., 2016a, A&A, 595, A1

Gaia Collaboration et al., 2016b, A&A, 595, A2

Gaia Collaboration et al., 2018a, A&A, 616, A1

Gaia Collaboration et al., 2018b, A&A, 616, A14

Gallart C., Bernard E. J., Brook C. B., Ruiz-Lara T., Cassisi S., Hill V., Monelli M., 2019, Nature Astronomy, 3, 932

Gardiner L. T., Hatzidimitriou D., 1992, MNRAS, 257, 195

Gardiner L. T., Noguchi M., 1996, MNRAS, 278, 191

Gardiner L. T., Sawa T., Fujimoto M., 1994, MNRAS, 266, 567

Gibbons S. L. J., Belokurov V., Evans N. W., 2014, MNRAS, 445, 3788

Gillessen S., Eisenhauer F., Trippe S., Alexand er T., Genzel R., Martins F., Ott T., 2009, ApJ, 692, 1075

Gillet D., Crowe R. A., 1988, A&A, 199, 242

Gilmore G., Reid N., 1983, MNRAS, 202, 1025

Girardi L., Bressan A., Bertelli G., Chiosi C., 2000, A&AS, 141, 371

Glatt K., et al., 2008, AJ, 135, 1106

Golubov O., et al., 2013, A&A, 557, A92

Gonzalez O. A., Rejkuba M., Minniti D., Zoccali M., Valenti E., Saito R. K., 2011, A&A, 534, L14

Gonzalez O. A., Rejkuba M., Zoccali M., Valenti E., Minniti D., Schultheis M., Tobar R., Chen B., 2012, A&A, 543, A13

Graczyk D., et al., 2014, ApJ, 780, 59

Gravity Collaboration et al., 2019, A&A, 625, L10

Grebel E. K., Gallagher John S. I., Harbeck D., 2003, AJ, 125, 1926

Grevesse N., Sauval A. J., 1998, SSRv, 85, 161

Gruberbauer M., et al., 2007, MNRAS, 379, 1498

Guggenberger E., et al., 2012, MNRAS, 424, 649

Guggenberger E., Barnes T. G., Kolenberg K., 2016, Communications of the Konkoly Observatory Hungary, 105, 145

Guiglion G., et al., 2015, A&A, 583, A91

Hajdu G., Catelan M., Jurcsik J., Dekany I., Drake A. J., Marquette J. B., 2015, MNRAS, 449, L113

Hajdu G., Dékány I., Catelan M., Grebel E. K., Jurcsik J., 2018, ApJ, 857, 55

Hamanowicz A., et al., 2016, AcA, 66, 197

Hamilton A. J. S., 1993, ApJ, 417, 19

Hansen C. J., et al., 2011, A&A, 527, A65

Hansen C. J., Rich R. M., Koch A., Xu S., Kunder A., Ludwig H. G., 2016, A&A, 590, A39

Hartigan J. A., Hartigan P. M., 1985, Ann. Statist., 13, 70

Haschke R., Grebel E. K., Duffau S., 2012a, AJ, 144, 106

Haschke R., Grebel E. K., Duffau S., 2012b, AJ, 144, 107

Hayden M. R., et al., 2015, ApJ, 808, 132

Hayden M. R., Recio-Blanco A., de Laverny P., Mikolaitis S., Worley C. C., 2017, A&A, 608, L1

Hayden M. R., et al., 2019, arXiv e-prints, p. arXiv:1901.07565

Hayes C. R., et al., 2018, ApJ, 852, 49

Haywood M., 2008, MNRAS, 388, 1175

Haywood M., Di Matteo P., Lehnert M. D., Katz D., Gómez A., 2013, A&A, 560, A109

Haywood M., Di Matteo P., Snaith O., Lehnert M. D., 2015, A&A, 579, A5

Haywood M., Di Matteo P., Lehnert M. D., Snaith O., Khoperskov S., Gómez A., 2018, ApJ, 863, 113

Helmi A., Babusiaux C., Koppelman H. H., Massari D., Veljanoski J., Brown A. G. A., 2018, Nature, 563, 85

Helminiak K. G., Devor J., Minniti D., Sybilski P., 2013, MNRAS, 432, 2895

Hernitschek N., et al., 2018, ApJ, 859, 31

Hernitschek N., et al., 2019, ApJ, 871, 49

Hertzsprung E., 1919, Astronomische Nachrichten, 210, 17

Hill S. J., 1972, ApJ, 178, 793

Hindman J. V., Kerr F. J., McGee R. X., 1963, Australian Journal of Physics, 16, 570

Holmberg J., Flynn C., 2000, MNRAS, 313, 209

Howard C. D., et al., 2009, ApJL, 702, L153

Ibata R., Lewis G. F., Irwin M., Totten E., Quinn T., 2001, ApJ, 551, 294

Iglesias C. A., Rogers F. J., 1996, ApJ, 464, 943

Indu G., Subramaniam A., 2015, A&A, 573, A136

Irwin J. B., 1952a, ApJ, 116, 211

Irwin J. B., 1952b, ApJ, 116, 218

Ivezić Ž., et al., 2008, ApJ, 684, 287

Ivezić Ž., Connelly A. J., VanderPlas J. T., Gray A., 2014, Statistics, Data Mining, and Machine Learning in Astronomy. Princeton University Press

Jacyszyn-Dobrzeniecka A. M., et al., 2016, AcA, 66, 149

Jacyszyn-Dobrzeniecka A. M., et al., 2017, AcA, 67, 1

Jacyszyn-Dobrzeniecka A. M., et al., 2020, ApJ, 889, 26

Jayasinghe T., et al., 2018, MNRAS, 477, 3145

Jayasinghe T., et al., 2019, MNRAS, 486, 1907

Johnson D. R. H., Soderblom D. R., 1987, AJ, 93, 864

Jordi C., et al., 2010, A&A, 523, A48

Jurcsik J., 1995, AcA, 45, 653

Jurcsik J., Kovacs G., 1996, A&A, 312, 111

Jurcsik J., Smitola P., 2016, Commmunications of the Konkoly Observatory Hungary, 105, 167

Jurcsik J., Clement C., Geyer E. H., Domsa I., 2001, AJ, 121, 951

Jurcsik J., et al., 2012, MNRAS, 419, 2173

Jurcsik J., Hajdu G., Dékány I., Nuspl J., Catelan M., Grebel E. K., 2018, MNRAS, 475, 4208

Jurić M., et al., 2008, ApJ, 673, 864

Kallivayalil N., van der Marel R. P., Alcock C., 2006, ApJ, 652, 1213

Kapakos E., Hatzidimitriou D., Soszyński I., 2011, MNRAS, 415, 1366

Karczmarek P., et al., 2015, AJ, 150, 90

Karczmarek P., Pietrzyński G., Górski M., Gieren W., Bersier D., 2017, AJ, 154, 263

Kennedy C. R., et al., 2014, ApJ, 787, 6

Kerr F. J., Lynden-Bell D., 1986, MNRAS, 221, 1023

Kervella P., et al., 2019a, A&A, 623, A116

Kervella P., et al., 2019b, A&A, 623, A117

Kilic M., Munn J. A., Harris H. C., von Hippel T., Liebert J. W., Williams K. A., Jeffery E., DeGennaro S., 2017, ApJ, 837, 162

Kim S.-L., et al., 2016, Journal of Korean Astronomical Society, 49, 37

Kinemuchi K., Smith H. A., Woźniak P. R., McKay T. A., ROTSE Collaboration 2006, AJ, 132, 1202

Kinemuchi K., Harris H. C., Smith H. A., Silbermann N. A., Snyder L. A., La Cluyzé A. P., Clark C. L., 2008, AJ, 136, 1921

Kinman T. D., Morrison H. L., Brown W. R., 2009, AJ, 137, 3198

Kochanek C. S., et al., 2017, PASP, 129, 104502

Kolláth Z., Molnár L., Szabó R., 2011, MNRAS, 414, 1111

Koopmann R. A., Lee Y.-W., Demarque P., Howard J. M., 1994, ApJ, 423, 380

Koposov S. E., Rix H.-W., Hogg D. W., 2010, ApJ, 712, 260

Kordopatis G., et al., 2013, AJ, 146, 134

Kormendy J., Kennicutt Robert C. J., 2004, ARA&A, 42, 603

Kovacs G., 2016, Commmunications of the Konkoly Observatory Hungary, 105, 61

Kunder A., Chaboyer B., 2009, AJ, 138, 1284

Kunder A., et al., 2011, AJ, 141, 15

Kunder A., et al., 2012, AJ, 143, 57

Kunder A., et al., 2015, ApJL, 808, L12

Kunder A., et al., 2016, ApJL, 821, L25

Kunder A., et al., 2017, AJ, 153, 75

Kunder A., et al., 2018, AJ, 155, 171

Kunder A., et al., 2019, ApJL, 877, L17

Kurucz R. L., 2005, Memorie della Societa Astronomica Italiana Supplementi, 8, 14

Lambert D. L., Heath J. E., Lemke M., Drake J., 1996, ApJS, 103, 183

Landy S. D., Szalay A. S., 1993, ApJ, 412, 64

Laskarides P. G., 1974, Ap&SS, 27, 485

Layden A. C., 1994, AJ, 108, 1016

Layden A. C., Hanson R. B., Hawley S. L., Klemola A. R., Hanley C. J., 1996, AJ, 112, 2110

Le Borgne J. F., et al., 2007, A&A, 476, 307

Lee Y.-W., Demarque P., 1990, ApJS, 73, 709

Lee Y. S., et al., 2011, ApJ, 738, 187

Lee J.-W., López-Morales M., Hong K., Kang Y.-W., Pohl B. L., Walker A., 2014a, ApJS, 210, 6

Lee C.-U., Kim S.-L., Cha S.-M., Lee Y., Kim D.-J., Park B.-G., 2014b, in Ground-based and Airborne Telescopes V. p. 91453T, doi:10.1117/12.2055571

Li L.-J., Qian S.-B., 2014, MNRAS, 444, 600

Li L.-J., Qian S.-B., Zhu L.-Y., 2018, ApJ, 863, 151

Lindegren L., et al., 2018, A&A, 616, A2

Liska J., Skarka M., 2016, Commmunications of the Konkoly Observatory Hungary, 105, 209

Liu S., Zhao G., Chen Y.-Q., Takeda Y., Honda S., 2013, Research in Astronomy and Astrophysics, 13, 1307

Liška J., Skarka M., Mikulášek Z., Zejda M., Chrastina M., 2016, A&A, 589, A94

Liška J., Skarka M., Zejda M., Mikulášek Z., de Villiers S. N., 2016, MNRAS, 459, 4360

Lomb N. R., 1976, Ap&SS, 39, 447

Lütticke R., Dettmar R. J., Pohlen M., 2000, A&AS, 145, 405

Madore B. F., 1976, in The Galaxy and the Local Group. p. 153

Madore B. F., et al., 2013, ApJ, 776, 135

Maintz G., de Boer K. S., 2005, A&A, 442, 229

Majaess D., Turner D., Dékány I., Minniti D., Gieren W., 2016, A&A, 593, A124

Marconi M., Fiorentino G., Caputo F., 2004, A&A, 417, 1101

Marconi M., et al., 2015, ApJ, 808, 50

Marsakov V. A., Gozha M. L., Koval V. V., 2018, Astronomy Reports, 62, 50

Marsakov V. A., Gozha M. L., Koval' V. V., 2019a, Astrophysics, 62, 467

Marsakov V. A., Gozha M. L., Koval' V. V., 2019b, Astronomy Reports, 63, 203

Martinez-Valpuesta I., Shlosman I., Heller C., 2006, ApJ, 637, 214

Mateu C., Vivas A. K., 2018, MNRAS, 479, 211

Mateu C., Vivas A. K., Downes J. J., Briceño C., Zinn R., Cruz-Diaz G., 2012, MNRAS, 427, 3374

McMillan P. J., 2011, MNRAS, 414, 2446

McNamara D. H., Barnes J., 2014, AJ, 147, 31

McWilliam A., Zoccali M., 2010, ApJ, 724, 1491

Medina G. E., et al., 2018, ApJ, 855, 43

Messier C., 1781, Connoissance des Temps ou des Mouvements Célestes, for 1784, p. 227-267, pp 227–267

Miceli A., et al., 2008, ApJ, 678, 865

Minniti D., et al., 2010, NewA, 15, 433

Minniti D., et al., 2017, AJ, 153, 179

Miyamoto M., Nagai R., 1975, PASJ, 27, 533

Monelli M., Fiorentino G., Bernard E. J., Martínez-Vázquez C. E., Bono G., Gallart C., Dall'Ora M., Stetson P. B., 2017, ApJ, 842, 60

Mowlavi N., et al., 2018, A&A, 618, A58

Muraveva T., et al., 2015, ApJ, 807, 127

Muraveva T., Delgado H. E., Clementini G., Sarro L. M., Garofalo A., 2018, MNRAS, 481, 1195

Myeong G. C., Evans N. W., Belokurov V., Sanders J. L., Koposov S. E., 2018, ApJL, 863, L28

Nataf D. M., Udalski A., Gould A., Fouqué P., Stanek K. Z., 2010, ApJL, 721, L28

Nataf D. M., et al., 2013, ApJ, 769, 88

Navarro J. F., Frenk C. S., White S. D. M., 1997, ApJ, 490, 493

Nemec J. M., 1985, AJ, 90, 204

Nemec J. M., et al., 2011, MNRAS, 417, 1022

Ness M., et al., 2012, ApJ, 756, 22

Ness M., et al., 2013a, MNRAS, 430, 836

Ness M., et al., 2013b, MNRAS, 432, 2092

Netzel H., Smolec R., Moskalik P., 2015a, MNRAS, 447, 1173

Netzel H., Smolec R., Dziembowski W., 2015b, MNRAS, 451, L25

Netzel H., Smolec R., Moskalik P., 2015c, MNRAS, 453, 2022

Netzel H., Smolec R., Soszyński I., Udalski A., 2018, MNRAS, 480, 1229

Newberg H. J., et al., 2002, ApJ, 569, 245

Nishiyama S., et al., 2005, ApJL, 621, L105

Nissen P. E., Schuster W. J., 2010, A&A, 511, L10

Nordström B., et al., 2004, A&A, 418, 989

Norris J., Zinn R., 1975, ApJ, 202, 335

Obreja A., Domínguez-Tenreiro R., Brook C., Martínez-Serrano F. J., Doménech-Moral M., Serna A., Mollá M., Stinson G., 2013, ApJ, 763, 26

Olah K., Szeidl B., 1978, Communications of the Konkoly Observatory Hungary, 71, 1

Oosterhoff P. T., 1939, The Observatory, 62, 104

Oosterhoff P. T., 1944, BAN, 10, 55

Oswalt T. D., Smith J. A., Wood M. A., Hintzen P., 1996, Nature, 382, 692

Paczynski B., 1991, ApJL, 371, L63

Pancino E., Britavskiy N., Romano D., Cacciari C., Mucciarelli A., Clementini G., 2015, MNRAS, 447, 2404

Papadakis I., Hatzidimitriou D., Croke B. F. W., Papamastorakis I., 2000, AJ, 119, 851

Paparo M., Saad S. M., Szeidl B., Kollath Z., Abu Elazm M. S., Sharaf M. A., 1998, A&A, 332, 102

Pawlak M., et al., 2016, AcA, 66, 421

Pedregosa F., et al., 2011, Journal of Machine Learning Research, 12, 2825

Peebles P. J. E., 1980, in Ninth Texas Symposium on Relativistic Astrophysics. pp 161–171, doi:10.1111/j.1749-6632.1980.tb15927.x

Petersen J. O., 1973, A&A, 27, 89

Pickering E. C., 1901, Astronomische Nachrichten, 154, 423

Pickering E. C., Bailey S. I., 1895, ApJ, 2

Pieres A., et al., 2017, MNRAS, 468, 1349

Pietrinferni A., Cassisi S., Salaris M., Castelli F., 2004, ApJ, 612, 168

Pietrukowicz P., et al., 2015, ApJ, 811, 113

Pietrzyński G., et al., 2008, AJ, 135, 1993

Pietrzyński G., et al., 2012, Nature, 484, 75

Pietrzyński G., et al., 2013, Nature, 495, 76

Pietrzyński G., et al., 2019, Nature, 567, 200

Pojmanski G., 1997, AcA, 47, 467

Pojmanski G., 2002, AcA, 52, 397

Popielski B. L., Dziembowski W. A., Cassisi S., 2000, AcA, 50, 491

Poretti E., Le Borgne J.-F., Klotz A., Rainer M., Correa M., 2018, in The RR Lyrae 2017 Conference. Revival of the Classical Pulsators: from Galactic Structure to Stellar Interior Diagnostics. pp 151–156

Preston G. W., 2009, A&A, 507, 1621

Preston G. W., Paczynski B., 1964, ApJ, 140, 181

Preston G. W., Smak J., Paczynski B., 1965, ApJS, 12, 99

Pritzl B., Smith H. A., Catelan M., Sweigart A. V., 2000, ApJL, 530, L41

Prudil Z., Skarka M., 2017, MNRAS, 466, 2602

Prudil Z., Smolec R., Skarka M., Netzel H., 2017, MNRAS, 465, 4074

Prudil Z., Grebel E. K., Dékány I., Smolec R., Skarka M., 2018a, in The RR Lyrae 2017 Conference. Revival of the Classical Pulsators: from Galactic Structure to Stellar Interior Diagnostics. pp 37–41

Prudil Z., Grebel E. K., Dékány I., Smolec R., 2018b, MNRAS, 480, 669

Prudil Z., Dékány I., Catelan M., Smolec R., Grebel E. K., Skarka M., 2019a, MNRAS, 484, 4833

Prudil Z., Skarka M., Liška J., Grebel E. K., Lee C. U., 2019b, MNRAS, 487, L1

Prudil Z., Dékány I., Grebel E. K., Catelan M., Skarka M., Smolec R., 2019c, MNRAS, 487, 3270

Prudil Z., Dékány I., Grebel E. K., Kunder A., 2020, MNRAS, 492, 3408

Qu Y., Di Matteo P., Lehnert M. D., van Driel W., Jog C. J., 2011, A&A, 535, A5

Recio-Blanco A., et al., 2016, A&A, 585, A93

Reddy B. E., Tomkin J., Lambert D. L., Allende Prieto C., 2003, MNRAS, 340, 304

Reid M. J., Brunthaler A., 2004, ApJ, 616, 872

Reimers D., 1975, Memoires of the Societe Royale des Sciences de Liege, 8, 369

Renzini A., Mengel J. G., Sweigart A. V., 1977, A&A, 56, 369

Rimoldini L., et al., 2019, A&A, 625, A97

Ritter A., 1879, Annalen der Physik, 244, 157

Roederer I. U., Preston G. W., Thompson I. B., Shectman S. A., Sneden C., Burley G. S., Kelson D. D., 2014, AJ, 147, 136

Roelens M., et al., 2018, A&A, 620, A197

Rosenbaum P. R., 2005, Journal of the Royal Statistical Society: Series B (Statistical Methodology), 67, 515

Saha A., White R. E., 1990, PASP, 102, 148

Sandage A., 1981, ApJ, 248, 161

Sandage A., 2004, AJ, 128, 858

Sandage A., 2006, AJ, 131, 1750

Sandage A., Katem B., Sandage M., 1981, ApJS, 46, 41

Scargle J. D., 1982, ApJ, 263, 835

Schlafly E. F., Finkbeiner D. P., 2011, ApJ, 737, 103

Schönrich R., 2012, MNRAS, 427, 274

Schönrich R., Binney J., Dehnen W., 2010, MNRAS, 403, 1829

Schwarzschild M., 1940, Harvard College Observatory Circular, 437, 1

Sérsic J. L., 1963, Boletin de la Asociacion Argentina de Astronomia La Plata Argentina, 6, 41

Sesar B., Jurić M., Ivezić Ž., 2011, ApJ, 731, 4

Sesar B., et al., 2013, AJ, 146, 21

Shappee B. J., et al., 2014, ApJ, 788, 48

Shen J., Rich R. M., Kormendy J., Howard C. D., De Propris R., Kunder A., 2010, ApJL, 720, L72

Shibahashi H., 2017, in European Physical Journal Web of Conferences. p. 03006, doi:10.1051/epjconf/201715203006

Silva Aguirre V., Catelan M., Weiss A., Valcarce A. A. R., 2008, A&A, 489, 1201

Simion I. T., Belokurov V., Koposov S. E., 2019, MNRAS, 482, 921

Simon N. R., 1988, in Stalio R., Willson L. A., eds, Pulsation and Mass Loss in Stars. Springer Netherlands, Dordrecht, pp 27–50

Skarka M., 2013, A&A, 549, A101

Skarka M., Liska J., Zejda M., Mikulasek Z., 2016, Communications of the Konkoly Observatory Hungary, 105, 141

Skarka M., Liška J., Dřevěný R., Guggenberger E., Sódor Á., Barnes T. G., Kolenberg K., 2018, MNRAS, 474, 824

Skarka M., Prudil Z., Jurcsik J., 2020, arXiv e-prints, p. arXiv:2001.00754

Skowron D. M., et al., 2014, ApJ, 795, 108

Skowron D. M., et al., 2016, AcA, 66, 269

Skrutskie M. F., et al., 2006, AJ, 131, 1163

Smith H. A., 1995, Cambridge Astrophysics Series, 27

Smolec R., 2005, AcA, 55, 59

Smolec R., 2016, in Różańska A., Bejger M., eds, 37th Meeting of the Polish Astronomical Society Vol. 3, Proc. of the Polish Astron. Soc. p. 22 (arXiv:1603.01252)

Smolec R., Moskalik P., 2008, AcA, 58, 193

Smolec R., et al., 2013, MNRAS, 428, 3034

Smolec R., et al., 2015a, MNRAS, 447, 3873

Smolec R., et al., 2015b, MNRAS, 447, 3756

Smolec R., Prudil Z., Skarka M., Bakowska K., 2016, MNRAS, 461, 2934

Solano E., Garrido R., Fernley J., Barnes T. G., 1997, A&AS, 125, 321

Soszyński I., 2018, in XXXVIII Polish Astronomical Society Meeting. pp 168–174

Soszyński I., et al., 2009, AcA, 59, 1

Soszyński I., et al., 2011, AcA, 61, 1

Soszyński I., et al., 2014, AcA, 64, 177

Soszyński I., et al., 2015a, AcA, 65, 233

Soszyński I., et al., 2015b, AcA, 65, 297

Soszyński I., et al., 2016a, AcA, 66, 131

Soszyński I., et al., 2016b, MNRAS, 463, 1332

Soszyński I., et al., 2017a, AcA, 67, 103

Soszyński I., et al., 2017b, AcA, 67, 297

Soszyński I., et al., 2019, AcA, 69, 321

Sparke L. S., Gallagher III J. S., 2007, Galaxies in the Universe: An Introduction, 2 edn. Cambridge University Press, doi:10.1017/CBO9780511807237

Stanimirović S., Staveley-Smith L., Jones P. A., 2004, ApJ, 604, 176

Steinmetz M., et al., 2006, AJ, 132, 1645

Sterken C., 2005, in Sterken C., ed., Astronomical Society of the Pacific Conference Series Vol. 335, The Light-Time Effect in Astrophysics: Causes and cures of the O-C diagram. p. 3

Struve O., Blaauw A., 1948, ApJ, 108, 60

Subramanian S., Subramaniam A., 2009, A&A, 496, 399

Sweigart A. V., 1987, ApJS, 65, 95

Sweigart A. V., Renzini A., 1979, A&A, 71, 66

Sysoliatina K., et al., 2018, A&A, 614, A63

Szabó R., 2014, in Guzik J. A., Chaplin W. J., Handler G., Pigulski A., eds, IAU Symposium Vol. 301, Precision Asteroseismology. pp 241–248 (arXiv:1309.3969), doi:10.1017/S1743921313014397

Szabó R., et al., 2010, MNRAS, 409, 1244

Szeidl B., Olah K., Mizser A., 1986, Commmunications of the Konkoly Observatory Hungary, 89, 57

Tenenbaum J. B., de Silva V., Langford J. C., 2000, Science, 290, 2319

The Dark Energy Survey Collaboration 2005, arXiv e-prints, pp astro–ph/0510346

Tsapras Y., et al., 2017, MNRAS, 465, 2489

Udalski A., Szymanski M., Kaluzny J., Kubiak M., Mateo M., 1992, AcA, 42, 253

Udalski A., Kubiak M., Szymanski M., Kaluzny J., Mateo M., Krzeminski W., 1994, AcA, 44, 317

Udalski A., Szymanski M., Kaluzny J., Kubiak M., Mateo M., Krzeminski W., 1995a, AcA, 45, 1

Udalski A., Olech A., Szymanski M., Kaluzny J., Kubiak M., Mateo M., Krzeminski W., 1995b, AcA, 45, 433

Udalski A., Olech A., Szymanski M., Kaluzny J., Kubiak M., Krzeminski W., Mateo M., Stanek K. Z., 1996, AcA, 46, 51

Udalski A., Olech A., Szymanski M., Kaluzny J., Kubiak M., Mateo M., Krzeminski W., Stanek K. Z., 1997, AcA, 47, 1

Udalski A., Szymański M. K., Szymański G., 2015, AcA, 65, 1

VandenBerg D. A., Brogaard K., Leaman R., Casagrande L., 2013, ApJ, 775, 134

Vasiliev E., 2019, MNRAS, 484, 2832

Villalobos Á., Helmi A., 2009, MNRAS, 399, 166

Vivas A. K., et al., 2001, ApJL, 554, L33

Wade R. A., Donley J., Fried R., White R. E., Saha A., 1999, AJ, 118, 2442

Watson C. L., Henden A. A., Price A., 2006, Society for Astronomical Sciences Annual Symposium, 25, 47

Wegg C., Gerhard O., 2013, MNRAS, 435, 1874

Weiland J. L., et al., 1994, ApJL, 425, L81

Wright E. L., et al., 2010, AJ, 140, 1868

Wyse R. F. G., Gilmore G., Franx M., 1997, ARA&A, 35, 637

Zhevakin S. A., 1959, AZh, 36, 269

Zinn R., Dahn C. C., 1976, AJ, 81, 527

Zinn R., West M. J., 1984, ApJS, 55, 45

Zoccali M., Hill V., Lecureur A., Barbuy B., Renzini A., Minniti D., Gómez A., Ortolani S., 2008, A&A, 486, 177

de Grijs R., Bono G., 2015, AJ, 149, 179

de Jong R. S., et al., 2014, in Ground-based and Airborne Instrumentation for Astronomy V. p. 91470M, doi:10.1117/12.2055826

de Vaucouleurs G., Freeman K. C., 1972, Vistas in Astronomy, 14, 163

van Albada T. S., Baker N., 1973, ApJ, 185, 477

ACKNOWLEDGMENTS

“Cut to the chase..."

— Hal Roach Sr

The final remarks in this thesis belong to all the people without whom this piece of work would never came to be.

I would like to express my gratitude to my supervisor Eva Grebel, who welcomed me in her group, helped me to became a part of the Hector Fellow Academy, and gave me the freedom to explore all the possible projects that not always closely related to the Galactic archaeology. Thank you, for all the science and non-science discussions, especially for those related to current cinematography (and chocolates).

Special thanks go to my co-advisors István Dékány, and Radek Smolec who agreed to be on my thesis committee, and who guided me in our projects from start to finish. Your insight on statistics, machine learning, theory, and RR Lyraes stars as such, shaped me as a researcher I am today. Without you guys, I would never make it this far. I have to extend my gratitude to my collaborators Márcio Catelan, Marek Skarka, Jiří Liška, Bertrand Lemasle, and Andrea Kunder, who always encouraged me to work on new projects, and our discussions always left me thinking how much I still have to learn. Thank you for challenging me to do more!

I am also thankful to Joachim Wambsganß for agreeing to be the second referee of my thesis, and to Mario Trieloff and Jochen Heidt for agreeing to take part in my examination committee. Thanks to Christian Fendt for managing the IMPRS and organizing events that brought us, students, together.

When it comes to the useful scientific and off-topic discussions, I have to express my gratitude to Andreas Just, Andreas Koch, Kseniia Sysoliatina, Anna Pasquali, Andreas Koch, Alessandro

Savino, Camilla Hansen, Bertrand Lemasle and the whole Spectros' coffee group. I have to also thank the Hector Fellow Academy for their financial support during my studies, useful seminars, networking, and state-of-the-art symposia.

Furthermore, I am grateful that have been part of the Galaxy evolution group with all its current and past members, thank you all for the introduction to science, many laughs, and chocolates (and cakes)! Special thanks go to all my friends at ARI and other equaly important institutes; Sarah Jeffreson, Marta Reina-Campos, Alex Hygate, Daniel Haydon, Matteo Mazzarini, Jonas Klüter, Thomas Jackson, Josefina Michea, Nico Winkel, Paula Sarkis, Manuel Riener, Ondrej Jaura, Theodoros Anagnos, and Gergely Hajdu. Without you, this Ph.D. rollercoaster would never be nearly as funny and enjoyable as it was.

A big shout-out goes to my current and past office mates; Gustavo Morales, Yasna Ordenes-Briceño, Gustavo Medina Toledo, Bahar Bidaran, for their positive attitude to my dark humour, and all the fun moments. Michael *Jägermeister*® Hanke, thank you for keeping me sane, occasionally drunk, and for always being ready to collaborate on the darkest, meanest, and the most politically incorrect one-liners.

None of the above would be even remotely possible without my parents that supported and believed in me on this path for the past decade, I will never be able to thank you enough. To my beloved Faezeh, words cannot express my gratitude for your unconditional support and love that immensely helped me during the Ph.D., thank you for everything, asheghetam Ferferi khanum.

Someone smarter than me once said

"*"It takes a village to raise a child.*"

well, this was my village.